The Infrared Driven *cis-trans* Isomerization Reaction of Nitrous Acid (HONO) and Energy Transport in Peptide Helices

---

Dissertation
zur
Erlangung der naturwissenschaftlichen Doktorwürde
(Dr. sc. nat.)

vorgelegt der
Mathematisch-naturwissenschaftlichen Fakultät
der
Universität Zürich

von
Virgiliu Botan
aus
Rumänien

Promotionskomitee
Prof. Dr. Peter Hamm (Vorsitz)
Prof. Dr. Stefan Seeger
Prof. Dr. Jürg Hutter

Zürich, 2008

List of publications

The results of this thesis have been published in the following articles:

- Roland Schanz, **Virgiliu Botan**, Peter Hamm
  A Femtosecond Study of the IR-driven Cis-Trans Isomerization of Nitrous Acid (HONO)
  J. Chem. Phys., 122, 044509, (**2005**)
- **Virgiliu Botan**, Roland Schanz, Peter Hamm
  The infrared-driven cis-trans isomerization of HONO II: Vibrational relaxation and slow isomerization channel
  J. Chem. Phys., 124, 234511, (**2006**)
- **Virgiliu Botan**, Peter Hamm
  Temperature Dependence of the IR Driven Cis-Trans Isomerization of Nitrous Acid (HONO)
  J. Chem. Phys., *in press*, (**2008**)
- **Virgiliu Botan**, Peter Hamm
  Intramolecular Energy Redistribution in Nitrous Acid (HONO)
  J. Chem. Phys., *in press*, (**2008**)
- **Virgiliu Botan**, Peter Hamm
  Rotational dynamics of nitrous acid (HONO) in Kr matrix
  J. Chem. Phys., 129, 044507, (**2008**)
- **Virgiliu Botan**, Ellen H. G. Backus, Rolf Pfister, Alessandro Moretto, Marco Crisma, Claudio Toniolo, Phuong H. Nguyen, Gerhard Stock, Peter Hamm
  Energy Transport in Peptide Helices
  Proc. Natl. Acad. Sci., 104, 12749, (**2007**)
- Ellen H. G. Backus, Phuong H. Nguyen, **Virgiliu Botan**, Rolf Pfister, Alessandro Moretto, Marco Crisma, Claudio Toniolo, Gerhard Stock, Peter Hamm
  Energy transport in peptide helices: A comparison between high- and low-energy excitations
  J. Phys. Chem. B, 112, 9091, (**2008**)
- Ellen H. G. Backus, Phuong H. Nguyen, **Virgiliu Botan**, Alessandro Moretto, Marco Crisma, Claudio Toniolo, Oliver Zerbe, Gerhard Stock, Peter Hamm
  Structural flexibility of a helical peptide regulates heat transport properties
  J. Phys. Chem. B, submitted (**2008**)

Contents

Abstract

This thesis contains the results of two distinct scientific inquiries. The first part investigates a model system for ground state chemical reactions whereas the second part examines the energy transport in peptide helices.

The *cis-trans* isomerization of nitrous acid (HONO) in solid matrices is a model system of a chemical reaction in the electronic ground state. The isomerization reaction is reversible and can be triggered by the photo-excitation of the OH stretch. Exciting OH_{cis} in an IR pump - IR probe experiment, we observed vibrationally hot *trans* molecules on an ultrafast time scale (20-50 ps) with the isomerization following a two step process. The first step corresponds to the direct coupling of the vibrational excited state with the reaction channel state(s), whereas the second step represents the energy that is re-fed in the reaction channel from intermediate states (states that get populated by the OH_{cis}). The quantum yield of the *cis→trans* isomerization reaction after exciting OH_{cis} increases by 30% when cooling the matrix from 30 K to 15 K, being (at the low temperature) 50-70%. We also estimated that the quantum yield of the backward reaction decreases by approximatively 40% in the same temperature range. This behavior is explained in the framework of Marcus theory of electron and proton transfer in the barrierless regime. In this regime, the theory predicts a 40% increase in quantum yield of the forward reaction, in agreement with the 30% from experiment. Hence, quantum yield could go up to 100% at sufficiently low temperatures. A wealth of information about the dynamics of the isomerization reaction and the cooling process following excitation was obtained by performing two color experiments, in which OH stretch, N=O stretch and HON bend were excited and probed in different combinations. The rotational dynamics of the *cis* and *trans* isomers were investigated in the Kr matrix at 30 K. We observed that the central atoms of the molecule rotate in a hula hoop motion upon the H isomerization. With these series of experiments, we were the first to study the ultrafast dynamics of a ground state reaction in the low excitation regime.

To investigate the mechanism of heat transport in peptide helices, we designed an eight amino acid peptide helix to which we attached an azobenzene

chromophore. After exciting the azobenzene with a UV pulse, we followed the heat propagation through the helix using the shifts in the amide I band in the IR. With the help of isotope labeling, we were able to spectroscopically isolate specific amino acids in the sequence at different positions along the helix. We found that the heat does not propagate through the hydrogen bonds, as it was theoretically suggested, but rather through the backbone of the helix. Furthermore, fitting our data to a rate equation system, we estimated a heat diffusion coefficient D=2 Å^2/ps. Exciting the molecule with IR light, we calculated a heat diffusivity coefficient four times higher than the one when UV excitation was used. Below 270 K, the heat transport is inefficient and mostly ballistic whereas above this temperature it is more efficient and diffusive in character. These studies are the first steps towards the investigation of vibrational energy transport in large bio-polymers and proteins.

Zusammenfassung

Diese Arbeit setzt sich aus zwei unterschiedlichen wissenschaftlichen Teilprojekten zusammen. Im ersten Teil dieser Dissertation wird ein Modellsystem für eine chemische Reaktion im Grundzustand behandelt. Das zweite Projekt beschäftigt sich mit dem Energietransport in helikalen Peptiden.

Die *cis-trans* Isomerisierung von Salpetriger Säure (HONO) in einer Edelgasmatrix ist ein Modellsystem einer chemischen Reaktion im Grundzustand. Mittels Photoanregung der OH Streckschwingung kann man eine reversible Isomerisierungsreaktion auslösen. Regt man in einem IR pump - IR probe Experiment die OH_{cis} Streckschwingung an, so beobachtet man die Bildung von vibrationsangeregten *trans* Molekülen auf einer ultrakurzen Zeitskala (20-50ps). Die Photoprodukte weisen auf einen zweistufigen Mechanismus hin. Der erste Weg verläuft mittels direkter Kopplung der schwingungsangeregten Zustände mit den reaktiven Zuständen. Im Gegenteil dazu kann im zweiten Weg die Energie der Zwischenzustände in den Reaktionskanal transferiert werden (Zustände, die durch OH_{cis} populiert sind). Kühlt man die Matrix von 30 auf 15 K ab, so nimmt die Quantenausbeute der *cis*→*trans* Isomerisierung nach Anregung der OH_{cis} Streckschwingung um 30% zu. Bei 15 K beobachtet man ein Quantenausbeute von ungefähr 50-70%. Unsere Ergebnisse zeigten, dass die Quantenausbeute der Rückreaktion im gleichen Temperaturbereich um ungefähr 40% abnimmt. Diese Beobachtungen können mithilfe der Marcus Theorie von Elektron- und Protontransfer im barrierefreien Regime beschrieben werden. Die Marcus Theorie sagt für die Vorwärtsreaktion in diesem Regime eine Zunahme der Quantenausbeute von 40% voraus, was in guter Übereinstimmung mit dem experimentellen Wert von 30% ist. Dies würde bedeuten, dass man bei ganz niedrigen Temperaturen ein Qunatenausbeute von bis zu 100% erreichen könnte. Ein Grossteil der Informationen über die Dynamik der Isomerisierung und den Kühlprozess wurde mittels eines Zweifarbenexperiments erhalten, indem die HON Beuge- und OH und N=O Streckschwingung in unterschiedlichen Kombinationen angeregt und detektiert wurden. Die Rotationsdynamik der *cis* und *trans* Isomere wurde in einer Kryptonmatrix bei 30 K untersucht. Diese Experimente zeigten, dass

sich das Zentralatom des Moleküls in Hula-Hoop Form bewegte, nachdem das H isomeriserte. Diese Untersuchungen sind die ersten, die die Ultrakurzzeitdynamik einer niederenergetisch angeregten chemischen Reaktion beschreiben.

Um den Mechanismus des Wärmetransport innerhalb von helikalen Peptiden zu untersuchen, wurde eine Helix bestehend aus acht Aminosäuren entwickelt, die mit einem Chromophor (Azobenzol) versehen war. Nach Anregung des Azobenzols mit UV Pulsen wurde die Wärmeausbreitung innerhalb der Peptidhelix anhand der Verschiebungen der Amid I Banden im IR verfolgt. Eine selektive Isotopenmarkierung im Molekül erlaubte es die einzelnen Aminosäuren an ihren unteschiedlichen Positionen innerhalb der Peptidhelix zu identifizieren. Die experimentellen Ergebnisse zeigten, dass die Wärmeausbreitung innerhalb der Helix nicht über Wasserstoffbrückenbindungen - wie theoretisch vorhergesagt - stattfindet, sondern über das Peptidrückgrat. Ein Fit der experimentellen Daten in einem kinetischen System lieferte eine Wärmediffusionskoeffizienten von $D=2$ Å^2/ps. Bei Anregung des Moleküls mit IR Licht anstelle von UV Licht, erhielt man einen Wärmediffusionskoeffizienten der viermal grösser ist. Unterhalb von 270 K ist der Wärmetransport ineffizient und hauptsächlich ballistisch. Oberhalb dieser Temperatur jedoch ist er effizienter und diffusiv. Mit diesen Ergebnissen sind die ersten entscheidenden Schritte für die Untersuchung von Schwingungsenergietransport in grossen Biolpolymeren und Proteinen gemacht worden.

Chapter 1

Dynamics of the *Cis - Trans* Isomerization Reaction of the Nitrous Acid (HONO)

1.1 Introduction

Chemical reactions are at the core of chemistry. Although a deep understanding of chemical processes (the reaction conditions, catalysts, etc.) was developed during time, until 1980's no direct real time observation of the dynamics (to be contrasted to the kinetics) of these processes was achieved on the microscopic level. The goal of investigating the dynamics of a molecular chemical reaction is observing *how reagent molecules approach, collide, exchange energy, sometimes break bonds and make new ones, and finally separate into products* [1, 2]. It was the advent of the ultrafast lasers that granted the opportunity of such experiments. The work of A. Zewail et al. was pioneering in the field of observing directly, with the help of femtosecond laser pulses, a chemical reaction. In these experiments, a pump probe technique is used to investigate the dissociation of NaI, ICN, MgI_2, etc. There are two or more pulses used to perform these experiments. Specifically, the first pulse is triggering the reaction and the subsequent pulse(s) are probing the progress of the reaction. One of the first experiments was the dissociation of ICN in which both the fragments I and CN and the transition state could be identified. Measuring the dynamics of these species, the change in internuclear distance with time could be measured for the first time [3]. The even more interesting experiment was the dissociation of NaI, because it involved two electronic potential energy surfaces (one covalent and one ionic) [4]. It demonstrated for the first time *resonance behavior* (in real time) of a bond converting from covalent to ionic [1]. A wide range of characteristics (atomic scale resolution, single-molecule trajectory, coherent trajectories in reaction, intuitive physical picture) made this experiment a milestone of the research in chemical reactions.

All the experiments detailed above involve electronically excited states. While important chemical processes take place following excitations to electronic excited states (photosynthesis, the process of vision, electron and proton transfer, Diels-Alder reactions, pericyclic addition, etc.), the majority of chemical reactions evolve on the ground state potential energy surfaces. Hippler et al. investigated, in a pioneering work, the ground state isomerization reaction of cycloheptatriene after UV excitation [5]. The reaction takes place in gas phase and proceeds on a microsecond time scale. Scherer and Zewail investigated also ground state reactions: dissociation of H_2O_2 after overtone excitation [6] and $H+CO_2 \rightarrow OH+CO$ after UV photoactivation of a van der Waals complex [7]. All these experiments, while in the electronic ground state, share a high excitation energy (16000 to 40000 cm^{-1}).

There is a scarcity of studies of chemical reactions at lower excitation energies in the time domain. Due to the ubiquitous character of these reactions it is of paramount importance to gain a deep understanding of the dynamics of these processes at the microscopic level. For this purpose, we decided to investigate the dynamics of the *cis* - *trans* isomerization reaction of nitrous acid (HONO) in Kr matrices with IR pump - IR probe spectroscopy. This isomerization reaction acts as a prototype ground state chemical reaction, with the size of the molecule (four atoms) allowing a full quantum chemical description.

The matrix isolation technique was initiated in the '50s by a seminal letter by Whittle, Dows and Pimentel [8]. They proposed this technique for *the accumulation of a reactive substance under environmental conditions which prevent reaction.* As it is acknowledged in the letter, the idea of trapping molecules of interest in inert materials was even older, being traced to Lewis et al. which used glassy matrices to study the phosphorescence of suspended materials [9]. As in the original concept, in the decades following Pimentel's paper the matrix isolation technique was further developed and extended. A wide variety of molecules were studied with the help of this technique, of which the main attention was given to radicals and unstable compounds. This experimental approach made possible even the discovery of new molecules and compounds [10, 11]. For the inert material used to trap reactive molecules different rare gas crystals were used (Xe, Kr, Ar, Ne) but sometimes also N_2, CO_2, CH_4, CCl_4, etc..

1.2 HONO in solid matrices

One of the first chemical processes studied in the matrix environment was the *cis* - *trans* isomerization of HONO. Pimentel and coworkers observed that photolyzing HN_3 in the presence of O_2 in an inert matrix (Ar, N_2) yields *cis* and *trans* HONO [12]. The assignment was based on gas phase spectra taken earlier by D'Or et al. [13] and Jones et al. [14]. In fact, these works were the first to establish, based also on temperature effects, that HONO has two stable isomers. Pimentel et al. followed with more detailed experiments in which they varied a broad range of parameters like relative concentration of precursors, different spectral filters to light-trigger the reaction, different isotope substitutions, deposition and measuring temperatures. Choosing different sets of filters they were able to narrow down the 3200 to 3650 cm^{-1} spectral range as the active region for triggering interconversion between the two isomers [15, 16]. Thus, it became evident that the isomerization reaction was triggered by the OH excitation. Estimating the photon flux, absorption coefficients, initial sample concentration and the interconversion rate constants, the authors suggested that the quantum yield of the *cis→trans* isomerization reaction was *of the order of unity* [16]. With the reaction coordinate being the HON torsional mode, the question of the nature of the very strong coupling arose immediately. Following this pioneering studies, HONO and in particular the *cis-trans* isomerization reaction were investigated in detail both experimentally [15–19] and theoretically [20–32]. Due to the role it plays in generating tropospheric OH radicals [33–35], gas phase HONO was investigated thoroughly. Cox and coworkers obtained the structure of both isomers from rovibrational measurements [36]. The energy difference between the two isomers was determined from *cis-trans* equilibrium measurements by UV absorption [37], infrared absorption [14] and microwave measurements [38]. The results indicate that the *trans* isomer is more stable than the *cis* with a difference of 100-200 cm^{-1}. The barrier height between the two isomers is estimated to be 4000 ± 500 cm^{-1} hence, in the same range as the OH vibration energy (≈ 3500 cm^{-1}) [32]. In table 3.2 we present the frequencies for normal modes of HONO in Kr matrices.

The isomerization reaction was revisited by Shirk and coworkers [17, 18] and Khriachtchev and coworkers [19] with modern laser apparatus with which they were able to selectively excite either one of the isomers. Shirk et al. observed nonexponential reaction kinetics in N_2 and Ar matrices which they attributed to migration of the photoreaction energy inside the rare gas crystal. Due to weak absorption of the *cis* OH stretch (OH_{cis}) their *cis→trans* rate was *subject to large errors*. Even more detailed experiments were done by Khriachtchev et al. [19] in which they investigated both *cis→trans* and *trans→cis* isomerization reactions. Due to their

	ν_1 OH stretch	ν_2 N=O stretch	ν_3 HON bend	ν_4 N-O stretch	ν_5 ONO bend	ν_6 HON tor.
trans	3552	1681	1286	$799^{(a)}$	$608^{(a)}$	$550^{(a)}$
cis	3401	1630	$1315^{(a)}$	$849^{(a)}$	$616^{(a)}$	$637^{(a)}$

Table 1.1: Vibrational frequencies (in cm^{-1}) of HONO in solid Kr. $^{(a)}$ taken from Ref. [19]

narrow band laser they could selectively excite different bands in the substructure of the OH absorption band finding identical kinetics for all sub-bands. The dynamics were exponential indicating a unimolecular process. They determined accurately that the ratio of *cis→trans* to *trans→cis* rates is 7 in solid Kr at 7 K. Based on this precise measurement and on estimates about the absolute quantum yield of the *trans→cis* reaction they suggested that the *cis→trans* quantum yield is *possibly approaching 1*. Fig. 1.1 presents the Fourier transformed infra-red (FTIR) spectrum of HONO in the spectral region of OH stretch. For both *cis* and *trans* isomers the OH stretch band has a substructure containing two respectively three separate bands. These bands are associated with different positions that the molecule occupies in the matrix cell being a well know effect of trapping molecules in rare gas matrices. Also depicted are cartoon structures of the *cis* and *trans* isomers and the corresponding OH stretch wavelengths which lead to isomerization. Khriachtchev et al. also found isomerization from exciting the overtones of N=O bend (*cis* and *trans*) in the 3200-3300 cm^{-1} spectral region, but with much lower quantum yields (factor 2.5 less for both isomers).

The question that arises from these experiments is how can this 100% quantum yield be explained? Pimentel et al. suggested that the reactive mode is an overtone of the torsional mode with very low oscillator strength [16]. Hence, the energy from the excited mode (OH stretch) has to be transferred highly efficiently to overtones or combination modes of the torsional mode of the same symmetry. All the experimental work listed above investigated only the kinetics of the isomerization reaction, estimating the rates from the photon flux, absorption coefficients and concentration of irradiated sample. The dynamics of the photoreaction (i.e. transient species, the energy path) was not known. The mechanism that provides the strong coupling between the OH stretch and overtones of the HON torsional along with the time scale of the process (femtoseconds, picoseconds or milliseconds) and whether the process involves a coherent wave packet motion or tunneling were all unclear.

1.3 Theoretical results

Some of these aspects were addressed from a theoretical point of view. With the help of molecular dynamics (MD) simulations, Thompson, Raff and coworkers found that the isomerization occurs on a picosecond time scale and that it is the matrix that randomizes the energy levels within the molecule [22–25, 27]. In order to account for zero point energy and still be below the dissociation threshold they used excitation levels of $\approx$13000 cm^{-1}. They proposed a mechanism for the reaction in which energy goes through a *vibration→lattice phonon*

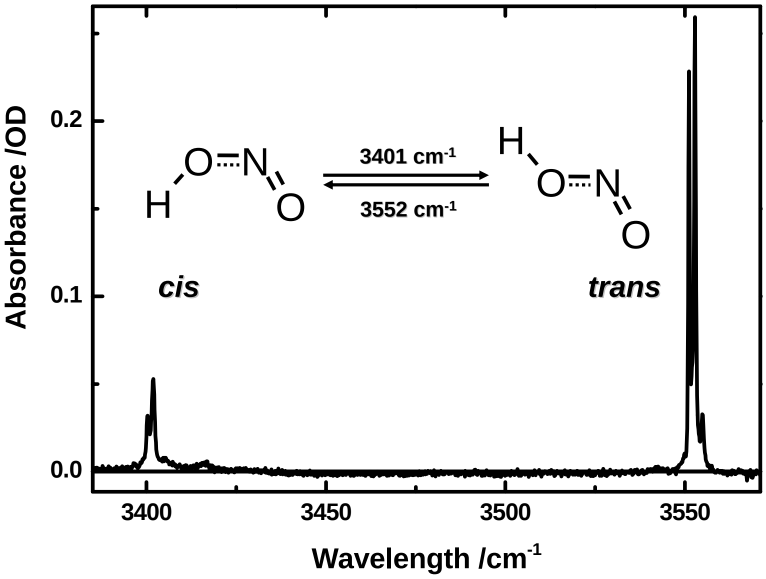

Figure 1.1: Steady stated FTIR spectrum of HONO in the OH spectral region in a Kr matrix at 30 K. Depicted are cartoon structures of the *cis* and *trans* isomers and the excitation for interconversion

modes→rotation→torsional vibration path. All the above theoretical works are classical in nature and ignore the quantum character of the proton. This issue was addressed in a semi-classical approach for gas phase HONO on a empirical valence bond potential [26]. In the gas phase the coupled vibrational problem has been computed on a full quantum level including all six degrees of freedom of the molecule [20,29]. Moreover, the coherent wave packet dynamics of an initially constructed localized state was investigated [21,30].

In fig. 1.2 we present a scheme of the energy levels in gas phase taken from ref. [29]. Bright colors (red for *cis* and blue for *trans*) represent states with high oscillator strength whereas the gray colors relate to low oscillator strength states. All these works, which model the system in the gas phase found that the *cis* and *trans* OH vibrational normal modes (ν_1) are localized on either one of the isomers. This was the reason why, in their study Richter et al. [30] found no significant isomerization yield when propagating a wave packet initially localized on OH (*trans* or *cis*). Much higher yields (one order of magnitude) were found when the initial state contained overtones of ν_3 (HON bend) and ν_4 (N-O stretch). Moreover, when comparing the isomerization quantum yields of exciting the same state in the two isomers the *cis→trans* was found to always exhibit higher yields. This was attributed to slightly higher overall delocalization of the *cis* combination modes than the *trans* ones in the 3500 cm^{-1} and above spectral region. Furthermore, only in the *cis* isomer there is an almost perfect resonance between the HON bend and the torsional mode ($\nu_3 \approx 2\nu_6$). This sheer accident could play an important role in the isomerization process due to the strong delocalization character of the high overtones of

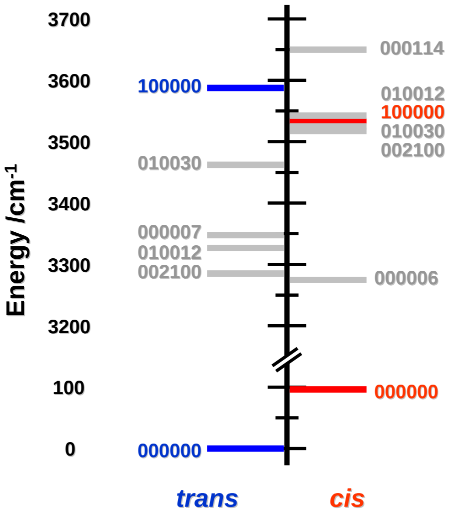

Figure 1.2: Scheme of the energy levels in an isolated molecule of HONO for the two isomers. Colors (red for *cis* and blue for *trans*) indicate oscillator strength (gray means very low oscillator strength). States are coded with a six digit number that stand for the number of quanta each state has of a specific normal mode in the order $\nu_1..\nu_6$

the torsional mode. While it gave critical insights about the energy levels and couplings, the gas phase calculation was not able to reproduce the extremely high quantum yield found in the experiment for the *cis*→*trans* isomerization reaction.

1.4 IR pump - IR probe technique

In this context we decided to investigate the *cis*-*trans* isomerization reaction of HONO with the help of femtosecond infrared (IR) spectroscopy. To this end, we use ultrashort IR pulses in a pump-probe scheme. We depict in fig. 1.3 a sketch of the interaction between the pump-probe pulses and a three level system. The interaction of the pump pulse with the system brings some of the molecules from the vibrational ground state to the vibrational excited state. When the second (probe) pulse acts on this excited system it probes the molecules that are in the ground and excited state. Since we record difference absorption spectra (difference between the excited and the unexcited sample), we will have negative as well as positive signals. The negative components correspond to absorption signals that disappear or emission signals that appear upon excitation, whereas the positive components stem from absorption bands being created by the irradiation. In the example given in fig. 1.3 the positive signal corresponds to the excited state absorption (ESA), while the negative band is the sum of the bleach (Bl) and stimulated emission (SE). Bl and SE appear at the same frequency and they have equal

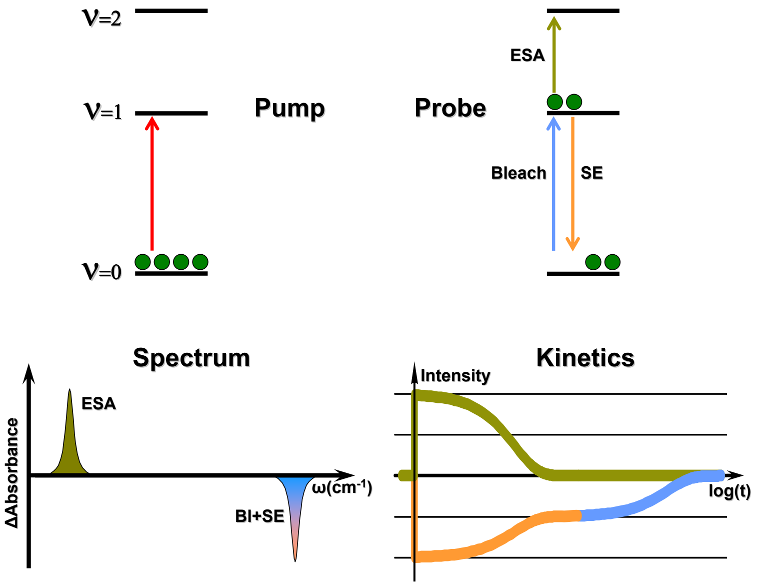

Figure 1.3: Upper part: Scheme of the interaction of pump and probe pulses with a 3 level system. Lower part: Spectrum and kinetics resulted from a pump-probe experiment on a 3 level system. The bleach/stimulated emission signal was drawn assuming a strong separation (3 orders of magnitude) between the time decays of the two components

intensities $\mu_{01} = \mu_{10}$. The dipole moment corresponding to the ESA is twice as strong as that of Bl, $\mu_{12} = \sqrt{2}\mu_{01}$ (assuming harmonic states). In our experiments we define time as the duration between the pump and probe pulses. Hence, we have *negative, zero* and *positive* time determined by the probe pulse arriving at the sample *before, at the same time* and respectively, *after* the pump pulse. Thus, at time zero the integrated intensity of ESA should be equal to that of Bl+SE signal (as seen in the lower panel of fig. 1.3). The ESA and SE emission components both decay with a time constant corresponding to the lifetime of the mode being excited. The recovery of the Bl signal is usually much slower, since it follows the overall vibrational cooling. When the difference in this two time scales is very large (two or more orders of magnitude) we see a clear two step process in the recovery of the Bl/SE signal (see fig. 1.3).

1.5 Time resolved experiments; early dynamics

In fig. 1.4 panel (a) we present the difference absorption transients in the OH spectral region after pumping OH_{trans}. In order to address the two isomerization reactions separately we spectrally filter our pump pulse with the help of a Fabry-Perot filter and we pump selectively either one of the isomers. In fig. 1.4 the negative signal corresponds to the Bl/SE of OH_{trans}, whereas the positive signal at $\approx 3390\ \mathrm{cm}^{-1}$ represents the ESA of OH_{trans}. We can observe that at early times the integrated intensities of the two signals are essentially identical. At later times we see

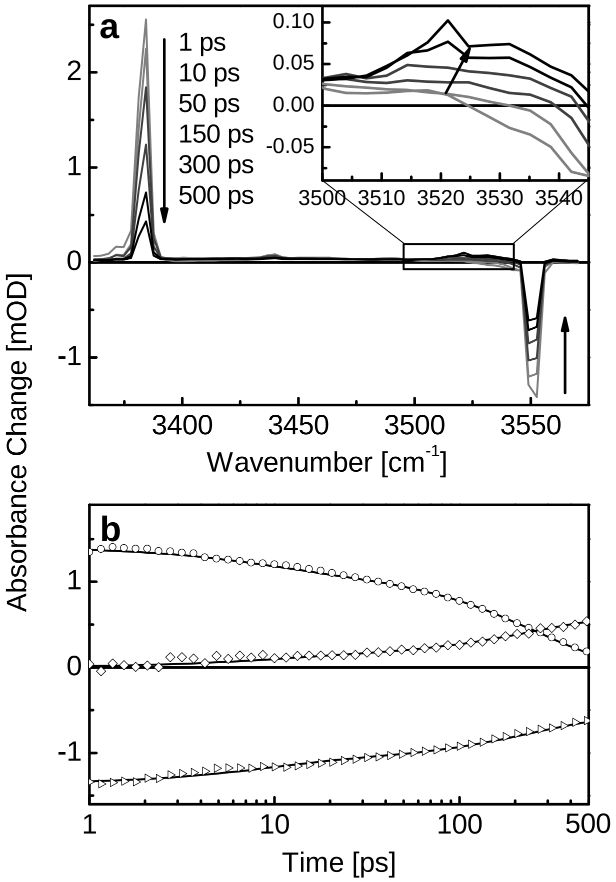

Figure 1.4: (a) Transient absorption spectra in the OH spectral region after exciting OH$_{trans}$ at different delay times in Kr matrix at 30 K. Panel (b) presents the kinetics of the three signals observed in panel (a): (O) excited state absorption (3390 cm^{-1}),(▷) bleach/stimulated emission (3552 cm^{-1}) and (◇) "dark states" signal (3515-3550 cm^{-1})

the development of a positive band red shifted from the Bl signal. In the inset of fig. 1.4 panel (a) we plot a detailed view of this spectral region with an arrow indicating time evolution. We will call this signal hereafter "dark states" signal (for details see also chapter 3.1). In order to understand the origin of this signal we perform a Dunham expansion for the anharmonically coupled vibrational levels [39]:

$$E = \sum_i \hbar\omega_i (n_i + 1/2) + \sum_{i,j} x_{ij} (n_i + 1/2)(n_j + 1/2), \tag{1.1}$$

where ω_i is the harmonic frequency of mode i, n_i its excitation level and x_{ij} the anharmonic coupling constants. From this expression one can derive the transition frequency of a particular

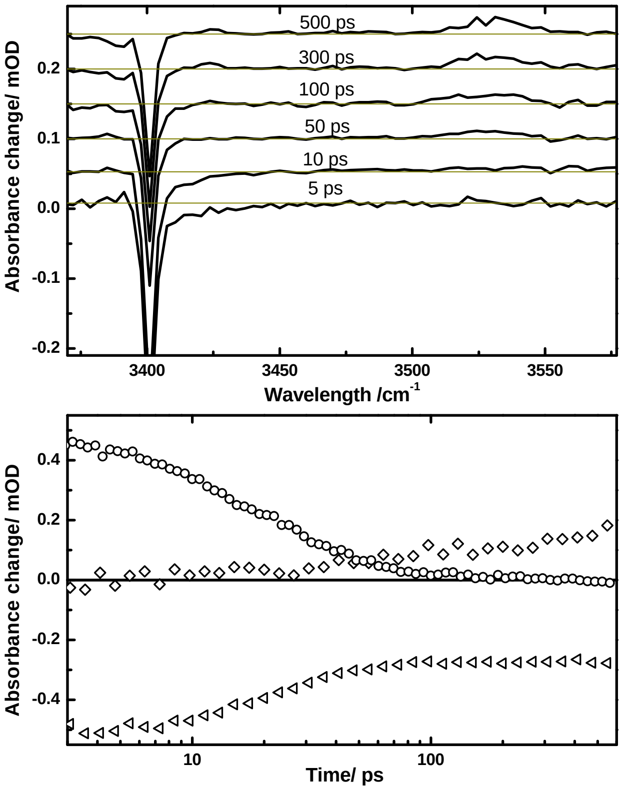

Figure 1.5: (a) Transient absorption spectra in the OH spectral region after exciting OH_{cis} at different delay times in a Kr matrix at 30 K. The thin lines mark the background of each transient spectrum. Panel (b) presents the kinetics of: (O) excited state absorption, (◁) Bleach/stimulated emission and (◇) *trans* "dark states"

mode k as:

$$\nu_{n_k \longrightarrow n_k+1} = \nu_k + 2n_k x_{kk} + \sum_{i \neq k} x_{ik} n_i, \tag{1.2}$$

with $\nu_k = \omega_k + 2x_{kk} + \sum_{i \neq k} x_{ik}/2$. The anharmonic coupling constants are symmetric, $x_{ij} = x_{ji}$, and are in most cases, but not necessarily, negative since the potential energy surface softens as one climbs up in energy. The dark states signal we observe red shifted from the OH_{trans} corresponds to *trans* molecules that are not in the vibrational ground state. We can globally fit the kinetics of the signals in fig. 1.4 with a bi-exponential function with 8 and 260 ps time constants. The need for two time constants is probably caused by the existence of two sub-bands which might have different lifetimes (*vide infra*).

We repeated the same experiment, but now selectively exciting the *cis* isomer. Difference absorption transients of this experiment are presented in fig. 1.5. The spectra are dominated by the Bl/SE signal at $\approx$3400 cm^{-1}. In the blue part of the spectrum (3515-3550 cm^{-1}) we see as time progresses the development of a broad band. It starts as a broad, unstructured band but in time we see the development of a structure with one, and then at later times, two peaks. When we spectrally compare this band with the "dark states" signal that we observe when we excite the *trans* isomer we find a perfect match. Thus, after exciting *cis* molecules we observe isomerized, vibrationally hot *trans* molecules. To our knowledge this is the first time when a one quantum, one photon chemical reaction was observed directly, in time domain. Moreover, it is the first time that a time scale of the *cis*→*trans* isomerization reaction has been measured experimentally. Taking the integrated intensity of this "dark states" band (see fig. 1.5 panel b) we observe the ultrafast (20-50 ps) rise of the hot, isomerized *trans* molecules. The ESA of OH_{cis} is 180 cm^{-1} red shifted from the bleach/stimulated emission and was measured in a different experiment. In fig. 1.5 panel (b) we present also the kinetics of the Bl/SE and ESA signals of OH_{cis}. We can fit both signals (Bl/SE and ESA) with a single exponential decay with a time constant of 21±1 ps, this being the lifetime of OH_{cis}. As explained in section 1.4, we observe how as the excited mode relaxes, the ESA signal goes to zero while the Bl/SE signal goes to half of the original amplitude. Hence, the integrated intensity signal that we see at 200-500 ps of the Bl/SE band corresponds exclusively to the Bl signal and it is a direct measure of the number of molecules being excited. In order to calculate the quantum yield of the *cis*→*trans* isomerization reaction we have to divide the integrated intensity of the "dark states" signal to the bleach signal, taking also into account the oscillator strength. We estimated the oscillator strength ratio from steady state experiments (*vide infra*) and we obtained $OH_{trans}/OH_{cis} \approx 1.6$. This value is somewhat lower than the 2.4 value published by Khriachtchev et al. [19], but we think these values are affected by systematic errors owing to the way they are measured. We believe their value probably overestimates whereas ours underestimates the real oscillator strength ratio. Hence, we assume that the oscillator strength ratio is 2±0.4. Considering these arguments, we estimate the *cis*→*trans* quantum yield after 500 ps to be $\approx$15%. Analyzing the kinetic of the integrated intensity of the *trans* hot band in fig. 1.5 we observe that the signal does not saturate in this time interval, and it probably grows at later times.

1.6 Time resolved experiments; nanosecond dynamics

To allow measurements of significantly longer delay times we used two synchronized laser systems. Thus, the IR light for pump and probe pulses comes from two independent optical parametric amplifiers (OPA) pumped by the two lasers. The synchronization procedure was developed previously in our group [40] for achieving very long delay times (up to microseconds), in the context of protein folding research. In fig. 1.6 we present the response of HONO in the OH spectral region following the excitation of either one of the isomers. The response when pumping OH_{trans} (panel a), as in the case of short delay times, is dominated by two bands: the positive ESA ($\approx$3390 cm^{-1}) and the negative Bl/SE ($\approx$3550 cm^{-1}). But at longer delay times we observe that the small, broad band corresponding to vibrational hot *trans* molecules

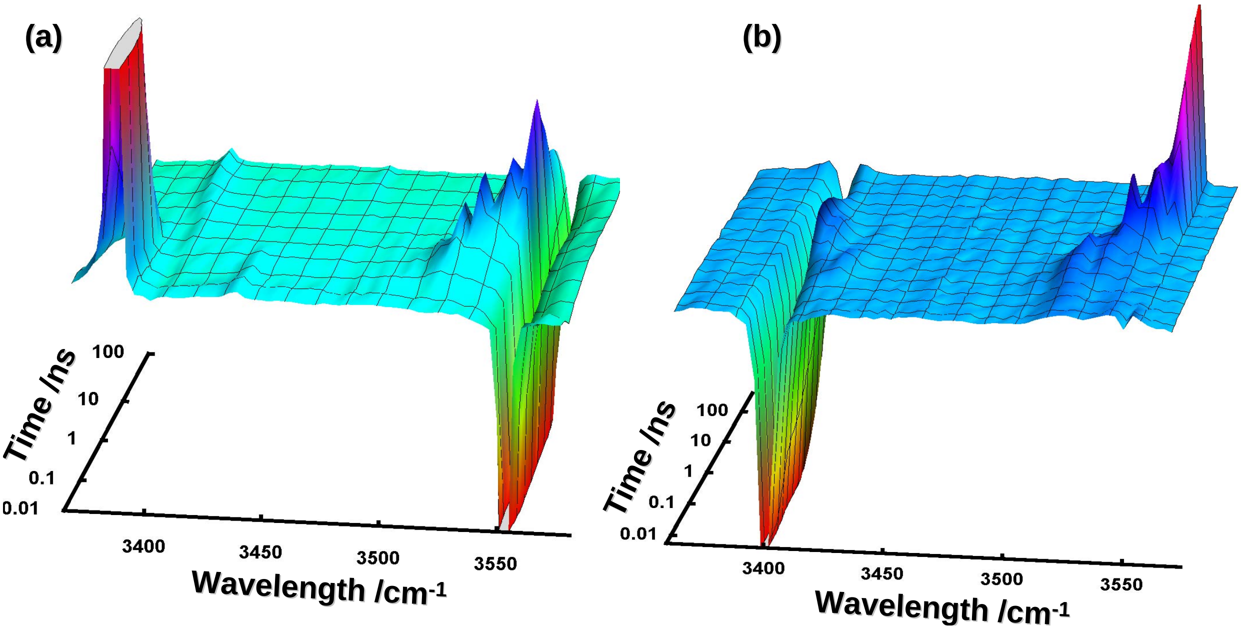

Figure 1.6: Overview representation of the OH spectral region response following the excitation of (a) OH_{trans} and (b) OH_{cis}

("dark states") is growing and developing in a structure of four absorption bands that have a "relay" type dynamics (see fig. 1.6 panel a). Moreover, these four bands are spectrally equally separated suggesting that they are harmonics of one and the same mode. The number of quanta that we observe, the separation between states ($\approx 8\ \mathrm{cm}^{-1}$) combined with the published theoretical [29] and experimental [41,42] values for the anharmonic coupling constants suggest that the mode responsible for this relay is ν_5, the ONO bending (for details see also chapter 3.2). At the position of OH_{cis} we observe at later times the development of a positive band. The band initially appears slightly blue shifted, nevertheless the shift is smaller than our spectral resolution ($3\ \mathrm{cm}^{-1}$). Evaluating the integrated intensity of the *cis* band versus the *trans* bleach, we calculate the quantum yield of the *trans*→*cis* isomerization reaction to be 7-11%.

Fig. 1.6 panel (b) depicts the response following the excitation of OH_{cis}. At early times we observe the strong negative band corresponding to the Bl/SE and later the progress of the vibrational hot *trans* signal. The "dark states" signal, as in the case of exciting OH_{trans}, develops through the same cascade of states with similar kinetics. Likewise, we observe dark states signals of the *cis* isomer blue shifted from the Bl/SE position.

In fig. 1.7 (lower part) we present the combined evolution of the Bl/SE signal from the short and long delays measurements. The SE signal decays very fast, with a 21 ps time constant whereas the Bl signal recovers slowly following an exponential decay with ≈ 13 ns time constant. In the upper part of fig. 1.7 we present the evolution of the integrated intensity signal of the photoisomerized *trans* molecules. We observe that this signal follows a two step process, with 58 ps and 5 ns time constants.

The sheer observation of two time scales for the isomerized *trans* molecules kinetics indi-

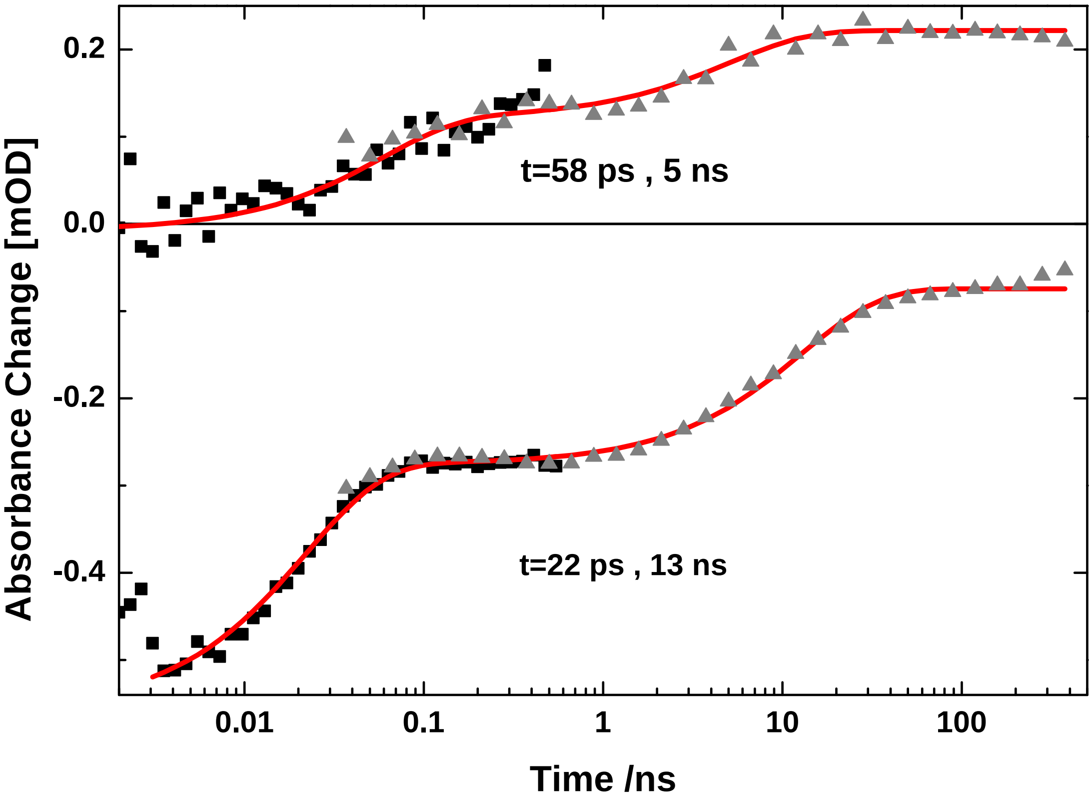

Figure 1.7: The lower curve follows the bleach and stimulated emission of OH_{cis} from a short (black) and long (gray) delays experiment. Upper curve follows the growth of the *trans* photoproduct in a short (black) and long (gray) delays experiment. The red lines double exponential fits with the timescales indicated in the figure

cates the existence of two channels for the reaction. We can associate the fast step with the deexcitation of the OH stretch and the second step with the cooling of the molecule as a whole. However, the excited OH_{cis} is totally localized on the *cis* side [21, 30, 43] and the coupling to the *trans* side is vanishingly small. Solving the vibrational Schrodinger equation we find that higher harmonics (>6) of the torsional mode start to be delocalized since the mode's wave function is extended into space towards the other isomer. Once the energy reaches the reactive "door way", isomerization proceeds essentially instantaneously. Theoretical studies [29] found three states to be almost (within 10 cm^{-1}) resonant with the OH_{cis}: 002100, 010012, 010030 (numbers stand for harmonics of normal modes in the order $\nu_1 ... \nu_6$). One of these states includes harmonics of the torsional mode and could be the "doorway" of the reaction, while the other could act as parking states for energy. This picture corresponds to a gas phase scenario.

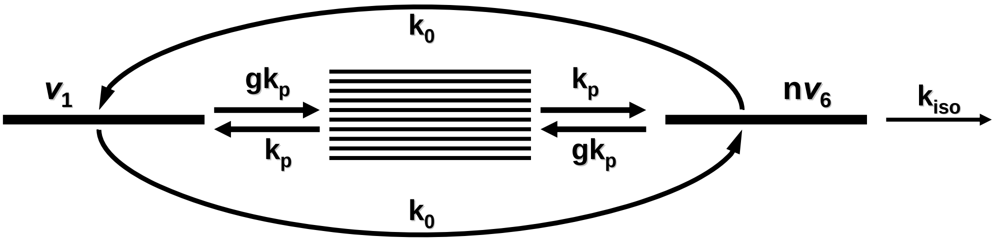

Figure 1.8: Kinetic scheme that describes the two step process in the *cis*→*trans* isomerization reaction

In the matrix, thermal randomization and mostly the fact that the *cis* and *trans* isomers have slightly different minima positions (due mostly to their different geometries) cause more states to come in and out of resonance with the OH vibration. There are 20-30 states that can possibly exchange energy with ν_1 without any significant loss in energy. This collection of states may act as a storage of energy that feeds the reactive channel, and the depopulation of these states follows to a certain degree the overall cooling of the molecule.

In fig. 1.8 we depict a possible scheme of states and kinetic links between them that can explain the two step process. The initially excited ν_1 is coupled to the reactive channel (probably some high harmonics and combination modes of ν_6) with rate k_0. The class of states that act as a storage of energy is linked to the reactive and ν_1 states with rates k_p and gk_p (see fig. 1.8 where g is a multiplicity factor) depending on the direction of energy flow. The reactive state couples very efficiently (high k_{iso} rate) to states corresponding to the *trans* conformer, and such leading to isomerization. If k_0=$k_p$$\ll$ k_{iso}, we would observe essentially a single exponential signal for the isomerized population. On the other hand if $k_p = 0.015k_0$ and $g = 60$ the double step behavior is reproduced exactly. While we do not take these numbers literally they express the essence of our experimental observation. The coupling between the ν_1 (OH) and the reactive state(s) (most likely harmonics and/or combination modes of ν_6, the torsional mode) is higher than coupling of the OH with other states and is responsible for the fast isomerization step. The collection of states that are close in energy with the OH act as an energy storage that re-feeds the reaction channel [44](see also chapter 3.2).

When we estimate the quantum yield of the *cis*→*trans* isomerization reaction, depending on the oscillator strength ratio, we obtain 30-50%. This value corresponds to the late delay times (>100 ns), when the molecules that isomerized are vibrationally cold. Nevertheless, this quantum yield is still lower than the *possibly approaching 1* (100%) reported by Khriachtchev et al. [19]. In their case, quantum yield was estimated from a steady state experiment in which the photon flux, amount of sample, absolute absorption coefficients entered the evaluation. Moreover, one very important experimental condition was significantly different compared to our experiments: temperature of the surrounding matrix. We did our experiments in Kr

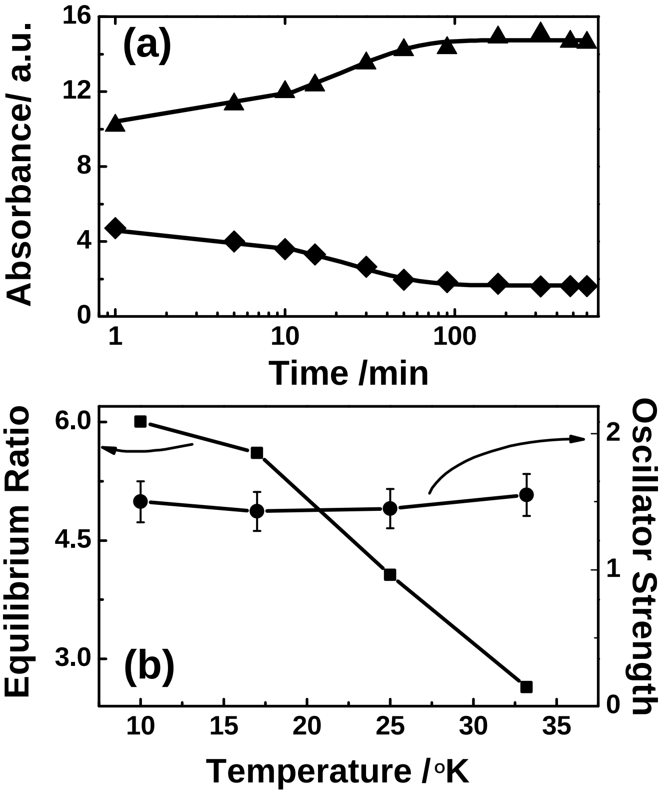

Figure 1.9: Panel (a): time evolution of the *trans* (▲) and *cis* (♦) integrated intensity under globar irradiation at 10 K. Panel (b): temperature dependence of the *trans/cis* photoequilibrium ratio (■, left axis) and oscillator strength (★, right axis)

matrices at ≈30 K whereas in ref. [19] the temperature was 7 K. In relative terms, there is more than four times more thermal energy in our experiments. Following OH excitation, there is a competition between cooling (nonreactive pathways) and isomerization (reactive pathways). Temperature may play a key role in shifting the balance between these two processes and hence, probably changing the quantum yield of the isomerization reaction.

1.7 Temperature Dependence

We performed a steady state experiment in which we followed the evolution of the *cis/trans* photoequilibrium as a function of temperature. To this end, we deposited Kr matrices at 32 K, changed the temperature to 10, 19, 25 or 32 K, irradiated the matrix with the light from the FTIR globar and recorded the photoequilibrium between the isomers. The only spectral range

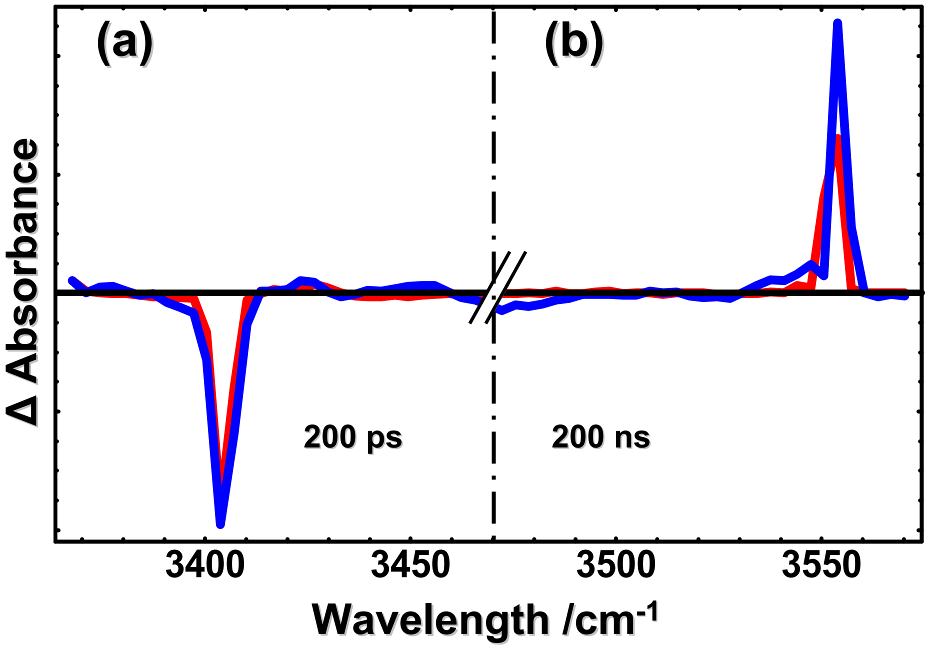

Figure 1.10: Transients absorption spectra at 15 K (blue line) and 30 K (red line) after pumping OH_{cis}. (a) OH_{cis} Bl at 200 ps (b) OH_{trans} photoproduct at 200 ns. Spectra are normalized to the bleach signal (the band at ≈3400 cm^{-1}).

that leads to non negligible isomerization is the OH spectral region, and we assume that the two isomers at ≈3400 cm^{-1} (*cis*) and ≈3550 cm^{-1} (*trans*) are irradiated with identical IR intensities. In fig. 1.9(a) we present the time evolution of the integrated intensity for the OH_{trans} and OH_{cis} in a Kr matrix at 10 K. We observe that under equal photon flux the equilibrium moves towards a higher *trans* concentration, saturating in hundreds of minutes. In panel (b) we display the photoequilibrium ratios as a function of temperature. We observe that varying the temperature from 32 K to 10 K the *trans*/*cis* ratio changes from below 3 to 6. The population ratio is directly proportional to the interconversion rate ratio. Hence, the *cis*→*trans* rate vs. *trans*→*cis* rate is increasing with decreasing temperature. This observation strongly suggests that the absolute *cis*→*trans* rate will increase with decreasing temperature.

We also performed pump-probe experiments at a lower matrix temperature. While the lifetimes of both OH_{cis} and OH_{trans} and the overall cooling seem to be longer at lower temperature, the differences are very small, within our signal to noise resolution [45]. When cooling to lower temperatures (<25 K) the quality of the matrix usually deteriorates, due to different expansion coefficients of the matrix and of the CaF_2 substrate. Owing to this effect our scattering signal was strongly increased, and thus lowering significantly our effective signal to noise ratio.

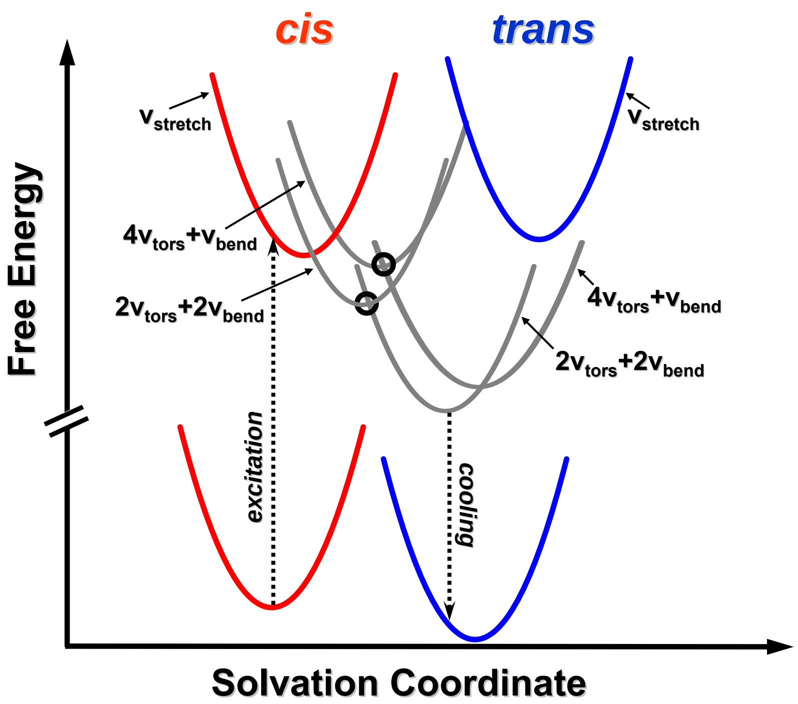

Figure 1.11: Suggested scheme of vibrational states as a function of solvation coordinate. The black circles mark the positions where nonadiabatic proton transfer between *cis* and *trans* HONO can take place in an essentially barrierless manner. All modes refer to the proton degrees of freedom (i.e. ν_{bend} is the HON_{bend})

Hence, comparing the isomerized, vibrational hot *trans* molecules for high (30 K) and low (15 K) temperatures was difficult. It is much easier, in order to assess any temperature effect, to compare the vibrationally "cold" photoproduct. In fig. 1.10, similar to fig. 1.5 we present transient absorption spectra at low and high matrix temperature. As we observed before (see also fig. 1.7), at 200 ps the OH_{cis} SE emission signal has completely decayed making the band at $\approx 3400\ \text{cm}^{-1}$ a purely bleach signal. In the blue part of the spectrum we present at 200 ns the vibrationally "cold" OH_{trans}. The signals presented in fig. 1.10, weighted by the oscillator strength ratio, are used to calculate the quantum yield of the *cis*→*trans* isomerization reaction. We observe from the fig. 1.10 that the lower temperature experiment exhibits a higher quantum yield. Quantifying the difference from integrated intensity (not absolute intensity) of the OH_{trans} we determine a 30% increase in quantum yield upon cooling the surrounding matrix from 30 K to 15 K. This result is quite surprising since the lifetime of OH and the cooling process are effectively temperature independent. Moreover, we observed in the steady state measurements that in a similar temperature range the *cis*→*trans*/*trans*→*cis* ratio of rates increased by a factor of 2. Combining these results, we estimate that the *trans*→*cis* rate must decrease by 40% in the same temperature range. Due to technical reasons (lack of a cw laser to pump OH_{cis}, see also chapter 3.3) we cannot measure the *trans*→*cis* isomerization reaction with the same signal to noise ratio in our pump-probe setup.

In order to understand this behavior we discuss the reaction mechanism in terms of Marcus theory of nonadiabatic electron transfer. The concepts of electron transfer have been extended also to proton transfer by many researchers before [46–49]. It was shown in ref. [50] that proton transfer is driven by matrix fluctuations. Due to thermal randomization, vibrational states come in resonance, and thus transferring population. These crossings are only weakly avoided due to small tunnel couplings. These are the premises of Marcus theory of nonadiabatic electron transfer. Accordingly, the proton transfer rate between each pair of *cis* and *trans* vibrational states can be expressed as:

$$k_{cis\rightarrow trans} = \beta^2 \sqrt{\frac{\pi}{\hbar^2 k_B T F_\lambda}} exp\left(-\frac{(\Delta F - F_\lambda)^2}{4F_\lambda k_B T}\right), \tag{1.3}$$

where β is the tunneling matrix element, ΔF the free-energy gain upon isomerization and F_λ the reorganization energy. The ratio of forward and backward rates fulfills detailed balance:

$$\frac{k_{cis\rightarrow trans}}{k_{trans\rightarrow cis}} = exp\left(\frac{\Delta F}{k_B T}\right), \tag{1.4}$$

With ΔF positive for a downhill reaction, the ratio above increases as temperature is lowered, as observed experimentally (see fig. 1.9). The only situation in which the forward rate will increase with decreasing temperature is when $\Delta F \approx F_\lambda$. This relation corresponds to the situation when the product free energy surfaces cross the reactant surfaces in their minima. Interestingly, the $1/\sqrt{T}$ term that makes the forward reaction rate increase with lowering temperature would predict a 40% increase in the measured temperature range, in agreement with the 30% measured. In fig. 1.11 we present a possible scheme of the vibrational states (based on data from quantum classical computations [50]) as a function of a solvation coordinate. The black circles mark the very weakly avoided crossings (between reactant and product surfaces) in the reactant's potential minima. Furthermore, the colors relate to the oscillator strength of different vibrations: red for *cis*, blue for *trans* and gray for very low oscillator strength combination modes ("dark states"). One can "visualize" the *cis*→*trans* isomerization process: molecules are excited from *cis* ground state to OH_{cis} excited state, from where, due to matrix fluctuation, they get onto harmonics and combination modes of the torsional mode. These states couple with significant coupling constants β to their corresponding *trans* states from where the molecules cool down to the *trans* ground state. The fact that the forward rate increases and the backward rate decreases with lowering temperature suggests (see fig. 1.11) that the reactive states in the *trans* configuration are lower and the isomerization takes place energetically downhill in a barrierless manner. This situation is further supported by the frequencies of the fundamental modes which are all (except OH and N=O) lower in the case of *trans* compared to their corresponding modes in the *cis* configuration (see table 3.2). Hence, in the case of *trans* (see fig. 1.11) there is no close resonance with what we believe are the reactive states, statement supported also by the significantly longer (one order of magnitude) lifetime of OH_{trans} compared to OH_{cis} (for details see also chapter 3.3).

In the view of these considerations, it seems that the *cis*→*trans* very high quantum yield stems from the fact that the reaction proceeds barrierless, energetically downhill. This is also one of the reasons why the *trans*→*cis* quantum yield is relatively small and it has an inverse temperature dependence compared to the forward reaction. An additional important aspect is the similarity between the vibrational cooling rate and the isomerization rate. If the cooling rate would be significantly slower, the molecules would thermalize with equal probabilities on both sides (same densities of states at 3500 cm^{-1}), clearly not what is observed. If the cooling rate would be significantly faster than isomerization, the molecule would have no time to isomerize and the sum of forward and backward quantum yields would be significantly lower than 1. Tentatively, this is what is happening at higher temperatures.

1.8 IVR in HONO

In order to further investigate the dynamics (to be contrasted to kinetics) of the *cis-trans* isomerization reaction and the cooling that follows the excitation of molecules we widened our investigation to other vibrations of the molecule. We performed two color experiments in which we excited and probed in various combinations ν_1, ν_2 and ν_3 (see table 3.2). These experiments gave us different probes of the same underlying process, with the help of which we gained further insight into the energy dynamics (for details see chapter 3.5). In fig. 1.12 we present a collection of spectra in which the rows correspond to different pumping modes (OH - first row, N=O - second row and HON - third row) and the columns to different probing modes (OH - right, N=O - middle and HON - left). The most important positive bands (mostly transients but also stable photoproducts (first row)) are labeled with a three digit code corresponding to the pumping mode (first digit), probed mode (second digit) and the mode that the probed mode couples to (third digit). The modes that we have tentative assignments for we label with y and z. The indices correspond to the character of the specific mode: *c* for *cis* and *t* for *trans*. We observe for instance in fig. 1.12 in the first row (panels a, b, and c) the response after exciting OH_{cis} (the spectrum in panel (c) is the same data as presented in fig. 1.6 panel (b)). Through this spectra we follow the dynamics of the *cis*→*trans* isomerization through the response of OH, N=O and HON. For instance, based on its kinetics and amplitude we tentatively assign band $1_c2_cz_c$ to the storage and reactive states that are essential for the isomerization reaction.

Another interesting observation arises when we compare the response of OH_{trans} after exciting the OH, N=O and HON. We can distinguish in the cooling process a progression of four states (see also fig. 1.6 panel (a)) when exciting at the OH energy level. Furthermore, when exciting lower in energy, the N=O and HON, we can observe a progression of only three and respectively two states. These observations suggest that, irrespective the mode that is excited, the final steps of cooling proceed through harmonics of the same mode, which we assign to be ν_5. We schematically present this observation in fig. 1.13, in which we draw all the energy levels to scale.

There is a wealth of information about the dynamics of the isomerization and the vibrational relaxation in this collection of spectra. Information about excitations lifetimes, self anharmonicities and anharmonic coupling constants are obtained. In table 3.4 we present the pub-

	trans			cis		
	calc.$^{(a)}$	exp.$^{(b)}$	exp.$^{(d)}$	calc.$^{(a)}$	exp.$^{(c)}$	exp.$^{(d)}$
x_{11}	-87.0	-83.78	-83	-97.55	-94.00	-95$^{(e)}$
x_{12}	-9.8		-7	-13.39		-6
x_{13}	-26.84	-24.36	-21	-35.25		
x_{14}	-7.64	-2.95		-1.38	2.9	
x_{15}	-3.20		(-8)	-4.15		
x_{16}	-33.61			-1.44		
x_{22}	-16.13	-13.7	-11	-14.40	-11.53	-11
x_{23}	-10.71		-8	-16.46		
x_{24}	9.47			-4.44	0.5	
x_{25}	0.99		(-0.5)	-3.80		
x_{26}	13.01			-0.92		
x_{33}	-11.28	-11.34	-10	-12.07		
x_{34}	-14.33			-7.96		
x_{35}	-7.97		(-7)	-14.43		
x_{36}	-5.79			-3.99		
x_{44}	-11.49			-8.58		
x_{45}	-12.99			-13.55		
x_{46}	-33.51			-14.60		
x_{55}	-6.34			-6.09		
x_{56}	-8.42			-5.27		
x_{66}	-4.41			-3.89		

Table 1.2: Calculated and experimental anharmonic coupling constants x_{ij} of HONO (in cm^{-1})
$^{(a)}$ theoretical values from Ref. [29]
$^{(b,c)}$ gas phase experimental values from Ref. [41,42]
$^{(d)}$ experimental values in solid Kr. A typical error bar is ± 1 cm^{-1} due to the limited spectral resolution of our setup. Values in parentheses are assigned assuming that the cooling mode is indeed ν_5.
$^{(e)}$ taken from Ref. [43]

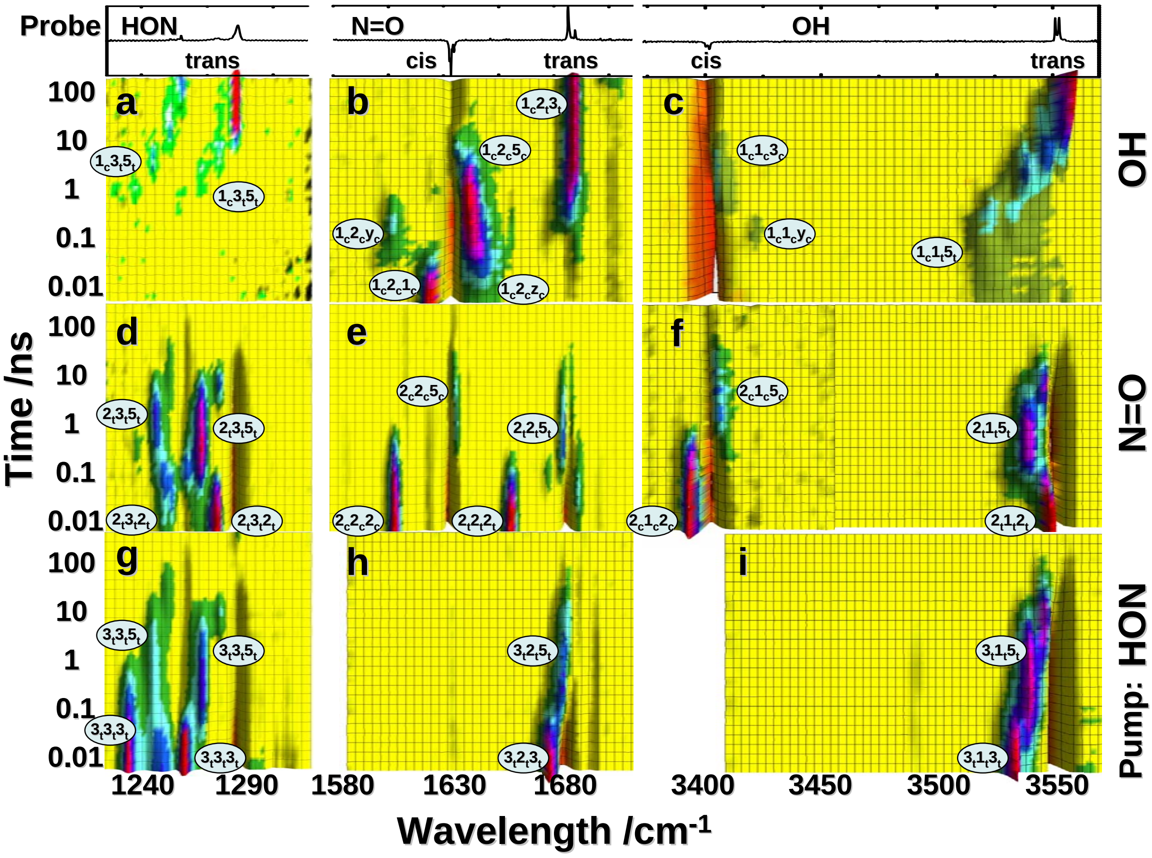

Figure 1.12: Transients in the spectral range of HON bend (left column), N=O stretch (middle column) and OH stretch (right column) after exciting OH$_{cis}$ (top row; the very top shows a stationary difference spectrum measured as a reference) N=O$_{cis}$ or N=O$_{trans}$ (middle row) and HON$_{cis}$ (bottom row). The most relevant positive bands are coded with a three digit label which represents pump mode (first digit), probed mode (second digit) and the mode to which the probed mode anharmonically couples (third digit). For the bands that we have tentative assignments, "y" and "z" are used. Indices refer to the character of the state: c for *cis* and t for *trans*

lished theoretical and experimental values for the anharmonic coupling constants of the *trans* and *cis* isomers. To this table we add (third column for each isomer) the values we measured in our two color experiments detailed above. In parenthesis we present values that we assign to ν_5 (for details see chapter 3.5). Having the knowledge of the complete set of experimental anharmonic coupling constants one would be able to pinpoint with unprecedented accuracy the energy flow inside molecules.

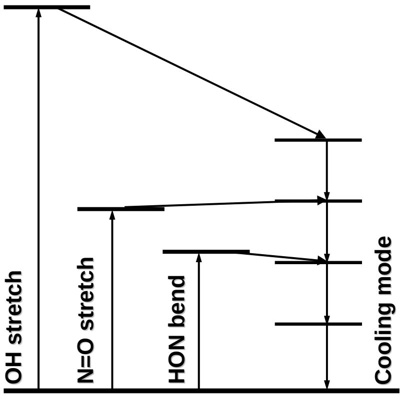

Figure 1.13: Cooling cascade after pumping OH_{trans}, $N{=}O_{trans}$ and HON_{trans}. Energy levels are drawn to scale; for the energies of the cooling mode we use the overtones of ν_5 (ONO bending) from ref. [29]

1.9 Rotational Dynamics

It is not well known in literature what are the rotational dynamics of molecules in rare gas matrices. Pump-probe experiments in which the dynamics of depolarization was followed were done in the Schwentner group. Interestingly, they found that while ClF rotates freely in an Ar matrix, I_2 displays no rotation whatsoever in a Kr matrix [51]. This effect was attributed to qualitatively different immediate surroundings for the two molecules: isotropic for the ClF and cylindrical for the I_2. These experiments reveal the insight that can be gained by performing polarization sensitive experiments.

In this context we performed polarization dependent pump-probe experiments on HONO in Kr matrices at 30 K. In order to follow the rotation dynamics of each isomer we calculated the anisotropy from the Bl/SE signal with the pump polarization being either parallel or perpendicular to the one of the probe pulse:

$$r = \frac{I_{||} - I_{\perp}}{I_{||} + 2I_{\perp}}, \tag{1.5}$$

Surprisingly, we found that the *cis* isomer does not exhibit any significant rotation in the measured time interval (1 ps - 400 ns) but stays constant at $r \approx 0.3$. In the same time the *trans* isomer follows a nonexponential decay from $r = 0.38$ to $r \approx 0.2$ [53](see also chapter 3.5). This value remains constant even on minute time scale (data obtained from steady state measurements in a FTIR spectrometer). The fact that for both isomers the isomerization does not start from the theoretical $r = 0.4$ suggests that the investigated sample spot ($\approx 100\mu$m) is not entirely homogenous. An additional possible reason is that the molecules may exhibit a small degree of wobbling motion governed by the inertia moment. Performing MD calculation we

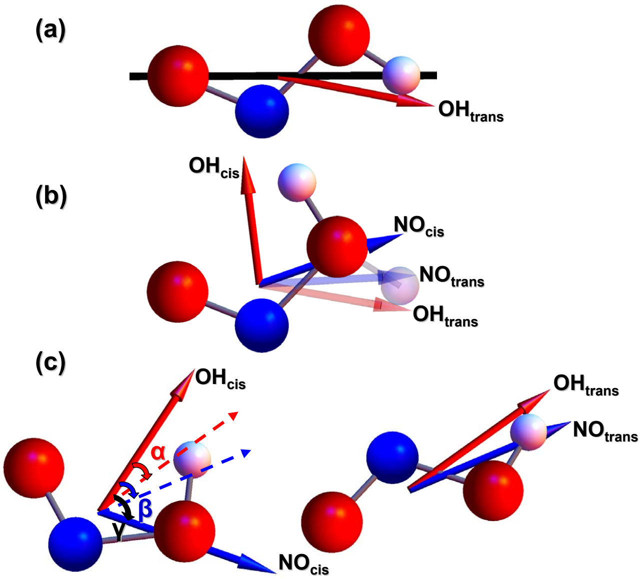

Figure 1.14: Molecular structure and the dipoles moment probed in experiments. The transition dipole moments were determined in a QCISD/cc-pVDZ gas-phase quantum chemistry calculation [52]. (a) Angle θ between the OH$_{trans}$ transition dipole moment and the long-axis that connects the end atoms. (b) Directions of the OH and N=O transition dipole moments assuming that the ONO body is fixed and H takes the position corresponding to *cis* or *trans*(fade colors). (c) Same as (b) but with the ONO body rotated revealing angles α and β that agree within error with experiment. Dashed lines in the left panel represent the corresponding vectors from the right panel

observed that the anisotropy of the *trans* isomer decays very fast in the beginning but then remains constant at $r = 0.13$. This behavior is explained by the dynamics of the *trans* molecule which rotates freely around the axis that links the end atoms (H and O), whereas this axis remains fixed. Our experimental value of 0.2 is somewhat larger and stems also from the fact that our observable is the OH transition dipole moment and not the OH bond (as in the MD simulation). From these two values we calculate an angle of θ=8° between the OH transition dipole moment and the OH bond, value which agrees reasonably well with 22° obtained from a quantum chemistry gas-phase calculation on the QCISD/cc-pVDZ level (see fig. 1.14 panel a).

When we analyze the anisotropy of the isomerized *trans* molecules we find something intriguing. In fig. 1.14 panel (b) we present the HONO molecule in the *cis* and *trans* (fade colors) isomers together with the OH and N=O transition dipole moments from the above mentioned calculation. In presenting this figure we assumed that the ONO atoms of the two isomers are fixed and is only the H atom that moves when the isomers interconvert from one to the other. We observe that the transition dipole moments for the N=O vibrations in the two isomers are almost parallel. Performing polarization sensitive two color experiments in which we pump OH$_{cis}$ and probe N=O spectral region (like the one in fig. 1.12 panel b) we observe that the N=O$_{cis}$ bleach has a constant negative anisotropy of $r = -0.12$ (determining angle γ in fig. 1.14 panel c). In the same time, the anisotropy of the *trans* N=O isomerized molecules is not negative as we expect but positive, $r = 0.14$ (angle β). Moreover, even more surprising is the anisotropy of the OH_{trans} photoproduct after pumping OH_{cis} (measured in an experiment like the one in fig. 1.12 panel c). Assuming a fixed ONO body (fig. 1.14 panel b) we expect a negative anisotropy for the *trans* photoproduct. Nevertheless, the anisotropy that we measure is positive ($r = 0.18$) and interestingly, it is almost equal to the value obtained when we excite the OH_{trans} vibration ($r = 0.2$). This observation renders a very small value for the angle α. This remarkable fact completely contradicts the common sense picture (fig. 1.14 panel b) that assumes that upon isomerization the ONO atoms remain fixed and only the H atom changes position. Therefore, we must conclude that it is the whole molecule that moves upon isomerization in a manner that leaves the end atoms least disturbed from their original positions. Thus, the isomerization proceeds via a hula hoop motion of the central atoms. Given the masses of these atoms and the mass of the H we believe that internally it is still the proton that isomerizes, but the proton transfer is followed by a reorientation of the molecule as a whole. However, the determined angles α and β are not fully consistent with each other assuming that the molecule remains in the same plane. In fig. 1.14 panel c we suggest a possible orientation of the molecule upon isomerization that is consistent (within error) with the experimental values for the angles α and β (for details see also chapter 3.3).

1.10 Conclusions

Chemical reactions are at the heart of our everyday life. Therefore, it is of critical importance an in-depth understanding of these processes. We studied the *cis* - *trans* isomerization reaction of hydrazoic acid (HONO) in Kr matrices as a model system for a proton transfer chemical reaction. With these studies we were the first to investigate the ultrafast dynamics of a chemical reaction in the electronic ground state at low excitation energies ($<3600\ \text{cm}^{-1}$).

When pumping the *cis* isomer we found vibrationally hot, isomerized *trans* molecules as early as 20-50 ps. Furthermore, the isomerization reaction proceeds in two steps. In a mixed quantum-classical calculation [50] it was found that, in the matrix environment, the OH_{cis} prominently exchanges population with three states (001004, 002002 and 003000). Two of them (001004 and 002002) contain harmonics of the torsional mode, which are more delocalized compared to other states, hence having higher probabilities of acting as reactive channels. Moreover, there are 20-30 states that, upon thermal fluctuation, come in resonance with the OH without significant loss in energy. These observations help us assign the fist step of the isomerization process to the direct coupling between the excited mode (OH) and the reactive state(s), whereas the second step represents population that is transferred to the reactive state(s) through the pool of states that come in resonance with the OH and which act as an energy storage (for a detailed discussion see chapter 3.4). Calculating the overall *cis*→*trans* quantum yield we obtain 30-50% and 7-11% for the backward reaction in a Kr matrix at 30 K. Lowering the temperature to 15 K we observe an increase of 30% in the *cis*→*trans* quantum yield. Moreover, the ratio of rates *cis*→*trans*/*trans*→*cis* increases by a factor of 2 when cooling the Kr matrix from 32 K to 10 K. Hence, it follows that the *trans*→*cis* quantum yield should decrease by ≈40% in the same temperature range. This result can be explained with the help of Marcus theory for electron and proton transfer. The increase of the rate in the forward direction (*cis*→*trans*) and decrease in the backward one for the isomerization is a mere effect of a reaction that proceeds energetically downhill. This is the situation when the *trans* reactive states potentials cross the corresponding *cis* ones in their minimum, hence in the *barrierless regime* (see fig. 1.3). This suggested mechanism is consistent with the energy levels of the proposed reactive states and with the OH relaxation time for the two isomers. Considering this mechanism at even lower temperatures (down to 7 K, as in the ref. [19]) one can obtain up to 100% isomerization quantum yield.

Cooling of the OH_{trans} proceeds through a cascade of four equally separated states attributed to the harmonics of one specific mode (see details in chapter 3.2). Exciting lower in energy, the $N{=}O_{trans}$ and HON_{trans} we only observe three and respectively two of these states (see chapter 3.5). We assign this mode to ν_5, ONO bending. We make a tentative assignment for the reaction state(s) and storage states involved in the *cis*→*trans* isomerization reaction and we believe we observe these states spectroscopically in our two color experiments. These observations give key insights into the energy dynamics following photo-excitation.

With the help of polarization sensitive measurements we determined that the *trans* isomer rotates inside the Kr matrix at 30 K along an axis linking its end atoms with this axis remaining fixed. The *cis* isomer exhibits no rotation in the measured time. Upon isomerization the whole molecule readapts its position to the new structure resulting in a motion in which the central O and N atoms perform a hula hoop type of motion.

Chapter 2

Energy Transport in Peptide Helices

2.1 Introduction

Proteins are the building blocks of living cells and consequently are an ubiquitous element of life. Efficiently transporting heat is one among many roles that proteins perform inside the cells. One example is the removal of excess heat from chemical reactions which is of critical importance since proteins can function only in a limited temperature range. Since the functionality of proteins is directly linked to their structure it can be expected that their structure motifs play an important role in heat transport. The two most common secondary structures in proteins are helices and β sheets, both of them being stabilized by hydrogen bonds. Owing to this stabilization characteristic they have on the secondary structures, H bonds were believed to form effective vibrational channels through which heat can be transported [54].

To this end, we decided to investigate experimentally the heat transport in a 3_{10} peptide helix [55]. It is well known in literature that the C^{α}-tetrasubstituted α-amino acid α-aminoisobutyric acid (Aib) forms very stable 3_{10} helices [56] at a relatively low chain length. We dissolve this peptide in an apolar solvent (chloroform) in order to minimize the interaction of the solute with the solvent and to mimic the hydrophobic environment found in the interior of a protein. As a source of heat, we attach to the peptide the azobenzene molecule, which, upon UV excitation undergoes an ultrafast (200fs) internal conversion [57]. We excite the cromophore in the *cis* conformation at 425 nm and probe the heat transfer with IR light. As a heat "thermometer" we use the amide I band of each amino acid unit, and since this mode is almost entirely made by the C=O stretch we will use the two vibrations interchangeably. It was shown that the C=O vibrations shift in frequency upon an increase in their surrounding temperature [58], thus acting as local thermometers. In order to achieve spatial resolution, we isotope label one of the amino acids in the sequence (with ^{13}C), thereby spectrally separating its amide I band from all other modes by reducing its frequency with $\approx$30 cm^{-1}. Placing the isotope labeled amino acid at different positions in the peptide we can monitor the heat transfer as a function of distance from the heater. Hence, performing an UV pump - IR probe experiment with femtosecond pulses and using different samples with labels at different positions we are equipped with high time and space resolution in resolving the heat transport in a small peptide.

2.2 Experimental results

In fig. 2.1 panel (a) we present the structure of the PAZ cromophore attached to the $(Aib)_8$ peptide helix. We mark with labels 1..9 the positions of the spectrally separated absorption bands. In panel (b) the steady state absorption spectra are presented for molecules in which the ^{13}C labeled amino acid is placed at different positions along the helix, and (the black line) for the molecule without any ^{13}C labeling. The strong absorption band in the middle (main band) corresponds to all spectrally similar amino acids. Bands 1 and 9 correspond to the urethane group at the beginning of the helix and respectively the ester group at the end of the helix.

In fig. 2.2 we present the transient absorption spectra (a-c) for molecules with ^{13}C labeling at the second, third and respectively fifth C=O group (from the linker). The size of the bleach signal is interpreted as a direct measure of the local temperature. We can observe that band 1

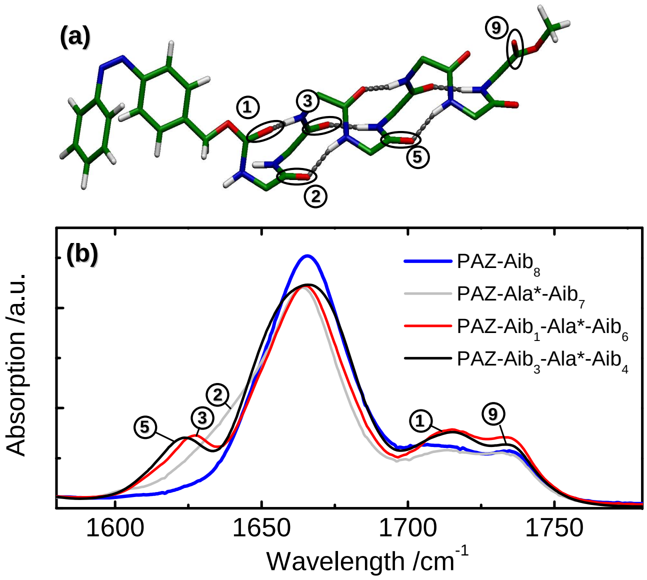

Figure 2.1: (a) Structure of PAZ-(Aib)$_8$-OMe in which with labels 1..9 we indicate the positions of ^{13}C isotope labeled C=O groups from the PAZ residue. (b) FTIR spectra of the above molecule in which different Aib units (see number) were replaced by Ala amino acids with a ^{13}C=O group.

has the highest intensity (not counting the "main band" which is a signal corresponding to six similar oscillators). This result is understood through the proximity of this group to the heater. Bands 2,3 and 5 have intensities that decrease monotonically with the distance from the source of heat. Although band 2 is not well separated from the main band we are confident to conclude that its intensity is higher (in terms relative to the energy received, i.e. band 1) than band 3. In fig. 2.1 panel (a) we notice that the C=O groups that give rise to bands 1 and 3 are linked by a hydrogen bond. If indeed the heat would be transported through the hydrogen bonds, band 3 would measure a higher temperature than band 2. Therefore, we conclude that the heat is actually transported through the backbone of the helix.

When analyzing the kinetics of these bands we observe that the heat is transferred within our time resolution to the helix. Following this initial step, the heat propagates diffusively along the helix, behavior observed through the kinetics of bands 2, 3 and 5. We constructed a rate equation system (see chapter 3.6) in which we model the peptide as a chain of 9 units with each unit changing heat with the neighboring units and the solvent. We fitted the kinetics of this system with the appropriate observables in our experiment, and calculated for the diffusion coefficient in peptides $D = 2\text{Å}^2/\text{ps}$ (for details see also chapter 3.6). Further experiments investigated the difference in heat conductivity when high or low excitation is applied [59]. It was found that heat diffusivity is four times higher when low excitation levels are used (for further details see chapter 3.7). When varying the temperature, a special transition from inefficient and mostly ballistic to more efficient and mostly diffusion was found at $\approx$270 K [60](see also chapter 3.8).

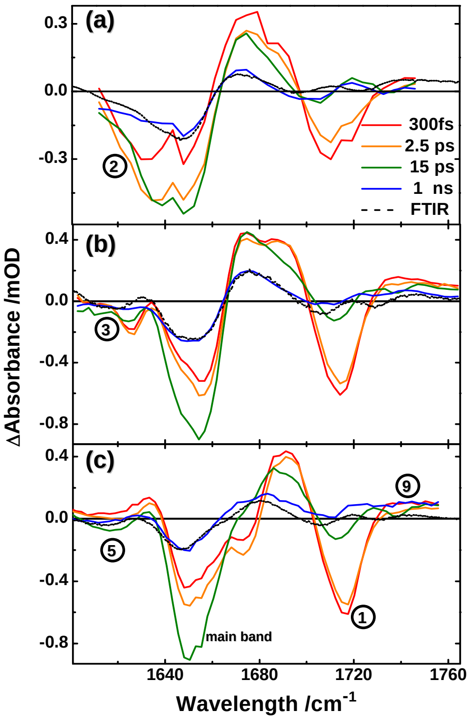

Figure 2.2: Transient absorption spectra of PAZ-Ala*-Aib$_7$-OMe (a) PAZ-Aib-Ala*-Aib$_6$-OMe (b) and PAZ-Aib$_3$-Ala*-Aib$_4$-OMe (c) at different delay times; black dashed line spectra correspond to temperature difference FTIR spectra. (d) kinetics of the spectrally separated bands of panel b; (e) kinetics of the spectrally separated bands of panel c.

2.3 Conclusions

Combining ultrafast pump-probe experiments with cleverly designed peptides we were able to address the proposed role of H-bonds in the heat transfer along the peptide helices [54]. We observed that heat propagates along the backbone of the helix and not along the H-bonds as predicted earlier. Furthermore, a value for the heat diffusion coefficient was calculated [55]. The excitation level and temperature were investigated as parameters of the heat diffusivity in peptide helices.

Chapter 3

The publications

3.1 A Femtosecond Study of the IR-driven *Cis-Trans* Isomerization of Nitrous Acid (HONO)

Roland Schanz, Virgiliu Botan, Peter Hamm

J. Chem. Phys., 122, 044509, (**2005**)

Abstract

We investigate the dynamics and mechanism of the IR-driven *cis-trans*-isomerization of nitrous acid (HONO) in a low-temperature krypton matrix applying ultrafast timeresolved IR spectroscopy. After excitation of the OH-stretching mode the *trans* HONO state decays bi-exponentially on a 8 ps and 260 ps timescale. The initially excited *cis* HONO state decays on a 20 ps time scale. *Cis* HONO isomerizes with 10% quantum yield on a 20 ps time scale to *trans* HONO. The quantum yield we observe is significantly smaller than the previously reported 100%, which could imply that additional, much slower reaction channels exist. We furthermore developed a 4D model of the system, which includes the three proton intramolecular degrees of freedom of HONO fully quantum-mechanically and one intermolecular translational degree of freedom of the molecule in the crystal cage. We find that *cis-trans* isomerization necessarily is accompanied by a translation of the molecule as a whole in the crystal cage. The translational degree of freedom tunes the intramolecular proton states of HONO with respect to each other. When resonances occur, the proton states might couple and transfer population. We suggest a possible reaction pathway, where the *cis* OH-stretch excited state first couples to a high *cis* torsional mode, which then may transfer almost instantaneously to the *trans* side. The model qualitatively explains all experimental observations.

3.1.1 Introduction

It is well established that electronically driven photochemistry is ultrafast in general [1]. However, most (not all) chemistry is happening on electronic ground state potential energy surfaces, rather than through electronically excited states. From the experimental point of view, very little is known about the dynamics (to be contrasted to the kinetics) of ground state chemical reactions in the condensed phase on a microscopic, atomic level. In the present paper we study the *cis-trans* isomerization of the nitrous acid (HONO) molecule in a low temperature rare-gas matrix. This reaction proceeds in the electronic ground state in the condensed phase and is triggered by excitation of the OH-stretch band (see Fig. 3.1, inset). It was first discovered by Pimentel et al. and it is one of the few known examples of a system which undergoes a conformational transition upon excitation of *one* quantum of a vibrational mode [12, 15, 16, 61]. Most remarkable about the reaction is the exceptionally high isomerization quantum yield which according to Pimentel et al. is '*of the order of unity*' [16]. This result is indeed astonishing given the fact that it is *not* the reaction coordinate which is excited by the IR pump light. Apparently, the excited OH-stretching mode and torsional modes (*i.e.* the reaction coordinate) are efficiently coupled. Presumably, the coupling is mediated through the matrix, as this reaction has not been reported in the gas-phase so far. It is the intention of this paper to explore the nature of this coupling between excited and reactive vibrational modes and the role of the matrix as mediator.

In the gas phase, pioneering pump probe measurements of ground state reactions have been performed, *e.g.* by Hippler et al. who have measured the isomerization of cycloheptatriene after UV-excitation followed by internal conversion [5]. The reaction proceeds on a microsecond time scale. Scherer, Zewail et al. investigated the ground state dissociation of H_2O_2 after overtone excitation (ca. 615 nm) [6] or even a bimolecular reaction ($H+CO_2 \rightarrow OH+CO$) after UV-photoactivation of a van der Waals-complex [7]. These reactions take place on the order of picoseconds. These experiments have in common that a large amount of energy (16000 cm^{-1} to 40000 cm^{-1}) is pumped into the system.

The stationary properties of HONO in the gas phase have been explored extensively because the molecule plays a crucial role in atmospheric chemistry as a source of tropospheric OH radicals after photodissociation [33–35, 62]. The structure of both isomers was obtained from rovibrational measurements by Cox and coworkers [36]. The energy difference between both isomers could be obtained from *cis-trans* equilibrium measurements by UV-absorption [37], infrared-absorption [14] and microwave measurements [38]: the energy of the *cis* isomer is $\approx$100-200 cm^{-1} above that of the *trans* configuration. The transition state, on the other hand, is located along the torsional coordinate with an energy of $\approx 4000 \pm 500$ cm^{-1} [32]. Hence, the energy of one quantum of the OH-stretch vibration ($\approx$3500 cm^{-1}) is in the same order as that of the transition state, but it is not known whether it is above or below.

More recent studies of the IR induced *cis-trans* isomerization of HONO, using modern laser techniques, are found in Refs. [17, 19]. McDonald and Shirk observed non-exponential reaction kinetics in solid N_2 and Ar, which they attributed to the fact that energy migration between crystal sites is involved in the photo reaction [17]. No value for the quantum yield was given (which would not have been meaningful given the non-unimolecular character of the kinetics). Later, Räsänen and coworkers repeated the experiment in solid Kr and found exponential kinetics [19]. In agreement with Pimentel, they concluded that the *cis-trans* quantum yield is high, '*possibly approaching 1*'. They furthermore determined the ratio of *trans-cis* and *cis-trans* quantum yield to be 0.14.

All published works so far are kinetic measurements, not dynamic measurements. They measure the kinetics of the isomerization reaction under a certain photon flux condition. The dynamics of the photoreaction, i.e. the transient intermediates after absorbing an IR photon, are not known. The mechanism of the photo isomerization, or merely the order of magnitude of its timescale (whether it is femtoseconds or milliseconds) is completely unknown. It is not known whether coherent wavepacket motion or tunneling is involved, or whether a quasi-classical random walk gives rise to the proton transfer. Pimentel suggested that the reactive mode is an overtone of the torsional mode of very small oscillator strength [16]. Hence, the energy has to be deposited in a fundamental or simple combination mode within the frequency range of the barrier height. Then the energy is transferred intramolecularly from the absorbing mode to a non-hindered torsional mode of same symmetry. From here it would be trapped with a 50% chance in one of the two potential wells.

From the theoretical point of view, the *cis-trans* isomerization was studied by molecular dynamic (MD) simulations [22–24]. These works, which use an excitation energy of $\approx$10000 cm^{-1}, suggest that isomerization occurs on a few picosecond timescale and that it is the interaction with the matrix which randomized the energy within the molecule. However, these simulations are classical in nature and ignore the quantum character of the proton. On the other hand, the gas phase system has been studied on a semi-classical level using an empirical valence bond potential [26]. Moreover, the coupled vibrational problem has been computed on a full quantum level, using a high-end potential energy surface and including all six internal degrees of freedom of the molecule [20,29]. More recently, both authors studied the coherent wave packet dynamics of an initially constructed localized state [21, 30]. These calculations, which model a gas phase system, suggest that the *cis* and *trans* OH vibrational eigenstates are localized on either side with only little interaction between them. Here, we report on a combined experimental/theoretical effort that provides evidence that both the quantum character as well as the matrix interactions in the condensed phase are crucial to understand the mechanism of the *cis-trans* isomerization.

3.1.2 Experimental

Experimental Methods

HONO was synthesized photochemically according to the procedure described by Hall and Pimentel [16]. A gas mixture of hydrazoic acid (HN_3), oxygen and krypton with a pressure ratio of 3/10/1000 was deposited inside a cryostat (DE-202AF/DMX-20B, Advanced Research Systems, Inc.) at 30 K on a calcium fluoride window. The crystalline film was then irradiated with a mercury lamp for about 1 h until all hydrazoic acid was photolyzed and reacted with oxygen to form HONO. A HN_3 band at 3317 cm^{-1} was used to monitor the completion of the reaction.

For the femtosecond IR pump-probe experiments we used pulses from a home-built optical parametric amplifier (OPA) [63]. The 150 fs pulses were centered at $\approx$3402 cm^{-1} (bandwidth of 360 cm^{-1} FWHM, with an energy of 1 μJ, with a repetion rate of 1 kHz, and focused to a spotsize of $\approx$ 150 μm). Every second pump-pulse was blocked with the help of a synchronized light chopper for referencing. A small fraction of the infrared pulse was split off to obtain broadband probe and reference pulses, which were spectrally dispersed in a 190 mm spectrometer and detected with a 63 channel HgCdTe detector array, covering a spectral range from 3370 cm^{-1} to 3560 cm^{-1} with a resolution of 3.3 cm^{-1}/pixel.

To enable selective excitation of either *cis* or *trans* HONO, the pump pulse was spectrally filtered with the help of a piezo controlled adjustable Fabry-Perot filter (bandwidth 17 cm^{-1}). The resulting pump pulse shape can be approximated as single-sided exponential with a time bandwidth product of $\tau\Delta\nu_{FWHM} = 1/2\pi \approx 0.16$ (i.e. pulse duration $\approx$300 fs). The experiment required fast alternation between both pump wavelengths to prevent depletion of the particular excited species. Hence, the measurements have been performed according to the following protocol: In each cycle, the Fabry-Perot filter was first tuned to the *cis* OH absorption band (3402 cm^{-1}) for a time of 1 second (i.e. 1000 laser shots), after which time *cis* HONO was essentially depleted. Only the first 250 ms were used for data collection, while the remaining 750 ms were used to shift the population to the *trans* side. Then, the Fabry-Perot filter was changed to the *trans* frequency (3552 cm^{-1}). To account for the lower *trans-cis* quantum yield, *trans* HONO had to be illuminated longer (12 s). Again, only the first 3 seconds were used for data collection, while the remaining 9 seconds were used to repopulate the *cis* species. This cycle was continuously repeated for each delay time position. In this way, each experiment was performed on an ensemble which to a large extent ($> 70\%$) contained either the *cis* or *trans* configuration. Together with the selectivity of the pump pulse (50/1), we conclude that contamination of the measurement signal from the reaction in the opposite direction is negligible. In total 130 time scans have been averaged, resulting in a dynamic resolution of $\approx$ 0.002-0.005 mOD (rms).

The $\nu = 1 \rightarrow \nu = 2$ excited state absorption band of *cis* HONO, which is located at 3204 cm^{-1}, is outside the spectral window of the setting described above. To measure its dynamics, we used a second OPA for the pump pulses, while the first OPA and the spectrometer were tuned to the 3204 cm^{-1} band. Since alignment of the Fabry-Perot filter requires a computer-controlled feedback loop through the spectrometer, it could no longer be used in this experiment (since the pump wavelength was now outside the spectrometer spectral window) and was put aside. In this way a photoequilibrium of both isomers was excited simultaneously by the broad band pump pulses.

If the optical phase between pump and probe pulse is fixed, both imprint a population grating into the matrix,

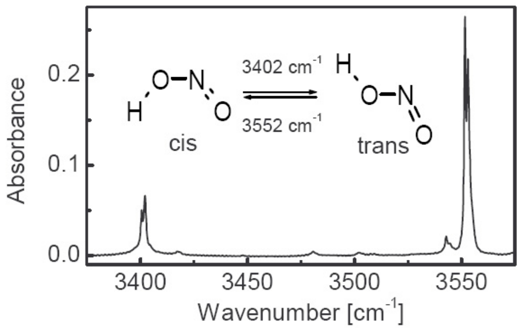

Figure 3.1: The steady state absorption spectrum of HONO in solid krypton at 30K with the OH-stretching bands of the *cis* (3402 cm^{-1}) and *trans* species (3552 cm^{-1}).

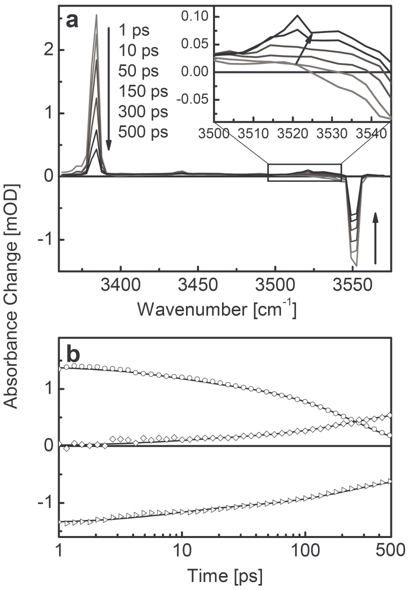

Figure 3.2: Selective excitation of the *trans* isomer. (a) Transient difference spectra at different delay times. They consist of a positive $\nu = 1 \rightarrow \nu = 2$ excited state absorption band (3390 cm^{-1}), a negative stimulated emission/bleach band (3552 cm^{-1}) and the "dark state" signal (3515-3550 cm^{-1}). (b) The corresponding transients of the frequency-integrated $\nu = 1 \rightarrow \nu = 2$ excited state absorption band (○), stimulated emission/bleach band (▷), and dark state signal (◇). They are globally fitted globally to a biexponential function with 8 ps and 260 ps time constants

revealing coherent artifacts that need to be suppressed (see the Appendix for a detailed discussion). The phase between pump and probe pulse was scrambled using a piezo mounted mirror in the pump beam that was driven by a noise generator with a cut-off frequency of 1 kHz such that the phase was randomized over a range of one light cycle.

Experimental Results

The steady state absorption spectrum of HONO in solid krypton at 30°K is depicted in Fig. 3.1. In the spectral region shown it consists of two main bands, the OH-stretching band of the *cis* isomer at 3402 cm^{-1} and that of the *trans* isomer at 3552 cm^{-1}, respectively. Both bands exhibit some substructure (hardly resolved on the scale of Fig. 3.1) which has been attributed to site inhomogeneities [19].

Selective excitation of trans HONO: Fig. 3.2(a) shows transient difference spectra after selective excitation of the OH stretching band of the *trans* isomer. The negative band at 3552 cm^{-1} appears at the same frequency as the originally pumped state, and is assigned to the $\nu = 0 \rightarrow \nu = 1$ bleach and $\nu = 1 \rightarrow \nu = 0$ stimulated emission signals. Both appear at the same frequency, since there is hardly any Stokes shift for vibrational transitions. The band at 3390 cm^{-1} is assigned to $\nu = 1 \rightarrow \nu = 2$ excited state absorption of the *trans* OH-stretching mode. The large anharmonic shift (162 cm^{-1}) is in agreement with overtone spectra measured in the gasphase [41, 64].

At later delay times a third signal appears slightly red-shifted from the bleach/stimulated emission signal of the *trans* OH stretching mode. We will refer to this band as "dark states". It stems from *trans* molecules that have relaxed from the originally excited OH-stretching state, the bright state, to lower lying vibrational modes which are not observed in the steady state absorption spectrum and thus called dark states. These states can be overtones and/or combination modes, of which many exist in the molecule (see Sec. 3.1.3). As a consequence of anharmonic couplings between these dark states and the bright OH-stretching mode, the later absorbs slightly red-shifted with respect to its original frequency, once one of the dark state is populated. In the difference spectrum of Fig. 3.2(a), population of dark states will manifest itself as a negative bleach of the OH stretching mode in the vibrationally relaxed molecule and a positive dark state signal. In other words, although overtones and combination modes do not carry oscillator strength, we may still observe them through their anharmonic coupling to the bright OH stretching mode. The effect has been described in detail in Ref. [58].

The anharmonic couplings x_{ij} giving rise to the red shift of the dark state band have been calculated on a high level and are relatively small (in the order of -10 cm^{-1}) [29]. Hence, we can safely conclude that the dark state signal in Fig. 3.2 is related to molecules that are in the *trans* configuration. In Fig. 3.2 we find no hint for *trans-cis* isomerization on the 500 ps timescale.

The temporal evolution of the three signals is depicted in Fig. 3.2(b). While the positive $\nu = 1 \rightarrow \nu = 2$ excited state absorption band decays nearly completely to zero within 500 ps (○), the negative band decays only to about 50% of the initial intensity (▷). The $\nu = 1 \rightarrow \nu = 2$ excited state absorption and $\nu = 1 \rightarrow \nu = 0$ stimulated emission signals both reflect the population of the initially excited OH stretching mode. In contrast, the bleach signal reflects the hole in the ground state population. We conclude that the originally excited state of *trans* HONO relaxes into the dark states within 500 ps, but not back into the vibrational ground state on this time scale. Therefore, the dark state signal (◇) rises as the $\nu = 1 \rightarrow \nu = 2$ excited state absorption and $\nu = 1 \rightarrow \nu = 0$ stimulated emission signal decay, but the bleach stays constant in time.

The relative intensities of the various contributions can be understood as well: bleach and stimulated emission have the same transition strength μ_{01}^2, explaining the drop of the negative band to 50% as the stimulated emission decays, while the $\nu = 1 \rightarrow \nu = 2$ excited state absorption is twice as strong, $\mu_{12}^2 = 2\mu_{01}^2$ (in the harmonic approximation), explaining the similar strength of both signals at early delay times. At late delay times, the (frequency-integrated) dark state signal roughly matches the remaining bleach signal.

The time-dependence of all three signals is clearly non-exponential. We fit them globally by applying a bi-exponential function, yielding a fast component with τ_1 = 8 ps (relative contribution 0.2) and a slow component with τ_2 = 260 ps (relative contribution 0.8).

The dark state band is significantly broader than the stimulated emission/bleach and the $\nu = 1 \rightarrow \nu = 2$ excited state absorption bands. We attribute this broadening to the fact that the dark state band actually consists of many transitions as a result of a population of more than one overtone or combination mode. A closer inspection shows that the dark state signal evolves spectrally (see inset Fig. 3.2(a)). In the beginning the band is broad and structureless. After about 300 ps we find the first spectral moment of the band moving towards higher frequencies. Simultaneously, a sharp peak is rising at 3521 cm^{-1} that probably reflects the population of one particular dark state with an anharmonic coupling of 30 cm^{-1}.

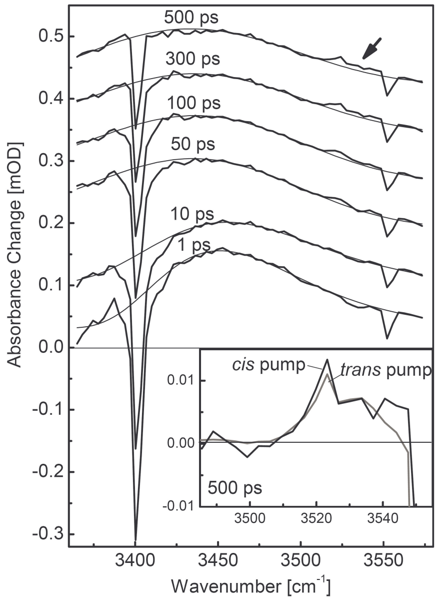

Figure 3.3: Transient absorption spectra after selective excitation of *cis* HONO (thick lines). The broad background signal was fitted as described in the text (thin lines). The arrow marks vibrationally excited nascent *trans* HONO, which reflects *cis-trans* isomerization. inset: Comparison of the *trans* dark state signal 500 ps after exciting *cis*-HONO (black) and *trans* HONO (gray). The broad band background is subtracted.

Selective excitation of cis HONO: Fig. 3.3 shows transient difference spectra after selective excitation of the *cis* isomer. The spectra are superimposed on a broad background which is due to a water film that is growing on the sample. At 3402 cm^{-1} we find the stimulated emission/bleach of the *cis* species. Another small signal with negative sign is located at 3552 cm^{-1}. One might be tempted to assign the latter to stimulated emission from *trans* HONO. If there would be a transfer from the *cis* to the *trans* OH stretching mode, stimulated emission should indeed occur. In this case also the corresponding $\nu = 1 \rightarrow \nu = 2$ excited state absorption band should appear at 3390 cm^{-1} with twice the intensity (i.e. $\mu_{12}^2 = 2\mu_{01}^2$), which, however, is not observed. Furthermore, the stimulated emission signal should decay

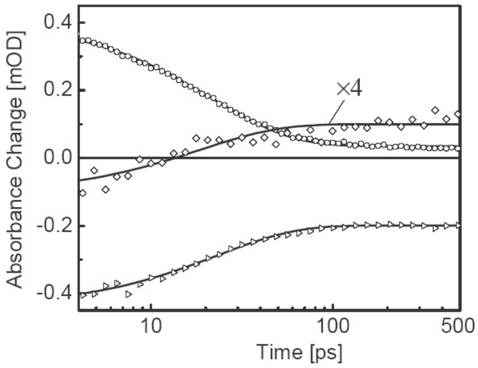

Figure 3.4: Transients of the integrated intensities of bleach/stimulated emission (▷), $\nu = 1 \rightarrow \nu = 2$ excited state absorption (○) and the product band (dark state signal of *trans* HONO, ◇). The $\nu = 1 \rightarrow \nu = 2$ excited state absorption signal occurring at 3204 cm^{-1} has been measured in a separate experiment with broad band pump pulses, that excited *cis* and *trans* HONO simultaneously, see Sec 3.1.2.

on the same time scale as when pumping *trans* HONO directly (i.e. 8 ps and 260 ps). In contrast, the peak at 3552 cm^{-1} stays constant in time. We therefore assign it to a measurement artifact, possibly due to heating of the sample and/or scattering at the *trans* absorption band.

Most important is a small, broad signal in the region between 3515 cm^{-1} and 3550 cm^{-1} (see arrow) which we attribute to *trans* dark states. This signal directly reflects the *cis-trans* isomerization. For data processing the background signal has been removed as follows: A sum of two log-normal functions [65] was fitted to the raw data omitting the spectral regions where we observe spectral contributions of HONO, i.e. 3375–3440 and 3500–3560 cm^{-1}. The background then was subtracted from the raw data. The inset of Fig. 3.3 compares the remaining signal at 500 ps with the dark state band observed after direct pumping of *trans* HONO. As both coincide very well we conclude that the signal rising after excitation of *cis* HONO indeed represents nascent *trans* HONO, which is vibrationally excited in combination modes and overtones, but is vibrationally relaxed with respect to the *trans* OH stretching coordinate.

Fig. 3.4 shows the transients of the stimulated emission/bleach (▷) and the $\nu = 1 \rightarrow \nu = 2$ excited state absorption signal (○) of *cis* HONO as well as the rise of the product band (◇), i.e. the *trans* dark state signal integrated from 3515 cm^{-1} to 3545 cm^{-1}. The product band rises in a step-like fashion which can be fit using a monoexponential function with 19 ps time constant. This matches very well the depopulation time of the *cis* OH stretching mode, being 23 ps and 21 ps for the $\nu = 1 \rightarrow \nu = 0$ stimulated emission and the $\nu = 1 \rightarrow \nu = 2$ excited state absorption, respectively. From these results we conclude that isomerization occurs from the *cis* excited OH-stretching state. As this state decays, formation of the *trans* product stops.

The ratio between the frequency-integrated product signal after 500 ps and the bleach signal at time zero is ≈1/4, which, when taking into account the different oscillator strengths of the *cis* and *trans* OH stretching modes (1:2.5) [19], reveals an estimate of 10% for the *cis-trans* isomerization quantum yield. This value is considerably smaller than the reported 100% *cis-trans* quantum yield [19]. We may offer two explanations for this discrepancy: (a) In our experiment we measure the *cis-trans* quantum yield after 500 ps. Clearly, the molecule is not relaxed after that time, and it might be that additional slower isomerization pathways from lower lying states exist which make up for the difference. In fact, when closely inspecting Fig. 3.4, the signal might keep increasing after the first 20 ps step, however, the present signal-to-noise is not sufficient to tell for sure. Pump-probe measurements with significantly longer delay times will be required to decide this question. (b) Ref. [19] leaves room for a large error bar of the 100% quantum yield. The authors do not specify any error bar, but write: *'.. possesses a high quantum yield, possibly approaching one. .... We emphasize that these numbers are not quantitatively reliable because some inaccurate parameters are involved in the estimate. Nevertheless, high quantum efficiency of the process is qualitatively evidenced, indeed.'* The work of Ref. [19] deduces the quantum yield from kinetic measurements, which includes severe uncertainties, in particular the *absolute* power density in the measurement spot, the *absolute* cross sections and concentrations, as well as propagation effects. Our experiment should be the more precise measurement of the quantum yield, since the bleach signal serves as an inherent calibration of the number of excited molecules. Only relative measurements, and no absolute measurements, are required to determine the quantum yield in our case.

To conclude the experimental part, we summarize the most important results (see Fig. 3.5):

- The initially excited *trans* HONO state decays bi-

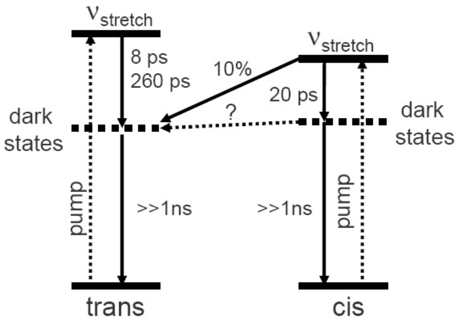

Figure 3.5: Reaction scheme after pumping either *cis* or *trans* HONO. The dark states represent combination modes and/or overtones of lower lying vibrational states.

exponentially on a 8 ps and 260 ps timescale.

- The initially excited *cis* HONO state decays on a 20 ps time scale.
- *Cis* HONO isomerizes with 10% quantum yield on a 20 ps time scale to *trans* HONO. The *trans* product is in the ground state, what the OH stretching mode is concerned, but it is vibrationally excited, what other modes are concerned. There is some indications for an additional slower isomerization channel ($\gg 500$ ps), which could make up for the reported 100% quantum yield [19].
- No *trans-cis* isomerization is observed, which, however, is not expected given the smaller *cis* cross section and the fact that the *trans-cis* quantum yield is reported to be 7 times smaller [19] (the relative quantum yields can be measured much more accurately than the absolute values).

In the following section, we will present a model that explains all these observations qualitatively.

3.1.3 Theoretical Modelling

Gas Phase Scenario: The anharmonic vibrational states of the molecule *in vacuo* have been calculated recently by Luckhaus [20] and by Meyer and coworkers [29]. They started from high level *ab initio* potential energy surfaces (on the B3LYP/6-311++G** level in Ref. [20] and on the CCSD(T)/cc-pVQC level in Ref. [29], respectively) and calculated the fully coupled vibrational problem in six dimensions. Both works consistently come to the following conclusion: Two independent sets of OH-stretch and bend states exist for each of the *cis* and *trans* configurations, which are *essentially localized* on either side. The torsional states, on the other hand, start to delocalize at the transition state energy, but remain largely decoupled from other degrees of freedom. Anharmonic couplings are too weak to efficiently mix modes even at energies above the torsional barrier. Anharmonic energy corrections x_{ij} for overtones and combination modes have been calculated [29] and are relatively small (in the order of -10 cm^{-1}, with a few exceptions). As a result, the states maintain their harmonic character, and can be assigned by their harmonic quantum numbers.

To our knowledge, IR-driven isomerization of HONO in the gas phase has not been observed experimentally. This would be in agreement with the gas phase calculations [20, 21, 29], according to which one would *not* expect the molecule to isomerize efficiently. In simple words, the density of states in the energy range of the OH-stretching modes ($\approx 0.25/\text{cm}^{-1}$) is too small and the coupling between *cis*- and *trans* configuration too weak. The average energy splitting between states is less than anharmonic couplings, and in particular much less than the tunneling coupling through the torsional barrier. Accidental (Fermi) resonances may occur. However, it seems unlikely that such Fermi resonances lead to isomerization out of the OH-stretching mode, since in that case, the tiniest modification of the potential energy surface, e.g. by isotope labeling or by matrix inhomogeneities, should completely modify the mechanism. In essence, the gas phase spectrum is discrete, and the states excited by IR pumping, i.e. the states that carry oscillator strength, are stationary eigenstates. We argue in the following that the matrix perturbs the proton vibrational states significantly and completely changes the picture sketched above.

3.1.4 Computational Methods

To that end, we have developed a 4D model with three HONO intramolecular degrees of freedom and one translational degree of freedom of the HONO molecule in a rigid matrix cage. We assumed that the -ONO body is stiff and considered as intramolecular modes only the three hydrogen degrees of freedom with respect to the -ONO body. To describe the quantum mechanical eigenstates of the proton, we used an empirical proton potential:

$$V_{HONO} = V_r(r,\phi) + V_\theta(\theta,\phi) + V_\phi(\phi) \qquad (3.1)$$

with

$$\begin{aligned} V_r(r,\phi) &= D_0\left[1 - e^{-\sqrt{\frac{m}{2D_0}}\omega(\phi)(r - r_0(\phi))}\right]^2 \\ V_\theta(\theta,\phi) &= k_\theta/2\left[\cos\theta - \cos(\theta_0(\phi))\right]^2 \qquad (3.2) \\ V_\phi(\phi) &= \sum_{j=1}^{3} E_{\phi,j}\left[1 - \cos(j(\phi - \pi))\right]/2 \end{aligned}$$

where r is the -OH bond length, ϕ the proton torsional angle and θ the NOH bond angle. The proton degrees of freedom were weakly coupled through:

$$\begin{aligned} \omega(\phi) &= \omega_{trans} + (\omega_{cis} - \omega_{trans})(1 + \cos\phi)/2 \\ r_0(\phi) &= r_{trans} + (r_{cis} - r_{trans})(1 + \cos\phi)/2 \qquad (3.3) \\ \theta_0(\phi) &= \theta_{trans} + (\theta_{cis} - \theta_{trans})(1 + \cos\phi)/2 \end{aligned}$$

Geometric parameters (r_{trans}=0.958 Å, r_{cis}=0.982 Å, $\theta_{trans} = 102.1°$, $\theta_{cis} = 104.0°$) were taken from experiments [36, 66]. The potential parameters were fit to reproduce the gas phase frequencies of the OH-stretch and the bend mode of *trans* (3590 and 1263 cm^{-1}) [41] and the OH-stretch of *cis* (3426 cm^{-1}) [42]. This way we obtained as parameters for the OH-stretch: ω_{trans}=3758 cm^{-1}, ω_{cis}=3576 cm^{-1}, D_0=42830 cm^{-1}, bend force constant: k_θ=47825 cm^{-1}. The torsional parameters $E_{\phi,j}$ define the relative energy ΔE between *trans* and *cis* ground state as well as the height E_a and position ϕ_a of the transition state. We chose $\Delta E =$ 178 cm^{-1} [38] and $\phi_a = 86°$ [32], which, together with the zero point energies, stabilizes the *trans* configuration by 90 cm^{-1}. The height of the barrier, E_a, turns out to be critical for the interpretation of the experiment, and we considered it to be a free parameters of the theory. We chose $E_a = 3610$ cm^{-1}, which is a little less than the commonly accepted value (≈ 4000 cm^{-1}), albeit still within the uncertainty range (see discussion below). The proton potential Eqs. 3.1- 3.3 is not thought to yield quantitative results (which is not expected anyway due to the neglect of the non-proton degrees of freedoms of the molecule). Nevertheless, a comparison with the *ab initio* potential [29] shows that it captures anharmonic couplings reasonably well.

The vibrational Schrödinger equation was solved using a *sinc*-function DVR basis in cartesian coordinates [67] with step size 0.09 Å and a cut-off energy of 18.000 cm^{-1}. The basis typically contained $\approx$8000 elements and it has been verified that the first OH-stretch excited state is converged to about 10 cm^{-1}. In agreement with the full 6D quantum calculation of Refs. [20, 29], we find that the vibrational states do not delocalize across the torsional barrier *in vacuo*. Due to the neglect of the non-proton degrees of freedom, the density of states in the energy range of the OH-stretching modes is reduced to roughly 0.025/cm^{-1}.

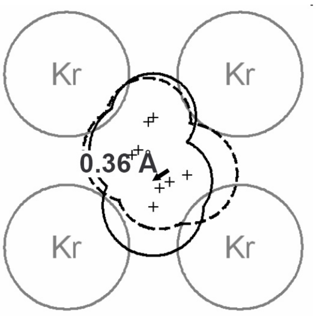

Figure 3.6: Minimum energy positions of *trans* HONO (solid line) and *cis* HONO (dashed line) in the Kr matrix cage; cut through the (100) plane. The arrow indicates the displacement of the center oxygen upon isomerization.

The interaction of the HONO molecule with the matrix was modeled using Lennard Jones pair potentials. Agrawal et al. have reported Lennard Jones parameters for HONO with Xe [22] and Ar [23]. Following their prescription, we deduced Lennard Jones parameters for HONO in Kr from Ref. [68]: $\sigma_{Kr-O} = 3.371$ Å, $\varepsilon_{Kr-O} = 6.42$ meV, $\sigma_{Kr-N} = 3.564$ Å, $\varepsilon_{Kr-N} =$ 5.77 meV, $\sigma_{Kr-H} = 3.624$ Å, $\varepsilon_{Kr-H} = 1.87$ meV. Experimental geometry parameters were used for the HONO molecule [36, 66], while the matrix cage was modeled as rigid *fcc* lattice with a Kr-Kr distance of 1.967Å, restricting the interaction to the first solvation shell only.

3.1.5 Computational Results

Condensed Phase Scenario: As a first step, we minimized the position of the HONO molecule in the matrix cage and found that the HONO molecule occupies an one-atom substitutional site, in agreement with Ref. [69]. Not surprisingly, however, we found that the minimum positions of the *cis* and *trans* isomers are slightly different with a separation of the center oxygen of ≈0.36 Å and a small twist of 5° of the ONO-axis (Fig. 3.6). This leads to the important conclusion that the *cis-trans* isomerization of HONO is *necessarily accompanied* by a translational motion of the molecule as a whole. We will see that it is this coupling between intramolecular and intermolecular degree of freedom which is responsible for efficient isomerization pathways.

Proton vibrational eigenstates of the HONO molecule perturbed by the matrix were calculated using a proton potential energy:

$$V = V_{HONO} + V_{VdW} \tag{3.4}$$

to which the van der Waals interaction with the matrix has been added. Since the latter depends on the position of the molecule in the matrix cage, *vibrational eigenstates are obtained whose energies vary with that position*. In that way, *translational* potential energy surfaces may be constructed for each OH vibrational state (which should not be confused with the *proton* potential energy surface Equ. 3.1). Fig. 3.7 shows an one-dimensional cut through these potential energy surfaces along a straight line that connects the *cis* and *trans* minimum positions. The various OH vibrational states are tuned with respect to each other as the molecule moves in the matrix cage. The potential energy surfaces are colored according to their transition dipole moments from the *trans* ground state (blue) or the *cis* ground state (red), respectively. Hence, the bright blue potential curve in Fig. 3.7, upper part, corresponds to the *trans* OH-stretch excited state ($\nu_{stretch,trans}$) and the bright red curve to the *cis* OH-stretch excited state ($\nu_{stretch,cis}$). All other states in this energy region are overtones and combination modes, i.e. are dark states which are colored in gray. When dark states couple with bright states, Fermi resonances may occur which transfer oscillator strength from the bright states to the dark state. This is depicted as gradual transition between gray to colored (see e.g. Fig. 3.7 inset).

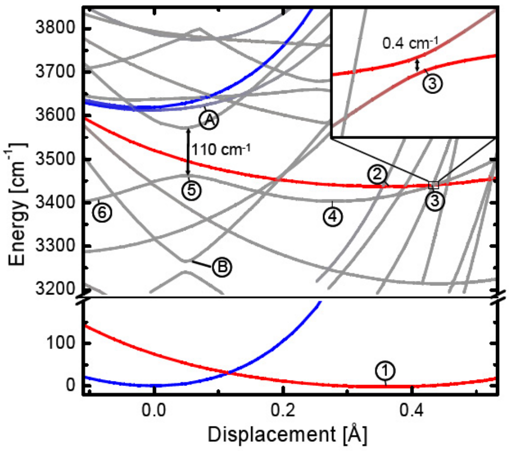

Figure 3.7: Translational potential energy surface of the various OH vibtional state as a function of position of the molecule in the matrix cage. The picture shows a one-dimensional cut along a straight line that connects the *cis* and *trans* minimum positions (see Fig. 3.6). The *trans* minimum is at 0 Å, the *cis* minimum at 0.36 Å (position **1**). The potential energy surfaces are colored according to their transition dipole moments from the *trans* ground state (blue) or the *cis* ground state (red); dark states (combination modes and overtones) are colored in gray. The labels refer to the wavefunctions shown in Fig. 3.8 and to positions discussed in the text. The inset enlarges the avoided crossing region between $\nu_{stretch,cis}$ and $8\nu_{tors,cis}$.

The potential energy surfaces can easily be classified as *cis* or *trans* species: Surfaces which have their minimum on the *cis* (right) side belong to *cis* vibrational states and surfaces which have their minimum on the *trans* (left) side belong to *trans* vibrational states. Potential energy surfaces that belong to spatially compact vibrational wavefunctions, such as the ground states and the OH-stretching modes, are perturbed little by the matrix cage, and thus run more or less in parallel. Potential energy surfaces that belong to vibrational wavefunctions with large spatial extension are steeper in general, since they interact stronger with the Lennard Jones repulsive part of the Kr atoms.

The molecule in the matrix cage has C_2 symmetry (such as the gas phase molecule as well). Hence, one can further classify the vibrational states into two symmetry classes: A' and A''. States with even number of torsional excitation, such as the fundamental OH-stretching modes, belong to A', while states with odd number of torsional excitations belong to A''. States of equal symmetry may couple and exhibit avoided crossings in the coupling region, albeit very small in most cases. In the avoided crossing regions, the wavefunctions mix (see e.g. wavefunctions **3** and **5** in Fig. 3.8) and exchange oscillator strength (as seen by the coloring of the curves in Fig. 3.7). The wavefunctions remain localized when they are energetically isolated (see e.g. wavefunctions **1, 2, 4** and **6** in Fig. 3.8). States of different symmetry cross without mixing.

In almost all cases, coupling through the torsional barrier is extremely weak ($\ll 0.1$ cm^{-1}), since the spatial overlap of the wavefunctions is very small. Hence, an A' state on the *cis* side does not couple effectively with an A' state on the *trans* side, although, from symmetry considerations, coupling would be possible. There is one important exception: Modes with high torsional excitation have a large spatial extension along the torsional coordinate (see e.g. wavefunctions **4** and **6** in Fig. 3.8), and hence, the spatial overlap between *cis* and *trans* side is significant, even at energies below the torsional barrier. As a result, they couple and form an avoided crossing with significant splittings up to 100 cm^{-1} (see position **5** in Fig. 3.7).

Although the number of potential energy surfaces is large (Fig. 3.7), surface crossings with appreciable couplings are actually rare: Most crossings appear between *cis* and *trans* potential energy surfaces, since they run perpendicular to each other. However, as discussed above, their coupling is negligible because the spatial overlap of the wave functions vanishes. Potential energy surfaces of two states which belong to the same isomer, on the other hand, tend to run in parallel, and are unlikely to cross. Nevertheless, such crossings do exist, and we believe they are the key to understand the mechanism of the reaction. Since the wavefunctions do spatially overlap in this case, the couplings are appreciable (see e.g. inset in Fig. 3.7).

Fig. 3.7 implicitly assumes an adiabatic separation of timescales of the fast motion of the proton and the slow translational motion of the molecule, in analogy to the Born-Oppenheimer approximation in electronic problems. The Born-Oppenheimer-like approximation seems well justified since the lowest frequency intramolecular mode (i.e. the OH torsional mode of the *trans* conformer with 490 cm^{-1} in our model and 540 cm^{-1} in the experiment [32]) is about one order of magnitude larger than the motion of the molecule within the cage (54 cm^{-1} for the *trans* conformer and 27 cm^{-1} for the *cis* conformer; as deduced from the curvature of the ground state potential energy curves in Fig. 3.7). However, as in the electronic case, the adiabatic approximation breaks down in avoided crossing regions, and proton and translational motion become strongly correlated. If the coupling is weak, the system will essentially stay on the diabatic potential energy surface (i.e. as if the crossing were not avoided) and will hop onto the other diabatic surface only with a small probability. If the coupling is strong, the system will stay on the adiabatic surfaces with a probability close to one.

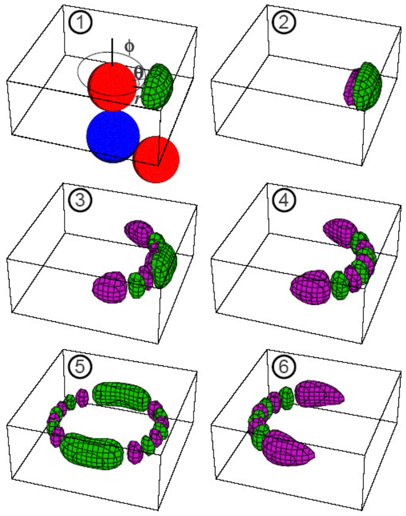

Figure 3.8: Proton wavefunctions at the positions labelled in Fig. 3.7. The -ONO body (not on scale) is sketched exemplarily for the *cis*-ground state with the coordinates r, θ and ϕ indicated. The colors (green and pink) represent the signs of the wavefunctions.

Putting these general consideration together, we may propose a possible reaction pathway for the *cis*-*trans* isomerization: After excitation from the *cis*-ground state (wavefunction **1**, Fig. 3.8 at position **1**, Fig. 3.7.), the *cis* OH stretch excited state ($\nu_{stretch,cis}$, wavefunction **2**) is populated. Direct coupling to the *trans* OH-stretch excited state ($\nu_{stretch,trans}$) will be extremely weak, because of the energy mismatch and the vanishing spatial overlap of the two wavefunctions. Accordingly, we do not observe any excited state absorption from $\nu_{stretch,trans}$ after the decay of the *cis* OH-stretching state. However, we do find a curve crossing between $\nu_{stretch,cis}$ and the 8th overtone of the torsional mode, $8\nu_{tors,cis}$ (wavefunction **3**). The coupling is weak (0.4 cm^{-1}), but nonzero (see enlargement in Fig. 3.7, inset). In the avoided crossing region, the system might hop from one diabatic surface to the other, and thereby transfer population from the stretching mode to a high torsional mode (wavefunction **4**). The latter is the only mode in our model calculation which effectively couples to the *trans* side (wavefunction **5**). Since the coupling between $8\nu_{tors,cis}$ and $8\nu_{tors,trans}$ is large

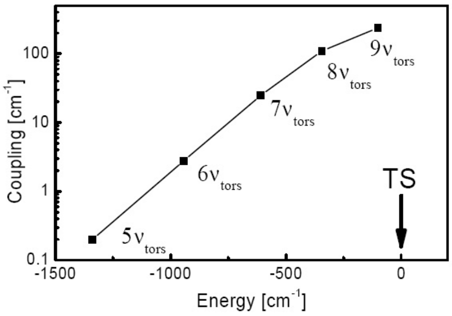

Figure 3.9: Tunnel splitting of highly excited torsional modes as a function of their energy below the transition state (TS, including the zero point energies of stretching and bending modes).

($\approx$ 110 cm^{-1}), the system will stay on the adiabatic potential energy surface and transfer population to the *trans* side of the molecule (wavefunction **6**).

The bottle neck of the reaction pathway sketched above is the transfer of population from $\nu_{stretch,cis}$ into a high torsional mode. The subsequent transfer to the *trans* side will be almost instantaneous since it proceeds on one adiabatic potential energy surface. Accordingly, we observe the appearance of vibrationally excited *trans* species on the same timescale as the disappearance of the *cis* OH-stretch excited state.

Of course, other curve crossings do exist, which either lead to non-isomerizing loss channels, or, when they are dead end pathways, may lead to the observed bi-exponential decay of the initially excited bright states. One example is $2\nu_{bend,trans} + 2\nu_{tors,trans}$ which approaches $\nu_{stretch,trans}$ at its minimum (position **A** in Fig. 3.7). $2\nu_{bend,trans} + 2\nu_{tors,trans}$ is a dark state, and hence, population transfer into it will diminish the intensity of the $\nu_{stretch,trans}$ stimulated emission and excited state absorption. As a result, the $\nu_{stretch,trans}$ signal will initially decay until equilibrium with $2\nu_{bend,trans} + 2\nu_{tors,trans}$ is reached, and then decay on a second slower timescale as a result of further relaxation through other channels. Fig. 3.7 does not show any obvious pathway for *trans-cis* isomerization, in agreement with the 7 times lower quantum yield observed experimentally [19].

The matrix interaction V_{VdW} increases the transition state energy by $\approx$ 570 cm^{-1} above the gas phase value E_a = 3610 cm^{-1}. When furthermore including the zero point energies of stretching and bending modes to the transition state energy, we find that $8\nu_{tors,cis}$ is 350 cm^{-1} below the transition state. The proton is tunneling through the barrier at position **5**. Position **B** shows the avoided crossing of $7\nu_{tors,cis}$ with a tunnel splitting that is considerably smaller ($\approx$ 30 cm^{-1}) than that of $8\nu_{tors,cis}$. Fig. 3.9 depicts the tunnel splitting of the various torsional modes as a function of their energy below the transition state. The splitting drops very quickly with decreasing energy. Only states with high torsional excitations may provide efficient pathways between the *cis* and *trans* configuration, while isomerization will become extremely unlikely, once the energy in the torsional mode drops significantly below the transition state energy.

It should be reemphasized that the potential energy surfaces in Fig. 3.7 have been adjusted by varying the barrier height E_a such that a curve-crossing between $\nu_{stretch,cis}$ and $8\nu_{tors,cis}$ does occur. Within our 4D model, the only other candidate that could yield a similar scenario is $6\nu_{tors,cis}$, which, however, could be tuned into the relevant energy range only by assuming an unreasonably high barrier of $E_a = 5050$ cm^{-1}. When choosing $E_a = 4000$ cm^{-1}, the most accepted value, $7\nu_{tors,cis}$ is energetically in the same region as $\nu_{stretch,cis}$, but may not couple because of its wrong A'' symmetry. When including all intramolecular degrees of freedom of HONO, on the other hand, the choice of modes becomes larger. For example a combination mode of $6\nu_{tors,cis}$ and the ONO-bending mode, which has roughly the same energy as $7\nu_{tors,cis}$, but has the correct A' symmetry, may take over the role of $8\nu_{tors,cis}$ in our model calculation. We want to stress again that we do not claim that the picture sketched in Fig. 3.7 is quantitative. However, we believe it gives insights into the types of couplings that might occur (the concrete assignment of states might change) and it does in fact explain qualitatively all observations we make in the experiment.

3.1.6 Conclusion

We have presented the first time resolved studies of the dynamics (in contrast to the kinetics) of the *cis-trans* isomerization of HONO. We find that *cis* HONO isomerizes on a fast 20 ps timescale with 10% quantum yield. Previous theoretical studies, which take into account the six internal degrees of freedom of the molecule, suggest that the molecule would not isomerize in the gas phase [20, 21, 29]. The density of states is too small in the gas phase to efficiently couple both isomers. In the gas phase, the proton states are discrete and are stationary eigenstates. This changes dramatically when the molecule is brought into the condensed phase where it is coupled to a quasi-continuum of states (Fig. 3.7). Tunnelling of the proton from the *cis* to the *trans* side is possible only when proton donor and acceptor states are in close resonance, and translational coordinates in the matrix cage may fine-tune this resonance. In the condensed phase, resonance is no longer a matter of an unlikely coincidence, but will almost necessarily occur at a particular position of the molecule in the matrix cage.

It is instructive to compare these conclusions with electronic photochemistry, which, of course, does occur in the gas phase, often very efficiently. In the electronic case, the molecules own vibrational degrees of freedom serve as the quasi-continuum of states which is necessary to efficiently couple the electronic wave functions. The difference is the energy scales: In the electronic case, the density of states is gigantic. When taking HONO as an example, the pure vibrational density of states at 30.000 cm^{-1} (the energy of the $S_0 - S_1$ electronic transition) is estimated to be $\approx 400/\mathrm{cm}^{-1}$ (in the harmonic approximation). In contrast, the density of states is only $0.25/\mathrm{cm}^{-1}$ at 3500 cm^{-1} (the energy of the $\nu_{stretch}$ vibrational transition).

However, Refs. [20, 29] do not include rotational degrees of freedom, which at 3500 cm^{-1} would sum up to a large density of states as well. Whether rotational degrees of freedom couple sufficiently to the vibrational degrees of freedom to mediate isomerization remains to be investigated. In that sense, it is not clear whether HONO does isomerize in the gas phase. In the condensed phase, rotations are hindered, but are replaced by translational degrees of freedom in the crystal cage. They couple very efficiently to the internal vibrational degrees of freedom due to the steep repulsive part of the Van der Waals interactions.

HONO in low temperature matrices is an extremely small and well defined system, which allows to study the dynamics and mechanism of ground state chemical reactions in the condensed phase in great detail. The excitation energy used in our experiment lies well within the range of what might occur in 'real world' chemistry - i.e. without IR excitation, but at room temperature - due to thermal excitations with a Boltzmann factor of $e^{-E_a/k_BT} \approx 5 \cdot 10^{-8}$. Hence, the reaction mechanism introduced here is thought to be quite general.

Acknowledgement: We wish to thank Gerhard Stock and Robert Huber for fruitful discussions.

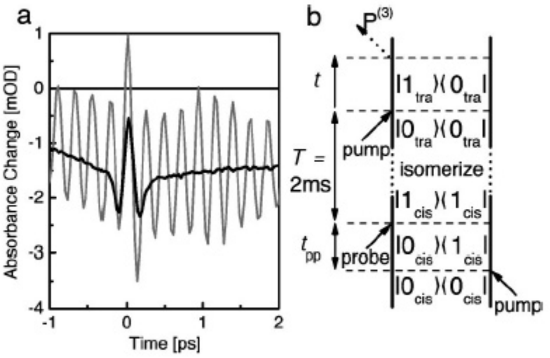

Figure 3.10: (a) The *trans* stimulated emission/bleach signal (black) is accompanied by oscillations if the phase between pump and probe is stable (gray). Both experiments were performed with broad band pump pulses that covered both *cis* and *trans* OH-stretch absorption lines simultaneously. (b) The Liouville-pathway responsible for the beatings represented as double-sided Feynman diagram: the first two interactions from pump and probe separated by the pump-probe delay time t_{pp} form a population grating in the *cis* excited state. After isomerization and relaxation into the ground state of *trans* the pump pulse from the next laser pulse, separated by T =2 ms (or much longer), induces a 3rd polarization $P^{(3)}$ evolving in time t.

Appendix

3.1.7 Accumulated grating effects

In a first set of experiments we used a vibration free helium flow cryostat and observed pronounced quantum beats in the transient absorption signal of HONO (in solid Ar in this case). The experiment was performed with broad band pump pulses (i.e. without the Fabry Perot filter) that covered both *cis* and *trans* OH-stretch absorption lines simultaneously. Fig. 3.10 (a), gray line, shows the transient of the stimulated emission/bleach signal of *trans* HONO, which is dominated by strong oscillations up to 30 ps. The oscillation period of 220 fs matches exactly the difference in frequency of 144 cm^{-1} between *cis* and *trans* absorption bands of HONO in solid argon. After replacing the helium flow cryostat by a closed cycle cryostat with its characteristic vibration of the sample volume due to the compressor, the quantum beats essentially disappeared. We now use in addition a piezo mounted mirror in the pump beam that is driven by a noise generator to entirely suppress the artifact (Fig. 3.10 (a), black line).

The artifact appears whenever pump and probe pulse are phase-locked. It is of similar nature as the accumulated photon echo-effect first observed by Hesselink and Wiersma [70] and can be explained as follows: Pump and probe pulse produce interference fringes in the sample. *Cis*- and *trans*-isomers will be excited depending on whether they are located in a constructive or destructive fringe. A fraction of the excited molecules isomerizes. Hence, the transient grating is turned into a stationary ground state population grating. One of the next pump pulses, after T =2 ms or much later, will be scattered on this population grating into the direction of the probe pulse and interfere with the subsequent probe pulse. This interference yields the observed quantum beats as a function of pump-probe delay time t_{pp}. If the phase of the consecutive pulse pairs is kept constant, the ground state population grating accumulates and gives rise to the strong signal observed in Fig. 3.10 (a), gray line. If the phase between pump and probe pulse is scrambled quickly enough by the piezo mounted mirror and/or by moving the grating in the closed cycle cryostat, two effects suppress the artifact [70]: (a) the grating will no longer accumulate and (b) the interference between the second pump pulse and the subsequent probe pulse will be random and hence appear as noise, but no longer as systematic beatings.

Fig. 3.10 (b) shows the corresponding Feynmann diagram for the case of the *cis* → *trans* isomerization (the same occurs also for the back-reaction). In the impulsive limit, it gives rise to a 3rd polarization :

$$P^{(3)}(t) \propto e^{i\omega_{cis}t_{pp}} \cdot e^{-(i\omega_{trans}+\Gamma)t} \tag{3.5}$$

where t_{pp} is the time delay between pump and probe, Γ a dephasing constant, and ω_{cis} and ω_{trans} are the absorption frequencies of the two isomers. After Fourier transformation with respect to t (which is what the spectrometer does) we obtain:

$$P^{(3)}(\omega) \propto e^{i\omega_{cis}t_{pp}} \cdot \frac{1}{i(\omega-\omega_{trans})-\Gamma}. \tag{3.6}$$

The second probe pulse acting as local oscillator field

$$E_{LO}(t) \propto \delta(t-t_{pp}) \tag{3.7}$$

is delayed by the pump-probe delay time t_{pp}, which reveals in the frequency domain

$$E_{LO}(\omega) \propto e^{-i\omega t_{pp}}. \tag{3.8}$$

After heterodyne detection the transient signal is

$$\begin{aligned} S(\omega) &= -2\Im\left[P^{(3)}(\omega)\cdot E_{\mathrm{LO}}(\omega)\right] \\ &\propto -2\Im\left[e^{i(\omega_{cis}-\omega)t_{pp}} \cdot \frac{1}{i(\omega-\omega_{trans})-\Gamma}\right] \end{aligned} \tag{3.9}$$

The detected signal corresponds to a complex-valued Lorentzian line centered at ω_{trans} oscillating with $(\omega_{cis}-\omega_{trans})\cdot t_{pp}$, in perfect agreement with the experiment. Beside the Feynmann diagram in Fig. 3.10 (b) an arbitrary number of higher order diagrams may exist. However, after effectively suppressing this very prominent signal we assume that all alternative grating effects are removed as well.

3.2 The infrared-driven *cis-trans* isomerization of HONO II: Vibrational relaxation and slow isomerization channel

Virgiliu Botan, Roland Schanz, Peter Hamm

J. Chem. Phys., 124, 234511, (**2006**)

Abstract

In a recent paper [R. Schanz et al., J. Chem. Phys., **122**, 044509, (2005)], we investigated the IR-driven *cis-trans* isomerization of HONO in a Kr matrix with the help of femtosecond IR spectroscopy. We found that isomerization occurs on a 20 ps timescale, however, with a *cis*→*trans* quantum yield of only 10% that is significantly below the value reported in the literature (close to 100%). At the same time, we concluded that vibrational energy has not completely dissipated out of the molecule at the maximum delay time we reached in this study (500 ps). In order to verify whether additional, slower reaction channels exist, we extend the study here to delay times up to 100 ns. At a temperature of 32 K, we indeed find an additional isomerization channel on a 2 ns timescale, which increases the total *cis*→*trans* quantum yield to ≈30%. The *trans*→*cis* quantum yield is ≈7%. There is still a discrepancy between the quantum yields we observe and the literature values, however we provide experimental evidence that this discrepancy is due to the different temperature of our study. Vibrational cooling occurs on a 20 ns timescale, and cascades in a highly non-statistical manner through one single normal mode (most likely the ONO bending mode ν_5). Inter-molecular energy dissipation into the rare gas matrix is more efficient than intramolecular energy redistribution (IVR) and the matrix environment can certainly not be considered a weak perturbation.

3.2.1 Introduction

Nitrous Acid (HONO) in rare gas matrices is a prominent model system which undergoes *cis-trans* isomerization upon IR-irradiation of a single quantum of a vibrational mode. Among the many molecules that perform such IR-driven photochemical reactions (for review articles see e.g. Refs. [61, 71]), HONO is the smallest, the best studied from both the theoretical [20–24,29,30,32] and stationary spectroscopy point of view [14,33,36–38,41,42,64], and it is exceptional in the sense that its isomerization quantum yield reaches a value close to one [16, 17, 19]. The reaction was first discovered by Pimentel et al. [12,15,16], and has more recently also been studied by modern laser based techniques [17,19].

The generally accepted picture of the molecule's IR-driven photoreaction is the following: The energy of the *cis* isomer is ≈100-200 cm^{-1} above that of the *trans* conformation. According to the highest level calculation available (on the CCSD(T)/cc-pVQZ level), the transition state is located along the torsional coordinate with an energy of $\approx 4105\ \mathrm{cm}^{-1}$ [30]. This value reduces to $\approx 3635\ \mathrm{cm}^{-1}$ when considering zero-point corrections [21, 30]. However, the effect of the matrix environment on the barrier is not known. Hence, the energy of one quantum of the OH-stretch vibration ($\approx$3500 cm^{-1}) is of the same order as that of the transition state, but it is not known exactly whether it is above or below. Upon pumping the OH-stretch vibration of *cis*-HONO, the molecule isomerizes into *trans*-HONO with a high quantum yield 'close to one' [16,19]. This result is remarkable given the fact that it is *not* the reaction coordinate which is excited by the IR pump light. Apparently, the excited OH-stretching mode and torsional modes (i. e. the reaction coordinate) are efficiently coupled. Presumably, the coupling is mediated by the matrix, as this reaction has not been reported in the gas-phase so far. The *trans*→*cis* yield is smaller by a factor of ≈ 7 [19].

All published works so far are kinetic measurements [16, 17, 19], not dynamic measurements. They measure the kinetics of the isomerization reaction upon a certain photon flux, and hence, can establish the isomerization quantum yields and their dependence on certain experimental parameters, such as the excitation frequency [19]. However, they provide no information on the course and timescales of the photo reaction itself. Only in a recent paper, we investigated the dynamics of the reaction with the help of ultrafast time resolved IR spectroscopy [43]. The essential results of this work were: When pumping the OH stretch vibration of *trans*-HONO, energy flows out of that mode on a 260 ps timescale, thereby populating overtones and combination modes of the molecule (which we called dark states). When pumping the OH stretch vibration of *cis*-HONO, on the other hand, vibrational relaxation is faster (20 ps). During that time, a small fraction reacts towards the *trans* side. However, the quantum yield of 10% we observed is significantly smaller than the literature value which was reported to be close to 100% [16, 19]). At the same time it was clear that the energy is not dissipated completely out of the molecule at the delay time of 500 ps we reached in this experiment (which was limited by the physical length of the translation stage used in the optical delay line). This made us speculate that there might be additional slower reaction channels that may lead to isomerization as long as there is energy in the molecule.

In the present paper, we explore the long-time kinetics of HONO from 50 ps to 100 ns, i.e. up to a delay time long enough such that energy is completely dissipated in order to assure that the reaction is over. To that end, we electronically synchronized our two Ti:S laser systems [40], and used one to generate IR pump pulses and the second to generate IR probe pulses. We do indeed find an additional, slow isomerization channel and furthermore are able to observe the complete process of vibrational cooling in great detail.

3.2.2 Experimental Methods

HONO was synthesized photochemically according to the procedure reported by Hall and Pimentel [16]. A gas mixture of 3:10:1000 HN_3:O_2:Kr was prepared in a glass container which was sprayed on a calcium fluoride window kept in a cryostat (DE-202AF/DMX-20B, Advance Research Systems, Inc.) at low pressure (10^{-7} mbar) and a temperature of approximately 32K. The 3317 cm^{-1} absorption band of HN_3 was used to monitor the growth of the matrix. After deposition, the matrix was irradiated with UV light from a mercury lamp which photolyzis the hydrazoic acid and then reacts with oxygen to form HONO. The completion of this process was monitored by the disappearance of the HN_3 band. The time-dependent experiments were all performed at 32 K.

For the femtosecond experiments, IR pump and probe pulses were generated from two optical parametric amplifiers (OPA) which were pumped from two synchronized Ti:S laser systems. The use of the two systems was necessary to achieve long delay times that are longer than what is possible with the commonly used delay stages. The synchronization of the two laser systems is described in Ref. [40]. Briefly, the laser systems are each composed of a passively mode locked Ti:S oscillator (Spectra Physics Tsunami) and a regenerative Ti:S amplifier (Spectra Physics Spitfire). Electronic synchronization of the two systems was achieved by setting one of the Ti:S oscillators as a master and then adjust the round trip time for the second one (the slave) according to the master. By shifting the relative phase of the two oscillators, as well as by controlling which laser pulses are amplified in the regenerative amplifiers, we could time delay the two pulses continuously from picoseconds to microseconds with a short term jitter of 2 ps. The lasers were approximately 30 m apart, but the beam pointing stability proved good enough to allow us to pump an OPA. In this way we obtained two 150 fs pulses centered at 3450 cm^{-1} with a bandwidth of $\approx$300 cm^{-1} FWHM. The energy of the pulse was 1.2μJ and they were focused to 150 μm spot size in the sample. The repetition rate of the lasers was 1 kHz and every second pump pulse was blocked by a synchronized chopper for referencing. The output of one OPA was used as a pump pulse and that of a second OPA as probe and reference pulse. The latter were spectrally dispersed in a 190 mm spectrometer and then detected by a 2×63 channel HgCdTe detector array, covering a spectral range from 3370 to 3580 cm^{-1} with a resolution of 3.3 cm^{-1}.

To enable selective excitation of the *cis* or the *trans* species we used a piezo controlled adjustable Fabry-Perot filter with a bandwidth of 17 cm^{-1}. The resulting pump pulse shape can be approximated by a single sided exponential with a time band width product of $\tau\Delta\nu = 1/2\pi$ (i.e. pulse duration 300 fs). In order not to deplete one or the other species we had to alternatively pump *cis* and *trans* HONO. We set the Fabry-Perot to the *cis* band (3402 cm^{-1}) for 1 s (1000 laser shots), using only the first 250 ms for data collection and the rest of the time for shifting population to *trans*, and then moved the Fabry-Perot to the *trans* band (3552 cm^{-1}) for 12 s, again using only the first 3 s for data collection and the rest to shift the population back. The difference in pumping time for the two isomers comes from the different quantum yields of the reaction in each direction. This cycle was repeated for each delay time position. By following this procedure we assured that in each experiment we deal with an ensemble which to a large extend ($> 70\%$) contains either one of the *cis* or *trans* species. In combination with the pump selectivity (50/1) we are confident the the contamination of the opposite reaction is negligible. In total we averaged 255 scans resulting in a dynamic resolution of $\approx 1.6\,\mu$OD(rms).

Due to the long total time of data collection ($\approx$ 60 h), there is some uncertainty concerning the delay zero position (±50 ps) which is significantly larger than the short term jitter. This is since both lasers reside on different laser tables some 30 m apart, and the slightest change of the optical path length shifts time zero by a few 10's of picoseconds. We consider here only spectra measured for delay times larger 50 ps, and combine them with our previously reported data [43] for the discussion of the overall process (see Fig. 3.14 below).

As a reference experiment (see Fig. 3.16 below), we also measured the ratio of *cis→trans* and *trans→cis* quantum yields as a function of temperature in a stationary experiment. To that end, we deposited the matrix at 32 K and afterwards cooled down to the desired temperature. After depositing the sample, the *cis-trans* ratio is initially arbitrary. The sample was then irradiated with the globar light in a conventional FTIR spectrometer, and the OH stretch band of both species was continuously monitored in order to find out when photo-equilibrium is reached (typically after 2 h). This experiment was also used to measure the ratio of the oscillator strengths of the OH stretch band of the two conformers (see Fig. 3.16 insert), an information which can be extracted from the difference of both bands before and after reaching photo-equilibrium. These measurement were done in a FTIR spectrometer with 0.25 cm^{-1} resolution.

3.2.3 Experimental Results

Fig. 3.11 shows an overview of the time-dependent response after selectively pumping the OH stretch band of (a) *trans* and (b) *cis* HONO. The wavelength regime covers that of OH stretch vibration of both species, and the delay time is scanned from 50 ps to 100 ns. Figs. 3.12, 3.14 and 3.15 below are extracted from these two sets of data. We focus here on two aspects of the long-time kinetics – vibrational cooling and isomerization – which we will discuss separately in the following sections.

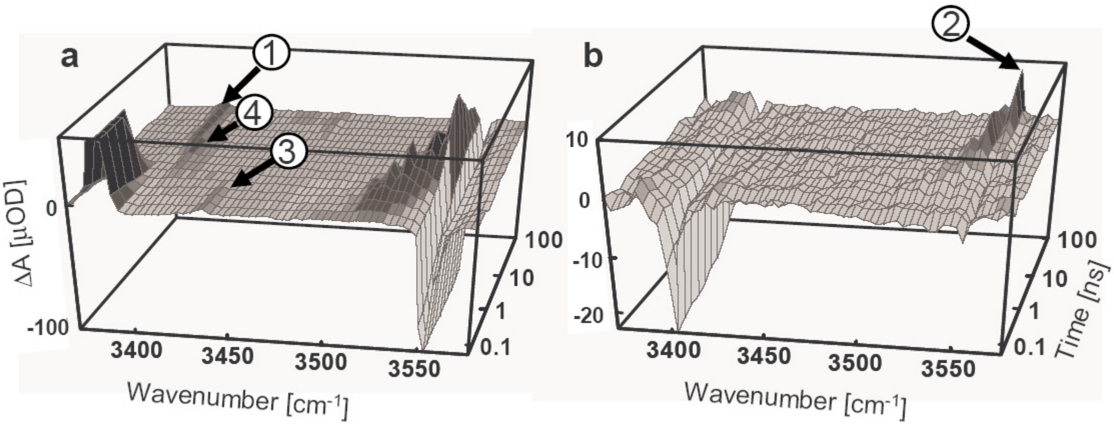

Figure 3.11: Overview of the transient response of HONO after selectively pumping the (a) *trans* and the (b) *cis* species. The labelled arrows mark certain features discussed in the text.

Vibrational Cooling

Three dominant bands can be seen when pumping *trans*-HONO (Fig. 3.11a). First we identify a negative band at 3552 cm^{-1}, which is composed of the $\nu = 0 \rightarrow \nu = 1$ *bleach* and $\nu = 1 \rightarrow \nu = 0$ *stimulated emission* transitions of the directly excited OH stretch vibration. In the red part of the spectrum we see a positive band which originates from the $\nu = 1 \rightarrow \nu = 2$ *excited state absorbtion* (3390 cm^{-1}). The anharmonicity of the OH stretch vibration is relatively large with 162 cm^{-1}, in agreement with stationary spectroscopy [41, 64] and also with theory [30]. The excited state absorption band decays with time as a result of vibrational relaxation of the initially excited OH stretch band.

Bleach and $\nu = 1 \rightarrow \nu = 0$ *stimulated emission* transitions cannot be separated *per se*, since both appear at the same frequency (the equivalent of a Stokes shift is at least very small for vibrational transitions [72]), are negative and have the same transition dipole moments $\mu_{01}^2 = \mu_{10}^2$. Yet, we observe a decay of the negative band to 50% of its original amplitude on a timescale which is exactly the same as that of the excited state absorption (see also Fig. 2 of Ref [43]). Hence, the initial decay of the negative band reflects the disappearance of the stimulated emission contribution, whereas the bleach contribution stays constant for significantly longer time.

Parallel with the disappearance of the OH stretch excited state, a broad and initially featureless band appears red shifted from the bleach/stimulated emission band. We focus into this feature in Fig. 3.12a and b. As explained in our previous work [43], this band is due to overtones and/or combination modes that are populated from the OH-stretch band. Due to anharmonic coupling, excitation of these states causes the OH stretch vibration to absorb red shifted (see discussion below). As time goes on, the initially featureless band becomes structured and develops into a series of four distinguishable bands (Fig. 3.12a). These bands appear to be, within the pixelling of our detector with a resolution of 3.3 cm^{-1}, equally spaced with a separation of around 8 cm^{-1}. As we can clearly see in Fig. 3.12a and b, the intensity of these four peaks develops from left to right (from band #4 to band #1) until finally it fills the bleach of the *trans* ground state (band #0). The ground state is re-populated in a highly non-exponential manner covering 3 orders of magnitudes in time from 100 ps to 100 ns.

Also visible in Fig. 3.11a at early delay times is a weak band at 3440 cm^{-1} (marked by arrow #3), the decay of which is compared with that of the excited state absorption band in Fig. 3.13. The intensity of the latter is about 50 times larger, but both bands exhibit essentially the same time dependence.

Isomerization

Fig. 3.11b shows the response when pumping the *cis* OH stretch band at 3402 cm^{-1}. We again find the negative $\nu = 0 \rightarrow \nu = 1$ *bleach* signal of *cis*-HONO. The stimulated emission contribution is already decayed after 50 ps, since the lifetime of the OH stretch vibration of cis-HONO is significantly shorter (20 ps) [43]. The bleach signal recovers on a 20 ns timescale as the

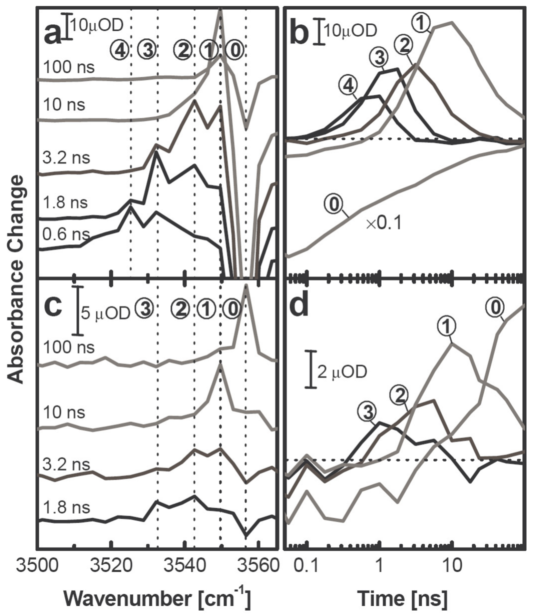

Figure 3.12: a) Transient spectra 0.6 ns, 1.8 ns, 3.2 ns, 10 ns and 100 ns, respectively, after pumping *trans*-HONO, focused into the *trans* band. Cooling cascades through one mode (presumably ν_5) with 4 – 0 quanta (see labels) of that mode excited. (b) Time-scans at selected frequency positions corresponding to 4 – 0 quanta (see labels) of that mode. (c,d) The same when pumping *cis*-HONO. The *trans* photo product relaxes through the same cooling cascade as when pumping *trans* directly. The trace with four quanta is omitted since signal-noise is insufficient to resolve it.

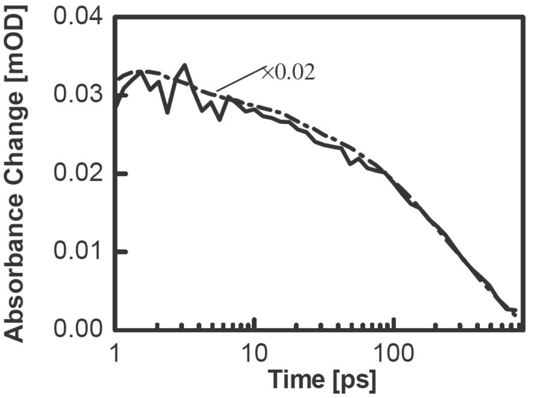

Figure 3.13: Solid line: Time dependence of the weak band at 3440 cm^{-1} marked by a white arrow in Fig. 3.11a, in comparison with the time dependence of the excited state absorption (3390 cm^{-1}, dotted line). The latter is down-scaled by a factor of 53. The data are taken from Ref. [43].

molecule finally cools (Fig. 3.14b). However, a small bleach remains as a result of the fraction of molecules that underwent *cis*→*trans* isomerization. In the blue part of the spectrum we see the creation of a band (marked by arrow #2), broad in the beginning and then more structured, which we assign to the *trans* photoproduct. The photoproduct is initially vibrationally hot, and relaxes through the same cooling cascade as when pumping *trans* directly (Fig. 3.12c,d).

Because of technical reasons related to the positioning of delay time zero (an unavoidable jitter of ≈ 2 ps and random low probability jumps of a few 10's of picoseconds between pump and probe pulse, see Sec. 3.2.2), we cannot rely on data at very short delay times. Therefore, we use our previously measured data [43], which were measured with only one laser system without any delay time uncertainties. We compared the two spectra at different time positions where they overlap and found that, besides an overall scaling factor, they are spectrally the same. For calculating the scaling factor we used the *bleach* band at 3402 cm^{-1} in the time region where both sets of data overlap (see Fig. 3.14b). This entitles us to consider the previous measurements for the short time dynamics and the new measurements for the long time dynamics. The signals are sitting on a broad background which is due to a water film that is growing on the sample. The background has been subtracted, as explained in Ref. [43]. However, due to the larger noise of the present data set as compared to that of Ref. [43], this leaves significant uncertainty, which is why the match of the two data sets is poor at early times (Fig. 3.14a). At later delay times, however, when the photoproduct band becomes sharper, the background can be subtracted more reliably.

Fig. 3.14 summarizes the overall isomerization process from 1 ps to 100 ns: Fig. 3.14a plots the integrated intensity of the *trans*-product band which, to a first order, reports on the *trans*-population independent on the way how energy is distributed over all vibrational degrees of freedom of the molecule. Fig. 3.14b plots the bleach/stimulated emission signal for comparison. In our previous experiment we observed a rise of the *trans* signal on a 20 ps time scale, giving rise to a quantum yield of ≈10 % [43]. That rise went in parallel with the decay of the stimulated emission, which halved the am-

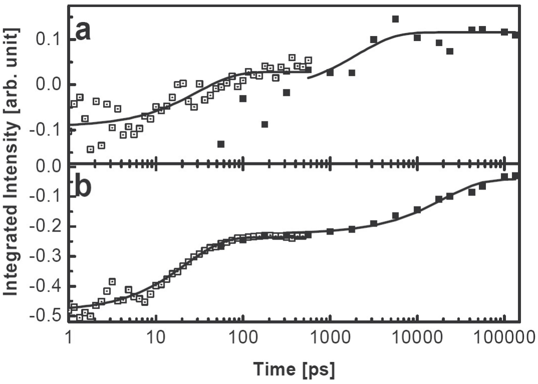

Figure 3.14: (a) Integrated intensity of the *trans* photo product band after selective excitation of *cis*-HONO and (b) the kinetics of the negative bleach/stimulated emission band of *cis*-HONO. The plot combines data from our previous publication (1-500 ps, open squares) [43] with that of the present work (50 ps - 100 ns, black squares).

plitude of the negative band (Fig. 3.14b). The new set of data shows a second, much slower isomerization step which occurs on a 2 ns timescale (Fig. 3.14a). The final bleach recovery, in contrast, occurs on an even slower, 20 ns timescale (Fig. 3.14b).

In Fig. 3.11a we can also spot a small band at the frequency position of *cis*-HONO when pumping *trans*-HONO (see arrow #1). This band is due to the *trans*→*cis* isomerization process. Due to the small size of the signal, however, we cannot resolve the initial isomerization process.

In order to estimate the isomerization quantum yields we present in Fig. 3.15 cuts through Fig. 3.11a,b at certain delay time positions. The black curves show the transient responses at 100 ns, when the process is over and energy has essentially decayed out of the whole molecule. These transients reflect the final state of the photoreaction. The grey curves, in contrast, show transient spectra at delay times when the stimulated emission of the OH stretch band is essentially gone (the weak band at 3390 cm^{-1} in Fig. 3.15a, grey line, corresponds to the remaining excited state absorption still present at 1 ns), but the bleach part is still fully present, i.e. when energy has decayed out of the OH stretch vibration, but is still in other degrees of freedom of the molecule. The bleach signal at this time reports on the number of molecules excited. Since vibrational relaxation of the OH stretch band occur on different

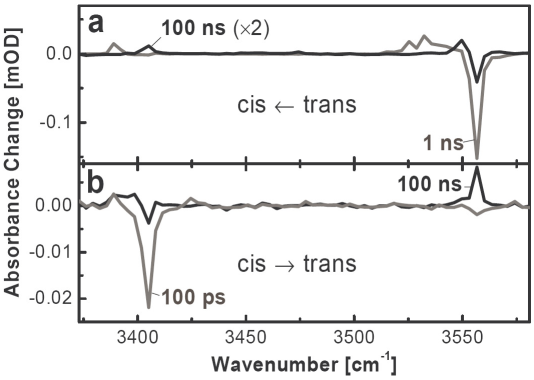

Figure 3.15: Transient spectra used to estimate (a) the *trans*→*cis* quantum yield and (b) the *cis*→*trans* quantum yield. The delay time positions are chosen such that either the OH stretch vibration has just relaxed, but the bleach part is still present (gray lines, 1 ns in the case of *trans*-HONO and 100 ps in the case of *cis*-HONO), or such that the energy has dissipated essentially completely out of the molecule (black lines, 100 ns in both cases).The 100 ns spectrum in (a) is scaled by a factor of 2 for better visibility.

timescales in both isomers, we chose 100 ps in the case of *cis*-HONO pumping and 1 ns in the case of *trans*-HONO pumping.

Comparing the bleach intensity at early times (grey curves) with the photoproduct intensity at late times (black curves) one can directly read off the quantum yields (when taking into account in addition the different oscillator strengths of the OH stretch bands of the two isomers $I_{trans}/I_{cis} = 1.5$, see Fig. 3.16, insert and right scale). This procedure reveals for the quantum yields: $\eta_{cis\rightarrow trans} = 30 \pm 5\%$, $\eta_{trans\rightarrow cis} = 7 \pm 2\%$ [73], and for the ratio $\eta_{cis\rightarrow trans}/\eta_{trans\rightarrow cis} \approx 4$. Note that since the molecules are excited by a broad band laser source here, it is the integrated – and not the peak – intensity of the two bands which counts for this analysis. Since the width of the *cis* OH stretch band is slightly larger than that of the *trans* species (Fig. 3.16, insert), the ratio $I_{trans}/I_{cis} = 1.5$ is smaller than what one might deduce by eye from just looking at the figure. In fact we believe that this explains the discrepancy of our value I_{trans}/I_{cis}=1.5 to that reported in Ref. [19] (I_{trans}/I_{cis}=2.4), where a narrow-band laser has been used, in which case the peak intensities are the relevant ones [74].

3.2.4 Discussion

Vibrational Cooling

We start with a Dunham expansion for anharmonically coupled vibrational states [39]:

$$E = \sum_i \hbar\omega_i (n_i + 1/2) + \sum_{i,j} x_{ij}(n_i + 1/2)(n_j + 1/2) \quad (3.10)$$

where ω_i is the harmonic frequency of mode i, n_i its excitation level, and x_{ij} the anharmonic coupling constants. From this one can derive for the transition frequency of a particular mode k:

$$\nu_{n_k \to n_k+1} = \nu_k + 2n_k x_{kk} + \sum_{i \neq k} x_{ik} n_i \quad (3.11)$$

with $\nu_k = \omega_k + 2x_{kk} + \sum_{i \neq k} x_{ik}/2$. Hence, the transition frequency of mode k (i.e. the OH stretch mode in our case) depends linearly on the excitation level of the other modes with a shift given by the corresponding anharmonic constant x_{ik} for each quantum of excitation.

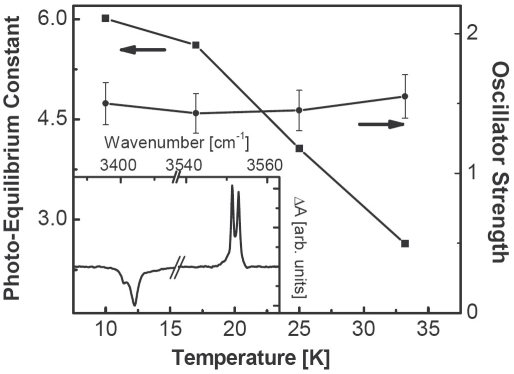

Figure 3.16: Dependence of the photo-equilibrium constant $\eta_{cis \to trans}/\eta_{trans \to cis}$ on temperature (squares, left scale), and that of the ratio of *integrated* cross sections of the OH stretch absorption bands I_{trans}/I_{cis} (circles right scale). The insert shows a *cis-trans* difference spectrum at 32 K measured under continuous irradiation in a FTIR spectrometer.

After relaxation of the OH stretch band, overtones and combination modes are populated. This leads to the observed red-shifted band (since almost all anharmonic constants x_{ij} are negative), which is initially broad and essentially featureless. Using Eq. 3.11 we conclude that the population is distributed over many different states in the beginning. Later on, however, we see a progression of four equally separated bands with a spacing of $\approx$8 cm^{-1} (measured with 3.3 cm^{-1} resolution due to the pixelling of our detector). This equal spacing suggests that vibrational cooling cascades through only one mode, and the different bands correspond to different excitation levels of this mode (see labels in Fig. 3.12). The spacing would then relate to the corresponding anharmonic constant x_{1i} between the OH stretch mode ν_1 and this mode. Note that the level spacing is too small to be consistent with a phonon progression (i.e. a zone boundary phonon, which lies around 60 cm^{-1} [75]).

We identify the mode through which cooling occurs by exclusion. First, because we see at least four quanta of this vibration, we can safely exclude ν_1,ν_2 or ν_3, because the energy of 4 quanta of these modes would be more than the energy that we put into the molecule. For the remaining possible bands we refer to published values of the corresponding anharmonic coupling. According to the theoretical study of Richter et al. [30], the anharmonic coupling x_{16} to the torsional mode is -34 cm^{-1}. The fact that this number is a factor of 4 larger than what we observe experimentally makes us exclude ν_6 from our consideration. This leaves us with only two possibilities: ν_4 and ν_5. The theoretically calculated values are x_{14}=-7.64 cm^{-1} and x_{15}=-3.2 cm^{-1}, respectively [30]. From experiment, the coupling between the OH stretch and the N-O stretch band ν_4 has been reported to be x_{14}=-2.59 cm^{-1} [41]; too small to be consistent with our finding. Hence, the only possibility that is left is the O=N-O bending mode (ν_5). As of our knowledge, there is no experimental value for the anharmonic coupling of this mode with the OH stretch mode, but the calculated one, x_{15}=-3.2 cm^{-1}, seems to be in the reasonable agreement with our observation of -8 cm^{-1} (assuming that the error in the calculation is a few wavenumbers in an absolute sense, not in a relative sense, which is what Tab. V in Ref. [30] suggests).

This result is unexpected since the cooling cascade does not occur through the lowest frequency mode ν_6. We do not see any significant population of ν_6 at any time, which would result in an transient signal at 3518 cm^{-1}, i.e. the *trans*-absorption band shifted by $x_{16} = -34$ cm^{-1}. According to common knowledge one would expect that vibrational cooling finally progresses through the lowest energy state, because the transition from there to the ground state is that with the largest energy gap, much larger than a typical phonon quantum [76]. The two modes ν_5 and ν_6 do have very similar frequencies (595.6 cm^{-1} and 543.8 cm^{-1}, respectively), yet, they differ very much in their character: ν_6 is the proton torsional mode with a reduced mass of $\mu_6 = 1.2$ AMU, whereas ν_5 is the ONO bending mode with a reduced mass of $\mu_5 = 11.6$ AMU (according to a B3LYP 6-311++G** calculation [52]). For two modes with roughly the same frequency (as in the case of ν_5 and ν_6), the classical oscillation amplitude, or the spatial extent of a quantummechanical wavefunction, scales like $\sqrt{\mu_5/\mu_6}$. The three times larger oscillation amplitude of the torsional mode might be responsible for a stronger interaction with the surrounding Kr-molecules, and hence might render cooling and/or scattering into other modes much more efficient. In fact, the spatial extent of the proton wavefunction is of the same order of magnitude as the Van der Waals radius of the proton, questioning any approach to estimate its interaction with the surrounding perturbatively.

Note, however, that cooling is not exclusively cascading through the thus identified ν_5 mode. This is seen from the highly non-exponential re-population of the *trans*-bleach signal (Fig. 3.12b, trace #0), which indicates that a certain fraction of the molecules decay very quickly on a sub-nanosecond timescale and bypass the cooling cascade through ν_5. It is furthermore important to stress that the intramolecular energy distribution never reaches a Boltzmann distribution during cooling (an observation which is not unexpected). This is seen, for example, from the fact that the lowest frequency mode ν_6 is never populated to any significant extent. But also within ν_5, the population progresses from four quanta to one quantum (i.e. left to right) with an inversion between level pairs at certain times (see Fig. 3.12ab), and not like a Boltzmann distribution would predict. In the latter case, the right-most level would always have the highest intensity. Hence, overall speaking, cooling into the matrix is more efficient than intramolecular vibrational energy redistribution (IVR), and the matrix environment certainly cannot be viewed as a weak perturbation of the HONO molecule. The matrix environment will have to be taken into account to theoretically account for the observed isomerization reaction (in contrast to the works in Refs. [20,21,29,30]).

Of course, we do expect to see an anharmonically shifted hot band also when pumping *cis*-HONO. Looking at Fig. 3.11b, we can indeed identify such a band, however, it is much less obvious due to the much poorer quality of the data. Furthermore, Fig. 3.11a (i.e. after pumping *trans* HONO) shows that the *cis* photo product is formed starting from higher frequencies, a signature which becomes prominent at delay times between about 1-10 ns (see Fig. 3.11a, arrow #4). This would imply a *positive* anharmonic coupling constant of the *cis* OH stretch band to the mode through which cooling cascades (i.e. presumably, again, ν_5). Positive anharmonic constants are rare, but not impossible, and in fact Ref. [41] tentatively assigns a positive anharmonic constant to ν_4 (no value is given for ν_5). The positive anharmonic constant could be explained by the intramolecular hydrogen bond present in *cis*-HONO.

Isomerization Quantum Yields

The original motivation of this study was a deficiency we found between the quantum yield measured by stationary experiments [16, 19], which was reported to be 'close to one', and the value of 10% we obtained in our previous work 500 ps after the excitation pulse [43]. This made us speculate that additional slower reaction channels exist, which we could indeed identify in the present work (the second step in Fig. 3.14b). However, although the total *cis*→*trans* quantum yield is now larger (30%), it is still significantly smaller than the reported value of 100% [16, 19]. Although the error in the absolute values of the *cis*→*trans* quantum yield of Refs. [16, 19] is large, the yield certainly is above 50%(L. Khriachtchev, private communication). Hence, a discrepancy still remains. Furthermore, the ratio of *cis*→*trans* and *trans*→*cis* yields has been reported as $\eta_{cis\to trans}/\eta_{trans\to cis} = 7/1$ [19], a number that is experimentally more reliable than the absolute values, since it relies on relative measurements only. We observe a ratio of $\eta_{cis\to trans}/\eta_{trans\to cis} = 4/1$, again seemingly in discrepancy with Ref. [19].

The only experimental parameter we could find that differs between the work of Ref. [19] and our work is temperature: We deposited and measured our sample at around 32 K, whereas the experiments in Ref. [19] have been performed at 7.5 K. In order to see whether temperature does have an effect on the outcome of the photoreaction we show in Fig. 3.16 the dependence of the photo-equilibrium constant $\eta_{cis\to trans}/\eta_{trans\to cis}$ on temperature, as measured by stationary irradiation of the sample with the globar in a conventional FTIR spectrometer. Indeed, the photo-equilibrium constant $\eta_{cis\to trans}/\eta_{trans\to cis}$ varies from ≈ 3 at 33 K (in agreement with the value from our time resolved experiment Fig. 3.15) to ≈ 6 at 10 K (in agreement with the value given in Ref. [19]). This proves that (i), at least concerning the ratio $\eta_{cis\to trans}/\eta_{trans\to cis}$, there is in fact no discrepancy between Ref. [19] and our result, and that (ii) temperature does have a significant influence on the outcome of the photoreaction.

It is interesting to note that the rate of the second isomerization step is still 10 times faster than the cooling rate (compare Fig. 3.14a and b). Assuming that energy initially decays linearly, we conclude that it needs about 90% of the total energy still in the molecule for isomerization to occur. Once the intramolecular energy drops below this threshold value, isomerization stops. This is in agreement with the observation that the quantum yield after pumping the first overtone of the N=O stretch vibration, $2\nu_2$, is 2.5 times smaller than when pumping ν_1 [19]. The energy $2\nu_2$ is 210 cm^{-1} (6%) below that of ν_1.

Clearly, there will be a trade-off between isomerization rate and cooling rate. When the former is faster than the latter, the system will achieve complete equilibration between the *cis* and the *trans* conformer. In that case, we expect $\eta_{cis\rightarrow trans} + \eta_{trans\rightarrow cis} = 1$ (at least in a statistical picture), since both reactions would proceed through the same set of states. That seemed to be the case in the studies of Ref. [16,19] at lower temperature. Here, we investigated the isomerization at 32 K, where cooling is expected to be faster. As a result, the *cis* and *trans* states do not have time to fully equilibrate and we obtain $\eta_{cis\rightarrow trans} + \eta_{trans\rightarrow cis} < 1$. However, clearly temperature dependent measurements will be needed to ultimately resolve this issue. This will be done in future work.

Two-step isomerization

We find that the *cis→trans* isomerization of HONO proceeds via two steps of roughly equal size: a fast step on a 20 ps timescale and a second step on a much slower 2 ns timescale. The fast process is correlated with the disappearance of energy out of the OH stretch vibration, whereas the slow process is correlated with cooling of the molecule as a whole. For the first fast step we conclude that isomerization proceeds directly from the initially excited OH stretch state ν_1, since the process stops when excitation relaxes out of that mode. However, the initially excited OH stretch state is totally localized on the *cis* side [21,30,43], and its coupling to the *trans* side is negligibly small. In Ref. [43] we have identified high overtones of the torsional mode (e.g. $8\nu_6$) as states that efficiently couple to the *trans* side, since the wavefunctions have a large spatial extent into the direction of the transition state. We assume that isomerization proceeds essentially instantaneously, once the excitation has been transferred to the reactive state(s). The bottleneck of the reaction is the transfer of energy from ν_1 to the reactive state(s) [77].

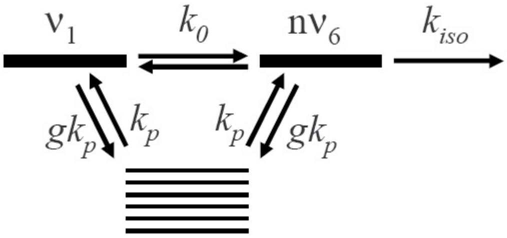

Figure 3.17: Kinetic scheme to describe the two-step isomerization process.

Given the large density of states of the molecule, however, there is no reason to assume that 100% of population is transferred exclusively to the reactive doorway state(s). There will be loss channels into other, non-reactive states, which are overtones and combination modes of the six vibrational degrees of freedom of the molecule. In that sense, our result of Ref. [43] is in fact expected, where we had observed an isomerization quantum yield of only 10-15% for the initial fast isomerization step.

The intramolecular density of states in the energy range of the OH stretch mode is 0.12/cm^{-1} (on either the *cis* or the *trans* side) [30,78]. At the same time, the tuning range as a function of the position of the HONO molecule in the crystal cage is some 200 cm^{-1} [43] so that 20-30 states may exchange energy with ν_1 and the reactive doorway state(s) without significant loss of energy. These states may 'park' energy for a time given by the overall cooling of the molecule, and feed it back into the reactive state(s) at some slower timescale. As long as vibrational energy is sufficient to reach the reactive state(s), isomerization may still occur. However, the bottleneck now is finding these reactive states.

A possible model to explain the two-step kinetics is shown in Fig. 3.35. The initially pumped stretch vibration ν_1 is connected to the reactive state(s) (presumably high torsional states $n\nu_6$) with a rate k_0, which in turn isomerizes with a much faster rate k_{iso}. Both ν_1 and the doorway state(s) are coupled with rate k_p to a large manifold of 'parking' states consisting of non-reactive overtones and combination modes. The multiplicity parameter g primarily describes the number of the accessible 'parking' sates. If we assume k_0=$k_p << k_{iso}$, we find essentially exponential kinetics. This is since ν_1 and the 'parking' states feed into the doorway state(s) with the same rate, independent on the partitioning of population between ν_1 and the 'parking' states. If, however, we set $k_p = 0.05 \times k_0$ and $g = 100$, the experimentally observed two-step behavior can perfectly be reproduced. The factor $g = 100$ seems to bee too large to be consistent with a density of states argument exclusively. We therefore assume that it may also include a temperature dependent Boltzmann factor that would take into account the possibility that the parking states are lower in energy. Given the crudeness of the model in Fig. 3.35, we do not take these numbers literally. Still, they express the essence: Two distinctively different timescales for isomerization, as we see it in the experiment (Fig. 3.14a), can be expected only when the coupling between the initially excited state ν_1 and high torsional states would be exceptionally high; much higher than the coupling to any of the parking states.

Why should that be so? Although we do not have any detailed explanation for this condition, we wish to point out that the torsional mode behaves in a nonconventional manner also with respect to cooling (see Sec. 3.2.4). We tentatively explained this by the large spatial extent of the proton wavefunctions, which (i) may increase the interactions of proton states with the matrix environment, and which (ii) strongly questions any perturbative approach to explain the strength of couplings (in which case the coupling between ν_1 and high torsional states would in fact be small). We propose that the same mechanism that renders the cooling of the torsional mode faster than that of, for example, the ONO bending mode ν_5 also enhances the coupling between proton degrees of freedom among each other. Hence, the proton degrees of freedom – i.e stretch, bend and torsional mode – may exchange population quicker (with a rate k_0), while the coupling to the larger manifold of 'non-exclusively' proton degrees of freedom (i.e. states which include at least one quantum of ON or NO stretch or the ONO bend mode) is weaker with rate $k_p < k_0$. Yet, this larger manifold of states cools slowly, and hence may park energy and thereby give rise to the second isomerization step. Detailed theoretical studies will be needed to clarify this issue.

Further evidence for this interpretation comes from the weak band marked in Fig. 3.11a by arrow #3. The band is shifted from the *trans* absorption band by -112 cm^{-1}, which almost perfectly matches the anharmonic shift expected for $2\nu_3 + 2\nu_6$, i.e. a combination of the first overtones of the torsional and the bending modes. This assignment takes into account the experimental value for $x_{13} = -24.3$ cm^{-1} [41], and the theoretical value for $x_{16} = -33.6$ cm^{-1} [30], revealing an expected shift of -116 cm^{-1}. According to a high level gas phase calculation, it turns out that $2\nu_3 + 2\nu_6$ is the state closest in frequency to ν_1 (separated by -25 cm^{-1}) that includes *only* proton degrees of freedoms [30]. Given the density of states of 0.12/cm^{-1}, however, there are on the order of five other states which include non-proton degrees of freedom that are equally spaced, or even closer in frequency to the initially pumped stretch vibration ν_1. Yet, there is no indication of any population of these other states at early times. Among these states is, for example, $\nu_3 + 4\nu_5$ with an expected anharmonic shift of -56 cm^{-1} (taking $x_{13} = -24.3$ cm^{-1} from Ref. [41] and $x_{15} = -8$ cm^{-1} from Fig. 3.12), which should be easily detectable. State $2\nu_3 + 2\nu_6$, in contrast, is populated essentially instantaneously (Fig. 3.13). Its small amplitude together with the fact that it decays exactly in parallel with the OH stretch band ν_1 suggest that the depopulation of $2\nu_3 + 2\nu_6$ is much quicker than its population from ν_1. Hence, this observation provides evidence that indeed the proton degrees of freedoms are coupled among each other very efficiently, whereas coupling to other degrees of freedom is weak.

3.2.5 Conclusion

The essential conclusions of the paper are:

- Vibrational 'cooling' of HONO occurs on a 20 ns timescale. However, the molecule never reaches intramolecular equilibrium during this energy dissipation process, since inter-molecular energy dissipation is faster than IVR. This seems to indicate that the matrix environment can not be viewed as a weak perturbation, but rather largely determines the course of the reaction. Furthermore, cooling is highly mode selective, and certain modes (e.g. ν_6) cool much more efficiently than other's (e.g. ν_5).
- At 32 K, *cis*-HONO isomerizes in two steps into *trans*-HONO with a total quantum yield of ≈30%, half of which on a fast 20 ps timescale, and the second half on a longer 2 ns timescale. This result seems to suggest that the coupling between the initially excited OH stretch vibration ν_1 to the reactive torsional mode ν_6 is stronger than that to other degrees of freedom of the molecule. The reason for this effect is presently not clear, and will require detailed theoretical investigations.

- *Trans*-HONO isomerizes into *cis*-HONO with a quantum yield of ≈7%.
- Temperature has a significant effect on the outcome of the photoreaction, which probably also explains the still existing discrepancy between our and earlier work [16, 19]. The temperature dependence of the photoreaction will be investigated in future work.

These conclusions are in agreement with recent gas-phase simulations on a full-quantum dynamic level [21, 29], according to which HONO would not isomerize on a 40 ns timescale, even when exciting high above the reaction barrier into the second overtone of the OH stretch vibration. Classical molecular dynamic (MD) simulations [22–24], in contrast, severely overestimate the reaction rate by many orders of magnitudes, even in the gas phase. Hence, the quantum character of at least the proton seems to be absolutely relevant. On the other hand, the matrix environment, as well as its temperature, strongly modifies the outcome of the reaction. We therefore conclude that one will need mixed quantum/classical simulations (with the proton subsystem described quantum mechanically) to theoretically account for the experimental observations.

Acknowledgement: We thank Jan Helbing for crucial help with the laser setup. The work was supported by the Swiss Science Foundation (SNF) under grant 200020-107492/1.

3.3 Temperature Dependence of the IR Driven Cis-Trans Isomerization of Nitrous Acid (HONO)

Virgiliu Botan, Peter Hamm

J. Chem. Phys., *in press*, (**2008**)

Abstract

With the help of ultrafast time-resolved infrared spectroscopy, we investigate the temperature dependence of the IR driven *cis→trans* isomerization of nitrous acid (HONO) in solid Kr. We find that the lifetime of the OH stretch vibration, as well as the final cooling into the matrix, is affected only minimally (if at all) by temperature. Nevertheless, the quantum yield of the *cis→trans* isomerization reaction increases by ≈30% to a total of 50-70% when lowering the temperature from 30 K to 15 K, whereas the *trans→cis* back yield is reduced by ≈40%. The results are discussed in analogy to Marcus theory of nonadiabatic electron-transfer for the essentially barrierless case. We present a unified view of this important prototype proton transfer reaction that can explain the high *cis→trans* quantum yield of close to one.

3.3.1 Introduction

Starting with Pimentel and collaborators [8] in the fifties, the matrix isolation technique has developed in a very powerful tool of investigating chemical compounds and reactions. Among many other applications, Pimentel and coworkers were also the first to observe that the conformation of certain molecules, most prominently nitrous acid (HONO), may be switched by vibrational excitation with the help of IR light [12, 15, 16]. Apart from being an important source of OH radicals in atmospheric chemistry [35, 79, 80], HONO has been studied extensively in the context of its IR-driven isomerization both theoretically [20–32, 50, 81] and experimentally [17–19, 38, 41–44, 53, 82]. Upon IR excitation of one quantum of the OH stretch vibration, the molecule isomerizes in the *cis→trans* direction with almost unity quantum yield [16, 19], whereas the back yield is significantly smaller. The excitation reaches an energy (i.e. ≈ 3500 cm^{-1}) just below the barrier separating *cis* and *trans* isomers (4105 cm^{-1} according to the best potential energy surface available [29]), hence the reaction must be quantum with the hydrogen tunneling through that barrier. However, neither experimental [33] nor theoretical [21, 30] studies could find the reaction taking place in the gas phase with significant yield, hence, isomerization seems to be facilitated by the dissipative forces of the matrix environment. The high quantum yield of close-to-one is remarkable given the fact that the mode being excited (the OH stretch vibration) is not the reaction coordinate (HON torsion).

We have recently revisited this important prototype proton transfer system using ultrafast IR spectroscopy [43, 44, 53], in order to study for the first time also the course of the reaction in a time-resolved manner. We found that the *cis → trans* isomerization occurs in two steps, one on a fast 20 ps timescale, and a second one on a significantly slower 2 ns timescale. The timescales of the two isomerization steps roughly correlate with that of two energy relaxation processes: The vibrational lifetime of the initially excited OH_{cis} stretch vibration (a few 10's of picoseconds), and the overall cooling of the molecule into the matrix ($\approx$20 ns). We have interpreted the slower reaction step by an essentially statistical picture [44], i.e. a feeding back of energy from a large manifold of states of the molecule into a few reactive states that act as channel for isomerization. The first step, in contrast, is related to a specific and much stronger coupling between the initially excited OH stretch vibration and these reactive states.

At a temperature of 30 K, both isomerization steps are of roughly the same size, and add up to a total quantum yield of $\eta_{cis\rightarrow trans} \approx 30\%$ for the *cis→trans* reaction. The back reaction yield is lower with $\eta_{trans\rightarrow cis} \approx 7\%$ [44]. We attributed the discrepancy between the isomerization yield we observe, and the close-to-unity yield reported in literature, to the four times higher matrix temperature in our case (30 K *versus* 7 K [16, 19]). In the present paper, we set out to investigate the effect of the matrix temperature on the isomerization yields.

In fact, the temperature dependence of the thermal equilibrium constant was a key ingredient in the fifties, when the first gas phase spectra of HONO were taken, to establish that two isomers coexist. Jones et al. [14] as well as D'Or et al. [13] observed that the characteristic frequencies of HONO came in doublets and by varying the temperature they could change the ratio of these absorption bands. Pimentel and coworkers [15, 16] have measured the isomerization of HONO in solid N_2 and varied a wide set of parameters: relative concentration of precursors, different spectral filters to light-trigger the isomerization, different isotope substitutions, deposition and measuring temperatures. By choosing more and more selective filters, they were able to single out the 3200 to 3650 cm^{-1} spectral interval as efficient to trigger the *cis→trans* isomerization. In order to eliminate the possibility that the reaction is triggered by bulk heating they cooled the matrix from 20 K to 4 K but did not observe any change *within the experimental uncertainty*. McDonald and Shirk [17] measured the isomerization of HONO in N_2 and Ar matrices, but this time with a narrow band laser which was able to selectively excite either one of the isomers. Due to weak absorption of the cis OH stretch their *cis→trans* isomerization rate was *subject to large(r) errors*. Nevertheless, when measuring the isomerization rate as a function of temperature they concluded there was no *qualitative ... temperature dependence*. On the theory side, Agrawal, Thompson and Raff [23] found that the isomerization rate increases by $\approx$40% when increasing temperature from 4K to 40K, suggesting that it is an activated process. They explain this behavior through the mechanism proposed for the isomerization, according to which energy goes through a *vibration→lattice phonon modes→rotation→torsional vibration* path. An increase in temperature would increase the energy transfer from lattice phonons to rotations and in this way speed up the overall isomerization rate.

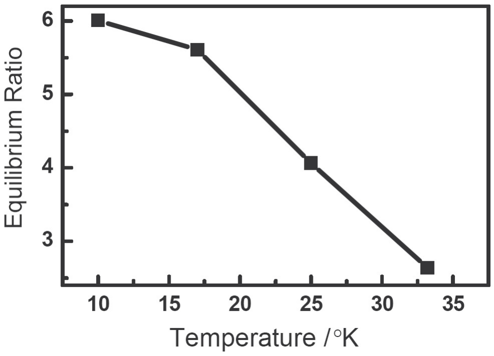

Figure 3.18: Temperature dependence of the photo-equilibrium ratio. Adapted from Ref. [44].

We have provided a first experimental evidence that temperature plays a role in Ref. [44] (see Fig. 3.18), where we measured the isomer photo-equilibrium ratio (i.e. the ratio of forward and backwards yields $\eta_{cis\rightarrow trans}/\eta_{trans\rightarrow cis}$) at different temperatures. In this stationary experiment, we irradiated the sample with the globar of a FTIR spectrometer, assuming that the spectral intensities are the same at the frequencies of the two isomers. Fig. 3.18 clearly shows that the photo-equilibrium ratio decreases with temperature, implying that either the *cis→trans* forward yield decreases or the *trans→cis* backward yield increases (or both).

We have speculated in Ref. [44] that the larger forward isomerization yield $\eta_{cis\rightarrow trans}$ at lower temperatures might be due to a slower cooling into the matrix environment, giving the molecule more time to isomerize. Consequently, in the present paper, we study both the temperature dependence of vibrational cooling of HONO, as well as the $cis \rightarrow trans$ isomerization yield in a time resolved manner. We will see that the isomerization yield indeed increases with lowering the temperature although the cooling time stays more or less constant, in contrary to our expectation. Nevertheless, the temperature dependence of forward and backward yields proves to be a key observation that helps to explain the high quantum yield of the reaction.

3.3.2 Experimental Methods

HONO was synthesized photochemically inside the matrix according to a procedure reported by Hall and Pimentel [16]. A gas mixture of 3:10:1000 HN_3:O_2:Kr was prepared in a glass container and sprayed on a calcium fluoride window in a cryostat (DE-202AF/DMX-20B, Advance Research Systems, Inc.) at a low pressure of 10^{-6} mbar and a temperature of ≈30 K. The 3317 cm^{-1} absorption band of HN_3 was used to monitor the growth of the matrix. After deposition, the matrix was irradiated with UV light from a mercury lamp, initiating photolysis of hydrazoic acid which then reacts with oxygen to form HONO. The progress of this process was monitored by the depletion of the HN_3 absorption band.

Two synchronized Ti:S laser/amplifier systems were used for the pump-probe experiments, covering time delays up to 400 ns [40]. Due to the time jitter of the two laser systems the effective time resolution was ≈10 ps. Each Ti:S laser/amplifier pumped one optical parametric amplifier (OPA) to generate tunable IR pulses centered at 3470 cm^{-1}, roughly 100 fs long and with a bandwidth of ≈300 cm^{-1} FWHM [63]. Pump and probe beams were focused to spot sizes of 150 μm and 100 μm, respectively, with a pump energy of 1.2 μJ. The repetition rate of the laser system was 1 kHz and every second pump pulse was chopped for referencing. The probe pulse was spectrally dispersed in a 190 mm spectrometer and then detected by a 63 channel HgCdTe (MCT) detector array, covering a spectral range from 3370 to 3580 cm^{-1} with a resolution of 3.3 cm^{-1}.To enable selective excitation of the *cis* species, we used a piezo-controlled adjustable Fabry-Perot filter with a bandwidth of ≈15-20 cm^{-1}, resonant with OH_{cis}. The pump intensities were kept low enough to be sure that we do not up-climb the vibrational ladder within the pump-pulse by multi-photon excitation; hence we excite only one quantum of the OH-stretch vibration. The photo-equilibrium was kept on the *cis* side by constantly exciting *trans*-HONO in excess with the help of a cw diode laser (Nanoplus GmbH, Germany, power ≈0.5 mW, wavelength 3550 cm^{-1}). The cw laser light is not polarized. In one experiment (Fig. 3.19A) we used broad band excitation (without the Fabry-Perot filter and without the cw-laser diode) to investigate the cooling of *trans*-HONO. Since the *cis→trans* yield is significantly larger than the opposite direction, the photo-equilibrium lies mostly on the *trans*-side under conditions of broad band excitation.

The matrices we prepare typically scatter significantly, thereby producing an offset of light scattered from the pump pulse into the direction of the probe pulse. This is particularly a problem at the lower temperature since the matrix cracks during cooling. We measure this scattering contribution at delay times be-

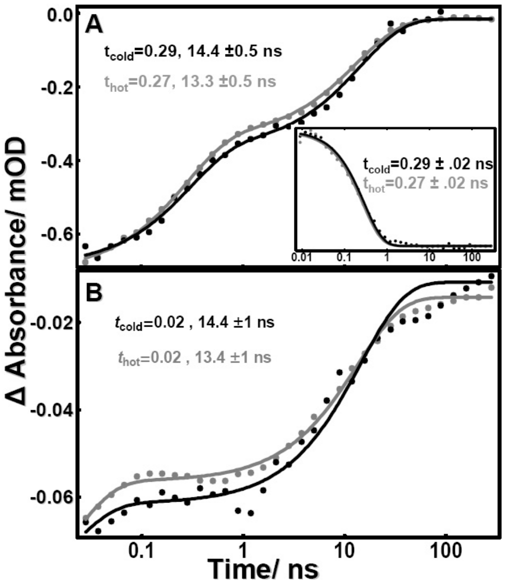

Figure 3.19: Stimulated emission and bleach kinetics of OH_{trans} (panel A) and OH_{cis} (panel B) at 30K (gray) and 15K(black). The change of absorbance is given in units of optical density (OD). The inset of panel A represents the decay of the excited state absorption of OH_{trans}.

fore zero (i.e. probe pulse before the pump pulse), and subtract it from the actual data. However, for delay times larger than $\gtrsim$ 100 ns, which is about the gating time of the electronic detection system, this subtraction is no longer perfect, and the quality of the data becomes worse.

Due to absorption of IR light, the temperature in the measurement spot might locally exceed that of the cold finger. Nevertheless, the thermal conductivity of both the window substrate CaF_2 [83] (and references therein) as well as that of the Kr matrix [84, 85] increases with lowering the temperature, so that the difference between the local and overall temperature is expected to be smaller at lower temperatures than at higher temperatures. The lowest temperature we can reach with our cryostat was 15 K.

3.3.3 Results

Fig. 3.19A compares the response of the OH_{trans} band after excitation (i.e. pumping and probing at 3550 cm^{-1}) at two different temperatures (15 K, black, and 30 K, gray). This response consists of both the bleach and stimulated emission signals that appear at the same frequency and are expected to be equally strong at early delay times [43, 44]. The stimulated emission signal decays as the OH-stretch vibration decays into closely resonant overtones and combination modes, while the bleach signal decays as the molecule finally cools into the matrix. This leads to the characteristic bi-phasic decay of the overall signal with a plateau at around 1 ns in this case. The inset of Fig. 3.19A shows the excited state absorption (probing at 3387 cm^{-1}), which responds on the decay of the OH-stretch vibration exclusively (and not the cooling into the matrix) and hence exhibits only the faster process. A global fit of the response reveals that both relaxation times are hardly affected by temperature; if at all they are somewhat slowed down (by ≈10%) as the matrix is cooled down. The fit values are reported in Tab. 3.1 (due to the reduced time-resolution of the present setup, compared to that used in Ref. [43], we were not able to resolve the faster component of the biexponential decay of the OH_{trans} vibration, which presumably is a result of matrix inhomogeneities).

Fig. 3.19B shows the corresponding response for OH_{cis} (i.e. pumping and probing at 3400 cm^{-1}). A bi-exponential fit again reveals that both relaxation times are hardly affected by temperature (within signal-to-noise, which is worse in this case because the signal is smaller, see Tab. 3.1). The faster relaxation process, occurring on a 20 ps timescale [43] in the case of OH_{cis}, is not fully resolved in the present experiment due to its reduced effective time-resolution of ≈10 ps.

In Fig. 3.20 we present IR difference spectra of OH_{trans} (Fig. 3.20B) and OH_{cis} (Fig. 3.20A) after pumping OH_{cis}. In order to calculate the *cis*→*trans* isomerization yield, we have to compare the number of molecules that have been excited with the number of molecules that isomerized. We deduce the first number

	OH_{trans}	*trans*-cooling	OH_{cis}	*cis*-cooling
15K	290±20 ps	14.4 ± 0.5 ns	20 ps*	14.4 ± 1 ns
30K	270±20 ps	13.3 ± 0.5 ns	20 ps*	13.4 ± 1 ns

Table 3.1: Fit results for vibrational relaxation of the OH-stretch vibration and the overall cooling into the matrix for both *trans* and *cis* HONO. * Since the time-resolution of the present experiment was not sufficient to fully resolve the vibrational relaxation of the OH-stretch vibration in *cis* HONO, the value (20 ps) was taken from Ref. [44], and assumed to be the same at both temperatures.

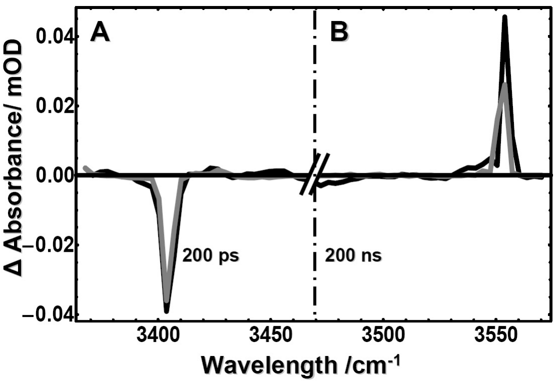

Figure 3.20: Response of OH_{cis} and OH_{trans} after exciting OH_{cis}. Panel (a) shows the bleach of OH_{cis} after 200 ps and panel (B) that of OH_{trans} at 200 ns. Gray and black lines compare the response at 30 K and 15 K, respectively. The change of absorbance is given in units of optical density (OD).

from the bleach signal at ≈3400 cm^{-1} at a delay time of 200 ps , i.e. the plateau between decay of stimulated emission and overall cooling (Fig. 3.20, left half), and the second number from the positive signal of OH_{trans} at 3550 cm^{-1} at late delay times 200 ns, when cooling into the matrix is completed (Fig. 3.20, right half). The signal at 15K is normalized to that at 30 K in order to facilitate comparison of the isomerization yields. From the integrated intensities of the *trans* photo-product bands, we estimate a 30% rise in the *cis*→*trans* isomerization yield when temperature is reduced from 30K to 15K (note that the product band is narrower at 15 K, hence the effect on the integrated intensity is smaller than that on the peak intensity). Correcting the signals in Fig. 3.20 with the ratio of transition dipoles of the OH stretch vibration in *cis* and *trans* HONO (1.6-2 [44]), we conclude that the total quantum yield is $\eta_{cis\rightarrow trans}$ ≈50-70% at 15 K.

However, it should be noted that this estimate of the quantum yield implicitly assumes an isotropic sample. As the sample is excited with polarized light, this is not necessarily the case; in fact we have shown recently that at least *trans*-HONO does not undergo full orientational diffusion on even a minute timescale [53]. Also the degree of polarization of the laser used to switch back will play a role. In the present study, we used a cw-laser diode for this purpose, which was not polarized, whereas in Ref. [44] we had used light derived from the fs-OPA which was polarized. This might explain the difference in absolute numbers between the present study and the results of Ref. [44]. We therefore concentrate in the discussion more on the temperature induced change of quantum yield, rather than the absolute values.

3.3.4 Discussion

In a first set of experiments, we measured the lifetime of OH_{trans} of HONO and found little or no temperature dependence in the interval from 30 K to 15 K. Also the cooling of the HONO molecules into the matrix proves to be only very weakly temperature dependent, if at all. To the best of our knowledge, there is no published work of similar experiments in which vibrational lifetimes have be studied as a function of temperature in matrix environment. The closest situation we are aware of is the vibrational relaxation of C=O groups in globular proteins like myoglobin, measured by Fayer and coworkers [86]. The lifetime of the CO (≈30 ps) changes by less then 20% in a large temperature interval from 310 K to 10 K. Also the vibrational lifetimes of the OH vibration in ice [87] as well as the amide I (C=O) vibrations of the backbone in peptides and proteins have been shown to be largely temperature independent [88]. Our observation of essentially temperature independent relaxation rates of HONO in solid Kr is in accordance with these studies.

The *cis* → *trans* isomerization yield, on the other hand, increases by ≈30% when the temperature is lower from 30 K to 15 K, resulting at a total quantum yield of 50-70% at 15 K. This value is still smaller than the reported quantum yield of close-to-one [19]. The two results are nevertheless consistent within experimental uncertainty, in particular when considering that the temperatures are still different (15 K *versus* 7 K). That is, if we were to extrapolate our value to 7 K, based on what one would expect from Fig. 3.20, we might indeed conclude that the quantum yield could reach values close to 100%.

Due to technical limitations related to the tuning range of the cw-diode laser used in our experiment, we cannot measure the temperature dependence of the *trans*→*cis* yield directly. We can nevertheless estimate it from Fig. 3.18, which plots the ratio of yields, $\eta_{cis\rightarrow trans}/\eta_{trans\rightarrow cis}$. This ratio increases by ≈80% when lowering the temperature form 30 K to 15 K, implying that $\eta_{trans\rightarrow cis}$ actually decreases by ≈40% in the same temperature range.

We discuss the reaction mechanism in analogy to

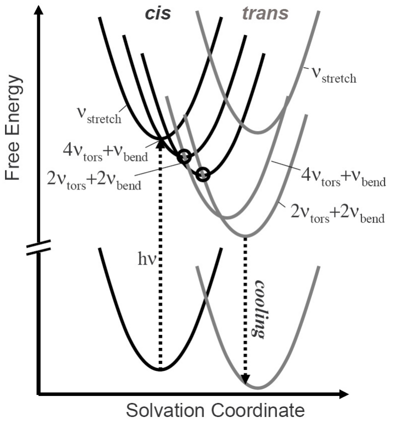

Figure 3.21: Possible arrangement of the free energy surfaces of the various vibrational states as a function of a generalized solvation coordinate. The black circles mark the positions where nonadiabatic proton-transfer between *cis* and *trans* HONO can take place in an essentially barrierless manner, explaining the increase of the rate as temperature is decreased.

Marcus theory of nonadiabatic electron transfer. The concepts of electron transfer theory have been extended to other types of reactions, most notably proton transfer reactions, by many researchers before [46–49]. We have shown in a mixed-quantum-classical simulation [50] that proton transfer is driven by matrix-fluctuations, i.e. transfer of population between two vibrational states takes place when they become resonant due to matrix-fluctuations, and that these curve crossings are only weekly avoided due to a small tunnel couplings. These are exactly the prerequisites of Marcus theory of nonadiabatic electron transfer. Accordingly, the proton transfer rate between each pair of *cis* and *trans* vibrational states can be expressed as:

$$k_{cis\to trans} = \beta^2 \sqrt{\frac{\pi}{\hbar^2 k_B T F_\lambda}} \exp\left(-\frac{(\Delta F - F_\lambda)^2}{4 F_\lambda k_B T}\right) \qquad (3.12)$$

where β is the tunnelling matrix element, ΔF the free-energy gain upon isomerization and F_λ the reorganization energy, i.e. the energy it would cost to deflect the solvation degrees of freedom to the *trans* situation, however, keeping the proton on the *cis* side. The ratio between forward and backward rates, of course, fulfills detailed balance:

$$\frac{k_{cis\to trans}}{k_{trans\to cis}} = \exp\left(\frac{\Delta F}{k_B T}\right) \qquad (3.13)$$

With ΔF positive for a downhill reaction, this ratio increases as temperature is reduced, exactly as observed experimentally (Fig. 3.18). The only situation for which also the forward rate $k_{cis\to trans}$ can increase when lowering the temperature is the essentially barrierless case with $\Delta F \approx F_\lambda$, when the product free energy surface crosses the reactant surface close to its minimum (see black circles in Fig. 3.21). In this case, the $1/\sqrt{T}$ dependence of the pre-exponential factor of Eq. 3.12 exceeds that of the exponential term. In fact, the $1/\sqrt{T}$ term would predict a 40% increase of the forward rate when the temperature is reduced by a factor two, in very good agreement with our experimental value (30%). The barrierless case is also the situation that renders the rates maximal (i.e. the maximum in the so-called Marcus parabola).

Fig. 3.21 shows a possible arrangement of the relevant vibrational states, plotted as a function of a generalized solvation coordinate. Upon IR excitation of *cis*-HONO, the OH-stretch vibration ν_{stretch} is reached. It has been shown in Ref. [50] that ν_{stretch} decays predominantly into $4\nu_{\text{tors}} + \nu_{\text{bend}}$, $2\nu_{\text{tors}} + 2\nu_{\text{bend}}$ and $3\nu_{\text{bend}}$ since these states are closely resonant. The two states $4\nu_{\text{tors}} + \nu_{\text{bend}}$ and $2\nu_{\text{tors}} + 2\nu_{\text{bend}}$ probably play the most important role in the isomerization reaction since they have a sufficiently large number of quanta in the torsional coordinate responsible for a significant tunnelling coupling β. The temperature dependencies of both forward and backward yields suggest that the corresponding states in the *trans* configuration are energetically lower and furthermore cross the *cis*-states in essentially a barrierless manner. This special arrangement is supported by the observation that the corresponding fundamental modes are indeed lower in frequency in the *trans* configuration: $\nu_{\text{tors}} = 549\ \text{cm}^{-1}$ in *trans*-HONO *versus* $637\ \text{cm}^{-1}$ in *cis* and $\nu_{\text{bend}} = 1287\ \text{cm}^{-1}$ in *trans*-HONO *versus* $1315\ \text{cm}^{-1}$ in *cis* (in solid Kr [19]). The $\text{OH}_{stretch}$ vibration, in contrast, is higher in frequency in *trans*-HONO ($3351\ \text{cm}^{-1}$ *versus* $3401\ \text{cm}^{-1}$). Hence, the initially pumped $\text{OH}_{stretch}$ vibration is not in resonance with the reactive modes in the *trans* configuration (see Fig. 3.21), explaining why the decay of the former is less efficient (270 ps in *trans*-HONO *versus* 20 ps in *cis*).

Putting these considerations together, we can now discuss the reason for the high quantum yield. The high quantum yield is merely a result of the fact that the reaction proceeds energetically downhill (Eq. 3.13). However, it is not the ground state surfaces that are relevant (for which the tunnel coupling would be negligible), but the surfaces of a few reactive states that are energetically close enough to the barrier. The second important ingredient for the high quantum yield is the cooling rate, that is of the same order of magnitude as the isomerization rate. This is seen from the fact that the sum of forward and backward yields $\eta_{cis \rightarrow trans} + \eta_{trans \rightarrow cis} \approx 60 - 80\%$ is close to one, but does not quite reach this value at 15 K. If cooling would be significantly slower, then the molecule would have time to fully thermalize on either side, in which case the ratio of forward and backward yields would be determined by the densities of states in both configuration. However, these densities of states are almost identical in the relevant energy range [29]. On the other hand, if isomerization would be significantly slower than cooling, the molecule wouldn't have time to isomerize and the sum of forward and backward yields $\eta_{cis \rightarrow trans} + \eta_{trans \rightarrow cis}$ would be significantly below 1. Tentatively, this is what is happening at higher temperatures.

3.3.5 Conclusion

In conclusion, we have studied the temperature dependence of energy relaxation processes as well as of the $cis \rightarrow trans$ isomerization yield of HONO in solid Kr. While the former are hardly temperature dependent, the $cis \rightarrow trans$ forward yield increases by $\approx$30% when lowering the temperature from 30 K to 15 K. The $trans \rightarrow cis$ backward yield, in contrast, decreases by $\approx$40% in the same temperature range. This peculiar temperature dependence is the key observation that helps to explain the observed high quantum yield of this important model reaction. That is, the temperature dependencies suggest that the reaction can be described in analogy to Marcus theory of electron transfer for the essentially barrier-less case. This, in turn, suggest an ordering in energy of the relevant vibrational states as depicted in Fig. 3.21. This model explains all experimental observations so far in a self-consistent manner.

Acknowledgements: We thank Gerhard Stock for careful reading of the manuscript. The work has been supported by the Swiss National Science Foundation (SNF) under grant 200020-115877.

3.4 Intramolecular Energy Redistribution in Nitrous Acid (HONO)

Virgiliu Botan, Peter Hamm

J. Chem. Phys., *in press*, (**2008**)

Abstract

Intramolecular energy redistribution (IVR) in nitrous acid (HONO) is studied with the help of ultrafast two-color pump-probe spectroscopy. In a previous paper [V. Botan et al. J. Chem. Phys. 124, 234511 (2006)], it has been observed that *trans*-HONO cools through a cascade of overtones of one specific mode after pumping the OH stretch vibration. We had suggested that this cooling mode is the ONO bend vibration. Furthermore, molecules that have initially been excited by the OH stretch vibration of *cis*-HONO, and then underwent isomerization, follow the same relaxation pathway. In the present study we extend the investigation of IVR of *cis* and *trans* HONO to the N=O-stretch and HON-bend spectral regions, finding further evidence that the bottleneck of *trans*-cooling is indeed the ONO bend vibration. In combination with information on the anharmonic coupling constants of different modes, the energy relaxation dynamics preceding this cooling cascade can also be followed in unprecedented detail.

3.4.1 Introduction

Intramolecular energy redistribution (IVR) is of paramount importance in chemical reactions owing to its influence on the outcome of such processes. The primary challenges in directly observing IVR were achieved by the advent of ultrafast lasers and the development of tunable infrared (IR) sources. One of the pioneering developments in the field was done by Laubereau and Kaiser [89], addressing the problem of vibrational dephasing in condensed phase systems. Two decades earlier Pimentel and collaborators proposed the matrix isolation technique as a mean to study chemical reaction and chemical compounds [8]. One of their first experiments discovered the IR-driven *cis-trans* isomerization reaction of nitrous acid (HONO) which proved to be a prototype proton transfer system. Probably the most tantalizing aspect of this reaction is its very high *cis*→*trans* quantum yield, qualitatively approaching unity [16, 19] following IR excitation of OH stretch vibration. This number is particularly surprising given the fact that the initially excited mode is not the reactive mode (the OH-torsion). The *trans*→*cis* back reaction yield is significantly less, with the ratio between the two varying with temperature [44] from 3 at 30 K to 7 at 10 K. The large ratio between the forward and backward reaction yields is suggestive since the energy reached after OH excitation of both isomers is almost identical and, after most estimates, just slightly below the barrier separating both species [29, 32]. Hence, the reaction must be to some extent mode specific, and the competition between IVR and the reaction rate determines its outcome. That is, if IVR were faster than the isomerization, then the outcome of the reaction would be determined by the ratio of density of states of *cis* and *trans*-HONO, which is essentially unity in the relevant energy range [29]. Vibrational relaxation of diatomic molecules in matrix environment has been studied in great detail [90–92]

The HONO system has been studied intensively both theoretically [20–32, 50, 81] and experimentally [15–19, 43–45, 53]. Neither experimental [33] nor theoretical [21, 30] studies could find the reaction taking place in the gas phase with significant yields, hence, isomerization seems to be facilitated by the dissipative forces of the matrix environment. In this context we decided to investigate the isomerization of HONO in the time domain with the help of ultrafast IR pump-probe spectroscopy [43]. We found that the *cis* → *trans* isomerization occurs on stretched timescales, from 20 ps timescale to 2 ns, and we measured a combined reaction yield of ≈30% at a temperature of 30 K [44]. Further investigations, related to the temperature dependence of quantum yield [45], anisotropy of the two isomers [53] and improvements in signal to noise ratio led us to conclude that the *cis*→*trans* quantum yield at low temperatures is indeed very high (50-70% at 15K). Furthermore we observed that cooling of *trans*-HONO proceeds through the overtones of one particular mode. Based on the number of quanta we observed and the anharmonic coupling constants available in literature [29,41,42] we suggested that the "cooling mode" is the ONO bend vibration. This is not the lowest energy mode of the *trans* isomer but lies ≈60 cm^{-1} above the OH-torsional mode (see Tab. 3.2 for the normal mode frequencies of HONO in solid Kr). The torsional mode is spatially very extended and thus, strongly interacting with the surrounding matrix. We suggested that this is the reason why we don't see the OH-torsional mode as bottleneck in the cooling process.

We analyzed our pump-probe spectra in terms of a Dunham expansion for the anharmonically coupled vibrational levels [39]:

$$E=\sum_i \hbar\omega_i(n_i+1/2)+\sum_{i,j}x_{ij}(n_i+1/2)(n_j+1/2) \tag{3.14}$$

where ω_i is the harmonic frequency of mode i, n_i its excitation level and x_{ij} the anharmonic coupling constants. From this expression, one can derive for the transition frequency for one particular mode k:

$$\nu_{n_k\longrightarrow n_k+1}=\nu_k+2n_kx_{kk}+\sum_{i\neq k}x_{ik}n_i, \tag{3.15}$$

with ν_k=ω_k+2 x_{kk}+$\sum_{i\neq k}x_{ik}$/2. The anharmonic constants are symmetric, $x_{ij}=x_{ji}$, and are in most cases, but not necessarily, negative since the potential energy surface softens as one is climbing up the vibrational ladder. The anharmonic constants of HONO have been calculated on the CCSD(T)/cc-pVQZ level of theory [29], and some of them are known experimentally [41, 42] (see Tab. 3.4 below).

If mode k is vibrationally excited ($n_k>0$), its transition frequency will be shifted due to diagonal anharmonicity $2n_kx_{kk}$. If, however, mode k has already relaxed to its ground-state ($n_k=0$), but vibrational energy is in other modes of the molecule, then the transition frequency of mode k is still shifted; we call this a "hot band" or "dark states". The shift is given by the corresponding anharmonic coupling constant x_{ik} times

	trans	cis
OH stretch (ν_1)	3552	3401
N=O stretch (ν_2)	1681	1630
HON bend (ν_3)	1286	1315$^{(a)}$
N-O stretch (ν_4)	799$^{(a)}$	849$^{(a)}$
ONO bend (ν_5)	608$^{(a)}$	616$^{(a)}$
OH-torsion (ν_6)	550$^{(a)}$	637$^{(a)}$

Table 3.2: Vibrational frequencies (in cm^{-1}) of HONO in solid Kr. $^{(a)}$ taken from Ref. [19]

the number of quanta of excitation. Hence, knowing the anharmonic constants, we can in principle follow the energy-relaxation process through all modes, even though we perform the spectroscopy only on one particular spectator mode k. However, although the molecule is small and vibrational transitions are relatively sharp in the matrix environment, the density of states is significant in the 3000-4000 cm^{-1} region and the thus obtained spectra are quite congested.

The aim of the present paper is to extend our relaxation studies [44] by pumping and/or probing two additional, lower-frequency modes, the N=O stretch and HON bend vibration. Thereby, the hot band spectra are thinned out due a lower density of states in the corresponding energy range. Furthermore, since the set of anharmonic constants x_{ik} is different for a different spectator mode k, it might help to identify the IVR through different modes i. Compiling the information of the three sets of data, we obtain a very detailed picture of IVR. Furthermore, we add a few more experimental values to the list of anharmonic constants of HONO.

3.4.2 Materials and Methods

HONO was synthesized photochemically according to a procedure reported by Hall and Pimentel [16]. A gas mixture of 3:10:1000 HN_3:O_2:Kr was prepared in a glass container and sprayed on a calcium fluoride window kept in a cryostat (DE-202AF/DMX-20B, Advance Research Systems, Inc.) at very low pressure (10^{-6} mbar) and a temperature of approximately 30 K, which was also the temperature of the measurements. The 3317 cm^{-1} absorption band of HN_3 was used to monitor the growth of the matrix. After deposition, the matrix was irradiated with UV light from a mercury lamp, initiating photolysis of hydrazoic acid which then reacts with oxygen to form HONO. The progress of this process was monitored by the depletion of the HN_3 absorption band.

For following the isomerization reaction and IVR dynamics we use an ultrafast IR pump-probe setup. Two synchronized Ti:S laser/amplifier were used to cover time delays up to 300 ns [40]. Due to jittering of the two laser systems our effective time resolution is $\approx$ 10ps. Each Ti:S laser/amplifier pumped one optical parametric amplifier (OPA) to generate tunable IR pulses, which are roughly 100 fs long and have a bandwidth of $\approx$300 cm^{-1} FWHM [63]. Pump and probe beams were focused to spot sizes of 150 μm and 100 μm, respectively, with a pump energy of 1.2 μJ. The repetition rate of the laser system was 1 kHz and every second pump pulse was chopped for referencing. The probe pulse was spectrally dispersed in a 190 mm spectrometer and then detected by a 63 channel HgCdTe (MCT) detector array, covering a spectral range of 100-200 cm^{-1} (depending on center wavelength and the grating used).

In some of the experiments, in order to enable selective excitation of either the *cis* or the *trans* isomer, we spectrally narrowed the pump-pulses with the help of a piezo-controlled adjustable Fabry-Perot filter (bandwidth $\approx$15-20 cm^{-1}). Furthermore, when pumping the OH-stretch vibration of *cis*-HONO (OH_{cis}), which leads to *cis* → *trans* isomerization, the photoequilibrium was kept on the *cis* side by constantly exciting OH_{trans} with the help of a cw diode laser (Nanoplus GmbH, Germany, power $\approx$0.5 mW, wavelength 3550 cm^{-1}). The detailed measurement modi of the various data of this paper were: In Fig. 3.22 we pumped both OH-stretch vibrations broad band (gray lines in the two panels), N=O_{trans} narrow band (black lines in panel A) and HON broad band (black lines in panel B). In Fig. 3.23a-c, we used the Fabry-Perot filter and the cw diode laser to selectively excite OH_{cis}, in Fig. 3.23d-f we used only the Fabry-Perot to selectively excite the *cis* or *trans* isomer, and in Fig. 3.23g-i we performed a broad band excitation, since only the *trans*-isomer carries oscillator strength.

3.4.3 Experimental Results

In Fig. 3.22 we present pump-probe spectra of OH_{trans} after excitation of OH_{trans} (gray, panel A and B), N=O_{trans} (black, panel A) and HON_{trans} (black, panel B), respectively. All spectra we present are difference spectra with negative contributions from the bleaching ground-state of the excited molecules (and,

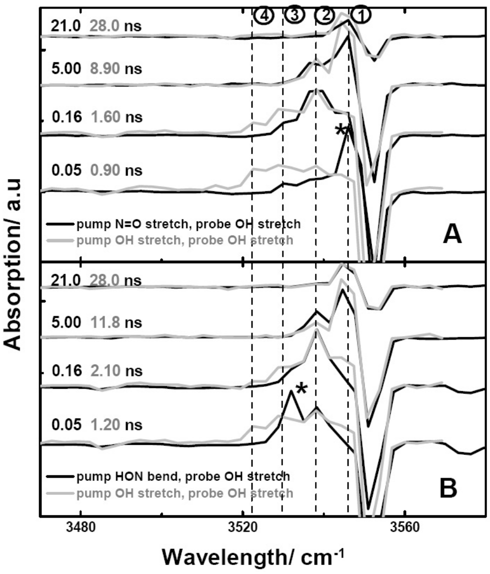

Figure 3.22: Transient difference spectra of OH_{trans} following the excitation of OH_{trans} (gray lines), $N{=}O_{trans}$ (panel A black lines) and HON_{trans} (panel B black lines). Vertical dashed lines labelled 4 to 1 mark the spectral positions of the four hot bands observed in the *trans*-cooling. To facilitate comparison, the delay times are chosen such that population peaks in a certain hot band. The bands labelled with * correspond to the direct anharmonic coupling between the pumped and probed vibrations (see text)

OH_{trans}	8 ps, 260 ps$^{(a,b)}$
OH_{cis}	20 ps$^{(a)}$
$N{=}O_{trans}$	70 ps
$N{=}O_{cis}$	300 ps
ONO_{trans}	420 ps, 60 ps$^{(a)}$

Table 3.3: Vibrational lifetimes.
(a) Taken from Ref. [43]
(b) Biexponential decay
(c) left and right subbands

.

at early times and in the case of OH_{trans} pumping also from stimulated emission from the excited states), and positive contributions from transient, vibrationally hot species as well as the isomerized photo-product. As discussed in our previous paper [44], the hot band starts out as a red shifted broad featureless band after OH_{trans} pumping (Fig. 3.22, gray curves), and becomes structured as the molecules cool down. Analyzing the energy spacings between the sub-bands, we had suggested that cooling proceeds through a cascade of overtones of one particular mode (the four dashed vertical lines in Fig. 3.22 labelled 4 to 1).

If, in contrast, we excite $N{=}O_{trans}$ (Fig. 3.22A, black line), the early time response is initially dominated by a strong positive peak at 3545 cm^{-1} (labelled with a * in the 0.05 ns spectrum) due to anharmonic coupling between the pumped (ν_1) and the probed mode (ν_2) with $x_{12} = -7 \ cm^{-1}$. This band decays with the vibrational lifetime of $N{=}O_{trans}$, ≈70 ps (Tab. 3.3). After vibrational relaxation of $N{=}O_{trans}$, the response is strikingly similar to that after OH_{trans} excitation. Cooling proceeds through the same cascade., however, due to the lower excitation energy we can identify only three quanta of that cooling mode after $N{=}O_{trans}$ excitation (see 0.05 ns spectrum), whereas it is four after OH_{trans} excitation. Fig. 3.22 panel B (black lines) presents the analogous experiment after exciting HON_{trans}. As before, the anharmonic coupling between the excited mode (ν_3) and the probed mode (ν_1) is observed at early delay times (labelled with *) with a anharmonic coupling constant x_{13}=-21 cm^{-1}, and the cooling cascade starts out with only two quanta of the cooling mode.

Fig. 3.23 gives a more complete account of IVR, where we excite and probe, in different combinations, the OH, N=O and HON vibrations. The data are presented as a 'matrix', where rows relate to the pumped mode and columns to probed mode. The data in Fig. 3.23f,i are the same as Fig. 3.22 (black lines); the data in Fig. 3.23c differ from Fig. 3.22 (gray line) by the fact that the *cis*-isomer is now pumped. Exciting OH_{cis} allows us to monitor the cooling dynamics of *cis*-molecules as well as the isomerization towards the *trans*-side with the subsequent cooling of the latter. The transient spectra at delay times later than 100 ns (Fig. 3.23a-c) perfectly match the stationary FTIR difference spectra (Fig. 3.23, very top), evidencing that the molecules have completely relaxed to the ground state. Excitation of the N=O and HON vibrations, on the other hand, does not result in any isomerization since the energy is too low to surmount the barrier. The absence of any reaction leads to a zero signal at later times in these cases (Fig. 3.23d-i).

The most pronounced positive bands are labelled with a 3 digit code in Fig. 3.23. The first digit corresponds to the pumped mode, the second to the probed

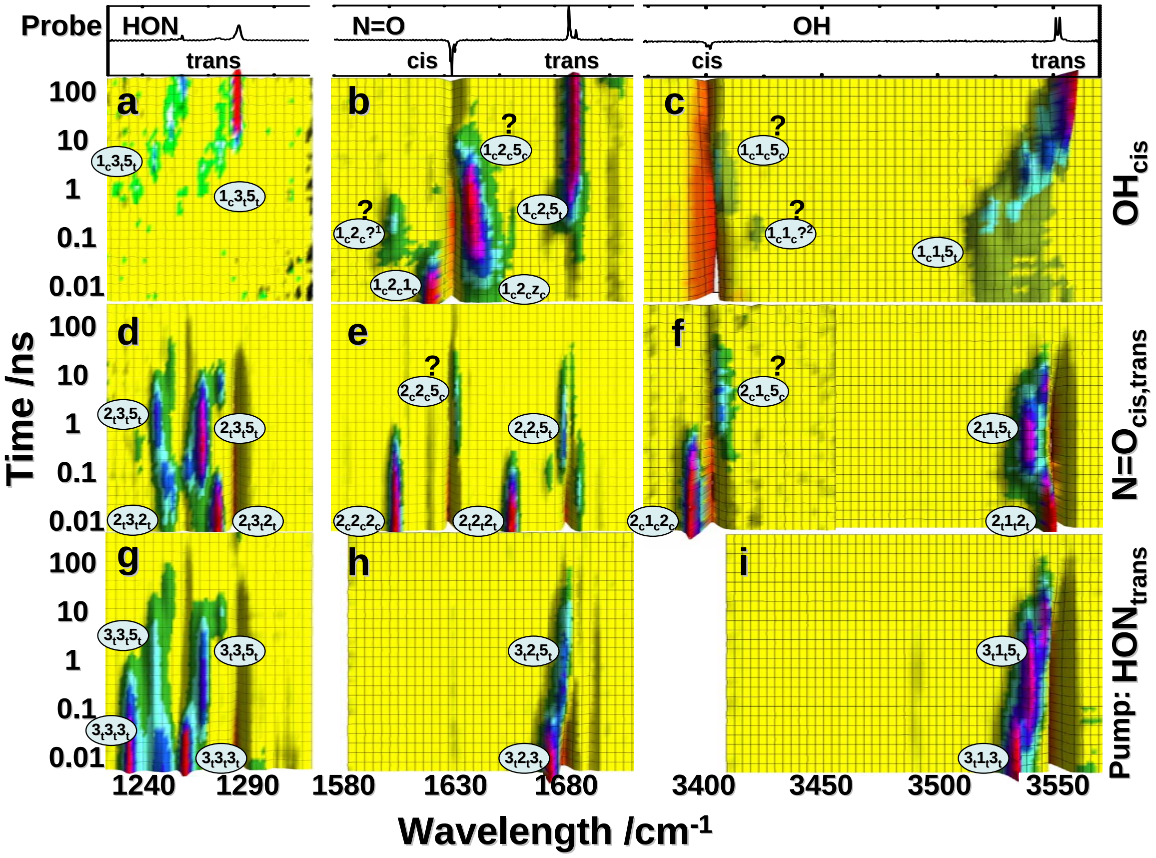

Figure 3.23: Transient difference spectra in the spectral range of HON bend (left column), N=O stretch (middle column), OH stretch (right column), after exciting either OH_{cis} (top row, the very top shows a stationary difference spectrum measured in a FTIR spectrometer as a reference), $N{=}O_{cis}$ and/or $N{=}O_{trans}$ (middle row) and HON_{cis} (bottom row). Transient bands are coded with a three digit label which represent pumped mode (first digit), probed mode (second digit) and the mode to which the probed mode anharmonically couples (third digit). Bands for which the assignment is speculative are labelled with an additional question mark

mode and the third to the mode to which the probed mode anharmonically couples. The last two indices indicate the anharmonic constant x_{ij} the corresponding peak determines. For example, the code $1_c1_t5_t$ corresponds to a band in which we excite OH_{cis} (ν_1), probe OH_{trans} (ν_1) and observe the anharmonic coupling of the latter to ONO_{trans} (ν_5). We will discuss the various spectra row by row:

OH_{cis}-Pumping: In the OH region, we observe in the red part of the spectrum the bleach/stimulated emission of *cis*-HONO, and in the blue part the molecules that isomerized into *trans*-HONO (Fig. 3.23c). The cooling of the latter proceeds through a cascade (bands $1_c1_t5_t$) which is identical to that after exciting OH_{trans} directly [44]. In analogy to cooling of *trans*-HONO, we assume that *cis*-HONO cools through the same cascade, hence we tentatively assign peak $1_c1_c5_c$ to the anharmonic coupling with ONO_{cis} with a very small positive x_{15}.

Evaluating the N=O spectral region (Fig. 3.23b) we observe at early delay times a *cis*-bleach signal paired with a positive band ($1_c2_c1_c$) which corresponds to the direct anharmonic coupling between OH$_{cis}$ and NO$_{cis}$ and hence determines the *cis*-anharmonic constant $x_{12} = -6$ cm^{-1}. Blue shifted from the bleach we take note of a strong positive band (band $1_c2_c5_c$) which presumably is part of the *cis*-cooling process (at least at later delay times), in analogy to band $1_c1_c5_c$. We can also see the isomerized *trans*-molecules and the corresponding band $1_c2_t5_t$ grows in with an estimated small anharmonic shift $x_{25} \approx -0.5$ cm^{-1}. Due to the small shift, we cannot resolve the relay of cooling states.

In the spectral region of the HON bend vibration (Fig. 3.23a), we can observe only the *trans*-isomer (the HON$_{cis}$ cross section is very weak) and the band is strongly split due to site inhomogeneities. For each of the matrix sites, we observe a cooling cascade (bands $1_c3_t5_t$ with $x_{35} = -7$ cm^{-1}) synchronous with band $1_c1_t5_t$.

N=O-pumping: In the response following the excitation of the N=O vibration (Fig. 3.23d-f) we can identify at early delay times bands $2_t3_t2_t$ (twice), $2_c2_c2_c$, $2_t2_t2_t$, $2_c1_c2_c$ and $2_t1_t2_t$ (see Tab. 3.4 for the corresponding anharmonic constants). It is interesting to note that the anharmonic constant determined from either band $1_c2_c1_c$ or band $1_c1_c2_c$ are indeed identical, reflecting the symmetry $x_{12} = x_{21}$. Bands $2_t3_t2_t$, $2_t2_t2_t$, and $2_t1_t2_t$ decay with the lifetime of NO$_{trans}$ ($\approx$70 ps), whereas bands $2_c2_c2_c$, and $2_c1_c2_c$ follow the dynamics of NO$_{cis}$ (lifetime $\approx$300 ps, see Tab. 3.3.).

As discussed above, cooling of NO$_{trans}$ proceeds through a cascade of up to three quanta of the cooling mode. This is evident in the OH spectral region (bands $2_t1_t5_t$) and the HON spectral region (bands $2_t3_t5_t$). Due to similar kinetics, we believe that band $2_t2_t5_t$ follows the same cascade. In the case of NO$_{cis}$ we see hot bands (bands $2_c2_c5_c$ and bands $2_c1_c5_c$) which probably are the same as bands $1_c2_c5_c$ and $1_c1_c5_c$, respectively.

HON-pumping: The response after HON$_{trans}$ excitation (Fig. 3.23g-i) differs form that after N=O$_{trans}$ excitation at early delay times due to the different mode excited (bands $3_t3_t3_t$, $3_t2_t3_t$, and $3_t1_t3_t$, see Tab. 3.4 for the corresponding anharmonic constants), but they become essentially identical once the cooling cascade is entered (bands $3_t3_t5_t$, $3_t2_t5_t$, and $3_t1_t5_t$). The vibrational lifetime differs for the two sub-bands and is $\approx$ 420 ps for the lower-frequency band and $\approx$ 60 ps for the dominant higher frequency band.

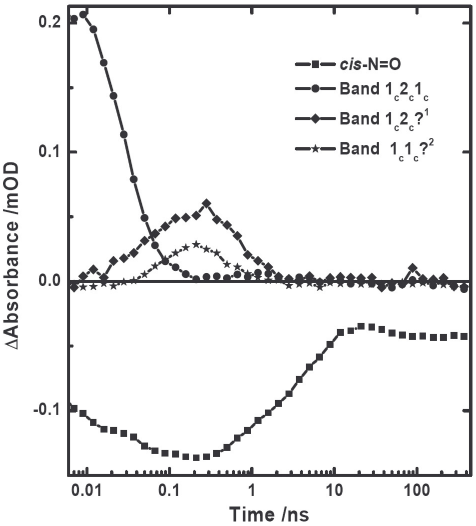

Figure 3.24: Time traces extracted from Fig. 3.23 for the *cis*-N=O bleach and stimulated emission (squares), the decay of *cis*-OH measured through band $1_c2_c1_c$ (circles), and the dynamics of the two bands $1_c2_c?^1$ and $1_c1_c?^2$ (rhombi and stars).

Peaks $1_c2_c?^1$ and $1_c1_c?^2$ in Fig. 3.23bc deserve an extra discussion: From the perfect frequency match of peak $1_c2_c?^1$ with peak $2_c2_c2_c$ (Fig. 3.23e) and the fact that the size of the negative signal at the frequency of N=O$_{cis}$ increases as peak $1_c2_c?^1$ appears (Fig. 3.24, circles), one is tempted to conclude that peak $1_c2_c?^1$ reflects direct population of N=O$_{cis}$ after relaxation of OH$_{cis}$. The additional negative signal is attributed to stimulated emission of the excited N=O$_{cis}$. However, if that were the whole story, then one would expect in Fig. 3.23c a signal appearing at the same time with negative frequency shift $x_{12} = 7$ cm^{-1}. This is not observed, instead, we find a peak $1_c1_c?^2$ with a positive frequency shift, which perfectly coincides in time with peak $1_c2_c?^1$ (see also Fig. 3.24, rhombi and stars). We tentatively assign the two peaks to one and the same combination mode $\nu_2 + n_?\nu_?$, which would result in different frequency shifts when observing it through the N=O vibration ($2x_{22} + n_?x_{2?}$) or the OH vibration ($x_{12} + n_?x_{1?}$). Given the long overall cooling times of 10's of nanoseconds, it would appear anyway very unlikely that energy drops within 100 ps from that of OH$_{cis}$ (3401 cm^{-1}) directly to N=O$_{cis}$ (1630 cm^{-1}). Hence, the N=O$_{cis}$ will be accompanied by the excitation of some other (unknown) mode. From the above discussion, this would imply $x_{2?} \approx 0$ and $x_{1?}$ relatively large and positive. Unfortunately, this does not match with any of the theoretically calculated anharmonic constants (Tab. 3.4) [29], hence we cannot assign the

	trans			cis		
	calc.[a]	exp.[b]	exp.[d]	calc.[a]	exp.[c]	exp.[d]
x_{11}	-87.0	-83.78	-83	-97.55	-94.00	-95[e]
x_{12}	-9.8		-7	-13.39		-6
x_{13}	-26.84	-24.36	-21	-35.25		
x_{14}	-7.64	-2.95		-1.38	2.9	
x_{15}	-3.20		(-8)	-4.15		
x_{16}	-33.61			-1.44		
x_{22}	-16.13	-13.7	-11	-14.40	-11.53	-11
x_{23}	-10.71		-8	-16.46		
x_{24}	9.47			-4.44	0.5	
x_{25}	0.99		(-0.5)	-3.80		
x_{26}	13.01			-0.92		
x_{33}	-11.28	-11.34	-10	-12.07		
x_{34}	-14.33			-7.96		
x_{35}	-7.97		(-7)	-14.43		
x_{36}	-5.79			-3.99		
x_{44}	-11.49			-8.58		
x_{45}	-12.99			-13.55		
x_{46}	-33.51			-14.60		
x_{55}	-6.34			-6.09		
x_{56}	-8.42			-5.27		
x_{66}	-4.41			-3.89		

Table 3.4: Calculated and experimental anharmonic coupling constants x_{ij} of HONO (in cm^{-1})

[a] theoretical values from Ref. [29]

[b,c] gas phase experimental values from Ref. [41,42]

[d] experimental values in solid Kr. A typical error bar is ±1 cm^{-1} due to the limited spectral resolution of our setup. Values in parentheses are assigned assuming that the cooling mode is indeed ν_5.

[e] taken from Ref. [43]

combination mode.

3.4.4 Discussion and Conclusion

Three essential results are obtained from this two-color pump probe study of HONO in solid Kr.

- First, we provide additional strong evidence that the cooling mode is indeed the *trans*-ONO-bending mode (ν_5). We observe for the anharmonic constants $x_{1?} = -8$ cm^{-1}, $x_{2?} < 0.5$ cm^{-1}, $x_{3?} = -7$ cm^{-1} (Fig. 3.23), where the ? stands for the cooling mode that is to be determined. Comparing these experimental values with theoretical ones calculated on the CCSD(T)/cc-pVQZ level of theory [29], we find the largest correlation with the ONO-bending mode (ν_5) with a rms-deviation of 3 cm^{-1}. The deviation would be 7 cm^{-1} for the N-O stretch (ν_4), and 17 cm^{-1} for the OH-torsional mode (ν_6), in both cases significantly larger. The best agreement between theoretical and experimental value is obtained for the lowest frequency mode (i.e. x_{35}), in agreement with the expectation that the *ab-initio* calculation is more reliable at lower energies. Complementary evidence comes from varying the excitation energy (Fig. 3.22), with a maximum number of quanta in the cooling mode that coincides with what we expect from the energy pumped into the molecule (Fig. 3.25). We might in fact expect more than the four quanta after OH$_{trans}$ pumping, however, those might be obscured by the very featureless spectrum at early delay times due to the large density of states in this high-energy regime. Complimentary information

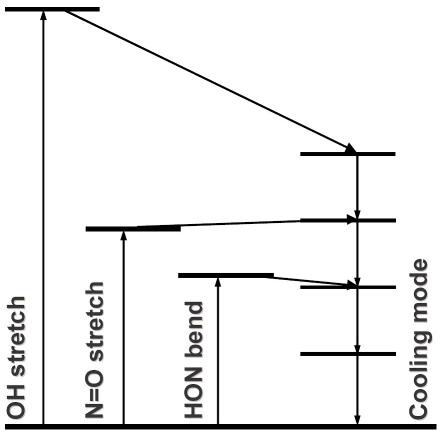

Figure 3.25: Cooling cascade after pumping OH_{trans}, $N=O_{trans}$, and HON_{trans}. Energy levels are drawn to scale; the energies of the overtones of the cooling mode ν_5 (ONO bending) are taken from Ref. [29].

The fact that different frequency spacings are observed for the cooling cascade when different vibrational modes are used as spectator mode (-8 cm^{-1} for OH_{trans}, -0.5 cm^{-1} for $N=O_{trans}$, and -7 cm^{-1} for HON_{trans}) evidences that this spectral feature is not a phonon side band along the lines of Ref. [93].

- Second, we could add several additional values to the list of experimental anharmonic constants (Tab. 3.4), which might serve as a benchmark for high-level quantum chemistry calculations along the lines of Ref. [29]. Where experimental gas-phase values are available [41, 42], we find small deviations on the order of a few wavenumbers, hinting to a matrix effect for these anharmonicities (just like the vibrational frequencies shift a bit in the matrix).

- Third, at early delay times, we can identify a mode-specific relaxation pathway (i.e. peaks $1_c2_c?^1$ and $1_c1_c?^2$ in Fig. 3.23b and c).

HONO is a small molecule sitting in a very well defined environment and may be described theoretically on the highest conceivable level. That is, high-level quantum chemistry potential energy surfaces are available and the fully coupled vibrational problem can be solved in all degrees of freedom of the molecule [20, 29], full-dimensional wavepacket calculations are conceivable [21,30,31], and the effect of the matrix can be added on the level of mixed-quantum-classical calculations [50]. At the same time, it is a reactive system, and the competition between IVR and the IR-driven photo-isomerization determines to a large extent the outcome of the reaction [45]. IVR is mode specific in HONO, e.g. the molecule cools through one particular mode probably because that mode interacts the least with the environment. The system might prove to be an ideal playground for further theoretical studies, emphasizing more the condensed phase character of the reaction than previous studies, which would give unprecedented insights into condensed phase reactions and possibly its manipulation.

Acknowledgements: The work has been supported by the Swiss National Science Foundation (SNF) under grant 200020-115877.

3.5 Rotational dynamics of nitrous acid (HONO) in Kr matrix

Virgiliu Botan, Peter Hamm

J. Chem. Phys., 129, 044507, (**2008**)

Abstract

With the help of ultrafast time-resolved infrared spectroscopy, we investigate rotational diffusion of *cis* and *trans* nitrous acid (HONO) in solid Kr at 30 K, as well as its reorientation upon the IR-driven *cis*→*trans* isomerization. We find different mobility for the two isomers: *cis*-HONO is pinned to the matrix with no decay of the anisotropy on the 100 ns timescale, whereas *trans*-HONO rotates around its long-axis, reducing its anisotropy partially on that timescale. The long-axis itself, defined by the terminal oxygen and hydrogen atoms of HONO, stays fixed on even a minute timescale. Accompanying molecular dynamics (MD) simulations reproduce the anisotropic rotational diffusion of *trans*-HONO correctly, albeit on a completely wrong timescale, whereas they would predict complete reorientation of *cis*-HONO within ≈10 ps, in harsh disagreement with the experiment. We attribute the mismatch of orientational timescales to either too soft interaction potentials, or to the fact that HONO occupies an interstitial rather than a mono-substitutional matrix site. The experiments furthermore show that the direction of the OH bond hardly changes during the IR-driven *cis*→*trans* isomerization, in contrast to the intuitive picture that it is mostly the light hydrogen which moves. Rather, it is the two central nitrogen and oxygen atoms that move during isomerization in a hula hoop fashion, whereas the terminal atoms are still pinned to the matrix cage.

3.5.1 Introduction

The matrix isolation technique has proven to be a very powerful tool to analyze a large variety of chemical processes and compounds. Whittle and Pimentel proposed this technique in a seminal paper in the fifties [8], leading to the characterization and discovery of a large class of chemical compounds in the following decades, among which are radicals and reactive intermediates (see e.g. Ref. [94]) as well as chemical compounds with noble elements [10, 11, 95]. The molecules are isolated in a nonreactive solid, in most cases rare gases (Xe, Kr, Ar, Ne) but sometimes also N_2, CH_4. Very little is known about the orientational dynamics of molecules inside rare gas matrices and analyzing this dynamics is the purpose of the present study. Small molecules (H_2O, HCl, CN, NH_3) may rotate essentially freely in certain rare gas matrices [96, 97], as seen from rovibrational side-bands in the IR spectrum. However, somewhat larger molecules of the size of, for example, CH_3, rotate in a thermally activated, diffusive manner, a process that has been studied by electron paramagnetic resonance (EPR) [98–100] as well as by IR hole burning [101, 102]. Another technique that looks directly at diffusive rotational dynamics is polarization-resolved optical pump-probe spectroscopy. For instance, in order to study the depolarization in the process of bond breaking and bond forming, Bargheer et al. [51] used laser induced fluorescence (LIF) for two different molecules in qualitatively different surroundings: ClF in Ar and I_2 in Kr. The two systems revealed completely different results: ClF undergoes a complete depolarization on a 1.2 ps timescale, whereas the I_2 shows no depolarization whatsoever. The authors attributed this difference to the different symmetries of the immediate surroundings of the molecules. It has been suggested that ClF sits in a mono-substitutional site, i.e. an essentially isotropic surrounding, and thus it is free to rotate whereas I_2 sits in a double substitutional site, i.e. in a cylindrical cage, hence being sterically fixed [51]. Thus, polarization measurements may serve as decisive probes of the immediate surrounding of the molecules embedded in rare gas solids.

In a series of papers [43, 44, 50], we have investigated the IR-driven *cis-trans* isomerization of nitrous acid (HONO) as well as the accompanying intramolecular vibrational redistribution (IVR) processes. Apart from being an important source of OH radicals in atmospheric chemistry [35, 79, 80], HONO has been studied intensively both theoretically [20–32] and experimentally [15–19] because of its IR-driven isomerization reaction. Upon IR excitation of the OH stretch vibration, the molecule isomerizes in the *cis*→*trans* direction with almost unity quantum yield [16, 19], whereas the back yield is significantly smaller. Neither experimental [33] nor theoretical [21, 30] studies could find the reaction taking place in the gas phase, hence, isomerization seems to be facilitated by the dissipative forces of the matrix environment. The high quantum yield of close-to-one is remarkable given the fact that the mode being excited (the OH stretch vibration) is not the reaction coordinate (HON torsion). A recent mixed quantum-classical simulation [50], treating the three degrees of freedom of the hydrogen as quantum and the remainder as classical, revealed good qualitative agreement with experimental results on a fast picosecond timescale, but also showed that energy dissipates relatively efficiently into all vibrational degrees of freedom of the molecule. Hence the reaction becomes statistical after a few 10's of picoseconds and the quantum yield of 100% is not understood.

In the present work we investigate the rotational diffusion of the two isomers of HONO in solid Kr in order to obtain information on the interaction forces of HONO with its matrix surrounding. The work is corroborated by classical MD simulations, using the same pair potentials as the mixed quantum-classical simulation in Ref. [50]. The comparison between experiment and MD simulation suggests that these pair potentials are significantly too soft, which could either be intrinsic to the potentials, or hint to a different matrix site (i.e. an interstitial rather than a mono-substitutional site). We furthermore determine the reorientation of the ONO-body upon isomerization, suggesting that isomerization is accompanied by a hula hoop motion of the two central nitrogen and oxygen atoms, pinning the terminal atoms to the matrix cage.

3.5.2 Materials and Methods

Experimental

HONO was synthesized photochemically according to a procedure reported by Hall and Pimentel [16]. A gas mixture of 3:10:1000 HN_3:O_2:Kr was prepared in a glass container and sprayed on a calcium fluoride window kept in a cryostat (DE-202AF/DMX-20B, Advance Research Systems, Inc.) at very low pressure (10^{-7} mbar) and a temperature of approximately 30 K. The 3317 cm^{-1} absorption band of HN_3 was used to monitor the growth of the matrix. After deposition, the matrix was irradiated with UV light from a mercury lamp, initiating photolysis of hydrazoic acid which then reacts with oxygen to form HONO. The progress of this process was monitored by the depletion of the HN_3 absorption band.

For measuring the depolarization dynamics we use a femtosecond IR pump-probe setup. For the short time scans (0-600 ps) we used one amplified Ti:S system and a conventional delay stage to achieve the retardation between pump and probe pulse, whereas two synchronized Ti:S laser/amplifier were used to cover longer time delays up to 400 ns [40]. Each Ti:S laser/amplifier pumped one optical parametric amplifier (OPA) to generate tunable IR pulses centered at 3470 cm^{-1}, roughly 100 fs long and with a bandwidth of $\approx$300 cm^{-1} FWHM [63]. In one experiment the wavelength of one IR-OPA was tuned in order to probe the N=O stretch region. Pump and probe beams are focused to spot sizes of 150 μm and 100 μm, respectively, with a pump energy of 1.2 μJ). The repetition rate of the laser system was 1 kHz and every second pump pulse was chopped for referencing. The probe pulse was spectrally dispersed in a 190 mm spectrometer and then detected by a 63 channel HgCdTe (MCT) detector array, covering a spectral range from 3370 to 3580 cm^{-1} with a resolution of 3.3 cm^{-1}. To enable selective excitation of the *cis* species we used a piezo-controlled adjustable Fabry-Perot filter with a bandwidth of $\approx$15-20 cm^{-1}. The polarization of the pump-beam was adjusted with the help of a computer-controlled λ/2-waveplate.

In our previous works [43, 44], in order not to deplete the sample, we had alternatively pumped the *cis* and *trans* OH stretch bands (OH_{cis} and OH_{trans}) in a cyclic manner, following a scheme which took into account the different isomerization yields. This procedure was very time consuming. We now apply a cw diode laser (Nanoplus GmbH, Germany) with the wavelength slightly tunable around 3550 cm^{-1} (OH_{trans} in solid Kr) to constantly irradiate the sample volume, thus keeping the photo-equilibrium at an excess of the *cis* isomer. The linewidth of this laser is $\approx$1.5 cm^{-1}. We aligned its center wavelength for maximum signal, and thus excited both the dominant site bands simultaneously (see inset of Fig. 3.26a). In this way we can follow the *cis*→*trans* isomerization using a narrow band pump pulse tuned to OH_{cis}, shortening the measurement time by almost one order of magnitude. The reverse *trans*→*cis* reaction is studied by broad band pumping both isomers with the IR pulse directly from the IR OPA without filtering in the Fabry-Perot filter (and without the cw laser). As the *cis*→*trans* quantum yield is significantly larger, the photo-equilibrium then will be mostly on the *trans* side, and the small *cis*-pumped contribution can be subtracted out using the previous experiment.

On a longer second to minute timescale, the anisotropy was measured in a Fourier transformed infrared (FTIR) spectrometer. The sample was excited with the cw diode-laser mentioned above, which was coupled into the FTIR spectrometer with a flipping mirror collinear to the FTIR spectrometer beam. A rotating wire-grid polarizer was placed in front of the sample allowing collection of absorption spectra with a polarization parallel and perpendicular to the excitation beam. As in the case of the time resolved measurements, difference spectra were collected, subtracting out the non-excited molecules.

Computational

The experiments where accompanied by all-classical molecular dynamics (MD) simulations, using the classical part of an in-house code described in Ref. [50]. In brief, a MD box was set up consisting of $9 \times 9 \times 9$ unit cells of a *fcc* lattice in a cubic box with periodic boundary conditions, each containing four Kr atoms with a Kr-Kr nearest neighbor distance of 3.934 Å. If not noted otherwise, HONO was placed in a mono-substitutional site, i.e. removed the central Kr atom and replaced it by either *cis*- or *trans*-HONO in its gas phase structure [32] with its position inside the cage energy-minimized. Random velocities were assigned to all atoms, resulting in a temperature equal to that in the experiment ($\approx$30 K) after equilibration in a NVE simulation. No quantum-corrections, such as an increased effective temperature to account for zero-point energy, have been added. A cut-off of 12 Å was applied for the Lennard-Jones interactions. The equations of motion were integrated using a leap-frog scheme with time step 2 fs. HONO was modelled as a rigid body (all internal degrees of freedom frozen), using quaternions to represent its orientations [103, 104].

The interaction of HONO with the matrix cage, as well as that of the Kr atoms among each other, was modelled using Lennard Jones pair potentials:

$$V_{ij} = \varepsilon_{ij} \left[\left(r_{ij}^{(eq)} / r_{ij} \right)^{12} - 2 \left(r_{ij}^{(eq)} / r_{ij} \right)^{6} \right] \qquad (3.16)$$

using the usual combination rules $r_{ij}^{(eq)} = r_i^{(eq)} + r_j^{(eq)}$ and $\varepsilon_{ij} = \sqrt{\varepsilon_i \varepsilon_j}$. The Lennard Jones parameters were

	Kr	O	N	H
ε [cm^{-1}]	140.3	19.1	15.4	1.64
$r^{(eq)}$ [Å]	2.003	1.368	1.561	1.621

Table 3.5: Lennard Jones parameters used in the MD simulation [22, 43, 68]

deduced from Ref. [68], in analogy to the way how the corresponding Xe-parameters have been extracted in Ref. [22], and are listed in Tab. 3.5.

The orientations of the transition dipoles relative to the molecular frame have been estimated from a gas-phase quantum-chemistry calculation on the QCISD/cc-pVDZ level of theory, using the Gaussian98 program suite [52].

3.5.3 Experimental Results

Background: Pump-Probe Spectroscopy of HONO

To set the stage, Fig. 3.26A shows an absorption spectrum of HONO in solid Kr in the OH stretch region. The bands at ≈3400 cm^{-1} and ≈3550 cm^{-1} correspond to the *cis* and *trans* isomers, respectively. Both bands exhibit some substructure due to matrix inhomogeneities (Fig. 3.26A, inset). Fig. 3.26B shows typical transient pump-probe difference spectra at 2 ns delay time. The black line depicts the response after selective excitation of OH_{cis}, whereas the gray line presents the response after broad-band pumping. In the second case, both *cis*→*trans* and *trans*→*cis* reactions happen at the same time, however, since the *cis*→*trans* quantum yield is significantly larger, the photo-equilibrium will mostly be on the *trans* side. In such transient difference spectra, negative signals originate from bleaching species (stimulated emission, also leading to negative signals, has decayed after 2 ns [43]), and positive signals from photo-products. For example, when pumping OH_{cis} (Fig. 3.26B, black line), we see a bleach at the wavelength of OH_{cis} and a broader positive band around 3525-3550 cm^{-1} originating from molecules that have isomerized to *trans*-HONO. The latter spectrum does not yet agree with OH_{trans} in Fig. 3.26A because the molecules are still hot 2 ns after excitation and the signal is red shifted due to intramolecular anharmonicity [44].

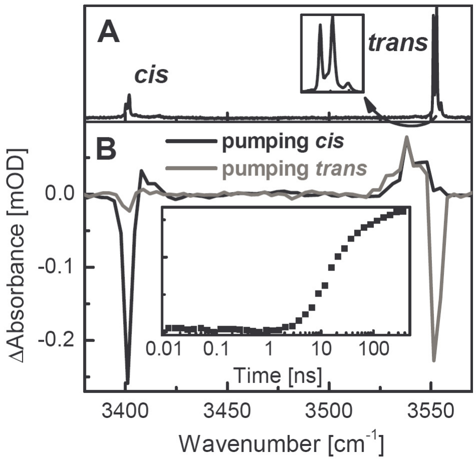

Figure 3.26: (A) FTIR spectrum of HONO in the OH stretch region. The inset enlarges OH_{trans}. (B) Transient absorption spectra 2 ns after selectively pumping either OH_{cis} (black) or broad-band pumping both isomers (gray). Inset: Kinetics at 3550 cm^{-1} after pumping OH_{cis}, reporting on the formation of cold *trans*-HONO.

Rotational Diffusion

In a first step, we study orientational diffusion of both *cis* and *trans* HONO. To this end, we pump the OH-stretch band of either isomer and measure the anisotropy of the negative bleach and stimulated emission signals of the pumped species, both appearing at the same frequency, i.e. the frequency of the initially pumped transition. The anisotropy of the bleach signal originates from HONO molecules that have not been pumped, hence it is not affected by absorbing any photon. The stimulated emission contribution, of course, originates from molecules that have absorbed a photon, but as long as they show stimulated emission they have not dissipated the photon energy. Hence the molecules and their surrounding are still cold and we assume that the orientational dynamics during that time is essentially the same as in equilibrium. After delay times longer than ≈ 2 ns, on the other hand, recovery of the excited molecules back to the ground state may locally heat the matrix cage and as such potentially affect orientational diffusion times (we will see that this is not happening).

Fig. 3.27B shows the anisotropy decay of OH_{cis}, defined as:

$$r = \frac{I_\parallel - I_\perp}{I_\parallel + 2I_\perp} \tag{3.17}$$

which was calculated from the bleach/stimulated emission signals shown in Fig. 3.27A with parallel and perpendicular polarizations of pump- and probe pulses. The anisotropy stays essentially constant at around $r = 0.3$ during the entire time window from 1 ps to 100 ns. It does not start from the theoretical value $r = 0.4$, which is the value expected from orientational averaging in an isotropic sample [105]. We attribute this discrepancy to either the fact that the molecules can rotate freely in a small restricted cone on a subpicosecond timescale and/or the fact that the sample is not perfectly homogeneous and isotropic. When estimating the anisotropy decay time constant due to free motion governed by the inertia moment $I_{\mathrm{HONO}} = 9.6 \times 10^{-47}$ kgm^2 we get $t = \sqrt{I/k_BT} \approx 0.5$ ps [106]. This would, in principle, be within our instrumental response function, however, is hidden underneath strong nonlinear optical Kerr signal originating from the CaF_2 windows that is present when pump and probe pulses still overlap partially in time (we therefore disregard the data before 1 ps). Nevertheless, this initial drop in anisotropy is small and the molecule exhibits no further rotation up to 100 ns. The anisotropy measured in two different scans (black and gray squares) behave qualitatively identically, albeit with a small offset. We attribute this offset to the fact that the two measurements have been performed in different matrices. Rare gas matrices are usually poly-crystalline and because the focus of the probe beam is small ($\approx 100\,\mu$m), the region of the matrix sampled by the probe beam might not be entirely isotropic.

Fig. 3.28 shows the anisotropy decay of OH_{trans}, using broad-band excitation. In this configuration we excite both isomers at the same time but we will argue (*vide infra*) that this experiment is essentially a *trans*-pump *trans*-probe experiment. Inherently, the photoequilibrium under broad band radiation strongly favors the *trans* isomer with ratios that vary from 3 to ≈7, depending on temperature [44]. Moreover, the molecules that isomerize from *cis* to *trans*-HONO are hot up to a few nanosecond timescale, and as a consequence they are red shifted from the OH_{trans} bleach/stimulated emission frequency and do not interfere with this signal. To illustrate this effect, we plot in Fig. 3.26B, inset, the response after pumping OH_{cis} and probing at the frequency of cold *trans*-HONO. The signal stays essentially zero up to a few nanoseconds, although isomerization has already occurred. On longer timescale, the OH_{trans} pumped signal can be singled out by subtracting the properly scaled OH_{cis}-pumped response (where the scaling factor is deduced from the small bleach of OH_{cis}).

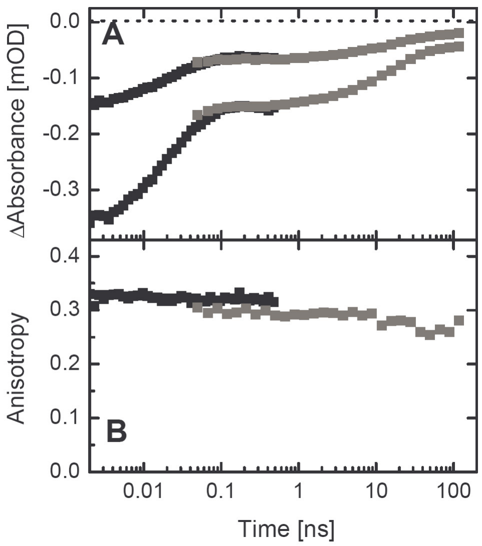

Figure 3.27: (A) Stimulated emission and bleach response when pumping and probing OH_{cis} with the polarizations of pump and probe pulse being parallel (lower) and perpendicular (upper). Black and gray squares are the results from a short delay time and a long-delay time scan, respectively (see Materials and Methods). (B) Anisotropy r deduced from (A)

The rotational dynamics of *trans*-HONO (Fig, 3.28B) is qualitatively different from that of *cis*-HONO. The anisotropy again starts with a value $r = 0.38$ slightly below the theoretical value 0.4, but, in contrast to *cis*-HONO, then decays to $r \approx 0.2$ in a highly non-exponential manner stretching from 1 ps to 100 ns. On an even longer second to minute timescale, this value $r \approx 0.2$ stays constant (Fig. 3.28B, black circles).

Computational Results

Fig. 3.29 shows the anisotropy decay deduced from a classical MD simulation, using the Lennard Jones parameters listed in Tab. 3.5 and assuming that HONO occupies a mono-substitutional matrix site. The anisotropy is calculated from the common expres-

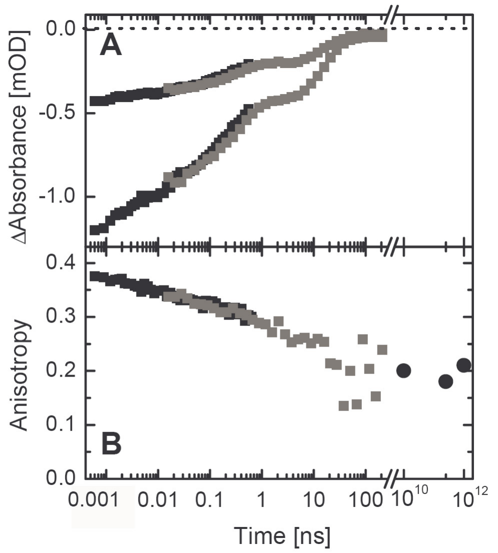

Figure 3.28: (A) Stimulated emission and bleach response when pumping and probing OH_{trans} with the polarizations of pump and probe pulse being parallel (lower) and perpendicular (upper). Black and gray squares are the results from a short delay time and a long delay times scan, respectively (see Material and Methods). The small contribution from the *cis*→*trans* reaction has been subtracted out from these data (see text for details) (B) Anisotropy deduced from (A). The black circles depict the anisotropy results measured in a FTIR spectrometer on a second to minute timescale.

sion [105]:

$$\begin{aligned} r(t) &= \frac{2}{5}\langle P_2(\overrightarrow{\mu}(0)\overrightarrow{\mu}(t))\rangle \\ &= \frac{1}{5}\left(3\langle(\vec{\mu}(t)\vec{\mu}(0))^2\rangle - 1\right) \end{aligned} \tag{3.18}$$

where P_2 denotes the second Legendre polynomial, $\vec{\mu}(t)$ a unit vector parallel to the OH bond (in this particular case), and $\langle ... \rangle$ an average over a 5 ns long equilibrium trajectory. While the overall timescale is wrong by many orders of magnitude, the MD simulation does reveal a qualitative difference between *cis* and *trans*-HONO: The anisotropy of *cis*-HONO decays essentially mono-exponentially like a spherical top (not seen in the experiment on a 100 ns timescale), while *trans*-HONO decays only partially with a long-time pedestal, just like in the experiment (Fig. 3.28). Analyzing the trajectories reveals that the fast initial component in the anisotropy decay of *trans*-HONO reflects the rotation of the molecule around its long-axis, whereas the long-axis itself does not rotate on the timescale of the MD trajectory (5 ns). In order to determine the nature of the long-axis, we integrate the angle $(\vec{\mu}(0)\vec{\mu}(t))$ in Eq. 3.18 over a cone with opening 2θ:

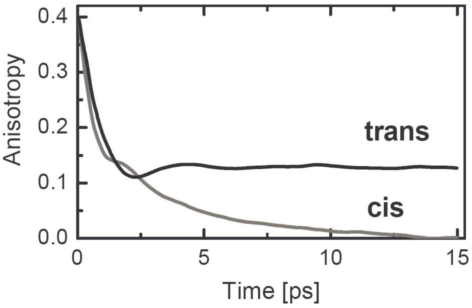

Figure 3.29: Anisotropy decay calculated from the MD simulation of *cis* (gray) and *trans* (black) HONO, using the Lennard Jones interaction potentials listed in Tab. 3.5, and assuming HONO occupies a mono-substitutional site.

$$r(\infty) = \frac{1}{40}\left(3\cos 2\theta + 1\right)^2 \tag{3.19}$$

This is the anisotropy pedestal expected at long delay times when the molecule has equilibrated completely around the long-axis, but when we assume the long-axis itself remains fixed. We find in the MD simulation $r(\infty) \approx 0.13$, corresponding to an angle $\theta = 32^\circ$, which agrees perfectly with the angle between the OH bond and a vector connecting the terminal hydrogen and oxygen atoms. Hence, the two ends of the molecule are tightly fixed by the matrix cage during this rotation, whereas the in-between N-O group rotates in a bicycle manner.

The long-time pedestal we observe experimentally, $r(\infty) \approx 0.2$, is somewhat larger, which is explained by the fact that the OH_{trans} transition dipole, which is our experimental observable, is slightly tilted with respect to the OH bond (Fig. 3.30A). From Eq. 3.19, we can estimate an angle of $\theta = 24^\circ$ for the angle between the OH_{trans} transition dipole and rotation axis ($r(\infty)$ was up-scaled in order to account for the fact that the initial anisotropy $r(0)$ does not start from the theoretical value 0.4), or 8° for the angle between the OH_{trans} transition dipole and the OH bond. The latter value agrees reasonably well with the result of 22° obtained from a gas-phase QCISD/cc-pVDZ quantum-chemistry calculation [52]. The discrepancy between both values might be explained by a matrix effect. For instance, the ab-

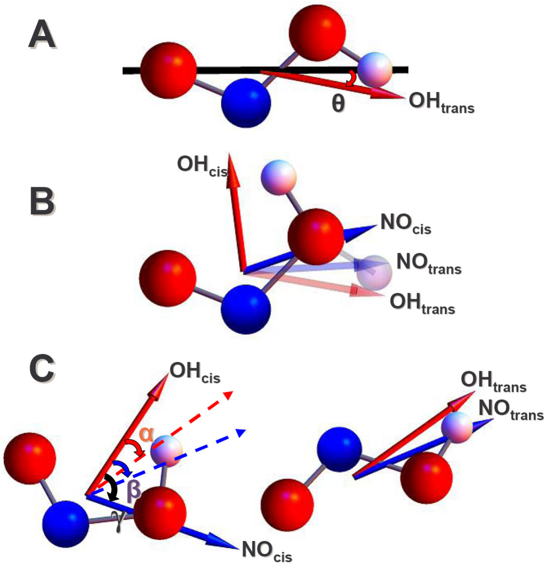

Figure 3.30: Molecular structure in relation to the directions of the transition dipoles investigated in the experiments. The transition dipoles were determined from a gas-phase QCISD/cc-pVDZ quantum-chemistry calculation [52]. (A) Angle θ between the OH$_{trans}$ transition dipole and the long-axis of *trans*-HONO around which the molecule diffuses. (B) Directions of the OH and N=O transition dipoles in *cis*-HONO and *trans*-HONO, respectively, assuming that the ONO-body does not move during isomerization. The fade colors depict *trans*-HONO. (C) The same as (B), however, allowing the ONO-body to rotate, revealing angles α and β that are conform (within error) with the experimental results. The dashed lines in the left panel represent the corresponding vectors from the right panel.

sorption frequencies of OH$_{cis}$ and OH$_{trans}$ are shifted by 25 cm^{-1} and 38 cm^{-1}, respectively, from the gas phase values [32], and we might just as well expect an effect on the direction of the transition dipoles.

3.5.4 Rotation upon Isomerization

In a second step, we investigate the rotation of the molecule during its IR-driven *cis*→*trans* isomerization. To this end, we excite OH$_{cis}$ and measure the anisotropy of *trans*-HONO photo-product bands. The angle α between both transitions can then be evaluated by using an expression equivalent to Eq. 3.18, but now interpreting $\vec{\mu}(0)$ as the direction of the pumped transition dipole, and $\vec{\mu}(t)$ as the direction of the probed transition dipole:

$$r = \frac{1}{5}\left(3\cos^2\alpha - 1\right) \tag{3.20}$$

This expression ignores the possibility that *trans*-HONO undergoes orientational diffusion around the long-axis after the photo-isomerization has occurred. In order to obtain redundant information and thereby making the result more robust against errors, we measured the relative angle of two transition dipoles: The angle α between the OH$_{cis}$ and OH$_{trans}$ transition dipoles and the angle β between the OH$_{cis}$ and N=O$_{trans}$ transition dipoles (see Fig. 3.30C).

Fig. 3.31A presents transient spectra 300 ns after pumping OH$_{cis}$ (after isomerization and cooling is complete) and probing in the OH stretch region. From the integrated band intensities, we find for the anisotropy of the OH$_{cis}$ bleach $r \approx 0.3$, equivalent to Fig. 3.27. The anisotropy of OH$_{trans}$ is r=0.18. We have seen in Fig. 3.27 that *cis*-HONO does not rotate, but it may rotate around the long-axis once it has isomerized to *trans*-HONO, reducing the long-time anisotropy to $r = 0.2$ (Fig. 3.28). The fact that both anisotropies – pumping OH$_{cis}$ and probing OH$_{trans}$ (Fig. 3.31A) versus pumping OH$_{trans}$ and probing OH$_{trans}$ (Fig. 3.28) – are essentially the same leads to the conclusion that the angle α between OH$_{cis}$ and OH$_{trans}$ transition dipoles is small.

A second, independent angle is measured when probing in the N=O spectral region (Fig. 3.31B). The response around 1630 cm^{-1} originates from N=O$_{cis}$ with a negative anisotropy $r = -0.12$, which is related to an angle between the OH$_{cis}$ and N=O$_{cis}$ transition dipoles of $\gamma = 69°$ (Fig. 3.30C). This result agrees well with the corresponding value obtained from a QCISD/cc-pVDZ quantum-chemistry calculation, $\gamma = 76°$ [52]. The anisotropy does not change over time, in agreement with our conclusion from Fig. 3.27 that *cis*-HONO does not rotate in equilibrium. The response around 1680 cm^{-1}, on the other hand, originates from the N=O$_{trans}$ of the *trans* photo-product with an anisotropy of $r = 0.14$, related to an angle $\beta = 41°$.

With these two angles, $\alpha \approx 0°$ and $\beta = 41°$ (or, $180° - \alpha \approx 180°$ and/or $180° - \beta = 139°$), one can try to determine the orientation of the *trans* photo-product relative to the reactant *cis*-HONO (three angles would in principle be needed to uniquely determine the orientation, if rotation occurs in all three dimensions). However it turns out that there is no solution for the particular values of the two angles. The uncertainty originating

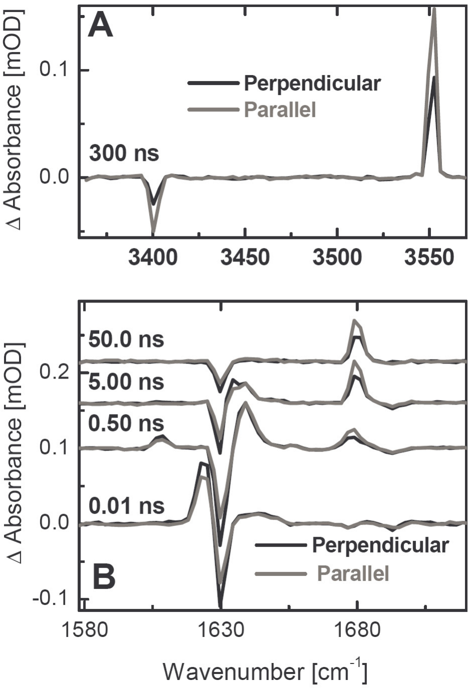

Figure 3.31: Absorption changes for parallel (gray) and perpendicular (black) polarizations of pump-and probe pulses, pumping OH_{cis} and probing either (A) the OH stretch and (B) the N=O stretch spectral regions.

from experimental noise, the quantum-chemistry calculation, the crystal which is not perfectly isotropic, the unresolved free rotation in a small restricted cone on a sub-picosecond timescale, as well as the complication of rotation around the long-axis in the *trans*-state results in an overall, mostly systematic error whose size is difficult to assess.

We can nevertheless exclude the situation which one might consider the most intuitive one: Fig. 3.30B depicts the transition dipoles assuming that the ONO-body is not moving during the isomerization, i.e. assuming that isomerization is essentially a motion of the lightest atom, the hydrogen. In this case, we would predict an angle between OH_{cis} and OH_{trans} transition dipoles, $\alpha = 113°$, which would result in a negative anisotropy $r = -0.11$, clearly outside the combined error. We know from Fig. 3.28b that the molecule is rotating around the long axis, once it is isomerized to the *trans* configurations. If we take this additional effect into account by integrating Eq. 3.20 over a cone whose axis is tilted by α, we would expect an anisotropy that is reduced to $r = -0.08$, still not in agreement with the experimental results. Any further random rotation, e.g. due to local heating, would reduce the anisotropy even further to $r = 0$, but never flip the sign. In Ref. [43], we had energy-minimized the molecule in a mono-substitutional site in both the *cis* and the *trans* configurations (Fig. 6 of Ref. [43]), revealing a small 2° rotation angle of the ONO-body, which however would go into the direction to render the anisotropy again more negative.

Fig. 3.30C, on the other hand, depicts a possible solution of the problem, minimizing the deviations from the measured angles α and β and at the same time taking into account that the angle β is probably better determined than α. The former is less affected by the rotation around the long-axis in the *trans* state, since the $N{=}O_{trans}$ transition dipole is essentially parallel to that axis. In Fig. 3.30C, the OH_{cis} and OH_{trans} transition dipoles are essentially parallel, responsible for the observed large positive anisotropy. As a result, the vectors connecting the terminal oxygen and hydrogen atoms are close to parallel as well. This would suggest, very surprisingly and counter-intuitively, that isomerization is happening for the central N-O atoms in a space-saving, hula hoop fashion, while HONO is pinned to the Kr cage by the terminal atoms, just like during rotational diffusion of the *trans*-isomer.

3.5.5 Discussion and Conclusion

We have studied the orientational diffusion of *cis* and *trans* HONO in solid Kr as well as its reorientation during the IR-driven *cis*→*trans* isomerization. In the first case, we cannot identify any rotation of *cis*-HONO on the 100 ns timescale (apart from a small unresolved drop of the anisotropy on a sub-picosecond timescale, see Fig. 3.27). It is interesting to note that even local heating of the matrix cage after recovery of the ground state, occurring after $\gtrsim 2$ ns, does not lead to any significant drop of anisotropy, i.e. does not accelerate rotational diffusion. Furthermore, the constant anisotropy argues against energy migration as a result of resonant inter-molecular vibrational energy transfer, as it has been suggested in the past [17]. Such a process would transfer energy to molecules with random orientations, and as such reduce the anisotropy, an effect whose concentration dependence has been studied in detail for example for HOD dissolved in H_2O [107].

The response of *trans*-HONO, on the other hand, is considerably more complex: Its anisotropy decays partially in a highly non-exponential manner, stretching from 1 ps to 100 ns, but then stays constant on a second to minute timescale (Fig. 3.28). Guided by accompanying MD simulations, we attribute this partial decay to a rotation around the long-axis of the molecule, whereas the terminal oxygen and hydrogen atoms are tightly fixed to the matrix cage, hindering the rotation of the long-axis itself. The non-exponentiality of the initial decay might be related to matrix inhomogeneities. Fig. 3.26A, inset, enlarges the absorption spectrum of OH_{trans}, revealing a substructure composed of two dominant peaks and a weaker one. It is believed that this substructure corresponds to different matrix sites and there have been assignments that range from interstitial [22] to mono- and double-substitutional [19]. The interaction forces between HONO and the matrix cage will be very different in these sites, and so will be the orientational diffusion times (due to the 3.3 cm^{-1} spectral resolution in our pump-probe setup we cannot address the sub-bands independently). One must furthermore keep in mind that a significant amount of O_2 and N_2 is present in the matrix as a result of the procedure we chose to synthesize HONO (see Materials and Methods). Both are spectroscopically dark but possibly responsible for additional matrix inhomogeneities [82].

Albeit the good qualitative agreement between MD simulation and experiment, what the partial decay of the anisotropy of *trans*-HONO is concerned, the overall timescales are completely wrong. Two possible reasons for this discrepancy come into ones mind:

- The Lennard Jones parameters (Tab. 3.5) may severely underestimate the interaction forces between HONO and the Kr cage. In fact, these Lennard Jones parameters, which were adapted from Ref. [68], can be traced back to a quantum-chemistry calculation from the year 1982 [108], and clearly there are more advanced methods available today. Furthermore, the Lennard Jones model *per se* might be inadequate in this case, since it ignores the possibility of anisotropic interactions as well as the polarizibility of the Kr atom interacting with the charges of HONO.

- HONO may occupy an interstitial rather than a mono-substitutional matrix site, in which case it would be fixed more tightly. Although this possibility may seem rather unlikely, since the in situ synthesis from an HN_3 + O_2 complex must have taken place in an even larger site, we discuss this scenario as well. Using the same Lennard Jones parameters as before, the MD simulation indeed reveals a significantly slower orientational diffusion time for an interstitial site. We saw only one rotational flip for *cis*-HONO and none for *trans*-HONO on a 70 ns timescale, hence, orientational diffusion is now too slow (the 'statistics' of one flip is, of course, insufficient to draw conclusions about the difference between *cis* and *trans*-HONO). We furthermore tried the two possible interstitial sites in a *fcc*-lattice, the octahedral O_h (6 nearest neighbors) and the tetrahedral T_d (4 nearest neighbors) site, as an initial condition for the MD simulation, however HONO disturbs the local structure of the matrix cage to an extent that the difference between these two sites is no longer apparent. If the non-exponential decay of the anisotropy of *trans*-HONO (Fig. 3.28) indeed reflects a distribution of mono-substitutional and interstitial sites, then the spread of rates predicted from the MD simulation is too large.

In a second set of experiments, we studied the rotation of HONO during its IR-driven *cis*→*trans* photoisomerization. Probing two vibrational bands of the *trans* photo-product, we could determine two independent angles (α and β), which are totally inconsistent with a picture in which essentially the hydrogen is isomerizing whereas the ONO-body stays fixed in the matrix cage (Fig. 3.30B). On the other hand, if we assume that isomerization is accompanied by a hula hoop motion of the two center atoms, pinning the terminal oxygen and hydrogen atoms to the matrix cage (Fig. 3.30C), we obtain angles α and β that are consistent with experiment within error. Any matrix site, interstitial or mono-substitutional, imposes less constraints to the center of the molecule than to the terminal atoms, explaining why these atoms are more free to move. According to the best potential energy surface available, the barrier against isomerization is higher than the energy put into the molecule by the IR photon [29]. It is very hard to imagine that the two central heavy atoms are tunneling through this barrier. However, from an intramolecular point of view, it is probably still be the proton which is tunneling, just that this process is coupled to a rotational motion of the molecule as a whole. In Ref. [50], we had modelled the isomerization reaction of HONO in a mixed-quantum-classical simulation, treating the motion of the hydrogen as quantum, whereas the ONO-body was assumed to be rigid. Fig. 3.30C seems to suggest that this is insufficient, and that one would have to extent the quantum part of the simulation to all degrees of freedom of the molecule i.e. all six intramolecular (internal) degrees of freedom as well as at least the three rotational (external) degrees of freedom.

Similar conclusions have been drawn for the isomerization of the retinal chromophore in rhodopsin [109, 110], responsible for the initial step during the process of vision. In this case, the chromophore is tightly fixed to the protein, and the 11-*cis* to all-*trans* isomerization occurs in a space-saving manner with only minor motion of the involved atoms, leaving the *trans* photoproduct in a highly distorted, twisted structure. However, in contrast to the present case, nuclear motion is typically considered classical in molecular systems like rhodopsin.

In conclusion, the measurement of orientational dynamics provides a framework for a very decisive discrimination of various matrix sites as well as for the mechanism of isomerization. This, however, requires more reliable models for the matrix-solute interaction forces which are within reach of modern quantum chemistry methods.

Acknowledgements: We thank Nikolaus Schwentner for instructive discussions. The work has been supported by the Swiss National Science Foundation (SNF) under grant 200020-115877.

3.6 Energy Transport in Peptide Helices

Virgiliu Botan, Ellen H. G. Backus, Rolf Pfister, Alessandro Moretto, Marco Crisma, Claudio Toniolo, Phuong H. Nguyen, Gerhard Stock, Peter Hamm

Proc. Natl. Acad. Sci., 104, 12749, (**2007**)

Abstract

Energy transport through an Aib-based 3_{10}-helix dissolved in chloroform is investigated in a combined experimental-theoretical approach. Vibrational energy is locally deposited at the N-terminus of the helix by ultrafast internal conversion of a covalently attached, electronically excited, azobenzene moiety. Heat flow through the helix is detected with subpicosecond time resolution by employing vibrational probes as local thermometers at various distances from the heat source. The experiment is supplemented by detailed non-equilibrium molecular dynamics (MD) simulations of the process, revealing good qualitative agreement with experiment: Both theory and experiment exhibit an almost instantaneous temperature jump of the reporter units next to the heater which is attributed to the direct impact of the isomerizing azobenzene moiety. After this impact event, helix and azobenzene moiety appear to be thermally decoupled. The energy deposited in the helix thermalizes on a sub-picosecond timescale and propagates along the helix in a diffusive-like process, accompanied by a significant loss into the solvent. However, in terms of quantitative numbers, theory and experiment differ. In particular the MD simulation seems to overestimate the heat diffusion constant (2 $\text{Å}^2\text{ps}^{-1}$ from the experiment) by a factor of five.

3.6.1 Introduction

Proteins are molecular machines that need to transport energy in order to work and function. Mainly, this occurs in two forms: Propagation of conformational changes and removal of excess heat. For example, consider a folding protein which undergoes a conformational transition to a state of lower energy. The transition may be facilitated, e.g., through a local conformational rearrangement (e.g., formation of a hydrogen bond) that in turn triggers further structural changes (e.g., via a zipping mechanism).

This propagation of conformational change is directly associated with a transport of energy along the protein backbone. To localize in the state of lower energy, the excess energy of the protein must be removed efficiently and rapidly. Excess heat must also be dissipated in the case of a chemical reaction, since proteins function in narrow temperature ranges. Another example in which both kinds of energy transport occur are photoproteins such as rhodopsins. On one hand, the energy of the photon is used to trigger a conformational rearrangement, but, on the other hand, the excess energy needs to be removed. Because the functionality of a protein is directly associated with its structure, one may expect that energy transfer mechanisms are also related to structural motifs such as α-helices or β-sheets, both of which are stabilized by hydrogen bonds. In particular, helices often span the whole protein, giving rise to the speculation that they actually channel vibrational energy through the biomacromolecule [54].

To study energy transport from the theoretical point of view, a commonly used approach tries to transfer the theory of heat diffusion of glasses onto the length scale of a protein [111–113]. Another very direct and intuitive approach is to run nonequilibrium molecular dynamics (MD) simulations, depositing energy into one vibrational mode and following its flow through the protein directly as a function of time [114–119]. On the experimental side, the study of energy and heat transport is well established for bulk systems (solids, glasses or liquids) [120]. For proteins, however, essentially nothing is known about heat diffusion from experiment. We are aware of only very few experimental studies [121–125], which all investigated the energy flow in heme proteins. However, it has been argued later that heat transport from the heme into the surrounding solvent water does not occur through the protein in this case, but through the propionate side chain of the heme molecule which connects it directly to the protein surface [117, 126]. In systems other than proteins, energy transport phenomena have been measured, for example, through bridged azulene-anthracene compounds [127], small molecules in solution [128] or through model membranes [129].

Employing a combination of peptide engineering, time-resolved infrared absorption spectroscopy, and nonequilibrium MD simulations, we set out to study energy transport specifically along peptide helices as one of the most important structural elements of proteins. To that end, we synthesized a molecule (Fig. 3.32a) that consists of a stable helix with a dye molecule attached covalently, the latter undergoing ultrafast internal conversion and thereby locally depositing energy.

In designing the helix, we were guided by the following considerations: Typical α-helices from C^{α}-trisubstituted α-aminoacids in solution are flexible, and need on the order of 20 amino acids to become marginally stable [130]. We therefore decided to use the C^{α}-tetrasubstituted α-amino acid Aib, which forms exceptionally stable 3_{10}-helices, even in a relatively short sequence of eight amino acids [56, 131, 132]. 3_{10}-Helices are less common, but are found in globular proteins [133]. Aib-based 3_{10}-helices dissolve in the apolar solvent chloroform, which minimizes potential loss of the heat flow into the surrounding solvent and moreover mimics the hydrophobic environment in the interior of a protein.

As heater, we chose azobenzene because it undergoes ultrafast internal conversion (*cis-trans* isomerization) on a 200 fs timescale [57]. The azobenzene moiety (PAZ) was introduced in the N^{α}-protecting group [134, 135] of the peptide chain, with electronic properties (i.e. UV-VIS spectra, isomerization yields and rates) that are essentially the same as that of unsubstituted azobenzene. In order to give an idea about the expected effects, one may assume a Boltzmann distribution of the photon energy ($\approx$3 eV) over all vibrational degrees of freedom of the azobenzene compound, in which case one would estimate a local temperature of 1150 K right after the photoreaction. That huge temperature gradient is then equilibrating either along the helix or into the solvent.

In order to follow the energy flow along the helix, we make use of the fact that vibrational bands shift in frequency upon heating of their surrounding. This effect has been studied in detail in Ref. [58], where it has been shown that vibrational modes can be used as local thermometers. In the present study, we employ the C=O groups of the peptide backbone as local thermometers. In order to obtain spatially localized and spectroscopi-

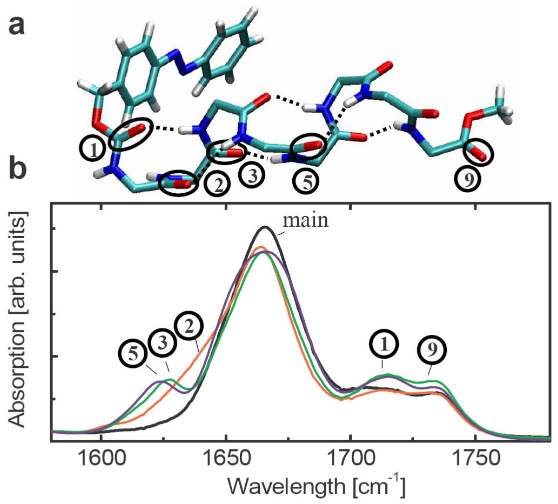

Figure 3.32: (a) X-ray structure of PAZ-Aib-Ala-(Aib)$_6$-OMe (molecule **A**, only the backbone is shown). The tags **1** to **9** refer to the corresponding absorption bands in (b) and count C=O groups with increasing distance from the azobenzene moiety. (b) FTIR absorption spectra of the ^{13}C-unlabelled reference molecule (PAZ-Aib-Ala-Aib$_6$-OMe, black line), and those of the ^{13}C-labelled peptides PAZ-Ala*-Aib$_7$-OMe (red), PAZ-Aib-Ala*-Aib$_6$-OMe (green) and PAZ-Aib$_3$-Ala*-Aib$_4$-OMe (blue).

cally separated vibrational transitions, we isotope-label these ^{13}C=O groups, frequency downshifting it by $\approx$ 30 cm^{-1} and thereby singling out one site from the remainder. Placing the isotope label at different positions in the helix, we can measure the local temperature at various distances from the heat source as a function of time. Since ^{13}C-Ala is more readily available commercially than ^{13}C-Aib, we used the former for isotope labelling. Disturbing the Aib$_8$ sequence by one residue (Ala), however, should not destabilize the 3_{10}-helix significantly [56, 132, 136] (see below).

The experimental studies are accompanied by extensive nonequilibrium MD simulations of the PAZ-Aib$_8$-OMe system in explicit solvent. After validation of the computational methods through the comparison to experiment, the simulations are able to draw a microscopic picture of the molecular processes underlying energy transport in peptides.

3.6.2 Structural Characterization

The terminally protected Aib$_8$ sequence is known to be folded in a fully developed 3_{10}-helical structure in chloroform solution [56]. In this work, we have examined the preferred conformation of the three host/guest octapeptides PAZ-Ala*-Aib$_7$-OMe, PAZ-Aib-Ala*-Aib$_6$-OMe and PAZ-Aib$_3$-Ala*-Aib$_4$-OMe. X-ray diffraction revealed for the crystal structure of PAZ-Aib-Ala-(Aib)$_6$-OMe two independent peptide molecules (**A** and **B**) in the asymmetric unit (see Fig. 3.32a and Fig. S1, Supporting Information). Both are regular 3_{10}-helices, stabilized by six consecutive, $i+3 \rightarrow i$ N-H...O=C intramolecular H-bonds. The two independent molecules differ by their helical screw sense, right-handed for molecule **A** and left-handed for molecule **B**, an uncommon, but not unique, observation for an Aib-based sequence with a single, internal, chiral residue [137].

In order to validate that the 3_{10}-helical structure is maintained in structure-supporting solvents (chloroform and 2,2,2-trifluoroethanol), FT-IR absorption , ^{1}H NMR, and CD techniques have been applied. The FT-IR absorption spectra in the N-H stretching region of all three peptides in CDCl$_3$ solution (Fig. S2) are similar, showing a weak band at about 3425 cm^{-1} (free N-H groups) [56] and a very intense band near 3325 cm^{-1} (hydrogen bonded N-H groups). As a change in peptide concentration (from 1.0 mM to 0.1 mM) does not significantly modify the spectra, the observed hydrogen bonding can be safely assigned to the intramolecular type. The ratios of the integrated intensity of the band of hydrogen bonded N-H groups to that of free N-H groups for the three peptides is in accordance with previously reported results for the 3_{10}-helical Aib$_8$ peptide [56].

The results of the ^{1}H NMR titrations in CDCl$_3$ solution upon addition of the hydrogen bonding acceptor solvent dimethylsulphoxide (Figs. S3-S5) clearly indicate that two NH protons for each octapeptide are exposed to the solvent, whereas the remaining six NH protons are solvent protected due to hydrogen bonding. One of these NH protons (that at highest field) is assigned to the N-terminal N(1)H proton by virtue of its urethane character [56]. In PAZ-Aib-Ala*-Aib$_6$-OMe the second solvent exposed NH proton is easily attributed to Ala* at position 2, on the basis of its different multiplicity. These ^{1}H NMR properties are those expected for peptides adopting a regular 3_{10}-helical structure [56].

As a typical example, the CD spectrum of PAZ-Aib-

Ala*-Aib$_6$-OMe in 2,2,2-trifluoroethanol solution is reported in Fig. S6. The positions of the two negative Cotton effects (205 nm, very strong, and 225 nm, weak) and the ratio of their intensities (0.25) are those expected for a 3_{10}-helix [138].

The potential destabilizing effect of a single Ala residue included in an Aib host peptide was also studied by comparing two 40 ns equilibrium MD simulations of PAZ-Aib$_8$-OMe and PAZ-Aib$_3$-Ala*-Aib$_4$-OMe. As an example, Fig. S7 shows the distribution of the number n_{HB} of intramolecular hydrogen bonds in the two cases. Although PAZ-Aib$_8$-OMe shows more conformations with the maximum number of possible intramolecular hydrogen bonds, $n_{\mathrm{HB}} = 6$, on average we find similar hydrogen bonding ($\langle n_{\mathrm{HB}} \rangle = 4.2$ and 3.6) for PAZ-Aib$_8$-OMe and PAZ-Aib$_3$-Ala*-Aib$_4$-OMe, respectively.

3.6.3 Experimental Results

Fig. 3.32b shows the stationary FTIR absorption spectrum in the C=O stretching region of the ^{13}C-unlabelled reference molecule (PAZ-Aib-Ala-Aib$_6$-OMe), together with those of the ^{13}C-labelled peptides PAZ-Ala*-Aib$_7$-OMe, PAZ-Aib-Ala*-Aib$_6$-OMe and PAZ-Aib$_3$-Ala*-Aib$_4$-OMe, respectively. The ^{13}C-unlabelled peptide shows three bands: the dominating 'main band' at 1665 cm^{-1} which is composed of all equivalent C=O groups in the helix, and two chemically different C=O groups which are split off from the main band, i.e., the urethane group at 1715 cm^{-1} (band **1**) which links the azobenzene moiety to the peptide helix, and the ester C=O band at 1734 cm^{-1} (band **9**) from the C-protecting group. The ^{13}C-labelled peptides PAZ-Aib-Ala*-Aib$_6$-OMe and PAZ-Aib$_3$-Ala*-Aib$_4$-OMe each exhibit one additional red-shifted band at about 1625 cm^{-1} (bands **3** and **5**, respectively), while the corresponding group in PAZ-Ala*-Aib$_7$-OMe reveals only a barely resolved shoulder (band **2**) on the low-frequency side of the main band.

Fig. 3.33a-c presents the UV-pump-IR-probe transients of the various samples at delay times from 300 fs to 1 ns. All vibrational modes do respond to the photoexcitation, albeit with different time dependencies. At the earliest delay time of 300 fs, band **1**, which is closest to the azobenzene moiety, responds with the largest signal. This signal decays relatively quickly (Fig. 3.34), whereas the main band leads to the dominating response 15 ps after excitation. The main band signal again decays partially until 100 ps (Fig. 3.34, inset) and then stays more or less constant till 1 ns. Its shape does not change very much during this time (compare 15 ps and 1 ns spectra in Fig. 3.33). The various labels (bands **2**, **3** and **5** in Fig. 3.33a-c, respectively) respond with relatively small, but distinctive, derivative-like signals of decreasing intensity as the distance from the heater is increased. Also band **9** (the ester C-protecting group) reveals a tiny derivative like response.

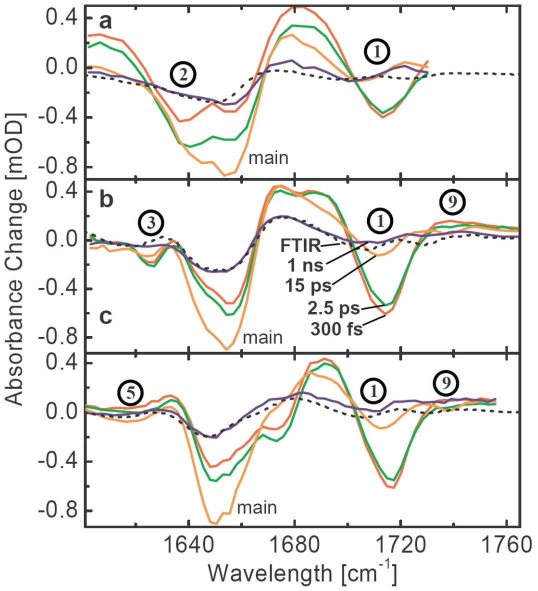

Figure 3.33: Pump-probe signals of (a) PAZ-Ala*-Aib$_7$-OMe, (b) PAZ-Aib-Ala*-Aib$_6$-OMe and (c) PAZ-Aib$_3$-Ala*-Aib$_4$-OMe at various delay times (300 fs: red, 2.5 ps: green, 15 ps: orange, and 1 ns: blue) after pump of the *cis*-azobenzene moiety with a femtosecond 425 nm pulse, compared to a stationary temperature induced difference spectra (black dotted) corresponding to a temperature jump of ≈0.5 K.

When *cis*-azobenzene is optically excited to the n→ π* transition by a 425 nm photon, it isomerizes towards the *trans* configuration within less than 200 fs with about 50% quantum yield [57]. Thereby, it will deposit a certain fraction of the photon energy (≈3 eV) into its vibrational degrees of freedom. The energy dumping will be relatively nonspecific, and, according to the MD simulations discussed below, thermalizes on an ultrafast sub-picosecond timescale. There are two major routes where the energy, or heat, can go: into the solvent or along the helix. Indeed, we do see the largest signal at early delay times from the C=O group **1** closest to the source of the 'heat' (Fig. 3.33a-c). The signal predom-

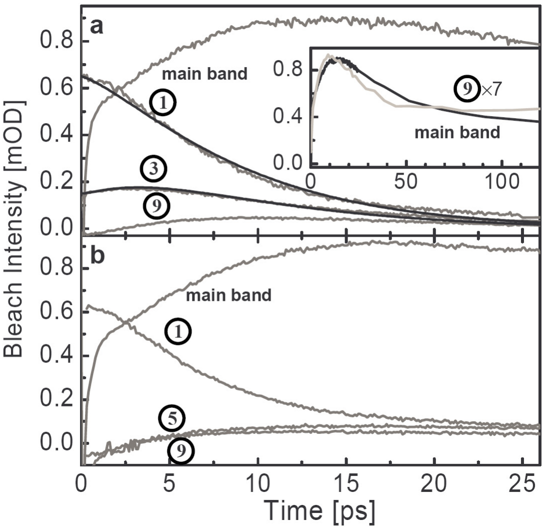

Figure 3.34: Time dependencies of the bleach intensity (with opposite sign as in Fig. 3.33) of bands **1** to **9** and the 'main band', of (a) PAZ-Aib-Ala*-Aib$_6$-OMe and (b) PAZ-Aib$_3$-Ala*-Aib$_4$-OMe, respectively (grey lines). The black lines show global fits according to a simple kinetic scheme (see text). The inset in (a) shows the recovery of the main band on a longer timescale together with that of band **9** (the latter being up-scaled by a factor of 7).

inantly relates to a red shift of band **1**, i.e., a negative bleach at the original position of the band and a relatively broad positive band red shifted from that position. We assign this signal to the local temperature at the N-terminus of the helix. Even at the highest conceivable temperatures reached in this experiment, a C=O mode with 1600-1700 cm^{-1} will not directly be excited according to a Boltzmann factor of $e^{-\hbar\omega/k_BT}$. However, thermal excitations of lower frequency modes that are in spatial vicinity to a specific reporter C=O group will cause anharmonic frequency shifts of the latter, an effect that has been studied in detail in Ref. [58].

The interpretation of the signal of band **1** as a local 'temperature' is supported by its 7 ps decay time shown in Fig. 3.34a,b, which roughly coincides with what is known as the typical cooling time in the solvent chloroform [139]. Cooling of organic dye molecules in various solvents has been studied extensively over the past decades [139–141]. In particular, it has been established that the cooling time is essentially a solvent property, which is more or less independent on the particular solute molecule.

Combining these two pieces of evidence, we assign a bleach and/or shift signal associated with a 7 ps decay component as 'heat' in the vicinity of the corresponding C=O group. Apart from unit **1**, the only other group that shows such a 7 ps decay component is unit **3** (Fig. 3.34a). However, the way how unit **3** builds up is different: after an instantaneous rise, it continues to grow until it peaks delayed after about 2.5 ps. We do not see any 7 ps decay component further away from the 'heater'; neither for band **5** in PAZ-Aib$_3$-Ala*-Aib$_4$-OMe nor for band **9** in either of the samples.

Hence, we do observe a propagation effect. If we assume that the signal amplitude is roughly proportional to the vibrational energy present at a particular position [58], one would conclude that the temperature jump at position **3** is about 1/3 of that at position **1**, whereas the temperature jump at position **5** or further away is unmeasurably small. The temperature jump at position **2** is lying somewhere in between that of **1** and **3** (due to spectral overlap we do not attempt to quantify the value), indicating that energy flow occurs through the backbone, and not through the hydrogen bond between unit **1** and **3**.

The 'main band' responds in a distinctly different way to heating of the molecule. The spectral response between 15 ps and 1 ns is dominated by the main band which reveals a blue shift, i.e., a negative bleach at the original position of the band and a positive band blue shifted from that position. These late delay time spectra strongly resemble stationary temperature induced difference spectra (Fig. 3.33, dotted lines) [142], suggesting that we are left with the response to an elevated temperature after about 15 ps. The temperature rise leads to an overall weakening of the hydrogen bonds of the helix and, in turn, results in a blue shift of the related C=O vibrators [143]. We associate the partial decay of this signal with a 35 ps time constant (Fig. 3.34a, inset) to heat diffusion from the first solvation shell into the bulk solvent, which occurs on a characteristic timescale of a few tens of picoseconds [144]. The C=O group furthest away from the chromophore (band **9**), as well as band **5** in PAZ-Aib$_3$-Ala*-Aib$_4$-OMe, exhibit a kinetics that closely mimics that of the 'main band' (Fig. 3.34a, inset). Hence, in contrast to unit **1** to **3**, any group further away from the 'heater' sees only a secondary effect due to partial destabilization of the hydrogen bonds.

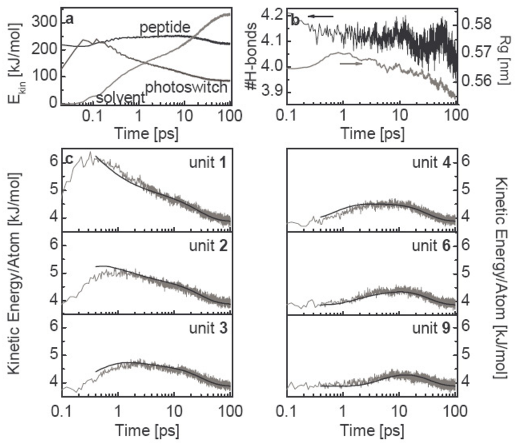

Figure 3.35: Time evolution of the photoinduced dynamics of PAZ-Aib$_8$-OMe from the MD simulation: (a) Total kinetic energy of the Aib$_8$ peptide (black), the photoswitch (grey) and the solvent (light grey). (b) Mean number of 3_{10}-helix hydrogen-bonds (black, left scale) and radius of gyration of the Aib$_8$ peptide (grey, right scale). (c) Mean kinetic energy of selected residues. The black lines show global fits according to the kinetic model described in the text.

3.6.4 Computational Results

To guide the interpretation of the experiments and to obtain a microscopic picture of the molecular processes underlying energy transport in peptides, we have performed nonequilibrium MD simulations of the photoinduced molecular dynamics. Although the quantitative description of these processes in general requires a quantum-mechanical modelling [113, 119], a simple classical approach to study energy transport [118] is to consider the time evolution of the kinetic energy in various parts of the molecular system (Fig. 3.35a). Following the photoexcitation at time $t = 0$, the kinetic energy is deposited into the azobenzene photoswitch within less than 0.1 ps. While the excitation of the photoswitch decays on a picosecond time scale, its energy is transferred to the Aib peptide (30 %) as well as directly to the solvent (70 %). The peptide energy rises within 0.3 ps and remains approximately constant up to 10 ps before it decays with an $\approx$ 20 ps time constant. The solvent energy $E_{\text{solv}}(t)$ [145] rises with time constants 0.5 ps and $\approx$ 20 ps, where the shorter time scale reflects the initial momentum transfer of the isomerizing photoswitch to its surrounding solvent molecules. Following the thermalization of the photoinduced energy, the 20 ps time scale of $E_{\text{solv}}(t)$ accounts for the subsequent cooling of the PAZ-Aib$_8$-OMe peptide.

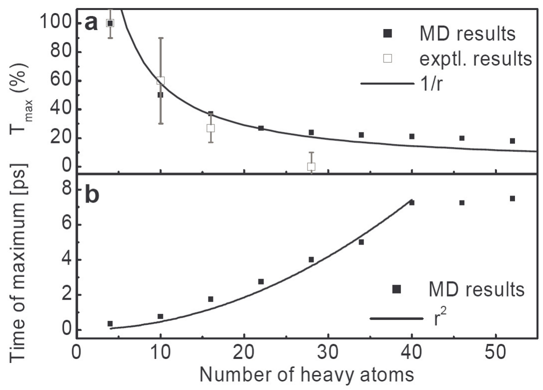

Figure 3.36: Maximal amplitudes (a) and peak times (b) of the energy transferred to residue Aib$_n$ from the raw MD data, plotted as a function of the number of heavy atoms along the peptide chain, together with $1/r$ and r^2 fits. In (a), the experimental results are included for comparison (open squares).

The time evolution of the main band (initial rise with a peak at $\approx$ 15 ps and recovery on a 35 ps time scale) was interpreted above to be associated with a transient weakening and reformation of the hydrogen bonds, thereby destabilizing the helix for some time. To investigate this issue, Fig. 3.35b shows the time evolution of the average number of stabilizing 3_{10}-helix hydrogen bonds n_{HB}. On average, photoexcitation causes only a small change of n_{HB} of ≈ 0.2. Similarly, the peptide radius of gyration, a measure of the size of the peptide, virtually remains constant (Fig. 3.35b). We therefore conclude that the photoexcitation does not lead to significant conformational changes of the peptide, and that the transient effect we observe in the experiment relates to this small change of n_{HB}.

To elucidate the energy transfer along the peptide chain, Fig. 3.35c displays the time evolution of the mean kinetic energy for most of the peptide groups. The time-delayed rise of these energies nicely illustrates the transport of energy (or ‘heat’) along the peptide backbone. Let us compare the simulated and experimentally observed energy transports along the peptide backbone. The kinetic energy of unit **1** (the linker unit to the photoswitch) reaches its peak at 0.3 ps, which nicely agrees with the experimental finding that unit **1** takes up substantial energy within the time resolution (0.2 ps). Unit **2** receives about 50 % of the energy from **1** and unit **3**

35% within 1 ps. According to the simulation, the terminal unit **9** still receives a small (20 %) amount of the excess energy due to the photoexcitation, but this effect is not measurable in the experiment.

Several tests were pursued to learn more about the mechanism of energy transfer. First, we performed two nonequilibrium simulations where the initial states of the peptide were chosen to represent conformations with high (4.7) and low (3.5) average number n_{HB} of stabilizing 3_{10}-helix hydrogen bonds, respectively. Comparing the time evolution of the mean kinetic energy of each of the Aib residues, Fig. S8 (Supporting Information) reveals that the energy transfer is essentially identical in both cases. Moreover, the time evolution of the kinetic energy including only the CONH atoms of the pepide unit (as done in Fig. 3.35c) was found to be quite similar to the case when all atoms were taken into account, see Fig. S9 (Supporting Information). In agreement with experiment, these findings indicate that the transport of energy is not primarily mediated through intramolecular hydrogen bonds or side-chain atoms, but rather proceeds through the backbone atoms.

3.6.5 Discussion

To discuss the molecular mechanisms underlying the energy transport, we start with the analysis of the computational data and plot the maximal amplitudes and the peak times of the transferred energy as a function of the number of heavy atoms along the peptide chain (Fig. 3.36). The number of heavy atoms, relevant for thermal properties such as heat capacity and thermal conductivity, is used as a measure for the distance from the heater. Considering Fig. 3.36 together with Fig. 3.35a, we find that the energy transport occurs in two stages, that is, an initial stage for times $t \lesssim 1$ ps and distances $r \lesssim 10$ heavy atoms, and a subsequent stage for larger times and distances. In the initial phase, two competing processes occur. Since the photoisomerizing azobenzene moiety essentially bumps into the surrounding solvent molecules, we observe an ultrafast (0.5 ps time scale) and efficient (70 % of the excess energy) heat transport into the solvent (Fig. 3.35a). At the same time, 30 % of the excess energy arrives within only 0.1 ps at C=O group **1**, that is, at distances of 4 heavy atoms or 2 Å. As this distance per time roughly corresponds to the speed of sound of about $v_s \approx 20$ Å/ps, we may refer to the process as *ballistic*. We note that this ballistic transport is restricted to distances shorter than ≈ 10 heavy atoms, where the peptide chain may be considered as relatively rigid. (For a completely rigid molecule, the transfer of conformational change would be instantaneous.) For longer distances, the increasing flexibility of the peptide chain hampers a direct ballistic transfer. In fact, since the energy of the peptide remains approximately constant for times $0.3\text{ ps} \lesssim t \lesssim 10$ ps (Fig. 3.35a), we find that the photoswitch and the peptide are thermally decoupled after 0.3 ps. In order to transport energy over longer distances, delocalized low-frequency modes are needed [111–113] which exist along the uniform peptide backbone, but presumably not between peptide and the azobenzene moiety.

Assuming thermal decoupling, the energy distribution of the atoms of unit **1** at $t \approx 0.3$ ps can be considered as the initial state of the subsequent energy transfer along the peptide chain. Interestingly, the latter is well fitted by a Maxwell distribution for 500 K, that is, unit **1** is thermalized at ultrafast times. Starting with a thermalized initial state and conserving energy, the second stage, that is, the subsequent energy transfer along the peptide chain, may be described by a 1D diffusion process. Indeed, the transferred energies and peak times shown in Fig. 3.36 exhibit the expected $1/r$ and r^2 behavior, respectively. As this model assumes energy conservation, however, the fits deteriorate for times $\gtrsim 10$ ps and distances $\gtrsim 40$ atoms, reflecting the dissipation of the peptide energy into the solvent.

To obtain a more realistic model of the diffusional transport along the peptide chain, we have constructed a simple rate-equation model which assumes that (i) each peptide unit exchanges energy with its nearest neighbor according to a (forward and backward) rate constant k_{p} and (ii) each peptide unit loses energy to the solvent with the rate k_{s}. A global fit of the time traces in Fig. 3.35c yields the relaxation times $1/k_{\mathrm{p}} = 0.4$ ps and $1/k_{\mathrm{s}} = 18$ ps. Apart from the ultrafast energy rise of the first few units, the fits match very well the simulation data, thus suggesting that the simple kinetic model is appropriate.

Comparing theoretical and experimental results, we find a good overall agreement. Also in the experiment we observe an instantaneous (within temporal resolution) rise of the temperature signal for units **1** to **3**, reporting on the impact of the switching azobenzene moiety that seems to perturb deeper into the helix as in the MD simulation (i.e., the instantaneous contribution to the rise of band **3** is larger in the experiment). Subsequently, energy propagates through the helix but drops very quickly with increasing distance from the heater

(Fig. 3.36a, open squares). Applying the above described heat propagation model to the experimental results, we obtain relaxation times $1/k_\mathrm{p} = 2$ ps and $1/k_\mathrm{s} = 7$ ps, respectively (see fits in Fig. 3.34). The small deviation between fit and the experimental data at times > 15 ps might reflect an elevated temperature of the solvent, and hence back-transfer of heat from the solvent to the molecule, which, in part, might stem from heat transferred directly into the solvent during the isomerization process of the azo-moiety. In this case, a power-law dependence would be expected for the final decay. However, experimental uncertainties in determining offsets do not allow us to discuss this effect. In ongoing work, we are currently investigating the temperature dependence of heat transport, providing evidence that viscosity affects in particular the initial impact event.

Compared to experiment, the MD calculations thus overestimate the peptide transport rate by a factor of five but underestimates the cooling rate by a factor of 2.5. As discussed elsewhere [118], the latter effect is most likely caused by the rigid force-field model used for the chloroform solvent. (Employing a flexible model of the solvent adds more degrees of freedom and therefore increases the heat capacity and the ability to cool the solute —albeit at the cost of other problems such as the classical description of high-frequency modes.) When the propagation rates are related to the heat diffusivity $D = k_\mathrm{p}\Delta x^2$ (with $\Delta x \approx 2$ Å being the helical translation per residue for a 3_{10}-helix [133, 136]), we obtain $D = 2$ and 10 Å^{2}ps^{-1} from experimental and calculated data, respectively. Our nonequilibrium MD result agrees well with results from a comparable simulation of cooling of a protein (7 Å^{2}ps^{-1} [115]), as well as with recent quantum-classical calculations ($\approx$ 20 Å^{2}ps^{-1} [111–113]). The latter were based on an equilibrium normal-mode analysis using a similar MD force field, augmented with a Golden Rule-type modeling of energy relaxation using cubic anharmonicities. This result indicates that the significant deviation between theory and experiment is less a matter of quantum effects, but is rather caused by the empirical potential-energy models used. Another indication for the minor importance of quantum effects is that the deviation is virtually independent of whether the peptide bond lengths are constraint (thereby mimicking quantum effects) or not in the MD simulation.

In fact, it is well-known from peptide folding simulations that the calculated folding transition temperature is typically well above ($\approx$ 30 %) the experimental value, that is, the force field is "too rigid" at high temperature (see, e.g., Ref. [146]). Apart from incomplete sampling, this observation appears to be a consequence of neglecting polarizability and many-body interactions and the fact that force field parameters are derived for room temperature rather than for the high temperature range. The problem considered here is similar in that the typical temperature of the peptide is between 400-500 K during the first 10 picoseconds (see Fig. 3.35c) and that a too rigid force field may enhance the transport of energy. As one may expect a better agreement of theory and experiment at lower temperatures, it would be interesting to extend our studies to low-energy excitation.

3.6.6 Conclusions

Pursuing a joint experimental-theoretical investigation, we have drawn a molecular picture of the energy transfer processes in a photoactivated peptide. Following ultrafast *cis-trans* photoisomerization of the azobenzene moiety, the energy transfer was found to occur in two stages: (i) Initially, 70 % of the excess energy is dissipated into the solvent on a 0.5 ps time scale. The high efficiency of this process is crucial for biomolecules in order to survive photoexcitation or to remove excess heat of chemical reactions. The remaining 30 % of the energy is transferred in a ballistic way to the beginning of the peptide helix, where it is thermalized within only 0.3 ps. (ii) The subsequent energy transfer along the peptide chain was found to be well described by a 1D diffusion process with a heat diffusivity of 10 Å^2/ps, as contrasted to the experimental value is 2 Å^2/ps. Achieving the propagation of conformational changes, this process is crucial for the functionality of the biomolecule.

Solitonic effects, if at all existent, apparently do not play a role in stabilizing and funnelling energy through the helix efficiently, as is has been speculated quite some time ago by Davydov [54]. Heat propagation rate along the helix only slightly (by a factor 3-4) exceeds that into the solvent. This finding seems surprising since covalent and hydrogen bonds exist within the helix, whereas coupling to the surrounding was reduced as much as was possible by the choice of an apolar solvent. However, low frequency modes dominate heat transport, since they tend to delocalize over large distances [111–113]. Apparently, even the weak Van der Waals interactions with the solvent give rise to intermolecular solvent-peptide modes in the right frequency range, that efficiently transport energy into the solvent. Currently, it is not clear how heat transfer between adjacent helices would occur in a larger protein. Nevertheless, the present study provides the first direct measurement of the heat diffusion constant of a peptide helix that is considered an important structural element of proteins.

Acknowledgement: We are grateful to Dr. David M. Leitner for many intriguing discussions. The work was partially supported by Netherlands Organisation for Scientific Research (NWO) and the 'Forschungskredit' of the University of Zurich by postdoc fellowships granted to EB. We furthermore acknowledge support by the Swiss Science Foundation (grant 200020-115877), Frankfurt Center for Scientific Computing, the Fonds der Chemischen Industrie, and the Deutsche Forschungsgemeinschaft.

3.6.7 Materials and Methods

Synthesis: Deuterated PAZ-Aib-OH was synthesized by nitrating toluene-D_8 to *p*-nitrotoluene, oxidizing to *p*-nitrobenzoic acid, reducing with zinc to *p*-aminobenzoic acid, and then making the methyl ester using methanol and thionyl chloride. Reduction of the ester with lithium-aluminium-deuteride [147] leads to the full deuterated *p*-aminobenzyl alcohol. Nitrosobenzene-D_5 was obtained by reduction of nitrobenzene-D_5 as described in Ref. [148]. Coupling these two deuterated compounds and covalently linking the resulting alcohol to L-Ala* and Aib was performed in the same way (via PAZ-Cl) as reported in Ref. [134, 149]. Peptide synthesis was performed in solution by activating the carboxyl function with 1-(3-dimethylaminopropyl)-3-ethylcarbodiimide and 7-aza-1-hydroxy-1,2,3-benzotriazole [150]. Details of the synthesis and characterization are reported in the Supporting Information.

Time Resolved Experiments: The peptides were investigated by UV-pump-IR-probe spectroscopy exciting *cis*-azobenzene at a wavelength of 425 nm [57], and probing the amide I region with an IR-probe pulse centered at 1680 cm^{-1} (spectral width 200 cm^{-1}). The probe pulse was frequency dispersed in a spectrometer and imaged onto a 64 channel IR array detector (or a 32 channel IR array detector in case of Fig. 3.33a) covering the total region of C=O vibrations. The time resolution of the apparatus was 200 fs. The sample was dissolved in $CHCl_3$ at a concentration of typically 10 mM, circulated in a closed cycle CaF_2 flow cell with optical path length of 100 μm, and continuously irradiated with cw-light at 320 nm (FWHM 70 nm) from a properly filtered Hg-lamp in order to accumulate the cis-species to about 80%.

Computational Methods: All simulations were performed with the GROMACS program suite [151], using the GROMOS96 force field 43a1 [152] to model the PAZ-Aib$_8$-OMe peptide and the rigid all-atom model of Ref. [153] to describe the chloroform solvent. Additional force field parameters for the azobenzene unit were derived from density functional theory as described in Ref. [154]. Starting with a 3_{10}-helical conformation, the PAZ-Aib$_8$-OMe peptide was placed in an octahedral box containing $\approx$ 700 chloroform molecules. After energy minimization, the system was simulated for 40 ns at NTP equilibrium conditions (1 atm, 300 K). Employing the same protocol, we also performed an equilibrium simulation of the peptide PAZ-Aib$_3$-Ala*-Aib$_4$-OMe. From the equilibrium trajectory of PAZ-Aib$_8$-OMe, 800 statistically independent conformations were obtained for the subsequent nonequilibrium simulations.

In order to model the laser-induced photoisomerization process, we use a minimal model for the corresponding potential-energy surfaces that diabatically connects the excited-state S_1 of the *cis* isomer with the ground state S_0 of the *trans* isomer [155]. The photoexcitation of the system by an ultrafast laser pulse is mimicked by instantly switching from the ground-state N=N torsional potential to the excited-state potential. Following this nonequilibrium preparation at time $t = 0$, the system isomerizes along an excited-state N=N potential within $\approx$ 0.2 ps. After isomerization (i.e., for times $\geqslant$ 0.5 ps), the N=N torsional potential is switched back to its ground state form, and a constant-energy MD simulation is performed up to 100 ps. Following the nonequilibrium simulations, the time-dependent observables of interest are obtained via an ensemble average over 800 equilibrium conformations.

3.7 Energy transport in peptide helices: A comparison between high- and low-energy excitations

Ellen H. G. Backus, Phuong H. Nguyen, Virgiliu Botan, Rolf Pfister, Alessandro Moretto, Marco Crisma, Claudio Toniolo, Gerhard Stock, Peter Hamm

J. Phys. Chem. B, 112, 9091, (**2008**)

Abstract

Energy transport in a short helical peptide in chloroform solution is studied by time-resolved femtosecond spectroscopy and accompanying nonequilibrium molecular dynamics (MD) simulations. In particular, the heat transport after excitation of an azobenzene chromophore attached to one terminus of the helix with 3 eV (UV) photons is compared to the excitation of a peptide C=O oscillator with 0.2 eV (IR) photons. The heat in the helix is detected at various distances from the heat source as a function of time by employing vibrational pump-probe spectroscopy. As a result, the carbonyl oscillators at different positions along the helix act as local thermometers. The experiments show that heat transport through the peptide after excitation with low-energy photons is at least four times faster than after UV excitation. On the other hand, the heat transport obtained by nonequilibrium MD simulations is largely insensitive to the kind of excitation. The calculations agree well with the experimental results for the low-frequency case; however, they give a factor of five too fast energy transport compared for the high-energy case. Employing instantaneous normal mode calculations of the MD trajectories, a simple harmonic model of heat transport is adopted which shows that the heat diffusivity decreases significantly at temperatures initially reached by high-energy excitation. This finding suggests that the photoinduced energy gets trapped, if it is deposited in high amounts. Being a quantum effect, this temperature dependence is not reproduced by the classical MD calculations. The various competing mechanisms, such as vibrational T_1 relaxation, resonant transfer between excitonic states, cascading down relaxation, and low-frequency modes transfer are discussed in detail.

3.7.1 Introduction

Energy transport through molecular systems has received considerable interest in particular due to its importance in molecular electronics and the functioning of biological systems. For example, experimentally the energy transport through long-chain hydrocarbon molecules [156], small molecules in solution [128], and bridged azulene-anthracene compounds [127] has been studied. Also the energy transport in biological systems, like micelles [157], reverse micelles [129], and proteins [111–119, 121, 122, 124, 125], has been investigated from both an experimental and theoretical point of view. In spite of these efforts, the role of specific protein structural elements (like α-helices and β-sheets) in the energy transport is still not well understood. As α-helices often span the whole protein, it has been speculated that helices channel vibrational energy through biomacromolecules [54]. To test this hypothesis, we have recently studied both experimentally and theoretically the transport of energy through a short but stable peptide 3_{10}-helix [55]. To deposit a large amount of energy in the molecule, a chromophore (an azobenzene-moiety) was attached to the helix, which is electronically excited at $\approx$425 nm (i.e. from the n to the π^* state) and dissipates this photon energy on an ultrafast timescale after internal conversion (via *cis-trans* isomerization) of the chromophore. We found experimentally that the heat travels through the backbone of the helix with a diffusivity of 2 $\text{Å}^2\text{ps}^{-1}$. Supplementary molecular dynamics (MD) simulations revealed a five times higher diffusivity (10 $\text{Å}^2\text{ps}^{-1}$). We assigned this difference to a "too rigid" force field in the simulations and suggested that it would be interesting to perform experiments with low-energy excitation [55]. Following this line, in this article we compare the energy transport through the helix after excitation with high-energy ($\sim$400 nm) light by optically exciting the chromophore with that with low-energy ($\sim$6μm) light by direct excitation of various C=O groups. This procedure lowers the energy deposited into the molecule by a factor 14.

The stable octapeptide 3_{10}-helix [136] consists of seven Aib (α-aminoisobutyric acid) residues, a natural but non-coded amino acid, and one L-Ala residue. Carbonyl groups in the helix are employed as local thermometers, making use of an effect that has been described in detail in Ref. [58]: Vibrational transitions become broader and shift to lower frequency upon heating, due to anharmonic coupling to thermally excited lower frequency modes. To be site-sensitive, we prepared peptides with a ^{13}C=O labelled Ala (which is more readily available commercially than ^{13}C=O-Aib) at different locations in the amino acid sequence, of which the vibrational frequency is shifted to the red compared to that of the Aib residues. The amino acid Ala is believed not to destabilize the 3_{10}-helix significantly, which has been confirmed by MD simulations as well as by NMR and IR spectroscopy [55]. More specifically, we synthesized two different molecules: one with the ^{13}C=O labelled Ala as the second residue (Fig. 3.37) and one with the label at residue [157], counting from the N-terminus of the helix. The isotope shift of $\approx$-30 cm^{-1} will essentially localize the excitation; hence, the isotope labelled amino acid serves as a local thermometer.

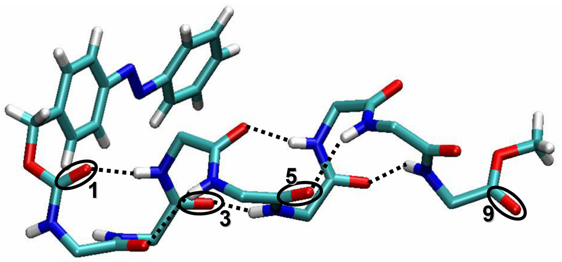

Figure 3.37: X-ray diffraction structure of the molecule showing the azobenzene, the urethane connection group and the peptide helix with the eight residues (seven Aib residues and one ^{13}C=O labelled Ala residue). In this work, the Ala residue is either the second or the fourth residue, resulting in the molecules dPAZ-Aib-Ala*-Aib$_6$-OMe (Aib16) and dPAZ-Aib$_3$-Ala*-Aib$_4$-OMe (Aib34), respectively. Amino acid side chains are not shown. The tags refer to the urethane (#1), the labelled peptides (#3 and #5), and the ester (#9) absorption bands in Fig. 3.38

At the N-end a urethane group and an azobenzene moiety are connected to allow pumping with UV light. The azobenzene moiety isomerizes on an ultrafast timescale and thereby locally deposits heat. The flow of heat through the helix was investigated in Ref. [55] by monitoring the IR response of the ^{13}C labelled amide groups as well as of the N-terminal urethane and C-terminal methyl ester groups with an IR probe pulse at various times after the excitation. The topic of the present paper is the heat response after low-energy ($\sim$6 μm) excitation of one of the C=O groups. The subsequent heat propagation along the peptide chain is measured by probing the various C=O vibrators.

3.7.2 Materials and Methods

Materials and experimental methods

The different laser pulses all originate from a commercial Ti:sapphire amplifier system. Part of the output was used to generate 425 nm light ($\sim$3 μJ, to pump the azobenzene moiety) by frequency doubling used for the high-energy excitation experiments. Infrared pulses (center frequency 1680 cm^{-1}, bandwidth 200 cm^{-1}, energy 1.7 μJ) were produced by difference frequency generation in a $AgGaS_2$ crystal of signal and idler pulses. These were generated by a white light seeded two-stage BBO optical parametric amplifier [158] pumped by another part of the output of the Ti:sapphire amplifier. A small fraction of the infrared pulses was split off to obtain broadband probe and reference pulses. The remainder, which was used as a pump pulse in the low-energy excitation experiments, was passed through a computer controlled Fabry-Perot filter to generate narrow band pump pulses (bandwidth $\sim$13 cm^{-1}, estimated energy 80 nJ/pulse) to excite a particular C=O group of the helix. With the broadband probe pulse all C=O oscillators were detected at once. The pump and probe pulses were focussed in the sample in spatial overlap. The reference pulse was focussed roughly 0.5 mm away. Both probe and reference pulses were frequency dispersed in a spectrometer and detected with a 2Œ63 pixel HgCdTe detector array resulting in a resolution of $\sim$3 cm^{-1}. The UV or IR pump pulse was delayed with respect to the probe pulse by an optical delay line. All beams were polarized parallel.

The two peptides used in this study are dPAZ-Aib-Ala*-Aib$_6$-OMe (Aib16) and dPAZ-Aib$_3$-Ala*-Aib$_4$-OMe (Aib34), where the asterisk (*) indicates ^{13}C=O labelling, dPAZ is an abbreviation for fully deuterated 4-(phenyldiazenyl-benzyloxycarbonyl) and OMe for methoxy. Deuterated PAZ-Aib-OH was synthesized by nitrating toluene-D$_8$ to *p*-nitrotoluene, oxidizing to *p*-nitrobenzoic acid, reducing with zinc to *p*-aminobenzoic acid, and then making the methyl ester using methanol and thionyl chloride. Reduction of the ester with lithium-aluminium-deuteride [147] leads to the full deuterated *p*-aminobenzyl alcohol. Nitrosobenzene-D$_5$ was obtained by reduction of nitrobenzene-D$_5$ as described in Ref. [148]. Coupling these two deuterated compounds and covalently linking the resulting alcohol to L-Ala* and Aib was performed as reported in refs. [134], [149]. Peptide synthesis was performed in solution by activating the carboxyl function with 1-(3-dimethylaminopropyl)-3-ethylcarbodiimide and 7-aza-1-hydroxy-1,2,3-benzotriazole [150]. For details of the peptide synthesis and the characterization of the molecules by IR, NMR and x-ray diffraction, we refer to Ref. [55].

The helical peptide was dissolved in chloroform ($\sim$5-10mM), an apolar and weakly interacting solvent to minimize heat transport into the solvent. The sample was kept between 2-mm-thick CaF_2 windows separated by a 100 μm spacer for the low-energy excitation and the FTIR experiments. For the high-energy excitation experiments a closed cycle flow cell was used with a 100 μm spacer. The experiments with low-energy excitation were performed for the molecule in the *trans* azobenzene state, while the experiments with high-energy excitation were performed with the *cis* state of the molecule, as the *cis* to *trans* yield is higher and the izomerisation is faster [57]. The *cis* state (up to $\sim$80%) was prepared by continuously irradiating at 320 nm (FWHM 70 nm) from a properly filtered Hg-lamp.

Computational methods

All simulations were performed with the GROMACS program suite [159]. We used the GROMOS96 force field 43a1 [152] to model the PAZ-Aib$_8$-OMe peptide and the rigid all-atom model of Ref. [153] to describe the chloroform solvent (we checked if heat transport depends on the rigid or flexible representation of the solvent and found only a minor effect). Additional force field parameters for the azobenzene unit were derived from density functional theory as described in Ref. [154]. Starting with a 3_{10}-helical conformation, PAZ-Aib$_8$-OMe was placed in an octahedral box containing $\sim$700 chloroform molecules. After energy minimization, the system was simulated for 40 ns at NTP equilibrium conditions (1 atm, 300 K). From this equilibrium trajectory, 400 statistically independent conformations were selected for the subsequent nonequilibrium simulations.

As the nonequilibrium MD simulation approach was described in detail in Refs. [118, 160], we only briefly summarize the main aspects of the method. In order to model the UV (high-energy) laser-induced photoisomerization process of the azobenzene [118], we use a minimal model for the N=N torsional potential energy surfaces that diabatically connects the excited-state S_1 of the *cis* isomer with the ground state S_0 of the *trans* isomer [118]. Starting with 400 statistically independent conformations, at time $t = 0$ the system is instantaneously switched from the ground-state potential to the "diabatic excited-state" potential. Following this nonequilibrium preparation, the system isomerizes along this "excited-state" potential within typically 0.2 ps. Subsequently, the N=N torsional potential is switched back to its ground state form and a constant-energy MD simulation is performed up to 100 ps. This rather crude description of the photoexcitation should be justified as long there is a clear time scale separation between the excitation process and the subsequent relaxation process (see Discussion below).

To model the IR (low-energy) excitation of a local C=O group [160], we represent the C=O stretch vibration as a harmonic oscillator with the reduced mass $\mu = (m_C + m_O)/m_C m_O$, coordinate $q_{CO} = q_C - q_O - < q_{CO} >$, and momentum $p_{CO} = p_C - p_O$. In terms of classical action-angle variables n, ϕ, these variables are represented as [161]:

$$q_{CO} = \sqrt{2n+1}\sin\phi \tag{3.21}$$

$$p_{CO} = \sqrt{2n+1}\cos\phi \tag{3.22}$$

where the factor 1 accounts for the zero-point energy of the oscillator. To obtain the initial position and momentum of the initially excited C=O, we associate the action n with the initial quantum state of an oscillator, e.g., $n = 1$ for the first excited state. The vibrational phases ϕ are picked randomly from the interval $[0,2\pi]$. This way, an ensemble of the positions and momenta are calculated, which provide a quasiclassical representation of the quantum initial state of the C=O oscillator.

Following the preparation of the nonequilibrium initial conditions described above, two sets of simulations were performed independently for the high- and low-energy excitation cases. The equation of motion was integrated by using a leap-frog algorithm with time step of 0.2 fs. We employed the particle-mesh Ewald method to treat the long-range electrostatic interaction [162]. The nonbonded interaction pair-list were updated every 10 fs, using a cutoff of 1.4 nm. All simulations were performed at constant energy (NVE ensemble) for 100 ps and data were collected every 0.02 ps.

3.7.3 Experimental Results

Steady-state spectra

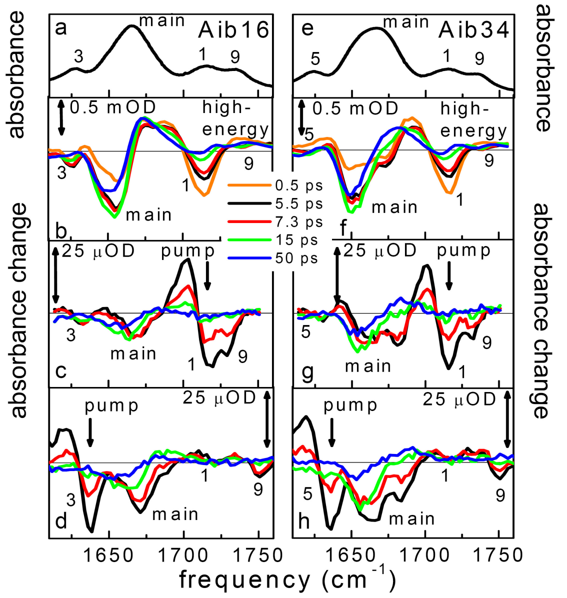

Figure 3.38: Absorption and transient spectra. (a) IR absorption spectrum of Aib16. (b) Transient signal for Aib16 after high-energy excitation of the azobenzene moiety at 0.5 (orange), 5.5 (black), 7.3 (red), 15 (green), and 50 ps (blue). (c) Transient signal for Aib16 after low-energy excitation of C=O #1 at 5.5, 7.3, 15 and 50 ps. (d) Transient signal for Aib16 after low-energy excitation of C=O #3 at 5.5, 7.3, 15 and 50 ps. (e-h) Same for Aib34. In panel h C=O #5 is pumped. The arrows locate the central position of the IR pump pulse. The measurements are performed at ~20°C.

Fig. 3.38a and e show the stationary FTIR absorption spectrum of the helical peptides Aib16 and Aib34 in the amide I (mainly C=O vibration) region. Because the band at 1627 cm^{-1} is not visible in a FTIR absorption spectrum of the peptide with all ^{12}C-Aib residues (data not shown) and because labelling leads to lower frequency, this band is assigned to the isotopically labelled group in the helix, C=O #3 for Aib16 or #5 for Aib34, respectively. The two bands at 1714 and 1735 cm^{-1} can be assigned to the C=O groups from the urethane moiety connected to the azobenzene (C=O #1) and from the ester group of the C-terminal Aib residue (C=O #9), respectively. These two C=O groups are shifted with respect to the others due to their -C(=O)O- nature. The intense band at 1665 cm^{-1} is attributed to all other non-isotope labelled peptide -C(=O)NH- groups (six in total) and is herein called the "main band".

High-energy excitation

The heat response of the helix after exciting the azobenzene moiety with high-energy (UV) photons has been discussed in detail in our recent paper [55]. Nevertheless, in order to facilitate the comparison with the low-energy excitation, we shortly repeat the essential results here. The photo-excited azobenzene undergoes an internal conversion (*cis-trans* isomerization) on a 200 fs timescale [57]. When the photon energy ($\sim$3 eV) has been distributed over the vibrational degrees of freedom of the azobenzene, an energy equivalent to a local temperature of $\sim$1150 K is estimated right after the photoreaction, assuming the system is thermalized and all energy remains in the azobenzene group. In reality, the temperature will be lower, as part of the photon energy is lost into the solvent due to friction during the isomerization process. In particular, the MD simulation predicted a temperature in the photoswitch of $\sim$750 K [55] (however, we will argue below that this number probably is somewhat too low). Nevertheless, these estimates give an idea of the order of magnitude of the effects to be expected. Despite these large "temperatures", the MD simulation of Ref. [55] indicated that the helix stays intact on the fast time scale of the experiment.

After photo-isomerization of the azobenzene moiety, bands #1 and #3 show instantaneous sharp bleaches (Fig. 3.38b and f) which decay on a 7 ps time scale (grey lines in Fig. 3.39a). These bleaches are due to anharmonic coupling of our spectator modes to thermally excited lower frequency modes and hence can be considered a measure of the amount of vibrational energy in the vicinity of the probe [58]. Note that such a spectral response is obtained although direct thermal excitation of the spectator modes is extremely unlikely (due to the large vibrational frequency), and also note that this response averages over many low frequency modes so we cannot deduce whether energy is thermalized or not. Guided by the MD simulation, we attributed this instantaneous signal to an impact event from the isomerising azobenzene moiety, where group #3 receives about 1/3 of the energy of group #1. No signal of this sort is observed any further in the helix (bands #5 and #9). After this impact event, heat diffuses from group #1 to group #3 [55]. From a simple diffusive rate equation [55] model along the lines of Fig. 3.40 (black arrows), assuming a backward and forward rate of energy transport k_p through low frequency modes and a cooling to the solvent with rate k_s, we deduced for the heat diffusivity $D = k_p \Delta x^2 = 2\text{Å}^2\text{ps}^{-1}$ (with $\Delta x \approx 2\text{Å}$ being the translation per residue [136]).

The main band responds in a distinctly different way than bands #1 and #3. It grows till $\sim$15 ps, followed by a decay on a 35 ps timescale to roughly 30% of its maximum value (Fig. 3.39b). Bands #5 and #9 only show broad bleaches which have the same dynamics as the main band. The spectral response between 15 ps and 1 ns is dominated by blue shifts of the corresponding bands. These late-delay-time spectra, for 50 ps delay depicted in the inset of Fig. 3.39b, strongly resemble stationary temperature-induced difference spectra (dotted line in the inset of Fig. 3.39b), suggesting that we are left with the response due to an elevated temperature of the system. The 35 ps decay is a characteristic time scale for heat diffusion from the first solvation shells into the bulk solvent [144]. Note that the spectrum at late times, when heat has diffused into the bulk solvent, is given by all molecules in the probe volume, while at early times only the molecules excited directly by the laser are probed.

Low-energy excitation

For low-energy (IR) excitation, depicted in panels c, d, g, and h of Fig. 3.38, we see remarkable differences at early times compared to the high-energy excitation, while the late delay time spectra are rather similar. We therefore discuss the various kinetic components backwards in time: the latest time spectra are independent of the excitation frequency (compare the blue curves in panel c with d and g with h) and again represent the elevated temperature of the surrounding solvent. In the inset of Fig. 3.39b the spectrum at 50 ps has been plotted together with a steady-state difference spectrum with a temperature jump of 0.015 K [163], revealing remarkable agreement despite the small size of the signal (8 μOD). Like in the high-energy excitation experiment, the temperature spectrum is largest at about 10 ps, then decays on a $\sim$35 ps timescale till $\sim$100 ps without much change in spectral shape, until it reaches a constant value with an intensity of roughly 1/4 of its maximum (Fig. 3.39b).

At early times (first few picoseconds) the spectra are dominated by excitation and relaxation of the directly pumped C=O oscillator. The remainder of this signal is still visible in the spectra at 5.5 ps as a strong signal at the pumping frequency, 1716 cm^{-1} (Fig. 3.38c and g) or 1637 cm^{-1} (Fig. 3.38d and h). The vibrational lifetime of C=O vibrators is 1.2 ps (Fig. 3.39a), so after 5.5

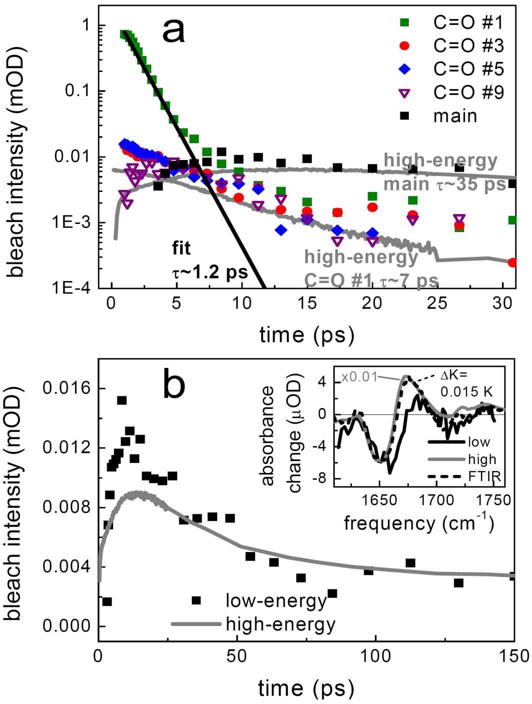

Figure 3.39: Time traces. a) The symbols are the bleach intensity (logarithmic scale and with opposite sign as in Fig. 3.38) as a function of time for C=O #1 to #9 and the main band. C=O #1, C=O #3 and the main band are obtained by low-energy excitation of C=O #1 in Aib16 (Fig. 3.38b), C=O #5 by low-energy excitation of C=O #1 in Aib34 (Fig. 3.38g), and C=O #9 by low-energy excitation of C=O #3 in Aib16 (Fig. 3.38d). The grey lines are the bleach intensity for C=O #1 and the main band after high-energy pumping (Fig. 3.38b) of the azobenzene moiety in Aib16, both downscaled by a factor 100. The black line is an exponential fit with $\tau = 1.2$ ps of the signal of C=O #1 at early times. If needed a baseline is subtracted from the data so that all signals for $t > 50$ ps are zero. b) Bleach intensity as a function of time for the main band after low-energy (black squares) and high energy (grey line, downscaled by a factor 100) excitation for Aib16 at long delay times. The inset shows the spectra 50 ps after low-energy excitation of Aib16 (black solid line, pumped at C=O #1) and high-energy excitation (grey, downscaled by a factor 100). The dashed line is a stationary temperature-induced difference spectrum of Aib16 corresponding to a temperature jump of 0.015 K.

ps this signal has decayed enough in amplitude not to obscure other spectral features. It is immediately clear from the spectrum at 5.5 ps that all oscillators feel an effect of the low-energy excitation: bands #1, #3, #5, and #9 all show a sharp bleach, in pronounced difference to the high-energy excitation case (Fig. 3.38b and f). To compare the amplitude and time dependence of the different signals, we plot in Fig. 3.39a the bleach intensities (with opposite sign) of the different bands on a logarithmic scale as a function of time. If needed, a flat baseline was subtracted from the data so that all signals for $t > 50$ ps approach zero. The data for low-energy excitation are depicted as symbols, while the response after high-energy excitation is depicted as grey lines for comparison. Already at 10-15 ps all C=O oscillators have roughly the same amplitude if we excite with low-energy photons, indicating that the energy is equilibrated over the whole molecule. It is immediately clear that the whole set of low-energy excitation data can be described with three time constants: 1.2, 7, and 35 ps. The main band shows a $\sim$35 ps decay time as in the experiments with high-energy excitation, reporting the dissipation of heat from the first solvent shells into the bulk solvent. The oscillator that is pumped (in Fig. 3.39a only C=O #1 is depicted but we observe the same decay for C=O #3 and C=O #5 if we pump these vibrators) decays bi-exponentially with a fast component of 1.2 ps, a typical T_1 time for the amide I band [164, 165]. At later times C=O #1 and all other oscillators show a common decay time of $\sim$7 ps (rate k_s in Fig. 3.40). In analogy to Ref. [55], we assign this signal to excitation of low frequency modes, to which the C=O vibrators are anharmonically coupled, and its decay to the dissipation of energy out of these low frequency modes into the surrounding solvent [139].

From the observation that all C=O groups have roughly the same bleach intensity at 10-15 ps (Fig. 3.40a), a lower limit for heat propagation through the chain can be obtained. We are unable to obtain an upper limit, because the signal till $\sim$5 ps is dominated by direct excitation of the C=O oscillators. If the process were ballistic, as argued recently by Wang et al. 1 for heat transport through a molecular chain (*n*-alkanethiol molecules), the velocity is at least 0.1 nm ps^{-1} (i.e. 6 times 2Å for each amino acids / 15 ps). On the other hand, when we assume diffusive heat transport (like in the high-energy excitation case [55], in other theoretical works [111, 115] and observed in an indirect way for energy transfer in phospholipid bilayer liposomes 4) we can extract an estimate of the thermal diffusivity from our rate-equation model schematically depicted in Fig. 3.40. To fully equilibrate heat after 15

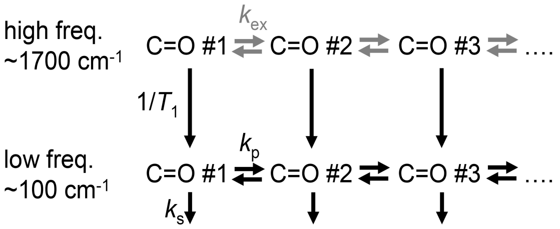

Figure 3.40: Schematic representation of the energy transport through the molecule. The grey arrows describe direct (excitonic) population transfer with a rate k_{ex}, while the black arrows illustrate energy transport through low-frequency modes with a rate k_p. Cooling to the solvent occurs with rate k_s. The lifetime of the high frequency modes is T_1.

ps over all C=O groups, an energy propagation rate of k_p >(0.5ps)$^{-1}$ is needed, corresponding to a thermal diffusivity $D > 8\text{Å}^2\text{ps}^{-1}$. Energy diffusion is thus at least four times more efficient after low-energy excitation (k_p >(0.5 ps)$^{-1}$) of one of the C=O bands compared to high-energy excitation (k_p ~(2 ps)$^{-1}$) of the azobenzene moiety.

From the amplitudes of the 50 ps spectra, we can estimate that the final temperature in the low-energy excitation experiment is 50 times less than in the high-energy one (taking into account the two times larger concentration in the UV-pump experiment). This result is expected based on the laser pulse intensities (~40 times less pulse energy in the narrow band low-energy pulse compared to the high-energy pulse) and the extinction coefficients (2-3 times lower for one C=O oscillator than for the $n-\pi^*$ excitation). The amount of energy per molecule immediately after excitation is ~14 times lower, because the photon energy is 23500 cm^{-1} (~3 eV) in the high-energy and 1700 cm^{-1} (~0.2 eV) in the low-energy case. Hence, 3 (50 divided by 14) times less molecules are excited in the low-energy pumping case. On the other hand, the signal at early times for group #1, measuring the heat in the helix, is 40-60 times stronger in the high-energy case compared to the low-energy case (Fig. 3.38), which follows from extrapolating the 7 ps component of C=O #1 after low-energy excitation to time zero and compare it to C=O #1 at time zero after high-energy excitation. As this signal at time zero is caused by 3 times more molecules in the high-energy excitation case, we conclude that indeed roughly 14 times more energy per molecule is present in the helix after high-energy excitation than after low-energy excitation (i.e. roughly equalling the ratio of photon energies).

3.7.4 Computational Results

To obtain a microscopic picture of molecular energy transport, we have performed nonequilibrium MD simulations of the high- and low-energy excitation cases. The main results of these simulations are comprised in Fig. 3.41, which shows the time evolution of the kinetic energy per atom of the peptide units along the helix. In the case of high-energy excitation (grey lines), the peak of the photoinduced energy reaches the first unit at about 0.3 ps. The time-delayed rise of the kinetic energies of the subsequent peptide units nicely illustrates the propagation of energy (or heat) along the peptide backbone. Using the simple rate equation model (Fig. 3.40), the time traces can be well fitted by assuming two transport rates, an exchange rate between two peptide units of k_p =(0.5 ps)$^{-1}$ and a dissipation rate to the solvent of k_s =(18 ps)$^{-1}$. Compared to the experimental findings, the energy transport along the peptide in simulation is thus about five times faster and the cooling rate is about two times slower [55].

In the case of low-energy excitation (red lines), the kinetic energy of the C=O oscillators is in overall about a factor of three lower than in the case of high-energy excitation. Due to the signal-to-noise ratio obtained from the average over 400 trajectories, the energy transport is hard to extract for distances larger than four peptide units from the excitation. Nevertheless, by using the same rate-equation model (Fig. 3.40), the data can again be modelled with a propagation rate k_p ~ (0.2-0.6 ps)$^{-1}$ and a cooling time to the solvent of k_s =(18 ps)$^{-1}$ (black lines in Fig. 3.41). However, it turned out to be necessary to explicitly include the initial, non-thermal, excitation of the high frequency C=O vibrator of group #1 and its 1/T$_1$1 vibrational relaxation into low frequency modes (see Fig. 3.40) into the fit. Neglecting this first step, the resulting fit of the kinetic energy of unit 1 (indicated by LF) starts significantly too low, while by plotting the sum of populations in both high frequency and low frequency modes (indicated by LF+HF) we obtain almost quantitative agreement. The deviation of the resulting fit of the kinetic energy of unit 2 for times $<$ 1ps indicates a small direct high-frequency energy transfer between C=O oscillators #1 and #2 (see Discussion).

To compare measured and calculated heat transport under low-energy excitation, Fig. 3.42 shows the time

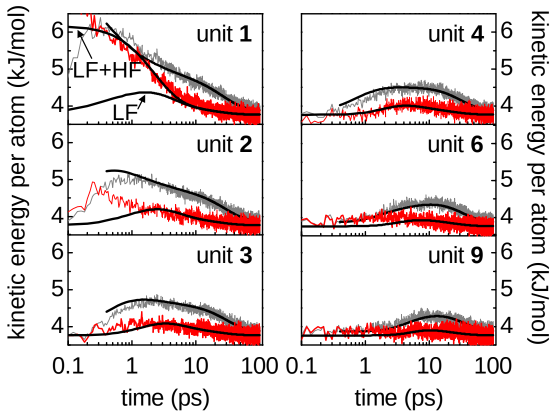

Figure 3.41: Time evolution of the dynamics of PAZ-Aib$_8$-OMe from the MD simulations. The mean kinetic energy of selected residues after high- (grey) and low- (red) energy excitation is plotted as a function of time. The black lines show global fits according to the model described in the text and for low-energy excitation schematically depicted in Figure 4. After low-energy excitation the C=O stretch vibration of C=O #1 is excited, a high frequency (HF) mode. Energy dissipates out of this mode with a time constant of 1.5 ps into low frequency (LF) modes around C=O #1. Subsequently, energy transport through the peptide units take place with a time constant of 0.4 ps. Cooling to the solvent occurs on a 18 ps timescale.

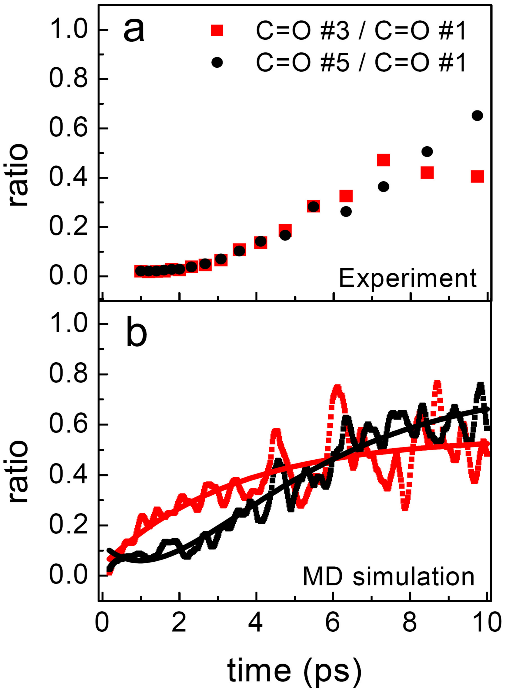

Figure 3.42: Comparison between experimental signals and simulation results. Shown are (a) the signals of sites C=O #3 (red) and C=O #5 (black) normalized to C=O #1 as well as (b) the corresponding calculated site-specific kinetic energy ratios [166]. For better comparison, the calculated rough data (dashed lines) were fitted by biexponential functions (full lines).

evolution of the bleach amplitude of the sites C=O #3 and #5 normalized to the amplitude of C=O #1 as well as the corresponding calculated result 43. These ratios start out at zero at $t = 0$ since C=O #1 is initially populated (but not yet C=O #3 and #5), and trend to one as population equilibrates throughout the helix. Both experimental and calculated curves are seen to rise on the same time scale and in a similar fashion. For times larger than 10 ps the signal-to-noise ratio hampers a detailed comparison. Nevertheless, it is clear that the agreement of theory and experiment is clearly better for low- than for high-energy excitation.

3.7.5 Discussion

Several of the results presented above appear surprising on a first account. In particular, our experiments have shown that the energy transport is significantly more efficient for low-energy excitation (although there is much less energy available) than for high-energy excitation. On the other hand, the MD calculations have revealed quite similar energy propagation rates in both cases. Two obvious differences come into one's mind for the two excitation scenarios: (a) In contrast to UV pumping, in the low-energy pump experiment we start with a direct excitation of C=O vibrations, which may delocalize significantly and to form excitonic states. (b+c) The energy deposited in the UV-pump case is considerably larger. We will discuss in the following how these two effects could affect energy transport.

(a) Excitonic Transport: It is well established that C=O vibrators in regular peptide structures form excitonic states that can be delocalized significantly [167–169]. In contrast to the high-energy excitation experiment, we directly excite these C=O vibrators in the present experiment. We therefore need to discuss to what extent excitonic coupling may facilitate energy transport, before T_1 relaxation randomizes energy. Excitonic coupling may contribute in two ways. Firstly, the C=O excited state might delocalize significantly so that vibrational energy would be present throughout the helix right after pumping. Typical excitonic through-space couplings in peptide helices are in the order of a few wavenumbers (e.g. in the case of an α-helix, the couplings have shown to be $\approx$5 cm^{-1} [170]). To obtain an estimate of the associated delocalization, we have employed a model exciton Hamiltonian [169], which assumes 5 cm^{-1} for nearest and next-nearest neighbour couplings and chooses diagonal site frequencies in order to reproduce the measured IR spectrum. For an isotope shift of $\approx$-30 cm^{-1}, we find that the excitation of the labelled C=O group localizes to about 96%. The same is true for group #9, which blue-shifts by about 70 cm^{-1} due to its different chemical nature (i.e. an ester group), thus yielding a localization of 99%. Furthermore, the spatial overlap of both eigenstates is negligible and direct excitonic transport between, e.g., group #3 and #9 (open triangles in Fig. 3.39) seems very unlikely.

The second way how exciton coupling might contribute is through dissipative energy transport between C=O vibrators directly (i.e. grey arrows and rates k_{ex} in Fig. 3.40). For one of the smallest possible building unit, trialanine, a typical timescale of this direct hopping process between two essentially localized states of 5-15 ps has been reported [164]; too slow to efficiently compete with T_1 relaxation. However, in the present case, two localized states are bridged by the main band, which consists of six largely delocalized states. It has in fact been shown that energy dissipation within delocalized excitonic states can be very efficient on a 500 fs timescale [171]. The dissipation of a localized state into such a bridge of delocalized excitonic states, and out of it, has not thoroughly been studied yet. Nevertheless, along the lines of Andersen localization [172], the spatial overlap for both transfer steps is still small, and therefore presumably inefficient (further theoretical studies will be needed to ultimately rule out the contribution of excitonic coupling between C=O states as a possible pathway of energy transport). Hence, we assume that heat transport goes predominantly through low frequency modes after T_1 relaxation is finished. Similar conclusions were drawn by Kurochkin et al. [173] for energy transport between C-N and C=O oscillators in small organic molecules. This hypothesis is also supported by our MD simulations, which showed only a small contribution of excitonic transfer from group #1 to #2 (see Fig. 3.41).

(b) Nonlinear Diffusion Equation: Consider the one-dimensional heat diffusion equation:

$$\frac{dT}{dt} = D_T \frac{d^2T}{dx^2} \tag{3.23}$$

which can be regarded as a continuous version of the rate-equation model introduced above. The usual derivation of this theory assumes that the energy gradients ΔT are much smaller than the background temperature T. Only in this limit the thermal diffusivity D_T is independent of temperature during heat propagation, revealing the linear regime of the heat diffusion equation (which is the regime normally considered). For low-energy excitation we presumably are in this regime $\Delta T \ll T$. However, after high energy excitation, the temperature jumps can easily approach the background temperature $\Delta T \approx T$. To study the temperature dependency of the thermal diffusivity, we adopt a simple harmonic model of one-dimensional diffusive transport as pursued by Yu and Leitner [111] and others [174]. Within this theory, the thermal diffusivity can be written as:

$$D_T = \frac{\int d\omega \rho(\omega) c(\omega) D(\omega)}{\int d\omega \rho(\omega) c(\omega)} \tag{3.24}$$

where $\rho(\omega)$ is the density of normal modes, $c(\omega)$ the contribution of a particular normal mode to the total heat capacity (depending on the occupation of a particular normal mode) and $D(\omega)$ the contribution of that normal mode to energy diffusion. This expression can be interpreted as a weighted sum over all contributions $D(\omega)$ to the total diffusivity, where $\rho(\omega)c(\omega)$ is the weighting factor. Of this three parameters, only the heat capacity per normal mode $c(\omega)$ is strongly temperature dependent

$$c(\omega) = \frac{(\hbar\omega)^2}{k_B T^2} \frac{e^{\beta\hbar\omega}}{(e^{\beta\hbar\omega} - 1)^2} \tag{3.25}$$

with $\beta = 1/k_B T$. This function increases strongly with temperature till it reaches the classical limit at $k_B T \approx \hbar\omega$, with a steeper slope for lower frequency modes. Therefore, higher-frequency modes become more important for the thermal diffusivity at higher temperatures in a relative sense. However, these high-frequency modes have a smaller diffusivity, because they tend to be more localized [111]. Therefore, the thermal diffusivity D_T decreases with temperature.

To estimate the magnitude of this temperature dependency, we have performed instantaneous normal mode calculations [175, 176] using our nonequilibrium MD trajectories. Fig. 3.43 shows the resulting density of normal modes pertaining to the photoswitchable peptide

$$\rho(\omega) = \rho_0 \sum_{r=1}^{N_{traj}} \sum_{k=1}^{N_{mod}} \int dt \rho(\omega - \omega_k^{(r)}(t)) \qquad (3.26)$$

averaged over all normal modes ω_k, trajectories r, and times t between 1 and 10 ps (in total 50000 snapshots were taken into account). As typically found for peptides, $\rho(\omega)$ shows a pronounced low-frequency band as well as the signatures of various bond stretching modes with frequencies between 1000 and 2000 cm^{-1}. Of particular interest here are instantaneous normal modes with imaginary frequency, which are represented in Fig. 3.43a by negative values of the frequency. Depending on the instantaneous conformation of the molecule, these modes account for unbound motion on inverted parabola and therefore reflect (within the limits of instantaneous normal mode theory [177]) the transport properties of the system. The typical frequency of 100 - 200 cm^{-1} obtained for these modes agrees well with the frequency of strongly delocalized modes in proteins [111]. To obtain an estimate of the diffusion constant $D(\omega)$ in Eq. 3.24) we therefore assume that only normal modes below a certain cut-off frequency ω_C contribute to $D(\omega)$ and approximate $D(\omega)$ by a simple step function with the value 1 below ω_C and 0 above it 55. The cut-off frequencies used are ω_C =50, 100, and 200 cm^{-1} in this case study, representing situations where different sets of normal modes are important for the thermal diffusivity. Fig. 3.43b shows the resulting thermal diffusivity D_T plotted as a function of temperature. As expected from the discussion above, we find that D_T significantly decreases with temperature. Assuming UV excitation with an initial temperature of 600 K, the thermal diffusivity may be reduced to ~50% of its value at 300 K. Hence, the temperature dependence of D_T may explain a factor 2 in the reduction of the heat transport. This is a significant factor but not quite the factor >4 we observe for the ratio of the low- and high-energy excitation case experimentally.

(c) Intra-site Relaxation Preceding Energy Transport: However, this factor 2 in D_T might just be a lower limit of the observed excitation energy dependence of heat transfer. The heat diffusion equation Eq. 3.23 implicitly assumes, by the very use of the concept of a local temperature, that the hot site thermalizes instantaneously as energy flows out through its lower frequency part of the spectrum. In other words, Eq. 3.23 implicitly assumes that thermalization *within* one individual peptide unit is significantly faster than thermalization *between* units. However, with a hopping rate between adjacent sites as fast as k_p =(0.5 ps)$^{-1}$, this is hardly possible. In fact we know, for example, that depopulation rate of the initially excited C=O vibration is $1/T_1$ =(1.2 ps)$^{-1}$, and similar timescales are expected for subsequent relaxation steps as energy cascades down [178, 179] from higher to lower energy states within one peptide unit.

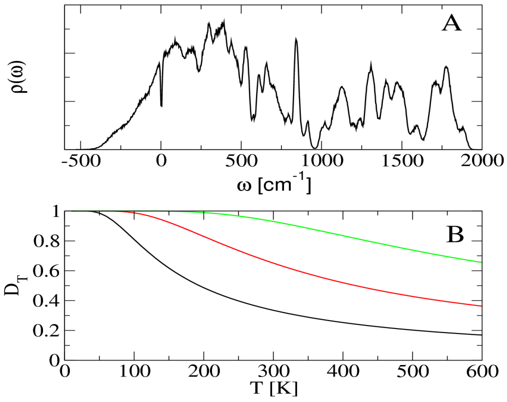

Figure 3.43: (A) Density of normal modes $\rho(\omega)$ of the photoswitchable peptide as obtained from instantaneous normal mode calculations using nonequilibrium MD trajectories. Instantaneous normal modes of imaginary frequency are represented by negative values of ω. (B) Thermal diffusivity D_T as a function of temperature, calculated from Eq. 3.24 using the instantaneous normal modes calculation. As further explained in the text, the frequency-dependent diffusion constant $D(\omega)$ was approximated by a step function with cut-off frequency (black) 50, (red) 100, and (green) 200 cm^{-1}.

The difference between the two scenarios is illustrated in Fig. 3.44. In either case, energy is deposited at site #1; however, at low excitation levels (Fig. 3.44a), this does not lead to significant changes of thermal population. In contrast, after high-energy excitation (Fig. 3.44b), higher-frequency states, which tend to be localized, get thermally excited at a temperature that locally exceeds that of the surrounding by a large amount. As these localized modes hardly contribute to energy transfer, the subsequent relaxation cascade (rate k_c in Fig. 3.44b) to delocalized low-frequency modes may represent the rate-limiting step rather than hopping from site to site k_p [178, 179]. However, we wish to stress that the two relaxation processes k_c and k_p, which at a first sight might appear to be distinctly different, might actually have the same physical origin. At the low excitation levels of the IR experiment, on the other hand, repopulation between vibrational modes does not really occur (Fig. 3.44a) and cooling within the individual peptide units will not be rate-limiting. We are currently developing an idealized model along the lines of Fig. 3.44, trying to reproduce this effect and understand it in more detail.

We now turn to the discussion of the MD results, which were found to be surprisingly insensitive with respect to the excitation energy. This finding is, at least in part, also explained by the above discussed temperature dependence of D_T, which resulted from the quantum-mechanical calculation of the specific heat. In classical MD simulations, however, the heat capacity per normal mode, $c(\omega)$, is constant with temperature. Consequently, following Eq. 3.24, the thermal diffusivity D_T will be essentially temperature independent and the heat diffusion Eq. 3.23 will be linear even under conditions of high-energy excitation.

Furthermore, the MD simulations underestimate the amount of energy arriving in the helix after high-energy excitation. Although high-energy excitation of the azobenzene moiety deposits 14 times more energy in the molecule than direct low-energy excitation of the first C=O group, the difference of kinetic energy for unit #3 to #9 is only ~3 times higher in the MD case (Fig. 3.41). Hence, a significant amount of the energy deposited in the azobenzene moiety does not reach the peptide but dissipates directly into the solvent during the isomerization process [55]. In contrast, from the experiments we deduce that the factor 14 of the photon energies indeed remains once the energy arrives in the helix. Compared to experiment, the calculated energy loss during isomerization of the azobenzene moiety is therefore significantly larger, which most likely is due to our simple model employed to describe the initial *cis-trans* photoisomerization of azobenzene. Disregarding virtually all aspects of multidimensional nonadiabatic photodynamics [180], our simplistic ansatz to initially deposit the entire photon energy in the central N=N torsion of azobenzene naturally effects that a large fraction of the initial energy is transferred directly into the solvent. To obtain a more realistic modelling of the initial step, true nonadiabatic *ab inito* MD simulations are required [181–183].

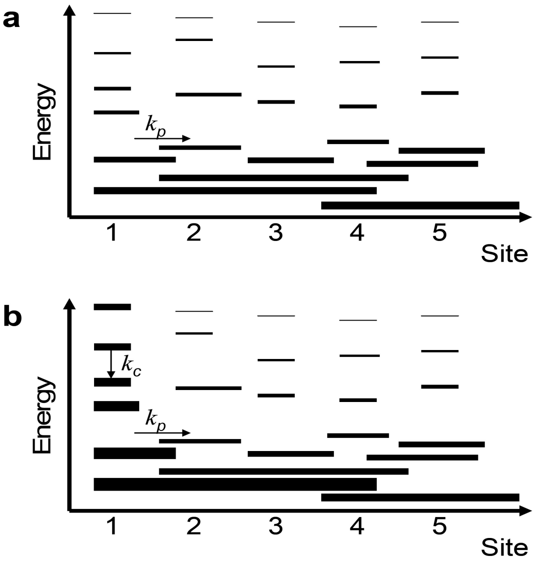

Figure 3.44: Sketch of 'thermal self-trapping'. Comparing (a) low-energy and (b) high-energy excitation, vibrational energy levels and their localization/delocalization over various sites are shown. The thickness of each line represents the population of the corresponding state. In either case, energy is deposited at site 1. At low excitation levels (a), this does not lead to significant changes of thermal population. In contrast, after high-energy excitation (b), high-frequency vibrational states, which tend to be localized, get thermally excited at a temperature that locally exceeds that of the surrounding by a large amount. Cascading of this energy down to the conducting low frequency modes with rate kc might then be the rate limiting step in energy transport (i.e. if $k_c < k_p$). The two relaxation processes k_c and k_p might have the same physical origin.

3.7.6 Conclusion

In the present paper, we have compared energy transport through a model peptide helix after high- and low-energy excitation in a combined experimental-computer simulation study. In the first case, energy is deposited through a photochemical reaction, whereas direct vibrational excitation has been used in the second case. This difference has not only a consequence for the amount of energy deposited, but also the form in which it is provided. Whereas energy is offered in an at least randomized, if not thermalized, form starting from the very beginning due to the impact of the isomerizing azobenzene-moiety on the helix [55, 58], the excitation process is mode specific in the second case. The concept of a local temperature becomes applicable only once energy is thermalized, which actually limits the effective time-resolution of the IR-pump experiment to a timescale dictated by the T_1 lifetime of the initially excited vibrator.

In our experiments, we find that energy transport occurs at least four times more efficient after low-energy excitation of a C=O group than after high-energy excitation of the azobenzene moiety. For IR excitation, we deduce a thermal diffusivity of $\approx 8\text{Å}^2\text{ps}^{-1}$ (or larger), in good agreement with experimentally and theoretically established values [111–113, 115]. We attribute the excitation-energy dependence of heat transport to three possible effects: (a) In the low energy experiment, C=O modes are excited directly, which may transport energy through excitonic coupling before T_1 relaxation is complete. Although appearing unlikely at the present stage, we cannot completely rule out this possibility. (b) When thermal gradients within the chain become large, $\Delta T \gg T$, the temperature dependence of the thermal diffusivity can no longer be neglected and the heat diffusion equation becomes nonlinear. Estimates of the size of this effect, based on the density of normal modes, result in a factor of about two. (c) Thermalization within individual peptide units is not necessarily ultrafast, and may further slow down the process. In particular, in the case of high-energy excitation, localized higher-frequency modes are thermally excited which do not directly contribute to energy transfer, but undergo a subsequent relaxation cascade to delocalized low-frequency modes.

The nonequilibrium MD simulations, on the other hand, did not reproduce the measured excitation-energy dependence of heat transport. We attribute this failure, in part, to the classical nature of the calculations, which results in a temperature-independent specific heat. Consequently, the thermal diffusivity D_T will be essentially temperature independent, too, and the heat diffusion will be linear even under conditions of high-energy excitation. Furthermore, the MD simulation overestimates the initial energy loss into the solvent during photoisomerization process. Most likely, this is due to our simple model employed to describe the nonadiabatic *cis-trans* photoisomerization of azobenzene. We note that both problems of the MD simulations only occur for UV excitation. In fact, the agreement of theory and experiment is clearly better and almost quantitative in the lower energy regime of the IR excitation. Hence, the present study resolves the problem with the unexpectedly low value for thermal diffusivity of $\approx 2\text{Å}^2\text{ps}^{-1}$ obtained in our previous study for high-energy excitation [55].

For most biophysical processes, where temperature gradients are expected to be small, the low-energy value of the thermal diffusion constant will be relevant and the heat diffusion equation will be linear. However, in photobiological processes such as the photoisomerization of retinal in bacteriorhodopsin [184, 185] or rhodopsin [186], the photodissociation of CO from myoglobin [124, 187], or the quenching of excitation energy in antenna complexes by carotenoids [188], it is not uncommon that the energy equivalent of a visible or UV photon is dissipated into the vibrational system of a protein on an ultrafast subpicosecond timescale, similar to our model system after photoisomerization of the azobenzene moiety. In this case, one might enter a nonlinear regime of heat diffusion, which leads to trapping of energy on a few picosecond timescale: energy gets trapped in localized high-frequency modes by the very form of the Boltzmann distribution (Fig. 3.44b), or, even more so, by a non-thermal distribution in even higher frequency modes. Note that this effect is distinctively different from vibrational self-trapping discussed in the context of Davidov's solitons [54] or vibrational polarons [189, 190] in that it does not rely on vibrational anharmonicity in a molecular chain with close to perfect translational symmetry. In fact, the effect described in this paper requires a certain amount of disorder characteristic for glasses and proteins, since only then we are in a situation where low-frequency modes are delocalized and contribute to energy transport, while high-frequency modes are localized. We might call the effect 'thermal self-trapping'.

3.7.7 Acknowledgments

We thank David Leitner as well as Dana Dlott for instructive discussions on the topic of this paper. The work has been supported by the Netherlands Organisation for Scientific Research and the Forschungskredit of the University of Zurich through postdoctorate fellowships to E.H.G.B. and by the Swiss Science Foundation (Grant 200020-115877), the Frankfurt Center for Scientific Computing, the Fonds der Chemischen Industrie, and the Deutsche Forschungsgemeinschaft.

3.8 Structural flexibility of a helical peptide regulates heat transport properties

Ellen H. G. Backus, Phuong H. Nguyen, Virgiliu Botan, Alessandro Moretto, Marco Crisma, Claudio Toniolo, Oliver Zerbe, Gerhard Stock, Peter Hamm

J. Phys. Chem. B, submitted (**2008**)

Abstract

Applying ultrafast vibrational spectroscopy, we find that heat transport along a helical peptide changes from inefficient but mostly ballistic below ≈ 270 *K*, into diffusive and significantly more efficient above. Based on molecular dynamics simulations, we attribute this change to the increasing flexibility of the helix above this temperature, similar to the glass-transition in proteins. Structural flexibility enhances intramolecular vibrational redistribution, thereby re-feeding energy into the few vibrational modes that delocalize over large parts of the structure and therefore transport energy efficiently. The paper outlines concepts how one might regulate heat transport properties in ultrafast photobiological processes, as well as in molecular electronic devices, by engineering the flexibility of their components.

3.8.1 Introduction

Heat transport is not only relevant in the macroscopic world, but also on the molecular scale of biomolecules and nanostuctures. To avoid overheating, e.g., after a photochemical reaction, excess energy needs to be removed efficiently [191]. Proteins transport energy through specific pathways to function as molecular machines [192]. Furthermore, an understanding of heat transport is an important prerequisite for the development of molecular electronic devices [193]. Despite its significance, very little experimental work has been done to unravel the molecular mechanisms of heat transport in *real space* (to discriminate it from intramolecular vibrational redistribution which is typically studied in *energy* or *state space*). Most studies have concentrated on the energy flow from a heme group in proteins into the surrounding solvent [121–124], which has been attributed to the transport through the propionate side chain [117]. The latter is part of the heme moiety and connects it directly to the protein surface. In systems other than proteins, energy transport phenomena have been measured, e.g. through bridged azulene-anthracene compounds [127], small molecules in solution [128], or through model membranes [129].

Employing time-resolved infrared (IR) spectroscopy and molecular dynamics (MD) simulations, we have recently suggested that heat transport along a peptide helix occurs in a diffusive manner with the mean distance increasing only with the square-root of time, $\langle \Delta x^2 \rangle \propto t$ [55, 59]. From the distance dependence of the peak temperatures we have concluded that diffusion occurs in 1D, i.e. along the helix and not through the solvent. In contrast, the heat transport through densely packed self-assembled monolayers of long-chain hydrocarbon molecules was shown to propagate ballistically, i.e. linear in time $\Delta x \propto t$ [156]. This discrepancy raises the question about the physical origin of these two mechanisms. Being densely packed, the latter system is probably more ordered and less flexible, which may facilitate a ballistic mechanism. In the present paper, we use temperature as a parameter to control the conformational stability of the peptide helix. We find that the structural flexibility significantly increases in a relatively narrow temperature range (260-280 K), thereby changing the mechanism of heat transport.

Our model system (Fig. 4.1A) consist of a α-aminoisobutyric acid (Aib)-rich segment with a strong propensity to fold into a 3_{10}-helix [136]. Attached to the helix is a chromophore, azobenzene, which undergoes a cis-trans isomerization after photoexcitation on an 200 fs timescale, depositing an energy equivalent of a local temperature which can be as high as $\approx$1000 K [55, 59].

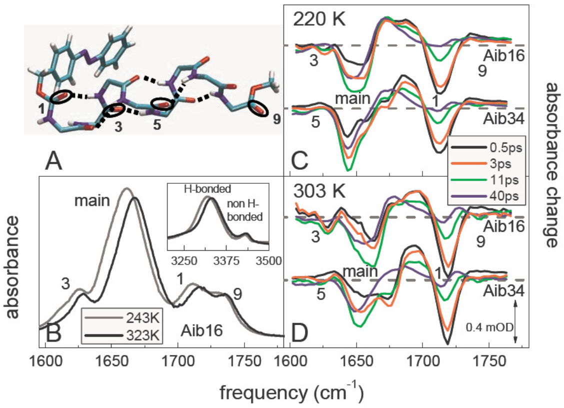

Figure 3.45: Molecular system and its stationary and transient pump-probe spectra. (A) X-ray diffraction structure of the peptide-backbone (amino acid side chains are not shown) [55]. The labels #1 to #9 count C=O sites with increasing distance from the azobenzene moiety. (B) FTIR absorption spectra of Aib16 at 243 and 323 K in the C=O and NH (inset) spectral regions. (C) Transient difference spectra of Aib16 and Aib34 at 220 K at specific times after pumping the molecule in the cis configuration with a 100-150 fs pulse of 425 nm. (D) Same, but at 303 K. The data at all times are normalized to reveal identical temperature jumps by comparing the spectra at 95 ps to corresponding FTIR difference spectra [55].

The subsequent propagation of heat along the helix is monitored via C=O reporter groups, whose vibrational bands experience frequency shifts together with a broadening upon heating due to anharmonic coupling to thermally excited low-frequency modes [58]. As long as the anharmonic shifts are small compared to the vibrational linewidth of the spectator mode, one may assume that the size of the response is a linear measure of the amount of vibrational energy in the vicinity of the probe. Note that such anharmonic shifts are obtained although direct thermal excitation of the C=O reporter groups is extremely unlikely even at the high temperatures achieved in the experiment ($\hbar\omega/k_B T \ll 1$). Furthermore, we note that this response may include many low frequency modes; hence we cannot deduce whether energy is thermalized or not.

In order to introduce site specificity, certain amino

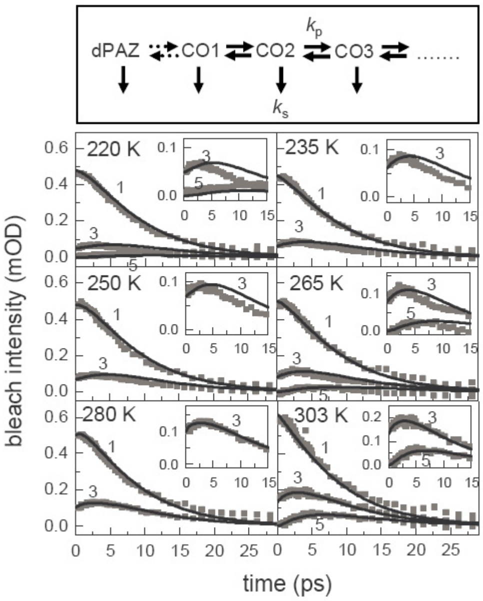

Figure 3.46: Energy transport: Time dependence of the bleach intensity (with opposite sign as in Fig. 4.1 and background corrected) of sites #1, #3, and #5 (symbols) at different temperatures. Band #1 and #3 originate from Aib16, and band #5 from Aib34 (site #5 has been measured only for three temperatures). The black lines show global fits according to a master equation (see top panel, the scheme is expanded on the right till site #9) with a cooling rate (k_s) to the solvent of 7 ps for all temperature and a diffusive heat transport rate constant (k_p) varying from 1.5 ps at high temperature (303 K) to 5 ps at low temperature (220 K). Heat is initially deposited in the dPAZ compound as well as to sites #1 to #3. After the initial heat deposition the helix is basically decoupled from the dPAZ unit (therefore the dotted arrow in the scheme), although a very weak heat transport is needed to explain the experimentally obtained flatness of the signal for site #1 in the first picosecond [55].

acids (one at a time) were ^{13}C-isotope labelled to distinguish their frequency from the remainder. Since ^{13}C=O-Ala is more readily available than ^{13}C=O-Aib, we used the former, resulting in only a very little destabilization of the 3_{10}-helix [55]. Fig. 4.1B exemplifies the IR spectrum of dPAZ-Aib-^{13}C-Ala-Aib$_6$-OMe (called Aib16 in the following), where dPAZ (deuterated 4-phenyldiazenyl-benzyloxycarbonyl) is the azobenzene moiety used for local heating. The bands at ≈1625, 1660, 1720 and 1730 cm^{-1} are assigned to the isotope labelled site #3, the main band originating from all the non-labelled amino acids, C=O #1 (an urethane group) and C=O #9 (an ester group), respectively. Site #3 is red-shifted from the main band by ≈35 cm^{-1} due to isotope labelling, whereas sites #1 and #9 are blue-shifted because of their different chemical environment. Using dPAZ-Aib$_3$-^{13}C-Ala-Aib$_4$-OMe (Aib34) in addition, which exhibits a very similar IR spectrum (not shown) as Aib16 with the exception that the lowest frequency band now originates from site #5, we have introduced local thermometers at sites #1, #3, #5, and #9. The molecules were dissolved in chloroform (concentration ≈8 mM), a weakly interacting solvent of low polarity, thereby minimizing heat transport into the solvent as well as mimicking the hydrophobic environment inside a protein. Furthermore, chloroform remains liquid in the temperature range of interest.

3.8.2 Material and Methods

Synthesis: Deuterated PAZ-Aib-OH was synthesized by nitrating toluene-D$_8$ to *p*-nitrotoluene, oxidizing to *p*-nitrobenzoic acid, reducing with zinc to *p*-aminobenzoic acid, and then making the methyl ester using methanol and thionyl chloride. Reduction of the ester with lithium-aluminium-deuteride [147] leads to the full deuterated *p*-aminobenzyl alcohol. Nitrosobenzene-D$_5$ was obtained by reduction of nitrobenzene-D_5 as described in Ref. [148]. Coupling these two deuterated compounds and covalently linking the resulting alcohol to L-Ala* and Aib was performed in the same way (via PAZ-Cl) as reported in Ref. [134, 149]. Peptide synthesis was performed in solution by activating the carboxyl function with 1-(3-dimethylaminopropyl)-3-ethylcarbodiimide and 7-aza-1-hydroxy-1,2,3-benzotriazole [150]. For details of the peptide synthesis and the characterization of the molecules by IR, NMR and x-ray diffraction, we refer to Ref. [55].

Time Resolved Experiments: The peptides were investigated by UV-pump-IR-probe spectroscopy exciting *cis*-azobenzene at a wavelength of 425 nm, and probing the amide I region with an IR-probe pulse centered at 1680 cm^{-1} (spectral width 200 cm^{-1}). The probe pulse was frequency dispersed in a spectrometer and imaged onto a 64 channel IR array detector covering the total region of C=O vibrations. The time resolution of the apparatus was 200 fs. The sample was dissolved in CHCl$_3$ at a concentration of typically 10 mM, circulated in a closed cycle CaF$_2$ flow cell inside a temperature controlled N$_2$ flow cryostat with optical path length of 100 μm, and continuously irradiated with cw-light at 320 nm (FWHM 70 nm) from a properly filtered Hg-lamp in order to accumulate the cis-species to about 80%.

Computational Methods: All simulations were performed with the GROMACS program suite [151], using the GROMOS96 force field 43a1 [152] to model the PAZ-Aib$_8$-OMe peptide and the rigid all-atom model of Ref. [153] to describe the chloroform solvent. Additional force field parameters for the azobenzene unit were derived from density functional theory as described in Ref. [154]. Starting with a 3_{10}-helical conformation, the PAZ-Aib$_8$-OMe peptide was placed in an octahedral box containing $\approx$ 700 chloroform molecules. After energy minimization, the system was simulated for 40 ns at NTP conditions (1 atm, 300 K). For details, see Ref. [55].

3.8.3 Experimental Results

Fig. 4.1C,D shows transient UV-pump-IR-probe difference spectra of Aib16 and Aib34 for 220 K and 303 K, respectively. At 303 K (Fig. 4.1D), strong sharp bleach signals are observed already 0.5 ps after photo-excitation for site #1 in both molecules Aib16 and Aib34, as well as for site #3 in Aib16 (black spectra). The instantaneous appearance of these signals results from the impact of the photo-isomerizing azobenzene moiety [55]. Subsequently, band #1 decays, while band #3 first increases, peaks at $\approx$3 ps, and decays afterwards. Comparing Figs. 4.1C and 4.1D, it is clear that less heat reaches site #3 at lower temperatures. A comparable bleach signal is measured for site #5 (via Aib34) only after $\approx$3 ps at higher temperatures. The main band, as well as band #9, exhibits a growing blue shift at later times, which we attribute to a secondary effect, i.e., a slight destabilization of the hydrogen bonds due to heating of the bulk solvent [55].

The dynamics of sites #1, #3 and #5 are summarized in Fig. 3.46 at a series of solvent temperatures. At sufficiently long delay times, signals at all sites #1, #3, and #5 decay exponentially with a time constant of $\approx$7 ps. As discussed in our previous paper [55], such a bleach – originating from anharmonic shifts due to thermal excitation of low-frequency modes [58] – associated with a $\approx$7 ps decay component – known as a typical cooling time in chloroform [139] – is assigned to heat in the vicinity of the corresponding C=O group. Vibrational energy is relayed from site #1 over #3 to #5 with maxima that appear in a sequential order. Note that we did not observe any heat signal for site #5 in our previous report were the temperature was only a few degrees lower [55]. This is due to the lower peptide concentration in this new set of experiments, resulting in a higher heat signal relative to the interfering secondary effect of the main band (which originates from heating of the bulk solvent and hence also includes contributions from unpumped molecules).

At temperatures $\geqslant$ 280 K, the overall response can be very well described using a simple rate-equation model (master equation Fig. 3.46, top panel), in which each site exchanges heat with the nearest neighbors (propagation rate k_p) and at the same time cools into the solvent (cooling rate k_s). To better mimic the experimental results, an initial intensity is given to sites #1 to #3 at time zero, corresponding to the impact of the switching azobenzene moiety. A fit of the data for 303 K (black line) reveals a cooling rate k_s=(7 ps)$^{-1}$ and a propagation rate k_p=(1.5 ps)$^{-1}$, slightly faster than the (2 ps)$^{-1}$ previously obtained at room temperature [55]. At lower temperature, heat propagation drops, e.g., at 280 K the fit gives k_p=(3 ps)$^{-1}$ while the cooling rate k_s remains essentially constant. Surprisingly, though, the diffusive model can no longer describe the data at 265 K and below (see insets in Fig. 3.46). If the fit is forced to model the intensity of signal #3 correctly, the maximum appears too late, whereas, *vice versa*, adjusting the time of the maximum renders the intensity too large. Within the framework of a diffusive model, reducing the propagation rate k_p will reduce the amplitude at site #3, since it is in competition with cooling into the solvent k_s, but at the same time will also delay its appearance. Apparently, at low temperatures the transport is no longer diffusive. Only a relatively small fraction of the total energy is still transported at low temperatures, however, on a timescale faster than a diffusive model would predict. Since diffusion is related to slowing down a process due to scattering events, we conclude that this small fraction of energy is transported in mainly a ballistic manner.

To compare the transport efficiencies at different temperatures in a model-independent way, Fig. 3.47A depicts the intensity raise of band #3 from time zero to the time when it reaches its maximum, normalized to the intensity of site #1. We relate the latter to the heat that had entered the helix. The heat transport capability is essentially constant from 220 to 265 K and then, more or less suddenly, rises steeply with temperature. This finding is surprising for two reasons: First, the common theory of heat transport in proteins predict a

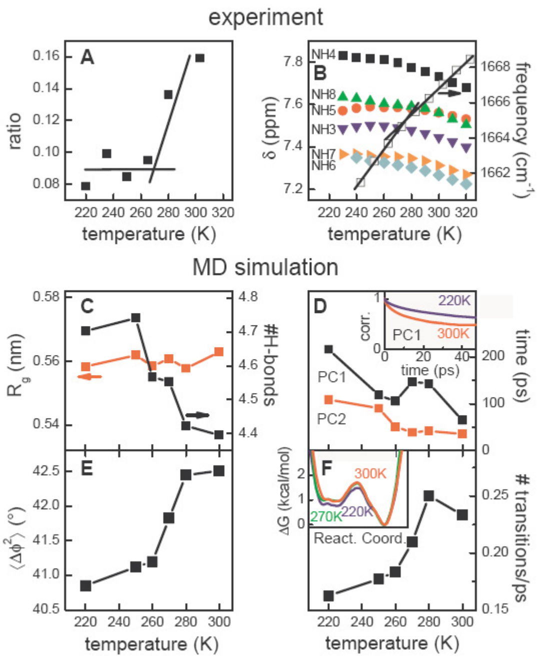

Figure 3.47: Comparison of experimental and MD results: (A) The heat signal increase of site #3 divided by the instantaneous heat at site #1 (the data are corrected for the decay of the instantaneous heat of site #3). The lines are to guide the eye. (B) Frequency of the main band of Aib34 as a function of temperature (right axis) and chemical shifts of the H-bonded amide protons (left axis) of Aib34 as a function of temperature, measured at 500 MHz proton frequency. Sequential resonance assignments were based on ROESY data, and the position of Aib following Ala was confirmed by ^{13}C-decoupling. (C) Average number of helix-stabilizing hydrogen bonds (black, right axis) and radius of gyration (red, left axis), calculated from the MD simulation. (D) Decay time τ of an stretched-exponential fit $\exp(-t/\tau)^{0.5}$ to the autocorrelation function (see inset) of the first two dihedral angle principal components (PC1 and PC2). (E) Root mean square fluctuations of all backbone dihedral angles. (F) Number of inter-basin transitions between the two dominant free-energy basins shown in the inset along a linear combination of its first two principal components.

gradual, monotonic *decrease* of thermal diffusivity with temperature [111, 112, 194], in contrast to our observation (Since Fig. 3.47A is a relative measure, it refers to the thermal *diffusivity*, and not the thermal *conductivity*; the latter would indeed increase with increasing temperature [112]). Second, the fact that not only the size (Fig. 3.47A), but also the temporal response (Fig. 3.46, insets) changes character around 260-280 K supports the conclusion that some sort of transition is taking place at this temperature.

The bulk solvent, chloroform, does not undergo any phase transition in the temperature range from 260-280 K (its melting point is 210 K). Furthermore, the intensity ratio between the two bands in the NH region (Fig. 1B, inset), which is indicative for a 3_{10}-helix [56], does not change with temperature, evidencing that the helix remains intact over the whole temperature range. These two bands originate from the intra-helical hydrogen bonded and N-terminal non-hydrogen bonded amide protons. The small change in the slope of the vibrational frequency of the main band as a function of temperature (Fig. 3.47B), on the other hand, possibly indicates a change in flexibility of the helix. To further support this interpretation we have also measured proton NMR spectra (Fig. 3.47B): At temperatures below ≈260-280 K, only minor temperature coefficients are obtained, while they are considerably larger above, consistent with the view that the corresponding hydrogen bonds become less persistent. We also know from the NMR measurements that the molecules aggregate to a certain extent at the concentrations used, most likely in a head-to-tail manner. This effect is superimposed to the temperature dependent flexibility of the molecule and hence hampers an unambiguous interpretation of the NMR data. We have however verified through concentration dependent measurements (ranging from 3 mM to 15 mM, only maximal 10% of the molecules aggregate at the lower concentration) of the effect shown in Fig. 3.46 that the essential observation of this work, i.e. the switch of energy transport from ballistic to diffusive as a function of temperature, is not affected at all by aggregation.

It is interesting to note that the shape of the curve in Fig. 3.47A strongly resembles the signatures of a glass transition in proteins [195]. The glass-transition is a dynamical transition occurring at ≈200 K in proteins, whose physical origin, however, is still discussed controversially [195–204]. In simple words, the molecules are trapped in various, essentially harmonic energy basins below the glass temperature T_g, whereas they are free to structurally diffuse above. Although the concept of a glass-transition in the context of peptides is by far less documented in literature, it has been used, e.g., to characterize the folding properties of small peptides that do form well-defined secondary structures [205, 206].

3.8.4 Simulation Results

To support the view of a glass-transition for our model system, we performed all-atom MD simulations. Overall, we found that the structure of the helix changes only little with temperature. As an example, Fig. 3.47C shows that the radius of gyration virtually remains constant at all temperatures, which is in agreement with the small change of the NH spectrum in Fig. 4.1B, inset. However, the average number of helix-stabilizing hydrogen bonds clearly drops above the transition temperature (Fig. 3.47C), in agreement with the NMR results (Fig. 3.47B). At the same time, the fluctuations of the backbone dihedral angles increase, as shown in Fig. 3.47E. This plot is essentially identical to Fig. 2b of Ref. [204] – in terms of its sigmoidal shape, the size of the effect ($\approx$5%) and the width of the transition ($\approx$20 K) – where it has been used as a signature indicative for the glass-transition in a protein, myoglobin. The smoothness of the transition also shows that the glass-transition is, of course, not a true phase transition with an infinitely sharp cross-over, neither in our case, nor in the case of larger peptides and proteins. Rather, the highly nonlinear character of the Boltzmann factor causes a rather abrupt rise of the structural flexibility in a relatively narrow temperature range.

In addition, the MD simulations allow studying the change of dynamics at the transition temperature. In order to identify the essential dynamics of the multidimensional system in terms of the most relevant collective coordinates, we performed a principal component analysis of the backbone dihedral angles [207], and characterized the timescale of the peptide fluctuations by considering the autocorrelation functions of the first few principal components [204]. Interestingly, for all temperatures, these autocorrelation functions could be well fitted by a stretched exponential function, $\exp(-t/\tau)^{\beta}$, with one common stretching factor $\beta = 0.5$. Stretched exponential relaxation is frequently used as indicative for a glassy state [199, 206]. Fig. 3.47D displays the decay times τ of the first two principal components as a function of temperature. As expected, the fluctuations are faster at higher temperatures (Fig. 3.47D) and their amplitude increases as well (Fig. 3.47E). The relaxation time of the first principal component shows a peak at the transition temperature, whereas the remaining principal components exhibit a temperature dependence similar to the second component with a step-like drop. The small stretching factor $\beta = 0.5$ is responsible for the fact these fluctuations have a considerable contribution on a few-picosecond timescale (Fig. 3.47D, inset), although the overall kinetics described by τ is much slower. The amount of these fast fluctuations rises steeply above the transition temperature, in accordance with recent photon echo experiments by Fayer and coworkers [195], who observed an abrupt rise of the homogeneous dephasing rate of vibrational probes embedded in proteins (homogeneous dephasing is caused by exactly such fast fluctuations with subpicosecond correlation times).

The hallmark of a glass transition is the ruggedness of the free energy landscape in relation to temperature [199]. Below the transition temperature T_g, various conformations of the system are trapped in different energy basins, whereas thermal energy is sufficient above T_g to overcome the barriers separating these wells and conformations may therefore interchange more quickly. To understand how this effect comes about, the free energy landscape of the peptide along a linear combination of its first two principal components is depicted in Fig. 3.47F, inset. The free energies associated with two local minima, as well as the barrier between them, changes only little with temperature, indicating that there is no large entropic contribution to the free energy. Due to the rise in thermal energy, though, the number of interbasin transitions shown in Fig. 3.47F increases significantly when the temperature approaches $T_g \approx$270 K. Moreover, these transitions occur on a timescale of a few picoseconds, which is also the time scale of energy transport. The temperature dependence of the interbasin transitions thus provides a direct link between the free energy landscape and the efficiency of heat transport capabilities.

3.8.5 Discussion and Conclusion

Based on the above considerations, we can explain our observations as follows. The energy initially deposited through the impact event of the isomerizing azobenzene moiety will be distributed over various normal modes of mainly site #1 in a rather randomized, unspecific manner [55, 59]. The fraction of the energy contained in low-frequency modes will propagate through the helix relatively efficiently, since these low-frequency modes tend to be delocalized over large parts of the helix [111, 112, 194, 208]. For a regular backbone structure, like the 3_{10}-helix, these low-frequency modes are expected to be phonon-like, and hence energy will be transported ballistically. However, this mechanism applies only for a relatively small fraction of the total energy. The majority will be contained in high-frequency modes which localize to single sites, and hence, cannot directly contribute to the transport. At low temperatures, at which the molecule is rigid on the timescale of the experiment, vibrational energy redistribution is inefficient, and little possibility of re-feeding energy from localized high-frequency modes into transporting low-frequency modes exists. As the temperature increases above the glass transition, the molecule becomes more flexible. As a result, vibrational eigenstates are constantly remixing and energy redistribution becomes significantly more efficient, opening a channel for this re-feeding. In addition, the onset of inter-basin large amplitude motion with high anharmonicity further enhances intramolecular vibrational energy redistribution (IVR) when approaching T_g [194]. Energy relaxation is probabilistic and energy transport now will be diffusive-like in the sense that it can be fitted by a master equation depicted in Fig. 3.46, top panel. In agreement with our previous paper [59], we however conclude that the rate-limiting step in energy transport is not the transport itself (which is expected to be ballistic on this short length scales [156]), but the re-feeding of energy into a relatively small subset of transporting modes. Similar cojnclusion have been drawn for the transport through a bridged azulene-anthracene compound [127].

Like in our model system, an energy equivalent of a visible photon is dissipated on an ultrafast sub-picosecond timescale also in many photobiological processes such as the photoisomerization of retinal in rhodopsin during the process of vision [209], or the quenching of excitation energy in antenna complexes by carotenoids in the photosynthetic apparatus [210]. A similar situation is expected for newly developed molecular electronic devices or nanostructures. Such processes result in enormous temperature gradients as large as many 100 K over length scales of a few chemical bonds only. Under these extreme conditions, heat transport is no longer diffusive in the same way as known from macroscopic physics. This is since thermalization *within* an individual building block of a macromolecule is not necessarily significantly faster than thermalization *between* building blocks. Here, we have outlined a concept how one can regulate energy transport properties of molecular devices under these extreme conditions by engineering the flexibility of their components. Nature might have applied these concepts to optimize ultrafast photobiological processes, and the same might be relevant for man-made molecular electronic devices.

Acknowledgement: We wish to thank David Leitner for numerous instructive discussions, Rolf Pfister for part of the synthesis of the molecule, and Nadja Bross for significant help with the NMR measurements. The work has been supported by the Netherlands Organisation for Scientific Research (NWO), the "Forschungskredit" of the University Zürich, the Swiss National Science Foundation (Grant 200020-115877), the Frankfurt Center for Scientific Computing, and the Deutsche Forschungsgemeinschaft.

Chapter 4

Appendix

4.1 Matrix Preparation

As a first step the gaseous precursors are prepared. HN_3 is prepared as a product of the following reaction: $NaN_3 + H_3PO_4 \rightarrow HN_3 + NaH_2PO_4$. HN_3 is released as a gas and is captured in a glass bulb. The oxygen and Kr gases come as readily available commercial substances in pressurized gas bottles. The recipients containing these three gasses are connected through a glass vacuum line with the sample container (see fig. 4.1). In the beginning the sample container is open through valve 2 to the vacuum line whereas all the precursors are closed. The HN_3 source bulb is open (valve 1) till the pressure in the vacuum line equilibrates to 2.4-2.6 m barr. This container as well as the sample container are closed and the vacuum line is evacuated (open valve 3). Connection to the pumps is closed (valve 3) and the oxygen tube is open until the pressure reaches 20-30 m barr. Then the sample container is shortly opened and the pressure in the main vacuum line drops by 10 mbar. Vacuum line is again evacuated and then the Kr bottle is opened until the pressure mounts to 900 - 1000 mbar. The sample container is open very shortly. The pressure usually drops to about 600 mbar. This operation is repeated until upon opening of the sample container the pressure does not drop significantly ($<5\%$). Usually this requires 4-5 repetitions which may increase in the original Kr pressure (i.e. first 900 then 950, 1000, 1050, etc but never exceed 1100 mbar). The sample recipient is then mounted on the matrix deposition line. The glass pipes are vacuumed to pressures of 10^{-5} mbar (by changing all the tubing from teflon to metal the vacuum was improved by an order or magnitude).

The matrix deposition line (fig. 4.1 panel B) with the sample flask is vacuumed for at least 12 h (overnight); matrix depositions with less vacuuming time were always unsuccessful. The vacuum in this line was in the beginning 10^{-5} mbar but it was reduced by use of exclusively metal tubing (no teflon) to 10^{-6} mbar. This line is connected through a valve and a spray like orifice to the cryostat's vacuum system. The cryostat has to be vacuumed for at least 2 days following a service opening, with the pressure being converged; no attempt of cooling should be performed before these requirements are met. Pressure is preferably measured as close as possible to the cryostat and it should normally be in the $4\text{x}10^{-7}$ - $1.5\text{x}10^{-6}$ mbar. One can check if there are any leaks in the cryostat vacuum system by closing a valve (not shown in fig. 4.1) between the pressure sensor and the vacuum pump. If the pressure drops to 10^{-4} mbar in less than 2 min, the chance of having a leak in the system is considerable. The existence of leaks and their origin can be tested with the in-house available *leak test unit*. For better vacuum in the cryostat the vacuum pumps should be connected with the least tubing possible and also with the highest diameter of the tubing. When connecting tubing the best seal that can be achieved is with the help of vacuum. The tube should be put in place, but not fixed there and the vacuum should be let to seal the connection, followed by fixation with the appropriate flange. Turbo pumps should be started only after a low vacuum (rotary, membrane, etc.) pump was active on that specific system for sufficient time in order to achieve a stable pressure. The same procedure should be followed at shutting the system down, the turbo pump should be shut off first, and only after it completely stopped the pre-vacuum pump can be switched off. It is not recommended to shut off the pumps when the cryostat is still at a low temperature (even if it is not cooling).

When the cryostat has reached the desired temperature, the deposition of the matrix can

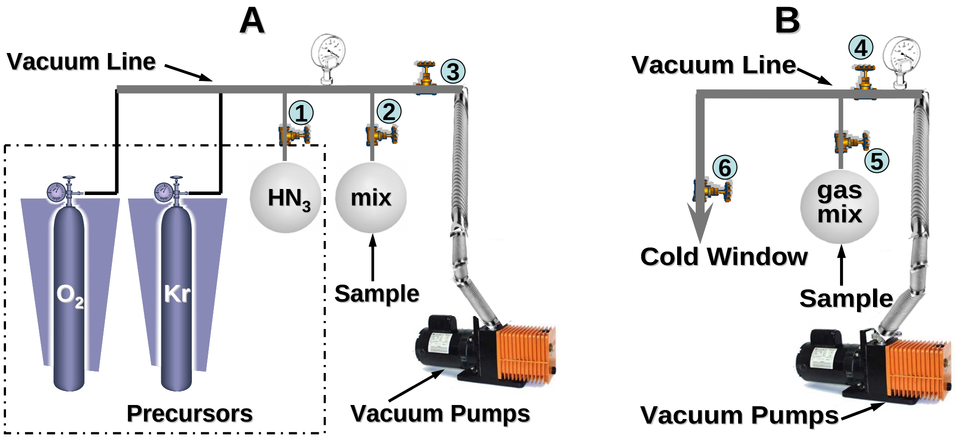

Figure 4.1: Scheme of the sample preparation (A) and deposition (B) process with the O_2, Kr gasses bottles, the HN_3 flask and the sample (where the gasses are mixed) flask along with the vacuum line and pumps

begin. First, one closes the valve to stop vacuuming the deposition line (valve 4), followed by opening the sample container (valve 5). Hence, the sample now is in the deposition line. In order to deposit the matrix one follows the 3317 cm^{-1} absorption line of HN_3. Due to very weak absorbance in the beginning of deposition, one can also follow the pressure indication in the cryostat system. This was found to respond very fast to the opening of the deposition valve (valve 6). Hence, one ideally keeps an eye on the computer monitor to observe the start of deposition and an eye on the pressure meter to see any changes there. At the knob of the deposition valve a special device (extension arm) should be installed that allows very small steps during opening. When beginning deposition the pressure meter should be observed and open valve 6 in order that the pressure jumps from 3 to $5x10^{-7}$ mbar. With this conditions deposition lasts ca. 30 min. Opening the valve more or less the deposition can be made faster or slower, in a trial and error procedure to establish which way leads to best results. Tentatively, a fast deposition rate leads to a more glassy structure whereas a very slow one creates the premisses for a more crystalline sample (all the late matrices were deposited very slowly $\approx$60 min). It is probable that the valve 6 relaxes during the deposition period, especially when this extends over 30, 40 min. In order to avoid this inconvenience the opening of the valve should be performed in several steps, with waiting periods in between (i.e. open the valve a little bit, wait 3 min, open a little bit, wait 3 min, etc. until the valve actually opens and the gaseous sample goes through). After the valve is opened (deposition proceeds) no additional opening, unless necessary, is recommended. If there are needed, additional openings should be performed with extreme caution due to the likelihood of "cracking" the already deposited film.

When performing the temperature dependence measurements the matrices were cracking strongly upon cooling from 30 to 13K. The problem was caused most likely by the different expansion coefficients of the Kr crystal and the CaF_2 substrate. In order to release the stress accumulated by changing the temperature several annealing procedures were undertaken (cooling for 3 degrees was followed by warming up of 1 degree, or variation of these numbers). The success of these procedures was rather limited.

When evaporation a matrix it is best to go up in temperature to the room temperature to avoid resident films of water or other stable compounds that might not evaporate easily. When fast evaporation is performed with the help of the heater, ramping of the temperature should be used in order to keep the heater at a maximum of 80% on the "High" scale. This is a safety procedure to avoid burning the heater (which happen several times before) and all the problems that comes with it. The sample substrate window must be changed or cleaned after several cycles of depositing matrices and evaporating them.

Bibliography

[1] Zewail, A. *Angew. Chem. Int. Ed.* **2000**, *39*, 2586.

[2] Levine, R.; Bernstein, R. *Molecular Reaction Dynamics and Chemical Reactivity;* 1987.

[3] Dantus, M.; Rosker, M.; Zewail, A. *J. Chem. Phys.* **1987**, *87*, 2395.

[4] Rose, T.; Rosker, M.; Zewail, A. *J. Chem. Phys.* **1988**, *88*, 6672.

[5] Hippler, H.; Luther, K.; Troe, J.; Wendelken. *J. Chem. Phys.* **1983**, *79*, 239.

[6] Scherer, N.; Zewail, A. *J. Chem. Phys.* **1987**, *87*, 97.

[7] Scherer, N.; Khundkar, L.; Zewail, R. B. A. *J. Chem. Phys.* **1987**, *87*, 1451.

[8] Whittle, E.; Dows, D. A.; Pimentel, G. C. *J. Chem. Phys.* **1954**, *22*, 1943.

[9] Lewis, G.; Lipkin, D.; Magel, T. *J. Am. Chem. Soc.* **1941**, *63*, 3005.

[10] Pettersson, M.; Lundell, J.; Räsänen, M. *J. Chem. Phys.* **1995**, *102*, 6423.

[11] Khriachtchev, L.; Pettersson, M.; Runeberg, N.; Lundell, J.; Räsänen, M. *Nature* **2000**, *406*, 874.

[12] Pimentel, G. C. *J. Am. Chem. Soc.* **1958**, *80*, 62.

[13] D'Or, L.; Tarte, P. *J. Chem. Phys.* **1951k**, *19*, 1064.

[14] Jones, L. H.; Badger, R. M.; Moore, G. E. *J. Chem. Phys.* **1951**, *19*, 1599.

[15] Baldeschwieler, J. D.; Pimentel, G. C. *J. Chem. Phys.* **1960**, *33*, 1008.

[16] Hall, R. T.; Pimentel, G. C. *J. Chem. Phys.* **1963**, *38*, 1889.

[17] McDonald, P. A.; Shirk, J. S. *J. Chem. Phys.* **1982**, *77*, 2355.

[18] Shirk, A. E.; Shirk, J. S. *Chem. Phys. Let.* **1983**, *97*, 549.

[19] Khriachtchev, L.; Lundell, J.; Isoniemi, E.; Räsänen, M. *J. Chem. Phys.* **2000**, *113*, 4265.

[20] Luckhaus, D. *J. Chem. Phys.* **2003**, *118*, 8797.

[21] Luckhaus, D. *Chem. Phys.* **2004**, *304*, 79.

[22] Agrawal, P. M.; Thompson, D. L.; Raff, L. M. *J. Chem. Phys.* **1994**, *101*, 9937.

[23] Agrawal, P. M.; Thompson, D. L.; Raff, L. M. *J. Chem. Phys.* **1995**, *102*, 7000.

[24] Guan, Y.; Lynch, G. C.; Thompson, D. L. *J. Chem. Phys.* **1987**, *87*, 6957.

[25] Guan, Y.; Thompson, D. L. *Chem. Phys.* **1989**, *139*, 147.

[26] Guo, Y.; Thompson, D. L. *J. Chem. Phys.* **2003**, *118*, 1673.

[27] Qin, Y.; Thompson, D. L. *J. Chem. Phys.* **1992**, *96*, 1992.

[28] Qin, Y.; Thompson, D. L. *J. Chem. Phys.* **1994**, *100*, 6445.

[29] Richter, F.; Hochlaf, M.; Rosmus, P.; Gatti, F.; Meyer, H. D. *J. Chem. Phys.* **2004**, *120*(3), 1306.

[30] Richter, F.; Rosmus, P.; Gatti, F.; Meyer, H. D. *J. Chem. Phys.* **2004**, *120*, 6072.

[31] Richter, F.; Gatti, F.; Leonard, C.; Quere, F. L.; Meyer, H.-D. *J. Chem. Phys.* **2007**, *127*, 164315.

[32] de Mare, G.; Moussaoui, Y. *Int. Rev. Phys. Chem.* **1999**, *18*, 91.

[33] Reiche, F.; Abel, B.; Beck, R. D.; Rizzo, T. R. *J. Chem. Phys.* **2000**, *112*, 8885.

[34] Reiche, F.; Abel, B.; Beck, R. D.; Rizzo, T. R. *J. Chem. Phys.* **2002**, *116*, 10267.

[35] Suter, H. U.; Huber, J. R. *Chem. Phys. Lett.* **1989**, *155*, 203.

[36] Cox, A. P.; Brittain, A. H.; Finnigan, D. J. *Trans. Faraday Soc.* **1971**, *67*, 2179.

[37] Bongartz, A.; Kames, J.; Welter, F.; Schurath, U. *J. Phys. Chem.* **1991**, *95*, 1076.

[38] Varma, R.; Curl, R. F. *J. Phys. Chem.* **1976**, *80*, 402.

[39] Herzberg, G. *Molecular Spectra and Molecular Structure. II. Infrared and Raman Spectra of Polyatomic Molecules;* 1945.

[40] Bredenbeck, J.; Helbing, J.; Hamm, P. *Rev. Sci. Instrum.* **2004**, *75*(11), 4462.

[41] Guilmot., J. M.; Godefroid, M.; Herman, M. *J. Mol. Spec.* **1993**, *160*, 387.

[42] Guilmot., J. M.; Melen, F.; Herman, M. *J. Mol. Spec.* **1993**, *160*, 401.

[43] Schanz, R.; Botan, V.; Hamm, P. *J. Chem. Phys.* **2005**, *122*, 044509.

[44] Botan, V.; Schanz, R.; Hamm, P. *J. Chem. Phys.* **2006**, *124*, 234511.

[45] Botan, V.; Hamm, P. *J. Chem. Phys.* **2008**, *submited.*

[46] Babamov, V.; Lopez, V.; Marcus, R. *J. Chem. Phys.* **1983**, *78*, 5621.

[47] Marcus, R. *J. Chem. Phys.* **2006**, *125*, 194504.

[48] Silverman, D. *Biochim. Biophys. Acta* **2000**, *88*, 1458.

[49] Peters, K.; Cashin, A.; Timbers, P. *J. Am. Chem. Soc.* **2000**, *122*, 107.

[50] Hamm, P. *Chem. Phys.* **2008**, *347*, 503.

[51] Bargheer, M.; Guhr, M.; Schwentner, N. *J. Chem. Phys.* **2002**, *117*, 5.

[52] Frisch, M. J.

[53] Botan, V.; Hamm, P. *J. Chem. Phys.* **2008**, *129*, 044507.

[54] Davydov, A. *Phys. Scr.* **1979**, *20*, 387.

[55] Botan, V.; Backus, E.; Pfister, R.; Moretto, A.; Crisma, M.; Toniolo, C.; Nguyen, P.; Stock, G.; Hamm, P. *Proc. Natl. Acad. Sci.* **2007**, *104*, 12749.

[56] Toniolo, C.; Bonora, G.; Barone, V.; Bavoso, A.; Benedetti, E.; Blasio, B. D.; Grimaldi, P.; Lelj, F.; Pavone, V.; Pedone, C. *Macromolecules* **1985**, *18*, 895.

[57] Naegele, T.; Hoche, R.; Zinth, W.; Wachtveitl, J. *Chem. Phys. Lett.* **1997**, *272*, 489.

[58] Hamm, P.; Ohline, S.; Zinth, W. *J. Chem. Phys.* **1997**, *106*, 519.

[59] Backus, E.; Nguyen, P.; Botan, V.; Pfister, R.; Moretto, A.; Crisma, M.; Toniolo, C.; Stock, G.; Hamm, P. *J. Phys. Chem. B* **2008**, *112*, 9091.

[60] Backus, E.; Nguyen, P.; Botan, V.; Moretto, A.; Crisma, M.; Toniolo, C.; Zerbe, O.; Stock, G.; Hamm, P. *J. Phys. Chem. B* **2008**, *submitted*.

[61] Frei, H.; Pimentel, G. C. *Annu. Rev. Phys. Chem.* **1985**, *36*, 491.

[62] Cotting, R.; Huber, J. R. *J. Chem. Phys.* **1996**, *104*, 6208.

[63] Hamm, P.; Kaindl, R. A.; Stenger, J. *Opt. Lett.* **2000**, *25*, 1798.

[64] Witonsky, S. K.; Canagaratna, M. R.; Coy, S. L.; Steinfeld, J. I.; Field, R. W.; Kachanov, A. A. *J. Chem. Phys.* **2001**, *115*, 3134.

[65] Siano, D.; Metzler, D. *J. Chem. Phys.* **1969**, *51*, 1856.

[66] Finnigan, D. J.; Cox, A. P.; Brittain, A. H.; Smith, J. G. *J. Chem. Soc. Faraday Trans. II* **1972**, *68*, 548.

[67] Groenenboom, G. C.; Colbert, D. T. *J. Chem. Phys.* **1993**, *99*, 9681.

[68] Raff, L. M. *J. Chem. Phys.* **1991**, *95*, 8901.

[69] Talik, T.; Tokhadze, K. G.; Mielke, Z. **2000**, *2*, 3957.

[70] Hesselink, W. H.; Wiersma, D. A. *Phys. Rev. Lett.* **1979**, *43*, 1991.

[71] Barnes, A. J. *Faraday Discuss. Chem. Soc.* **1988**, *86*, 45.

[72] Mukamel, S. *Principles of Nonlinear Optical Spectroscopy;* Oxford University Press: Oxford, 1995.

[73] Since the 30% for the total quantum yield is experimentally better defined than the 10% quantum yield reported in Ref. [43], and since the two steps in Fig. 3.14 have roughly the same size, we tentatively correct the yield of the fast isomerization step to 15%.

[74] A value of I_{trans}/I_{cis}=1.87 was reported in Ref. [16].

[75] Guhr, M.; Schwentner, N. **2005**, *7*, 760.

[76] Kosic, T. J.; Cline, R. E.; Dlott, D. D. *J. Chem. Phys.* **1984**, *81*, 4932.

[77] We learned in the meanwhile that the value of 0.2 cm−1 we reported in Ref. [43] for the direct coupling between ν_1 and $8\nu_6$ might be too large (the quantum calculation was not converged with respect to this coupling). We therefore now assume that the transfer between the initially pumped ν_1 and the reactive ν_6 proceeds via one or more intermediate steps..

[78] Only half of this density of states has right symmetry. However, we assume that thermal excursions of the system break the symmetry to an extent large enough that all states get involved at some instant of time..

[79] Finlayson-Pitts, B. J.; Jr., J. N. P. *Chemistry of the Upper and Lower Atmosphere;* 1999.

[80] Seinfeld, J. H.; Pandis, S. N. *Atmosferic Chemistry and Physics;* 1998.

[81] Le, H. M.; Raff, L. M. *J. Chem. Phys.* **2008**, *128*, 194310.

[82] Mielke, Z.; Talik, T.; Tokhadze, K. G. *J. Mol. Struct.* **1999**, *484*, 207.

[83] Slack, G. A. *Phys. Rev.* **1961**, *122*, 1451.

[84] Dudkin, V. V.; Gorodilov, B. Y.; Krivchikov, A. I.; Manzhelii, V. G. *Low Temp. Phys.* **2000**, *26*, 762.

[85] Klein, M. L.; Venables, J. A. *Rare gas solids;* Academic Press, London, 1977.

[86] Fayer, M. *Annu. Rev. Phys. Chem.* **2001**, *52*, 315.

[87] Woutersen, S.; Emmerichs, U.; Nienhuys, H.-K.; Bakker, H. J. *Phys. Rev. Lett.* **1998**, *81*, 1106.

[88] Peterson, K. A.; Rella, C. W.; Engholm, J. R.; Schwettman, H. A. *J. Phys. Chem. B* **1999**, *103*, 557.

[89] Laubereau, A.; Kaiser, W. *Rev. Mod. Phys.* **1978**, *50*, 607.

[90] Cherqui, M.; Schwentner, N. *Trends Chem. Phys.* **1992**, *2*, 89.

[91] Liu, Q.; Wang, J.-K.; Zewail, A. *J. Phys. Chem.* **1995**, *99*, 11321.

[92] Zadoyan, R.; Sterling, M.; Apkarian, V. *J. Chem. Soc. Farraday Trans.*

[93] Guhr, M.; Bargheer, M.; Schwentner, N. *Phys. Rev. Lett.* **2003**, *91*, 085504.

[94] Andrews, L.; Moskovits, M. *Chemistry and Physics of Matrix Isolated Species;* 1989.

[95] Pettersson, M.; Lundell, J.; Räsänen, M. *J. Chem. Phys.* **1995**, *103*, 205.

[96] Schallmoser, G.; Thoma, A.; Wurfel, B. E.; Bondybey, V. E. *Chem. Phys. Lett.* **1994**, *219*, 101.

[97] Hallam, H. E. *Vibrational Spectroscopy of Trapped Species;* John Wiley and Sons: London, 1973.

[98] Dmitriev, Y. A. *Physica B* **2004**, *352*, 383.

[99] Popov, E.; Kiljunen, T.; Kunttu, H.; Eloranta, J. *J. Chem. Phys.* **2007**, *126*, 134504.

[100] W. Weltner, J. *Magnetic Atoms and Molecules;* 1983.

[101] Dubs, M.; Ermanni, L.; Gunthard, H. H. *J. Mol. Spec.* **1982**, *91*, 458.

[102] Khademi, J.; Kunttu, H.; Apkarian, V. A. *Chem. Phys. Lett.*

[103] Evans, D. J. *Molec. Phys.* **1977**, *34*, 317–325.

[104] Evans, D. J.; Murad, S. *Molec. Phys.* **1977**, *34*, 327–331.

[105] Berne, B. J.; Pecora, R. *Dynamic Light Scattering;* Dover: New York, 2000.

[106] Helbing, J.; Nienhaus, K.; Nienhaus, G. U.; Hamm, P. *J. Chem. Phys.* **2005**, *122*, 124505.

[107] Woutersen, S.; Bakker, H. J. **1999**, *402*, 507.

[108] Gunde, R.; Felder, P.; Günthard, H. H. *Chem. Phys.* **1982**, *64*, 313.

[109] Rohrig, U. F.; Guidoni, L.; Rothlisberger, U. *ChemPhysChem* **2005**, *6*, 1836.

[110] Frutos, L. M.; Andruniow, T.; Santoro, F.; Ferre, N.; Olivucci, M. *Proc. Natl. Acad. Sci.* **2007**, *104*, 7764.

[111] Yu, X.; Leitner, D. M. *J. Phys. Chem. B* **2003**, *107*, 1698–1707.

[112] Yu, X.; Leitner, D. M. *J. Chem. Phys.* **2005**, *122*, 054902.

[113] Leitner, D. M. *Adv. Chem. Phys.* **2005**, *130B*, 205–256.

[114] Henry, E. R.; Eaton, W. A.; Hochstrasser, R. M. *Proc. Natl. Acad. Sci. USA* **1986**, *83*, 8982–8986.

[115] Tesch, M.; Schulten, K. *Chem. Phys. Lett* **1990**, *169*, 97–102.

[116] Okazaki, I.; Hara, Y.; Nagaoka, M. *Chem. Phys. Lett.* **2001**, *337*, 151–157.

[117] Sagnella, D. E.; Straub, J. E. *J. Phys. Chem. B* **2001**, *105*, 7057–7063.

[118] Nguyen, P. H.; Gorbunov, R. D.; Stock, G. *Biophys. J.* **2006**, *91*, 1224–1234.

[119] Fujisaki, H.; Straub, J. E. *Proc. Natl. Acad. Sci. USA* **2005**, *102*, 6726–6731.

[120] Cahill, D. G.; Fischer, H. E.; Klitsner, T.; Swartz, E. T.; Pohl, R. O. *J. Vac. Sci. Technol. A* **1989**, *7*, 1259–1266.

[121] Miller, R. J. D. *Annu. Rev. Phys. Chem.* **1991**, *42*, 581–614.

[122] Lian, T.; Locke, B.; Kholodenko, Y.; Hochstrasser, R. M. *J. Phys. Chem.* **1994**, *98*, 11648–11656.

[123] Li, P.; Champion, P. M. *Biophys. J.* **1994**, *66*, 430–436.

[124] Mizutani, Y.; Kitagawa, T. *Science* **1997**, *278*, 443–445.

[125] Deàk, J. C.; Chiu, H. L.; Lewis, C. M.; Miller, R. J. D. *J. Phys. Chem. B* **1998**, *102*, 6621–6634.

[126] Gao, Y.; Koyama, M.; El-Mashtoly, S. F.; Hayashi, T.; Harada, K.; Mizutani, Y.; Kitagawa, T. *Chem. Phys. Lett.* **2006**, *429*, 239–243.

[127] Schwarzer, D.; Kutne, P.; Schröder, C.; Troe, J. *J. Chem. Phys.* **2004**, *121*, 1754–1764.

[128] Wang, Z. H.; Pakoulev, A.; Dlott, D. D. *Science* **2002**, *296*, 2201–2203.

[129] Deàk, J. C.; Pang, Y. S.; Sechler, T. D.; Wang, Z. H.; Dlott, D. D. *Science* **2004**, *306*, 473–476.

[130] Crisma, M.; Formaggio, F.; Moretto, A.; Toniolo, C. *Biopolymers (Pept. Sci.)* **2006**, *84*, 3–12.

[131] Benedetti, E.; Bavoso, A.; Di Blasio, B.; Pavone, V.; Pedone, C.; Crisma, M.; Bonora, G. M.; Toniolo, C. *J. Am. Chem. Soc.* **1982**, *104*, 2437–2444.

[132] Karle, I. L.; Balaram, P. *Biochemistry* **1990**, *29*, 6747–6756.

[133] Toniolo, C.; Crisma, M.; Formaggio, F.; Peggion, C. *Biopolymers (Pept. Sci.)* **2001**, *60*, 396–419.

[134] Schwyzer, R.; Sieber, P.; Zatsko, K. *Helv. Chim. Acta* **1958**, *41*, 491–498.

[135] Rudolpf-Böner, S.; Krüder, M.; Oesterhelt, D.; Moroder, L.; Nägele, T.; Wachtveitl, J. *Photobiol A: Chem* **1997**, *105*, 235–248.

[136] Toniolo, C.; Benedetti, E. *Trends Biochem. Sci.* **1991**, *16*, 350–353.

[137] Valle, G.; Crisma, M.; Toniolo, C.; Beisswenger, R.; Rieker, A.; Jung, G. *J. Am. Chem. Soc.* **1989**, *111*, 6828–6833.

[138] Toniolo, C.; Polese, A.; Formaggio, F.; Crisma, M.; Kamphuis, J. *J. Am. Chem. Soc.* **1996**, *118*, 2744–2745.

[139] Dahinten, T.; Baier, J.; Seilmeier, A. *Chem. Phys. Lett.* **1998**, *232*, 239–245.

[140] Laubereau, A.; Kaiser, W. *Rev. Mod. Phys.* **1978**, *50*, 607–665.

[141] Sukowski, U.; Seilmeier, A.; Elsaesser, T.; Fischer, S. F. *J. Chem. Phys.* **1990**, *93*, 4094–4101.

[142] The temperature difference used in Fig. 3.33 was 10 K and was down-scaled to an effective temperature difference of ≈0.5 K. This roughly corresponds to the expected temperature jump in the time resolved experiment after the pump energy is dissipated completely into the bulk solvent..

[143] Pimentel, G. C.; McClellan, A. *The Hydrogen Bond;* Freeman: San Francisco, CA, 1960.

[144] Phillips, C. M.; Mizutani, Y.; Hochstrasser, R. M. *Proc. Natl. Acad. Sci. USA* **1995**, *92*, 7292–7296.

[145] In a NVE simulation, the change of the solvent energy can be calculated via $\Delta E_{\mathrm{solv}}(t) = E_{\mathrm{mol}}(0) - E_{\mathrm{mol}}(t)$, where $E_{\mathrm{mol}}(t)$ is the energy of PAZ-Aib$_8$-OMe. To roughly estimate the kinetic part of the solvent energy, $E_{\mathrm{solv}}(t) \equiv \frac{1}{2}\Delta E_{\mathrm{solv}}(t)$ was plotted in Fig. 3.35a..

[146] Nguyen, P. H.; Stock, G.; Mittag, E.; Hu, C.-K.; Li, M. S. *Proteins* **2005**, *61*, 796–808.

[147] Nystrom, R. F.; Brown, W. G. *J. Am. Chem. Soc.* **1947**, *69*, 2548–2549.

[148] Shine, H. J.; Zmuda, H.; Kwart, H.; Horgan, A. G.; Brechbiel, M. *J. Am. Chem. Soc.* **1982**, *104*, 5181–5184.

[149] Li, C. H. *Chem. Abstr.* **1963**, *59*, 10239e–10240e.

[150] Carpino, L. A. *J. Am. Chem. Soc.* **1993**, *115*, 4397–4398.

[151] van der Spoel, D.; Lindahl, E.; Hess, B.; Groenhof, G.; Mark, A. E.; Berendsen, H. J. C. *J. Comput. Chem.* **2005**, *26*, 1701–1718.

[152] van Gunsteren, W. F.; Billeter, S. R.; Eising, A. A.; Hünenberger, P. H.; Krüger, P.; Mark, A. E.; Scott, W. R. P.; Tironi, I. G. *Biomolecular Simulation: The GROMOS96 Manual and User Guide;* Vdf Hochschulverlag AG, ETH Zürich: Zürich, 1996.

[153] Tironi, I. G.; van Gunsteren, W. F. *Mol. Phys.* **1994**, *83*, 381–403.

[154] Nguyen, P. H.; Mu, Y.; Stock, G. *Proteins* **2005**, *60*, 485–494.

[155] Nguyen, P. H.; Stock, G. *Chem. Phys.* **2006**, *323*, 36–44.

[156] Wang, Z.; Carter, J. A.; Lagutchev, A.; Koh, Y. K.; Seong, N.-H.; Cahill, D. G.; Dlott, D. D. *Science* **2007**, *317*, 787–790.

[157] Kuciauskas, D.; Wohl, C. J.; Pouy, M.; Nasai, A.; Gulbinas, V. *J. Phys. Chem. B* **2004**, *108*, 15376.

[158] Hamm, P.; Kaindl, R. A.; Stenger, J. *Opt. Lett.* **2000**, *25*, 1798–1800.

[159] Lindahl, E.; Hess, B.; v. d. Spoel, D. *J. Mol. Mod.* **2001**, *7*, 306.

[160] Nguyen, P. H.; Stock, G. *J. Chem. Phys.* **2003**, *119*, 11350–11358.

[161] Schinke, R. *Photodissociation Dynamics;* University Press: Cambridge, 1993.

[162] Darden, T.; York, D.; Pedersen, L. *J. Chem. Phys.* **1993**, *98*, 10089.

[163] The temperature difference used was 10 K and was downscaled to an effective temperature difference of 0.015 K. This roughly corresponds to the expected temperature jump in the time-resolved experiment after the pump energy is dissipated completely into the bulk solvent.

[164] Woutersen, S.; Mu, Y.; Stock, G.; Hamm, P. *Proc. Natl. Acad. Sci. USA* **2001**, *98*, 11254–11258.

[165] Peterson, K. A.; Rella, C. W.; Engholm, J. R.; Schwettman, H. A. *J. Phys. Chem. B* **1999**, *103*, 557–561.

[166] We assume that the measured relative bleach amplitudes are directly related to the corresponding calculated site-specific kinetic energy ratios $A_n(t) = (E_n(t) - E_n(100ps)/(E_1(t) - E_1(100ps))$, where $n = 3$ and 5 labels the peptide unit and the long time limit was subtracted in both experiment and theory..

[167] Krimm, S.; Bandekar, J. *Adv. Protein Chem.* **1986**, *38*, 181–364.

[168] Torii, H.; Tasumi, M. *J. Chem. Phys.* **1992**, *96*, 3379–3387.

[169] Hamm, P.; Lim, M.; Hochstrasser, R. M. *J. Phys. Chem. B* **1998**, *102*, 6123–6138.

[170] Fang, C.; Hochstrasser, R. M. *J. Phys. Chem. B* **2005**, *109*, 18652–18663.

[171] Jansen, T. L.; Knoester, J. *J. Biophys.* **2008**, *94*, 1818.

[172] Anderson, P. W. *Phys. Rev. B* **1958**, *109*, 1492.

[173] Kurochkin, D. V.; Naraharisetty, S. R. G.; RubtsovĘ, I. V. *Proc. Natl. Acad. Sci. USA* **2007**, *104*, 14209Ű–14214.

[174] Allen, P. B.; Feldman, J. L. *Phys. Rev. B* **1993**, *48*, 12581.

[175] Buchner, M.; Ladanyi, B. M.; Stratt, R. M. *J. Chem. Phys.* **1992**, *97*, 8522.

[176] Keyes, T. *J. Phys. Chem. A* **1997**, *101*, 2921.

[177] Gezelter, J. D.; Rabani, E.; Berne, B. J. *J. Chem. Phys.* **1997**, *107*, 4618.

[178] Hill, J. R.; Dlott, D. D. *J. Chem. Phys.* **1988**, *89*, 830.

[179] Rey, R.; Moller, K. B.; Hynes, J. T. *Chem. Rev.* **2004**, *104*, 1915.

[180] Stock, G.; Thoss, M. *Adv. Chem. Phys.* **2005**, *134*, 243.

[181] Doltsinis, N. L.; Marx, D. *Phys. Rev. Lett.* **2002**, *88*, 166402.

[182] Toniolo, A.; Ciminelli, C.; Persico, M.; Martinez, T. J. *J. Chem. Phys.* **2005**, *123*, 234308.

[183] Nonnenberg, C.; Gaub, H.; Frank, I. *ChemPhysChem* **2006**, *7*, 1455.

[184] Polland, H.-J.; Franz, M. A.; Zinth, W.; Kaiser, W.; Koeling, E.; Oesterhelt, D. *Biophys. J.* **1986**, *49*, 651.

[185] Mathies, R. A.; Cruz, C. H. B.; Pollard, W. T.; Shank, C. V. *Science* **1988**, *240*, 777.

[186] Wang, Q.; Schoenlein, R.; Peteanu, L.; Mathies, R.; Shank, C. *Science* **1994**, *266*, 422–424.

[187] Martin, J. L.; Migus, A.; Poyart, C.; Lecarpentier, Y.; Astier, R.; Antonetti, A. *Proc. Natl. Acad. Sci.* **1983**, *80*, 173.

[188] Demmig-Adams, B. *Biochim. Biophys. Acta* **1990**, *1*, 1020.

[189] Scott, A. C. *Phys. Reports* **1992**, *217*, 1.

[190] Xie, A.; van der Meer, L.; Hoff, W.; Austin, R. H. *Phys. Rev. Lett.* **2000**, *84*, 5435–5438.

[191] Champion, P. M. *Science* **2005**, *310*, 980–982.

[192] Ota, N.; Agard, D. A. *J. Mol. Biol.* **2005**, *351*, 345–354.

[193] Chang, C. W.; Okawa, D.; Majumdar, A.; Zettl, A. *Science* **2006**, *314*, 1121–1124.

[194] Leitner, D. *Annu. Rev. Phys. Chem* **2008**, *59*, 233–259.

[195] Fayer, M. D. *Annu. Rev. Phys. Chem.* **2001**, *52*, 315–356.

[196] Hartmann, H.; Parak, F.; Steigemann, W.; Petsko, G. A.; Ponzi, D. R.; Frauenfelder, H. *Proc. Natl. Acad. Sci. USA* **1982**, *79*, 4967–4971.

[197] Doster, W.; Cusack, S.; Petry, W. *Nature* **1989**, *337*, 754–756.

[198] Rasmussen, B. F.; Stock, A. M.; Ringe, D.; Petsko, G. A. *Nature* **1992**, *357*, 423–424.

[199] Onuchic, J. N.; Luthey-Schulten, Z.; Wolynes, P. G. *Annu. Rev. Phys. Chem.* **1997**, *48*, 545–600.

[200] Réat, V.; Dunn, R.; Ferrand, M.; Finney, J. L.; Daniel, R. M.; Smith, J. C. *Proc. Natl. Acad. Sci. USA* **2000**, *97*, 9961–9966.

[201] Lee, A. L.; Wand, A. J. *Nature* **2001**, *411*, 501–504.

[202] Fenimore, P. W.; Frauenfelder, H.; McMahon, B. H.; Parak, F. G. *Proc. Natl. Acad. Sci. USA* **2002**, *99*, 16047–16051.

[203] Cornicchia, E.; Marconi, M.; Onori, G.; Paciaroni, A. *Biophys. J* **2006**, *91*, 289–297.

[204] Moritsugu, K.; Smith, J. C. *J. Phys. Chem. B* **2006**, *110*, 5807.

[205] Hansmann, U. H. E.; Okamoto, Y.; Onuchic, J. N. *Proteins* **1999**, *34*, 472–483.

[206] Hansmann, U. H. E.; Onuchic, J. N. *J. Chem. Phys.* **2001**, *115*, 1601–1606.

[207] Mu, Y. G.; Nguyen, P.; Stock, G. *Proteins* **2005**, *58*, 343–357.

[208] Segal, D.; Nitzan, A.; Hänggi, P. *J. Chem. Phys.* **2003**, *119*, 6840–6855.

[209] Kukura, P.; McCamant, D. W.; Yoon, S.; Wandschneider, D. B.; Mathies, R. A. *Science* **2005**, *310*, 1006–1009.

[210] Cerullo, G.; Polli, D.; Lanzani, G.; Silvestri, S. D.; Hashimoto, H.; Cogdell, R. J. *Science* **2002**, *298*, 2395–2398.

Acknowledgements

Writing a thesis at the end of the PhD studies is always a moment of celebration for the author. Performing matrix spectroscopy involved many lonely nights spent in the lab, yet, I was not alone in this endeavor. In the following I would like to acknowledge few of the people that made it possible. My deepest gratitude goes to Prof. Dr. Peter Hamm for taking me as his graduate student. It is Peter who contributed decisively to the genesis and the energy behind my research projects. I learned a lot from his vast experience and knowledge about lasers, spectroscopy and physics in general. I will never forget his smiling face entering the lab and asking: *And, how is it going?*.

Many thanks go to my former colleague Dr. Roland Schanz with whom I started my HONO studies. I am also grateful to Dr. Jan Helbing for always being there when things did not work. He was for me (and not only) the person to go when I did everything I could to solve a problem, but still did not manage. I also thank dr. Jens Bredenbeck, Dr. Julian Edler for answering the "stupid" beginners questions about the new field I entered by coming to Zürich. Many thanks go to Dr. Viktor Volkov for sharing with me his views about life and religion, Dr. Mariusz Kozinski for being a friendly lab mate, colleague and neighbor. I thank Dr. Cristoph Kolano for the nice office ambiance and for always being there when I needed help. Thanks go to Dr. Ellen Backus for her cheerful attitude and for her example of perseverance in our joined *Heat Transport* project, to Dr. Janne Ihalainen for always being a very supportive colleague. I particulary enjoyed the company of Valentina Cervetto and Harry Bregy with whom I was colleague all my Phd years. I like to acknowledge also the very friendly company of Dr. Paul Kocian with whom I share the office for my first year and with whom I debated a lot of political issues. I also thank Dr. Sean Garrett-Roe for his *english*, editing and conceptional expertise in writing documents. I want also to acknowledge my new colleagues Mathias Bonmarin, Dr. Andresen Esben Ravn, Julien Rehault and Marco Shade for bringing new color to the group.

I thank Rolf Pfister for always promptly synthesizing the compounds I needed, Maja Gossweiler for her cheerful attitude and friendliness. Many thanks go to the people in the workshop: Armin Küne, Roland Zehnder for doing an absolutely excellent job, for their suggestions in different designs and for their understanding of my impatience. Ueli Feusi and Jens Jacobs were always prompt in solving the ubiquitous "computer" problems.

At last, but certainly not the least, I would like to thank my family, especially my wife Irina, for her understanding. She was very patient with me for the moments when I was not sure when I will come home from the lab: in the evening, during the night or the other day. I also thank my parents and my brother for their love and unconditioned support.

Curriculum Vitae

Name: Virgiliu
Surname: Botan
Place and date of birth: Bistrita, Romania, 24.03.1978
Citizenship: Romanian

Education:

2003-pres. *PhD Program*
University of Zürich, Switzerland

2002-2003 *Master Degree*
Technical University of Chemnitz, Germany
Thesis Title :
Sulfur Passivation of GaAs Substrates

1997-2002 *Bachelor in Physics*
"Babes-Bolyai" University, Cluj-Napoca, Romania
Thesis Title :
Magnetic and Electric Properties of $La_xCa_{1-x}MnO_3$ Systems

1993-1997 *High school*
Colegiul Silvania, Zalau, Romania